

**THREE-DIMENSIONAL
MODEL CALIBRATION AND
SENSITIVITY STUDIES**

Y.S. Wu, G. Chen, C. Haukwa, and G.S. Bodvarsson

August 1996

8.1 Introduction

The objective of this Chapter is to provide a comprehensive summary of the 3-D model calibration and sensitivity analysis, as part of our continuous efforts in the development of the three-dimensional unsaturated-zone site-scale model of Yucca Mountain during the fiscal year of 1996. The primary objectives of development of the 3-D site-scale unsaturated-zone model of Yucca Mountain are to develop a reliable and defensible computer model to simulate and investigate the existing natural state of the system, and predict possible future system responses. In order to provide accurate predictions of the mountain conditions, the site-scale model must include the following capabilities:

- Estimate the ambient and future moisture, gas and heat distributions and movement at Yucca Mountain;
- Estimate the percolation fluxes at repository horizons and their spatial and temporal variations;
- Provide a "best" set of hydrogeologic and thermal parameters for Performance Assessment (PA) calculations;
- Evaluate different conceptual models for hydrologic, pneumatic and heat flow;
- Evaluate effects of future climatic changes; and
- Evaluate effects of thermal loading.

As a critical step of model development, a series of model calibrations and sensitivity analyses has been conducted with the 3-D site-scale model this year. The model has been calibrated against available field observation and laboratory data. The sensitivity analyses are used to investigate effects of variations in rock and fault properties, and in model boundary conditions and various issues regarding conceptual models. The purpose of these model calibrations and sensitivity analyses is to enhance the accuracy and to increase the credibility of the site-scale model in estimating the current and predicting future conditions. Also these studies are necessary to provide critical data and information for total system performance analysis (TSPA) of the repository.

A substantial amount of model calibration has been performed so far (Ahlers et al., 1995a and b). However, in-depth model calibration studies are still needed as more field data become available and new observation data from the ESF are generated. The model calibration efforts reported in this chapter use saturation and moisture tension data, gas flow data, geothermal conditions and heat flow data, perched water data, and environmental isotope data. The environmental isotope data include isotopic concentrations in liquid and gas phases, as well as isotopes measured in fracture coatings which provide age estimates. The uncertainties associated with the input data set and the results of the model calibrations are also evaluated.

The TOUGH2 code (Pruess 1991) was used and the data on the perched water ages was used (Rousseau et al., 1996; Yang et al., 1996) to calibrate the site-scale model against the observation data of moisture and water potentials from 7 boreholes (USW UZ-14, UE-25 UZ-16, USW NRG-6, USW NRG-7a, USW SD-7, USW SD-9, and USW SD-12). We have developed several three-dimensional models which incorporate the observed moisture and geothermal data. All these models are based on the current 3-D site-scale model grid. In these simulations, both the generalized effective continuum method (ECM) (Chapter 4, Wu et al.) and dual-permeability model have been used to account for fracture and matrix interactions.

Many model simulations have been performed to quantify the sensitivity of the model to the parameters and assumptions that were used in the model preparations. The results of these studies will be used to provide direction for future modeling work and field data collection efforts in order to reduce uncertainties in future modeling studies. The sensitivity studies related to model set-up and input parameters include: infiltration rates, rock parameter studies, fracture/matrix flow, boundary conditions, and fault representations.

Additional sensitivity studies have also been performed to assess the effects of the chosen numerical modeling approaches used to handle fracture/matrix interactions in welded and unwelded tuffs of the unsaturated zone. Comparison studies have been done of the treatment of fracture/matrix flow using the generalized ECM approach, as discussed in Chapter 4 (Wu et al.), and the dual-permeability approach (Pruess, 1991). The comparative studies are conducted using the full site-scale model grid under the same model conditions. The results of the model predictions from the two modeling approaches are compared in terms of moisture distributions and movement within the mountain, and it has been shown that the ECM approach gives almost identical simulation results, when compared with the predictions by the dual-permeability model, under the modeling conditions and conceptual model used.

Three different infiltration maps have been incorporated into the UZ site-scale model. The first one uses a uniform infiltration rate of 0.1 mm/yr over the entire mountain, and this case is intended to form a basis for comparisons. The

second one is a spatially distributed infiltration map from USGS (Hevesi and Flint, 1995) with an averaged infiltration value of 0.34 mm/yr over the model domain. The third map is the most recent (Flint, Hevesi, and Flint, 1996), and has a much higher average infiltration rate of 4.4 mm/yr over the model area.

The rock properties for fractures and matrix used in modeling studies in each geological unit are those estimated using the ITOUGH2 code, and the detailed procedures for parameter estimation are described in Chapter 3 (Bandurraga et al.). The inverse modeling studies using ITOUGH2 (Chapter 3) result in several different sets of rock properties, which depend on the initial input to the code, the quality of the observed measurements, and the infiltration conditions. As part of sensitivity studies, four different sets of rock properties are implemented and tested in the simulations to investigate effects of rock properties variations and heterogeneity.

Even though substantial progress was made in the site characterization studies of Yucca Mountain over the past few years (Wittwer et al., 1995; Ahlers et al., 1995a and b; and Rousseau et al., 1996), many uncertainties still remain with regard to properties and roles of fault zones in affecting moisture flow through the mountain. In an effort to better understand the roles played by the major faults, we have conducted a series of sensitivity studies of fault properties on lateral and vertical moisture movement. The fault properties tested are derived from the pneumatic data analysis, and inverse model analysis results for the corresponding geological formations, as well as assumed values.

In all the simulations conducted for 3-D model calibrations and sensitivity analyses, the model predicted moisture distributions match well with observed water saturation profiles, and are in reasonable agreement with observed water potential or capillary pressure data from the 7 boreholes. The heat flow through the unsaturated zone simulated by the models is also in reasonable match with field measurements. By analyzing the computed downward flow through fractures and matrix rock, we are also able to match the water age data reasonably well at the areas near boreholes UZ-1/14 and SD-7.

Based on the confidence built through the model calibration and sensitivity analysis, we present simulation results and predictions on (1) lateral fluid movement through the mountain; (2) percolation flux at the repository horizon; (3) recharge maps at the water table, and (4) possible fast water flow pathways from surface to water table.

8.2 QA Status of Data and Computer Software

All the liquid saturation and water potential data from the seven boreholes UZ-14, UZ-16, NRG-6, NRG-7a, SD-7, SD-9, and SD-12 are "Q" data, and the data tracking references are listed in Table 8.2.1. These data have been used in

Three-Dimensional Model Calibration and Sensitivity Studies

this study for rock property estimation and also for 3-D model calibrations of moisture flow.

Borehole	Saturation	Capillary pressure	QA	Reference
SD-7	*	*	Y	YMP DTN GS951108312231.009
SD-9	*	*	Y	YMP DTN GS950308312231.004
SD-12	*		Y	YMP DTN GS950308312231.002
UZ-14	*	*	Y	YMP DTN GS950308312231.005
UZ#16	*		Y	YMP DTN GS940508312231.006
NRG-6	*		Y	YMP DTN GS950608312231.007
NRG-7a	*		Y	YMP DTN GS951108312231.010

where * denotes the data are available.

The perched water zones are identified in five boreholes (UZ-1, UZ-14, SD-7, SD-9 and NRG-7a) in Yucca Mountain. The observations of depths, and relation to lithostratigraphy for perched water at UZ-14, SD-9, and NRG-7a are fully qualified (Rousseau et al., 1996). The perched water locations are used in the report to compare with the model results.

The temperature and heat flow data reported by Sass et al. (1988) were collected prior to implementation of the approved USGS-YMP quality-assurance program, and therefore are "non-Q". These temperature data are used in this study to generate model boundary conditions of temperature at the water table. The heat flow data are also employed to compare with model predictions. However, the surface temperature data from NRG-6 and NRG-7a are "Q" data.

The two infiltration maps used in this Chapter were from the two research reports of USGS (Hevesi and Flint, 1995; and Flint et al., 1996), which are in the process of being "Q'd" by the USGS.

The TOUGH2 code has been used as a primary computer tool in this simulation study, and it has been qualified (QA) for the YMP site characterization studies (Pruess et al., 1996). We also use one additional module, the ECM module of TOUGH2 as discussed in Chapter 3, which has been qualified for use in the YMP (Wu et al., 1996).

8.3 Model Description

8.3.1 Model Domain and Grid

The 3-D site-scale model domain and grid used in this study are shown in Figure 8.3.1 in a plan view. As shown in the figure, the model domain covers a total of surface area of approximate 37 km², extending roughly from borehole G-2, in the north, to borehole G-3, in the south, and from the Bow Ridge fault in the east to about one kilometer west of the Solitario Canyon fault. Figure 8.3.1 shows the numerical grid with increased discretization in the vicinity of the proposed repository. Also shown in Figure 8.3.1 are the locations of the seven boreholes which we will use for our model calibrations.

The model domain covered in the current site-scale model, as shown in Figure 8.3.1, was selected to focus our study at and near the potential repository area and to investigate effects of the major faults on moisture flow around the repository. All the model boundaries are located sufficiently far from the repository so that their effects on the simulation results at the repository are very small. The model domain may be need to be expanded in the future to the north to include the high water gradient effects.

The layering and subdivision of geological units in the numerical grid uses the geological model, discussed in detail in Chapter 2 (Bandurraga et al.). All grid layers have finite thicknesses across the model. The geological formation pinch-outs are represented by specifying the adjacent layer properties in the pinch-out locations. The site-scale model grid has 28 grid layers that represent different geological layers and altered zones in the unsaturated zone of Yucca Mountain. The top of the model is defined by subtracting the alluvium thickness from the topographical map. However, the alluvium unit is used in studies of pneumatic data (Ahlers et al., 1996). The Tiva Canyon unit (TCw) is vertically subdivided into three layers. Some layers are eroded and not present in certain locations. The Paintbrush unit (PTn) is represented using five grid layers with several layers pinching out in certain areas of the model. The Topopah Spring (TSw) uses seven sublayers and an additional three layers for the repository area. The Calico Hills (CHn) has a maximum of eight sublayers, but generally about five in most locations. The bottom boundary of the model is at the water table

Chapter 5 (Haukwa et al.) discusses the scheme and details on the grid generation. As shown in Figure 8.3.1, each grid layer has 983 element blocks, or the three-dimensional grid has 983 vertical grid columns. The total number of element blocks of the grid is 26,833, and the total connections between the blocks are 93,626.

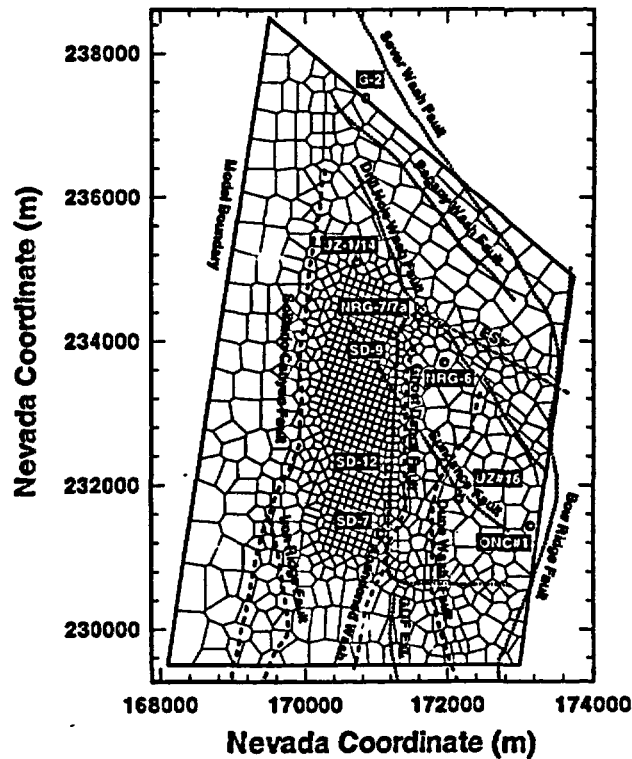


Figure 8.3.1
A plan view of the 3-D site-scale model domain, grid and incorporated major faults.

Several major faults are incorporated explicitly in the model, as shown in Figure 8.3.1. These faults are Solitario Canyon, Iron Ridge, Ghost Dance, Abandoned Wash, and Dune Wash faults. The Bow Ridge fault is treated as a boundary condition along the eastern boundary of the model domain. The faults are represented in the model as vertical zones with consideration of stratigraphic offsets and connections to adjacent gridlayers. The scheme used for generating the fault grid elements was outlined by Wittwer et al. (1995) and also briefly discussed in Chapter 5 (Haukwa et al.).

8.3.2
Modeling Approach

The simulation results presented here were conducted using the TOUGH2 code (Pruess, 1991). Model calibrations, sensitivity analyses and model predictions mostly utilize the steady-state simulations of the 3-D models, under given infiltration rates and other boundary conditions. In addition, transient 3-D simulations were also performed to look at a possible climate change scenario using higher infiltration rates. The numerical modeling approaches for treatment of fracture/matrix flow include both the generalized ECM method (Chapter 4, Wu et al.) and the more rigorous dual-permeability approach. The formulation for the generalized ECM is discussed in Chapter 3 (Wu et al.) for treatment of fracture/matrix flow. In most of the simulation results presented

in this Chapter, the ECM model is used. However, the dual-permeability (dual-k) method was employed to investigate the effects of higher infiltration rates in terms of a possible climate change using the entire site-scale model grid.

It has been a long-debated issue whether the ECM approximation is valid and accurate for use in the site characterization studies of Yucca Mountain. This is because in simulating fluid and heat flow in the fractured, welded tuffs of the Yucca Mountain site it is critical to evaluate fracture and matrix interactions under multi-phase, non-isothermal conditions. There are several methods that have been used for treatment of fracture and porous matrix interactions using a numerical model. These methods include: (1) explicit discrete fracture and matrix treatment; (2) the effective-continuum model approach (ECM); (3) the double- or multiple-porosity method; (4) the dual-permeability method; and (5) more generally, the multiple interacting continua (MINC) method (Pruess and Narasimhan, 1985). The TOUGH2 code provides all these options for modeling fracture/matrix flow. When applied to simulating moisture flow and heat transfer at the mountain, all these approaches require knowledge of fracture and matrix properties and their spatial distribution. These site-specific fracture/matrix parameters, however, are presently not well defined for the tuffs at Yucca Mountain. Currently, only the effective-continuum approach has found wide application because of its simplicity in terms of data requirements and computational intensity.

As implemented in the site-scale model with the TOUGH2 code (See Chapter 4, Wu et al.), the ECM can accommodate two-phase flow in a fracture/matrix system. When applicable, the ECM provides a substantial simplification in description of fluid and heat flow in fractured porous media, and in the requirement of extensive computational efforts. The favorable conditions for this method is when rock matrix blocks are relatively small and permeable, and the fracture network is relatively uniformly distributed. However, the effective-continuum approximation may break down under certain unfavorable conditions, such as for very tight, large, and low permeability rock matrix blocks with rapid transients through surrounding fractures, since it may take a long time to reach equilibrium conditions under such environments.

At Yucca Mountain, the averaged net water infiltration rate into the unsaturated zone has been estimated to be low, on the order of 1 mm /yr. At most, the highest infiltration rates may be up to 10 mm/yr, as suggested by recent studies in certain areas of the mountain (Hudson and Flint, 1995; and Flint, Hevesi and Flint, 1996, in prep.). The percolation flux of water through the mountain is expected to be small in most locations. Therefore, the local hydraulic equilibrium between porous rock matrix and fractures may be a reasonable approximation, when one is interested in the ambient flow conditions. As a result, the ECM may provide reasonable simulation results for predicting the fluid movement and the ambient hydrogeologic conditions. The ECM will be particularly suitable for a situation when a long-term, averaged, or steady-state

solution is to be sought. As concluded by Pruess et al. (1990a,b), the effective-continuum approximation will be applicable when "sufficiently" large space and time scales are considered. Both time and space discretizations in the three-dimensional site-scale unsaturated-zone model are relatively large, and the application of the continuum approach may be justified for time and space scales of interest to the site-scale modeling studies. Issues regarding the proper use of the various numerical approaches including ECM, dual-permeability, dual-porosity and others are evaluated for various processes in Chapter 6 (Doughty et al.).

The water ages determined from isotope data, perched water samples, fracture coatings, and water travel modeling results suggest that the water currently found at Yucca Mountain has been in the subsurface for thousands of years. Under such a large time scale, the ambient moisture flow and distributions at Yucca Mountain can be reasonably approximated using steady-state or near steady-state conditions. This is the reason that we mainly use steady-state simulations in the model calibration and sensitivity analysis studies of this chapter. Another reason is the fact that model results are dependent on poorly constrained transient infiltration events, and it is difficult to decide which transient infiltration conditions should be used to compare with the observed data.

8.3.3 Model Boundary Conditions

The ground surface of the mountain or bottom of the alluvium is taken as the top model boundary, and the water table is treated as the bottom boundary. Both top and bottom boundaries of the model are treated as Dirichlet-type conditions, i.e., constant (but distributed) temperatures, constant (but distributed) gas pressures and constant liquid saturations are specified along the boundary surfaces. In addition to the pressure and temperature conditions, the surface boundary is also subject to water recharge through infiltration, as discussed in the next section.

The constant values of temperatures on the boundaries are determined based on the field observations. For the bottom temperatures at the water table, the temperature values specified were taken and interpolated from the borehole temperature measurement data, reported by Sass et al. (1988). The results of temperature distributions, as implemented in the model, are shown in Figure 8.3.2. The temperature values at the water table are generally higher in the southern part, and lower in the northern part of the model domain. The highest temperatures are near the south-west corner, and the lowest are in the north, close to borehole G-2. The temperature map of the water table is consistent with that of Fridrich et al. (1994), with an averaged value of about 32°C.

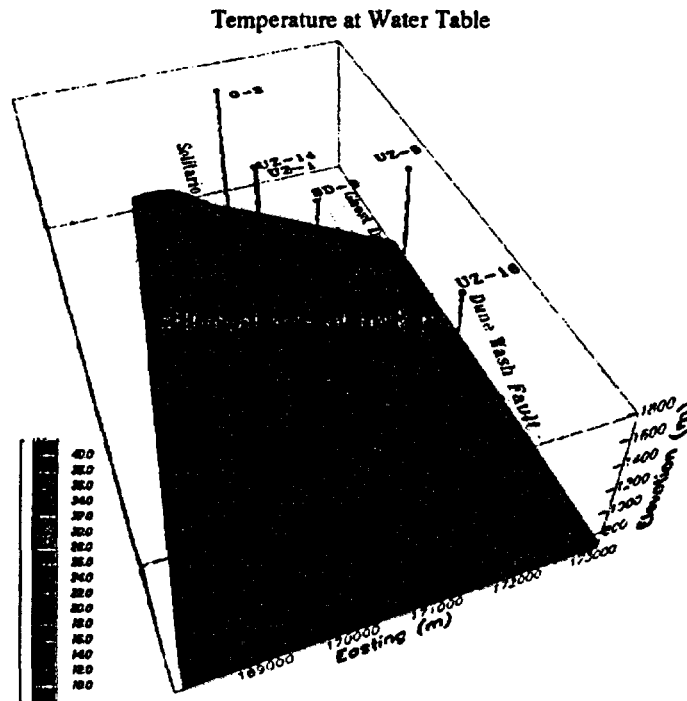


Figure 8.3.2
Temperature map at the water table for the bottom temperature boundary condition of the 3-D site-scale model.

To account for differences in temperature on the mountain at different elevations, we use both observed wellhead temperature data and the equation which correlates temperature with elevation. The surface temperatures are estimated using observed temperature data from boreholes USW NRG-6 and NRG-7a, which have more than a year of continuous temperature monitoring data (Rousseau et al., 1996). The following formulation (Lu and Kwicklis, 1995) is also used,

$$T_a = T_{ref} + \lambda(Z_{ref} - Z) \quad (8.3.3.1)$$

where T_a is ground surface temperature at elevation Z , T_{ref} is temperature at reference elevation Z_{ref} , and λ is atmospheric lapse rate ($^{\circ}\text{C}/\text{m}$).

The annually averaged temperature at NRG-6 is 18.23°C , and at NRG-7a, it is 17.78°C (Rousseau et al., 1996). Using the surface elevation data and the annually averaged temperatures at the two boreholes, we can calculate the atmospheric lapse rate, $\lambda \approx 0.01^{\circ}\text{C}/\text{m}$ at Yucca Mountain. Then the surface temperatures are determined using Equation (8.3.3.1) and elevations of the top model meshes. The resulting surface temperature distributions are shown in

Figure 8.3.3. The figure shows that there are relatively lower temperatures in the northern part and along the ridge of the mountain, where higher elevations exist, and the temperatures are at the lower teens in °C. In the rest of the model domain, Figure 8.3.3 indicates an average temperature of 16 - 18 °C.

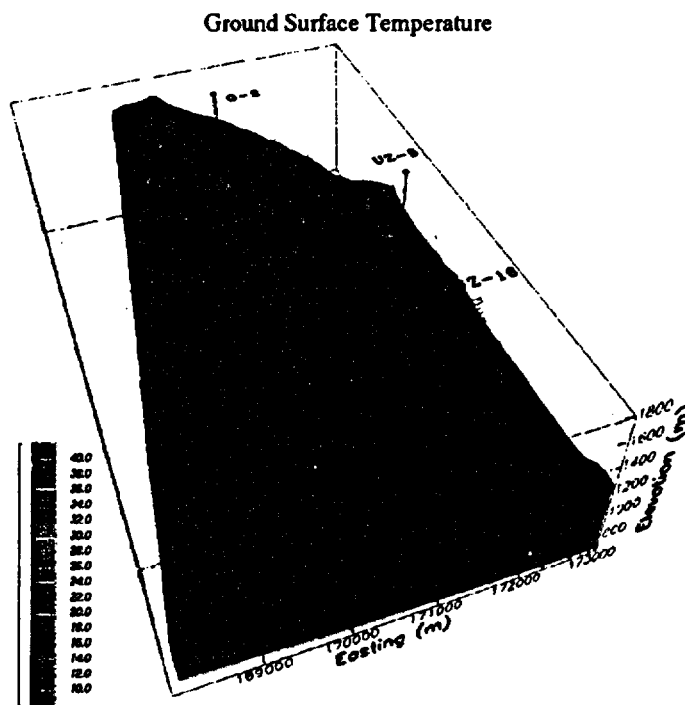


Figure 8.3.3
Temperature map on the ground surface for the top temperature boundary condition of the 3-D site-scale model.

The gas pressures at the bottom boundaries are calculated using the observed gas pressure value (Ahlers et al., 1995a). The water table, as the bottom boundary of the site-scale model, is a relatively flat, stable surface. The water table, in the eastern part to the Solitario Canyon fault, has an approximate elevation of 730 m. However, the water table rises 40 meters across the Solitario Canyon fault to the west. The gas pressures are estimated using a pressure value of 0.92 bars at an elevation of 730 m. All the gas pressures of the bottom boundary elements are then calculated using elevations relative to the 730 m elevation for each boundary grid block, assuming that hydrostatic conditions exist. The water table treatment in this Chapter follows mostly the work of Wittwer et al. (1995), and the apparent high potentiometric surface in the north of the model boundary is not considered.

Surface gas pressures are determined by running TOUGH2 to steady-state conditions under given temperature, bottom pressure, and surface infiltration conditions. This is necessary to generate a steady-state, equilibrated gas pres-

sure boundary to avoid artificial air flow or circulation, which may happen when non-equilibrated pressures are imposed on the ground surface boundaries.

All the lateral boundaries, as shown in Figure 8.3.1, are treated as no-flow, or closed boundaries, which are default options for the TOUGH2 code. This treatment should be reasonable for the eastern boundary, which is along the Bow Ridge fault, since high vertical permeability and lower capillary forces are expected for the fault. For the southern, western, and northern, lateral boundaries, no-flow boundaries may have little effects on moisture flow within and near the potential repository areas, since these boundaries are far away from the repository.

8.4 *Implementation of Different Infiltration Maps*

Infiltration, or net water infiltration, through the top soil layer of the mountain is the most significant factor affecting the overall hydrological and thermo-hydrologic behavior of the unsaturated zone. The net infiltration is the ultimate source of groundwater recharge and percolation through the unsaturated zone, and provides the water for flow and transport mechanisms for radionuclides from repository to water table. Net infiltration at Yucca Mountain is highly variable spatially because there exist significant variations in soil cover and different mechanisms controlling the net infiltration from the precipitation (Flint and Flint, 1994, Hudson and Flint, 1995). Even though substantial research efforts have been made in the past to determine the net infiltration over the mountain, direct measurements have proven impossible due to the low moisture flux resulting from the low precipitation and high potential evapotranspiration rates of the area.

Most of the effort on estimating the net infiltration at the site has been based on the average annual precipitation using an indirect method, with results ranging between 0 to more than 20 mm/yr. The spatial variability of net infiltration at the site estimated by Flint and Flint (1994) ranged from 0.02 to 13.40 mm/yr. Their estimation was based on hydraulic property measurements of the bedrock units close to the surface, the steady state water content, and an assumed unit gradient. In 1995, their work was extended to develop a map to describe the spatial distribution of shallow infiltration at Yucca Mountain (Hudson and Flint, 1995). This study, based on the neutron moisture meter data from 84 locations conducted over ten years and a multiple linear regression model, gave a much higher net infiltration over a modeled area of 150 km², with an average of 21.6 mm/yr.

A recent study for estimating precipitation and recharge in the Yucca mountain region by Hevesi and Flint (1995) provided another infiltration map, which gives an averaged value of 0.35 mm/yr net infiltration over the site-scale model

domain. The infiltration map was generated using the geostatistical Maxey-Eakin model. Figure 8.4.1 shows the distribution of net water infiltration over the model domain from this infiltration map. High infiltration rates are noticed at the northern part of the model domain and along the south-north ridge of the mountain. Much lower infiltration can be seen along or near the Bow Ridge fault, the eastern part, and near the south-west corner of the model area. This infiltration map has been implemented and used in our model calibration and sensitivity analysis studies, and it is referred as to Map #1 in this Chapter.

The most recent infiltration map has been recently supplied to us from the USGS (Flint, Hevesi and Flint, July, 1996). This new map is also used for the modeling studies in this report. Figure 8.4.2 shows how the net infiltration is distributed over the site-scale model domain. The averaged infiltration rate is 4.4 mm/yr, which is more than ten times higher than that shown in Figure 8.4.1. However, the spatial distributions of infiltration, in Figure 8.4.2, are very similar to that in Figure 8.4.1, with higher recharge values in the north part of the model domain and along the mountain ridge from south to north. This infiltration is referred as to Map # 2 in this study.

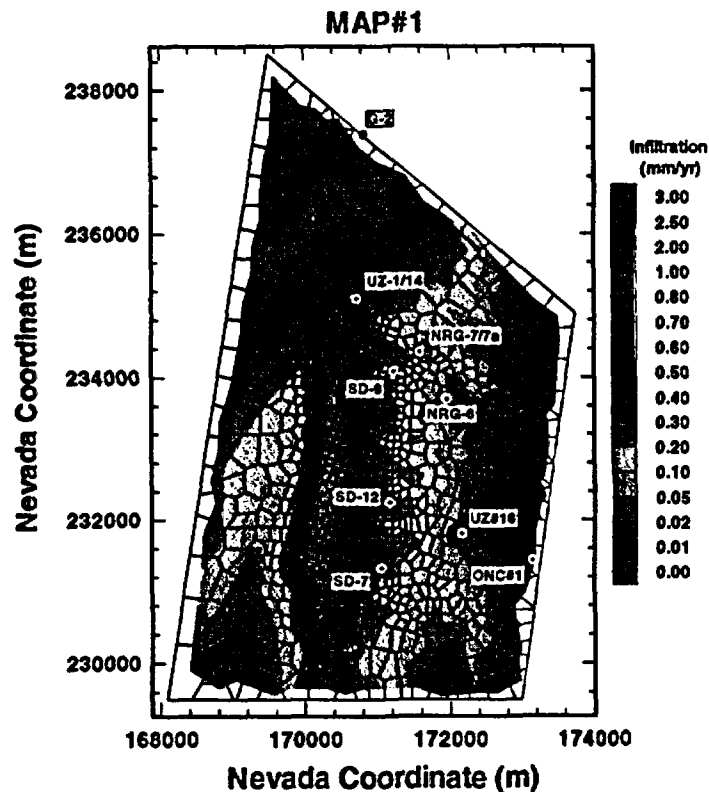


Figure 8.4.1
Net infiltration map (Map # 1) showing infiltration rates and distributions over the model domain of Yucca Mountain, based on Maxey-Eakin model (Hevesi and Flint, Nov., 1995).

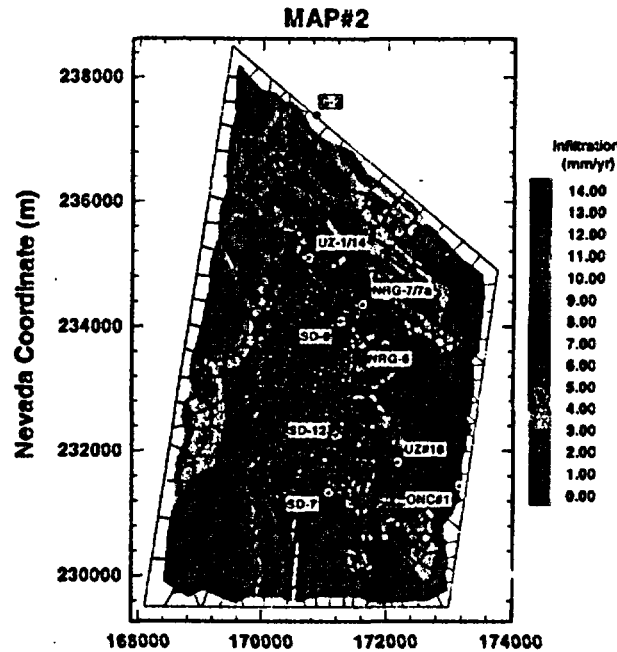


Figure 8.4.2
 Net infiltration map (Map # 2) showing infiltration rates and distributions over the model domain of Yucca Mountain (Flint, Hevesi and Flint, July, 1996).

In addition to the two infiltration maps from the USGS, we also use uniform infiltration rates, such as 0.1 mm/yr, in our sensitivity studies. The uniform infiltration rates are simpler to implement, and still can give us many insights into the effects of parameter variations. Also, use of uniform infiltration rates has resulted in a good match with the observed saturation and water potential data in many cases.

While there exists a high degree of uncertainty with regard to the steady-state net infiltration rates over the mountain, the past and future climate variations and their impacts on net infiltration are even more uncertain. We have tried to address the issue of climatic changes by using a much higher infiltration rate (actually 3 times) to cover the worst case scenarios. The high infiltration rates used are a step-change from the infiltration map # 2 (Figure 8.4.2), which follows the steady-state ambient condition based on the infiltration map # 2.

8.5 Model Parameters and Rock Properties

All the simulations presented in this Chapter were performed using the TOUGH2 code (Pruess, 1991). Thermophysical properties of liquid water and vapor in the TOUGH2 code are internally generated within experimental accuracy from steam table equations (International Formulation Committee, 1967).

Air is treated as an ideal gas and additivity of partial pressures is assumed for air/vapor mixtures.

The rock thermal conductivities and rock thermal capacities used are from Reference Information Base (RIB) (DOE, 1993) for the Yucca Mountain tuffs. The detailed discussion regarding the rock thermal properties is given in Chapter 9 (Bodvarsson et al.) of this report.

The rock properties used for matrix and fracture were estimated using the ITOUGH2 code (Finsterle, 1993), based on the QA saturation and water potential data as initial estimates. The methodology and procedure of the parameter estimation is presented in Chapter 3 (Bandurraga et al.). In the parameter estimation studies of Chapter 3, different infiltration rates, and initial estimates of parameters were used. Therefore, several sets of rock properties have been obtained, depending on the inverse model input specification and conceptual models. Four sets of the rock properties estimated in Chapter 3 have been used in this chapter for model calibration and sensitivity studies, as discussed below.

The rock parameter specification in the 3-D site-scale model is, in general, layer-wise, but some zones located in certain grid layers in the CHn unit are zeolitic regions. In these layers zeolitic and vitric tuff properties will be specified for corresponding geologic zones and locations. The whole unsaturated-zone formation system is subdivided, in general, into 28 hydrogeological units or gridlayers, as discussed in Chapter 2 (Bandurraga). We treat all of the geological units as fracture/matrix systems, except for the PTn unit, which is treated as a single continuum porous medium. This approach will be investigated in UZ modeling studies in FY 1997.

The tables for rock properties used are given in the following, and we also list bulk porosities for matrix and fracture rock. These porosity values were not estimated by our inverse model studies. The matrix porosities were taken from the USGS data (Flint, 1996, in prep.), and fracture porosities were from the GWTT-95 report (Ho et al., 1995).

8.5.1 Parameter Set # 1

The rock properties, parameter set #1, are considered the base-case parameter set. This set of parameters was estimated using a uniform infiltration rate of 0.1 mm/yr, and observations from five boreholes (Chapter 3). The initial estimates of parameters were based on the most updated rock properties from USGS (Flint, 1996, in prep.). The properties for matrix and fracture rock for parameter set #1 are listed in Table 8.5.1. The units in the table for the hydrogeologic units or grid layers are discussed in Chapter 2 (Bandurraga et al.) and later in this section.

Three-Dimensional Model Calibration and Sensitivity Studies

Table 8.5.1 The rock properties, parameter set #1, of matrix and fractures used in the model calibration and sensitivity studies.								
Units	k_m (m^2)	k_f (m^2)	α_m (Pa^{-1})	α_f (Pa^{-1})	m_m	m_f	ϕ_m	ϕ_f
tcw11	0.160E-18	0.601E-11	0.188E-04	0.155E-02	0.229	0.227	0.062	0.290E-03
tcw12	0.340E-16	0.575E-11	0.131E-05	0.123E-02	0.232	0.231	0.082	0.290E-03
tcw13	0.219E-16	0.575E-11	0.135E-05	0.123E-02	0.461	0.437	0.207	0.290E-03
ptn21	0.399E-12	n/a	0.219E-04	n/a	0.219	n/a	0.435	n/a
ptn22	0.239E-12	n/a	0.119E-04	n/a	0.310	n/a	0.222	n/a
ptn23	0.755E-14	n/a	0.365E-04	n/a	0.235	n/a	0.406	n/a
ptn24	0.880E-13	n/a	0.304E-04	n/a	0.289	n/a	0.499	n/a
ptn25	0.310E-12	n/a	0.183E-03	n/a	0.224	n/a	0.490	n/a
tsw31	0.253E-14	0.399E-11	0.257E-04	0.136E-02	0.205	0.203	0.048	0.243E-03
tsw32	0.676E-14	0.100E-10	0.181E-04	0.863E-03	0.248	0.250	0.156	0.243E-03
tsw33	0.214E-17	0.629E-11	0.659E-05	0.544E-03	0.248	0.268	0.154	0.243E-03
tsw34	0.252E-16	0.399E-11	0.801E-06	0.121E-02	0.321	0.320	0.110	0.243E-03
tsw35	0.334E-16	0.399E-11	0.350E-05	0.121E-02	0.224	0.227	0.130	0.243E-03
tsw36	0.959E-16	0.399E-11	0.561E-06	0.121E-02	0.414	0.416	0.112	0.243E-03
tsw37	0.200E-16	0.399E-11	0.112E-05	0.121E-02	0.370	0.368	0.036	0.243E-03
ch1vc	0.160E-11	0.723E-12	0.895E-04	0.121E-02	0.224	0.227	0.273	0.111E-03
ch2vc	0.218E-13	0.723E-12	0.716E-04	0.121E-02	0.219	0.227	0.344	0.111E-03
ch3vc	0.218E-13	0.723E-12	0.716E-04	0.121E-02	0.219	0.227	0.344	0.111E-03
ch4vc	0.218E-13	0.723E-12	0.716E-04	0.121E-02	0.219	0.227	0.344	0.111E-03
ch1zc	0.539E-15	0.100E-12	0.189E-06	0.729E-03	0.356	0.359	0.288	0.525E-04
ch2zc	0.713E-18	0.100E-12	0.518E-05	0.729E-03	0.225	0.225	0.332	0.525E-04
ch3zc	0.713E-18	0.100E-12	0.518E-05	0.729E-03	0.225	0.225	0.332	0.525E-04
ch4zc	0.840E-17	0.100E-12	0.150E-06	0.729E-03	0.475	0.476	0.266	0.525E-04
pp3vp	0.521E-15	0.299E-13	0.206E-04	0.121E-02	0.306	0.313	0.322	0.111E-03
pp2zp	0.170E-16	0.100E-12	0.179E-05	0.729E-03	0.311	0.312	0.286	0.525E-04
bf3vb	0.521E-15	0.299E-13	0.206E-04	0.121E-02	0.306	0.313	0.322	0.111E-03
bf2zb	0.170E-16	0.100E-12	0.179E-05	0.729E-03	0.311	0.312	0.286	0.525E-04
tm3vt	0.521E-15	0.299E-13	0.206E-04	0.121E-02	0.306	0.313	0.322	0.111E-03

In table 5.5.1 and the following tables, k_m and k_f are saturated matrix and fracture continuum permeabilities; α_m and α_f are van Genuchten's parameter of capillary pressure of matrix and fracture; m_m and m_f are van Genuchten's parameter of soil retention curves; and ϕ_m and ϕ_f are porosities of matrix and fracture systems, respectively.

Three-Dimensional Model Calibration and Sensitivity Studies

8.5.2

Parameter Set # 2

The rock properties, parameter set #2, were estimated using a uniform infiltration rate as in set #1, and data from five boreholes. But the initial estimates of parameters, as the input to the ITOUGH2 code, were based on the previous rock properties from USGS, L. Flint (see sensitivity studies, Chapter 3, Banduraga et al.). The properties for matrix and fracture rock for parameter set #2 are listed in Table 8.5.2.

Table 8.5.2 The rock properties, parameter set #2, of matrix and fractures used in the model calibration and sensitivity studies.								
Units	k_m	k_f	α_m	α_f	m_m	m_f	ϕ_m	ϕ_f
	(m^2)	(m^2)	(Pa^{-1})	(Pa^{-1})				
tcw11	0.179E-19	0.519E-11	0.351E-05	0.235E-03	0.414	0.585	0.062	0.290E-03
tcw12	0.104E-15	0.576E-11	0.226E-05	0.596E-03	0.486	0.412	0.082	0.290E-03
tcw13	0.116E-17	0.621E-11	0.351E-05	0.776E-04	0.545	0.501	0.207	0.290E-03
ptrn21	0.181E-14	n/a	0.253E-04	n/a	0.206	n/a	0.435	n/a
ptrn22	0.504E-14	n/a	0.150E-04	n/a	0.138	n/a	0.222	n/a
ptrn23	0.126E-13	n/a	0.200E-04	n/a	0.240	n/a	0.406	n/a
ptrn24	0.126E-13	n/a	0.286E-04	n/a	0.344	n/a	0.499	n/a
ptrn25	0.362E-14	n/a	0.376E-04	n/a	0.263	n/a	0.490	n/a
tsw31	0.385E-16	0.249E-11	0.125E-04	0.306E-03	0.368	0.294	0.048	0.243E-03
tsw32	0.276E-16	0.962E-11	0.751E-05	0.611E-04	0.243	0.254	0.156	0.243E-03
tsw33	0.636E-18	0.483E-11	0.251E-05	0.110E-03	0.333	0.418	0.154	0.243E-03
tsw34	0.359E-17	0.479E-11	0.667E-06	0.876E-04	0.552	0.459	0.110	0.243E-03
tsw35	0.179E-18	0.497E-11	0.173E-05	0.921E-04	0.289	0.419	0.130	0.243E-03
tsw36	0.322E-18	0.457E-11	0.592E-06	0.611E-04	0.387	0.399	0.112	0.243E-03
tsw37	0.669E-16	0.409E-11	0.735E-06	0.114E-03	0.464	0.438	0.036	0.243E-03
ch1vc	0.602E-11	0.723E-12	0.157E-05	0.240E-03	0.469	0.518	0.273	0.111E-03
ch2vc	0.199E-11	0.723E-12	0.320E-05	0.240E-03	0.554	0.742	0.344	0.111E-03
ch3vc	0.199E-11	0.723E-12	0.320E-05	0.240E-03	0.554	0.742	0.344	0.111E-03
ch4vc	0.199E-11	0.723E-12	0.320E-05	0.240E-03	0.554	0.742	0.344	0.111E-03
ch1zc	0.114E-14	0.100E-12	0.251E-06	0.735E-04	0.505	0.518	0.288	0.525E-04
ch2zc	0.266E-17	0.560E-13	0.547E-06	0.755E-04	0.319	0.321	0.332	0.525E-04
ch3zc	0.266E-17	0.560E-13	0.547E-06	0.755E-04	0.319	0.321	0.332	0.525E-04
ch4zc	0.741E-20	0.121E-12	0.103E-05	0.365E-04	0.489	0.639	0.266	0.525E-04
pp3vp	0.279E-11	0.300E-13	0.900E-05	0.133E-03	0.363	0.467	0.322	0.111E-03
pp2zp	0.956E-16	0.654E-13	0.823E-05	0.372E-03	0.213	0.206	0.286	0.525E-04
bf3vb	0.279E-11	0.300E-13	0.900E-05	0.133E-03	0.363	0.467	0.322	0.111E-03
bf2zb	0.956E-16	0.654E-13	0.823E-05	0.372E-03	0.213	0.206	0.286	0.525E-04
tm3vt	0.279E-11	0.300E-13	0.900E-05	0.133E-03	0.363	0.467	0.322	0.111E-03

Three-Dimensional Model Calibration and Sensitivity Studies

8.5.3 Parameter Set # 3

The rock properties, parameter set #3, was estimated using the infiltration map #1 (Figure 8.4.1), and data from five boreholes. The initial estimates of parameters, the same as those used for parameter set # 1, based on the updated rock properties from USGS (Flint, 1996). The properties for matrix and fracture rock for parameter set #3 are listed in Table 8.5.3.

Table 8.5.3 The rock properties, parameter set #3, of matrix and fractures used in the model calibration and sensitivity studies.								
Units	k_m (m^2)	k_f (m^2)	α_m (Pa^{-1})	α_f (Pa^{-1})	m_m	m_f	ϕ_m	ϕ_f
tcw11	0.821E-19	0.118E-10	0.104E-04	0.231E-03	0.497	0.575	0.062	0.290E-03
tcw12	0.406E-15	0.592E-11	0.219E-05	0.150E-02	0.523	0.411	0.082	0.290E-03
tcw13	0.191E-16	0.599E-11	0.384E-05	0.113E-02	0.501	0.516	0.207	0.290E-03
ptn21	0.303E-15	n/a	0.744E-04	n/a	0.219	n/a	0.435	n/a
ptn22	0.837E-12	n/a	0.119E-04	n/a	0.309	n/a	0.222	n/a
ptn23	0.134E-14	n/a	0.100E-03	n/a	0.352	n/a	0.406	n/a
ptn24	0.789E-14	n/a	0.123E-04	n/a	0.406	n/a	0.499	n/a
ptn25	0.123E-13	n/a	0.221E-03	n/a	0.289	n/a	0.490	n/a
tsw31	0.602E-16	0.723E-11	0.129E-04	0.432E-03	0.260	0.246	0.048	0.243E-03
tsw32	0.281E-16	0.125E-10	0.267E-04	0.109E-03	0.191	0.304	0.156	0.243E-03
tsw33	0.953E-18	0.168E-10	0.222E-05	0.139E-03	0.352	0.404	0.154	0.243E-03
tsw34	0.349E-18	0.440E-10	0.605E-06	0.496E-04	0.444	0.460	0.110	0.243E-03
tsw35	0.882E-19	0.967E-10	0.113E-05	0.105E-03	0.351	0.454	0.130	0.243E-03
tsw36	0.124E-16	0.436E-11	0.472E-06	0.111E-02	0.397	0.387	0.112	0.243E-03
tsw37	0.595E-16	0.419E-11	0.667E-06	0.112E-02	0.399	0.439	0.036	0.243E-03
ch1vc	0.787E-11	0.751E-12	0.949E-06	0.155E-02	0.469	0.517	0.273	0.111E-03
ch2vc	0.396E-11	0.660E-12	0.284E-05	0.133E-02	0.602	0.742	0.344	0.111E-03
ch3vc	0.396E-11	0.660E-12	0.284E-05	0.133E-02	0.602	0.742	0.344	0.111E-03
ch4vc	0.396E-11	0.660E-12	0.284E-05	0.133E-02	0.602	0.742	0.344	0.111E-03
ch1zc	0.117E-14	0.101E-12	0.876E-06	0.724E-03	0.469	0.518	0.288	0.525E-04
ch2zc	0.428E-17	0.617E-13	0.431E-06	0.628E-03	0.334	0.320	0.332	0.525E-04
ch3zc	0.428E-17	0.617E-13	0.431E-06	0.628E-03	0.334	0.320	0.332	0.525E-04
ch4zc	0.871E-20	0.210E-12	0.129E-05	0.384E-04	0.519	0.592	0.266	0.525E-04
pp3vp	0.126E-11	0.325E-13	0.472E-04	0.144E-02	0.196	0.466	0.322	0.111E-03
pp2zp	0.513E-15	0.100E-12	0.166E-05	0.660E-03	0.228	0.206	0.286	0.525E-04
bf3vb	0.126E-11	0.325E-13	0.472E-04	0.144E-02	0.196	0.466	0.322	0.111E-03
bf2zb	0.513E-15	0.100E-12	0.166E-05	0.660E-03	0.228	0.206	0.286	0.525E-04
tm3vt	0.126E-11	0.325E-13	0.472E-04	0.144E-02	0.196	0.466	0.322	0.111E-03

Three-Dimensional Model Calibration and Sensitivity Studies

8.5.4

Parameter Set # 4

The rock properties, parameter set #4, were estimated using the infiltration map # 2, and data from five boreholes. The initial estimates of parameters, the same as those used for parameter set # 1, are based on the updated rock properties from USGS (Flint, 1996). The properties for matrix and fracture rock for parameter set #4 are listed in Table 8.5.4.

Table 8.5.4 The rock properties, parameter set #4, of matrix and fractures used in the model calibration and sensitivity studies.								
Units	k_m (m^2)	k_f (m^2)	α_m (Pa^{-1})	α_f (Pa^{-1})	m_m	m_f	ϕ_m	ϕ_f
tcw11	0.160E-18	0.910E-11	0.147E-04	0.518E-03	0.238	0.182	0.062	0.290E-03
tcw12	0.540E-15	0.575E-11	0.174E-05	0.977E-03	0.233	0.223	0.082	0.290E-03
tcw13	0.220E-16	0.575E-11	0.129E-05	0.123E-02	0.463	0.437	0.207	0.290E-03
ptn21	0.400E-12	n/a	0.244E-04	n/a	0.215	n/a	0.435	n/a
ptn22	0.240E-12	n/a	0.159E-04	n/a	0.310	n/a	0.222	n/a
ptn23	0.111E-12	n/a	0.445E-04	n/a	0.243	n/a	0.406	n/a
ptn24	0.880E-13	n/a	0.341E-04	n/a	0.295	n/a	0.499	n/a
ptn25	0.105E-11	n/a	0.138E-03	n/a	0.243	n/a	0.490	n/a
tsw31	0.261E-12	0.400E-11	0.237E-04	0.122E-02	0.206	0.203	0.048	0.243E-03
tsw32	0.194E-12	0.445E-11	0.172E-04	0.969E-03	0.248	0.249	0.156	0.243E-03
tsw33	0.796E-17	0.743E-11	0.573E-05	0.243E-03	0.247	0.250	0.154	0.243E-03
tsw34	0.100E-14	0.159E-11	0.754E-06	0.686E-03	0.321	0.325	0.110	0.243E-03
tsw35	0.423E-15	0.400E-11	0.234E-05	0.108E-02	0.231	0.226	0.130	0.243E-03
tsw36	0.776E-16	0.400E-11	0.522E-06	0.122E-02	0.416	0.416	0.112	0.243E-03
tsw37	0.316E-15	0.400E-11	0.804E-06	0.122E-02	0.368	0.368	0.036	0.243E-03
ch1vc	0.160E-11	0.723E-12	0.760E-04	0.122E-02	0.221	0.227	0.273	0.111E-03
ch2vc	0.550E-13	0.723E-12	0.980E-04	0.122E-02	0.223	0.227	0.344	0.111E-03
ch3vc	0.550E-13	0.723E-12	0.980E-04	0.122E-02	0.223	0.227	0.344	0.111E-03
ch4vc	0.550E-13	0.723E-12	0.980E-04	0.122E-02	0.223	0.227	0.344	0.111E-03
ch1zc	0.540E-15	0.100E-12	0.190E-06	0.730E-03	0.359	0.359	0.288	0.525E-04
ch2zc	0.450E-17	0.100E-12	0.394E-05	0.388E-03	0.225	0.225	0.332	0.525E-04
ch3zc	0.450E-17	0.100E-12	0.394E-05	0.388E-03	0.225	0.225	0.332	0.525E-04
ch4zc	0.210E-16	0.100E-12	0.150E-06	0.730E-03	0.475	0.470	0.266	0.525E-04
pp3vp	0.542E-14	0.300E-13	0.194E-04	0.122E-02	0.316	0.313	0.322	0.111E-03
pp2zp	0.269E-15	0.100E-12	0.126E-05	0.730E-03	0.311	0.312	0.286	0.525E-04
bf3vb	0.542E-14	0.300E-13	0.194E-04	0.122E-02	0.316	0.313	0.322	0.111E-03
bf2zb	0.269E-15	0.100E-12	0.126E-05	0.730E-03	0.311	0.312	0.286	0.525E-04
tm3vt	0.542E-14	0.300E-13	0.194E-04	0.122E-02	0.316	0.313	0.322	0.111E-03

Three-Dimensional Model Calibration and Sensitivity Studies

8.5.5 Rock Name and Specification

As can be seen in the first columns of Tables 8.5.1 - 8.5.4, we have used "ROCK NAMES" or geological units for different model layers. The convention used for naming the rock types in different model grid layers is defined in Table 8.5.5. Table 8.5.5 also lists the corresponding information and definition regarding geological and hydrogeological units, formations, and model grid layers.

Table 8.5.5 The corresponding relations of rock names, geological and hydrogeological units, formation and model grid layers used in the site-scale model.			
Geological Unit	Welding Intensity/ Formation Name (Buesch et al., 1995)	Model Grid Layer Name	Hydrogeological Unit
PAINTBRUSH GROUP			
Tiva Canyon Tuff	M,D ¹ (Tpcoox)	tcw11 tsw12	Tiva Canyon (TCw)
	D- Basal Vitrophyre (Tpcpv3)		
	M (Tpcpv2)	tcw13	
Bedded tuff	N,P (Tpcpv1)	ptn21	Paintbrush (PTn)
	N (Tpbt4)		
Yucca Mountain Tuff	N,P,M (Tpy)	ptn22	
Bedded tuff	N (Tpbt3)	ptn23	
Pah Canyon Tuff	N,P,M (Tpy)	ptn24	
Bedded tuff	N (Tpbt2)		
Topopah Spring Tuff	N,P (Tptrv3)	ptn25	Topopah Spring (TSw)
	M (Tptrv2)	tsw31	
	D -Upper vitrophyre (Tptrv1)		
	M,D (Tptrm)	tsw32	
	M,D,L (Tptrl)		
	M,D,L (Tptpul)	tsw33	
	D (Tptpmn)	tsw34	
	M,D,L (Tptpll)	tsw35	
	D (Tptpln)	tsw36	
D (Tptpv3)	tsw37		
Bedded tuff	N,P,M; may be altered (Tptpv1, Tptpv2)		Calico Hills (CHn)
	N; may be altered (Tpbt1)	ch1zc, ch1vc	
Calico Hills Formation	N; unaltered (Ta - Vitric)	ch2vc	
	N; altered (Ta - Zeolitic)	ch3zc	
	N; may be altered (Tabt1)	ch4zc, ch4vc	
CRATER FLAT GROUP			

Table 8.5.5 (cont.)
The corresponding relations of rock names, geological and hydrogeological units, formation and model grid layers used in the site-scale model.

Geological Unit	Welding Intensity/ Formation Name (Buesch et al., 1995)	Model Grid Layer Name	Hydrogeological Unit
Prow Pass Tuff	N; may be altered (Tpc) Unit 4 ³		Crater Flat Undifferentiated (CFu)
	N,P,M Unit 3	pp3vp	
	N,P; generally altered Units 2,1	pp2zp	
Bedded tuff	N; generally altered (Tpcb1)		
Upper Bullfrog Tuff	N,P; generally altered (Tcb)		
Middle Bullfrog Tuff	N,P,M	bf3vp	
Lower Bullfrog Tuff	N,P; generally altered	bf2zp	
Bedded tuff	N; generally altered (Tcbbt)		
Upper Tram Tuff	N,P; generally altered (Tct)	tm3vt	

8.5.6
Fault Properties

Three sets of fault properties are used in this chapter to investigate effects of fault properties on moisture flow in the unsaturated zone of the mountain. The fault properties were based on the previous study (Wittwer et al., 1995; and Ahlers et al., 1995a), and the pneumatic data analysis at LBNL with USGS data (Ahlers et al., 1996). The major faults incorporated into the site-scale model are shown in Figure 8.3.1. Fault zones are treated as fracture/matrix media using the ECM approximation, instead of a single continuum porous medium, as specified in the previous study (Wittwer et al., 1995). The reason for using the ECM treatment is that fault zones consist of highly permeable fractures and matrix blocks with low permeability. However, the fracture system in faults has low porosity, or low storage capability for fluids. On the other hand, the matrix blocks are very low in permeability, but have large porosity, or more storage space. The ECM approach will include effects of both fractures and matrix in the fault zones.

The fault properties are based on our current understanding of the roles of faults, the pneumatic analysis, and the model calibrations. These are all considered to be Q data except for fault properties from Chapter 3.

The properties for Fault #1 are listed in Table 8.5.6, which shows that uniform fault properties are specified for all the incorporated faults in this case. A matrix permeability of 100 md is used for matrix blocks in faults, and horizontal and vertical permeabilities for fractures in faults are 10 and 100 darcies, respectively.

Three-Dimensional Model Calibration and Sensitivity Studies

Table 8.5.6 The rock properties for fault #1 used in the model calibration and sensitivity studies.									
Units	k_m (m^2)	$k_{f,h}$ (m^2)	$k_{f,v}$ (m^2)	α_m (Pa^{-1})	α_f (Pa^{-1})	m_m	m_f	ϕ_m	ϕ_f
All	1.00E-13	1.0E11	1.0-10	0.61E-4	0.61E-4	0.50	0.50	0.30	0.001

In Table 8.5.6, $k_{f,h}$ and $k_{f,v}$ are fracture permeabilities in horizontal and vertical directions, respectively, for the faults.

The second set of fault properties are provided in Table 8.5.7, and the only difference from the fault # 1 properties is that different continuum fracture permeabilities are used for fractures of the faults, which are subdivided into four geological units. The fracture permeability values are taken from the pneumatic data analysis of the fault permeability (Ahlers et al., 1996).

Table 8.5.7 The rock properties for fault #2 used in the model calibration and sensitivity studies.									
Units	k_m (m^2)	$k_{f,h}$ (m^2)	$k_{f,v}$ (m^2)	α_m (Pa^{-1})	α_f (Pa^{-1})	m_m	m_f	ϕ_m	ϕ_f
TCw	1.0E-13	2.0e-11	2.0e-11	0.61E-4	1.0e-3	0.50	0.50	0.30	0.001
PTn	1.0E-13	0.2e-12	0.2e-12		1.0e-3	0.50	0.50	0.30	0.001
TSw	1.0E-13	2.0e-11	2.0e-11		1.0e-3	0.50	0.50	0.30	0.001
CHn	1.0E-13	1.0e-14	1.0e-14		1.0e-3	0.50	0.50	0.30	0.001

The third set of fault properties are given in Table 8.5.8. In this data set the two-phase flow parameters for relative permeability and capillary pressures are modified from those in Table 8.5.6 or Table 8.5.7. The van Genuchten parameters were changed using the selected values of parameter set # 4, as given in Table 8.5.4, for the matrix properties in the corresponding four fault units, respectively.

Table 8.5.8 The rock properties for fault #3 used in the model calibration and sensitivity studies.									
Units	k_m (m^2)	$k_{f,h}$ (m^2)	$k_{f,v}$ (m^2)	α_m (Pa^{-1})	α_f (Pa^{-1})	m_m	m_f	ϕ_m	ϕ_f
TCw	1.0E-13	2.0e-11	2.0e-11	0.18E-5	0.97e-3	.234	.223	0.30	0.001
PTn	1.0E-13	0.2e-12	0.2e-12	0.44E-4	1.00e-3	.243	.500	0.30	0.001
TSw	1.0E-13	2.0e-11	2.0e-11	0.24E-5	1.08e-2	.228	.226	0.30	0.001
CHn	1.0E-13	1.0e-14	1.0e-14	0.98E-4	1.00e-3	.223	.227	0.30	0.001

8.6 Comparisons with Observed Borehole Data

As a first step for model calibrations of the site-scale model, borehole measured saturation and water potential data are used to compare with the model predictions, based on different parameter sets. The liquid saturation and water potential data are from 7 boreholes UZ-14, UZ-16, NRG-6, NRG-7a, SD-7, SD-9, and SD-12, which were collected by the USGS (OCRWM, DOE, 1995). These data have been used in this study for analyzing effects of rock property variations and comparative studies between model simulations and observations. The locations of these 7 boreholes are shown in Figure 8.3.1. The simulations using parameter set #1 and set #2 are based on a uniform infiltration of 0.1 mm/yr, and the simulation results with parameter set #3 and set #4 use infiltration map #1 and map #2, respectively.

In the following analysis, only one of the four comparisons carried out for each borehole is presented in the figures, because the comparisons are all similar in matching the observation data.

8.6.1 Comparisons with UZ-1/14 Data

Boreholes UZ-1 and UZ-14 are adjacent to each other in Drill Hole Wash, north of the potential repository area (Figure 8.3.1), with surface elevations of about 1,349 m above sea level. A possible perched water zone was detected in or just below the base the Topopah Spring Tuff at a depth of 387 m. Comparisons were made between the simulated and observed saturation and capillary pressure (water potential) data for boreholes UZ-1/14, using the 4 different parameter sets of Section 8.5. Since similar comparison results were obtained using these 4 sets of parameters, only one of the comparisons is shown in Figure 8.6.1. In this figure, the vertical saturation profiles simulated are extracted from the 3-D simulation results, and the borehole data are from UZ-14. As shown on the figure and for all other results, the simulation results are generally in good agreement with the measured saturation profiles at the location of UZ-14, but comparisons with capillary pressure data are not as good as for saturation. The reason of this discrepancy between the simulated and observed capillary data may be due to the inaccuracy in the measurement of these water potential data ranging from sample handling to equipment limitations.

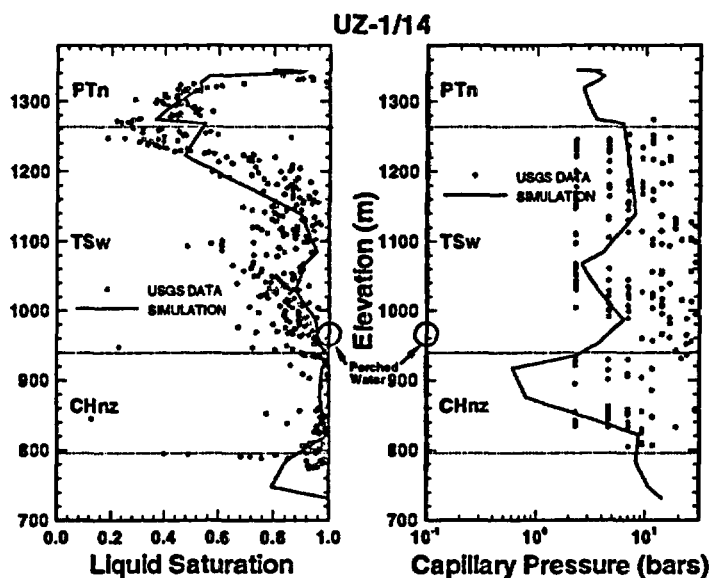


Figure 8.6.1

Comparisons of the simulated and observed saturations and water potentials of boreholes UZ-1/14 using parameter set #4 and infiltration map #2; (a) comparisons with saturation, (b) comparisons with capillary pressure. USGS data from L. Flint.

Figure 8.6.1 shows that the TCw unit is missing at this location. We have found that all four sets of parameters can match well with the saturation profiles from the ground surface until the bottom of the TSw unit in UZ-14. However, at the perched water location, as circled on the figure, the model results on Figure 8.6.1 fit better than models using the other sets of parameters. The comparisons in the altered CHnz unit also seem reasonable, considering the relatively coarse grids used in the 3-D model.

8.6.2
Comparisons with NRG-7a
Data

Borehole NRG-7a is also located in Drill Hole Wash, and it is close to the ESF (Figure 8.3.1) at a surface elevation of 1,282 m. Perched water was also detected in this borehole, just below the contact of the bedded tuff with the partially welded pyroclastic flow at the base of the Topopah Spring Tuff. The comparisons between the simulated and observed saturations at the location are shown in Figure 8.6.2, as an example, for set #1 parameters. Since no water potential data are available from this borehole, only simulated capillary pressure data are plotted in the figure.

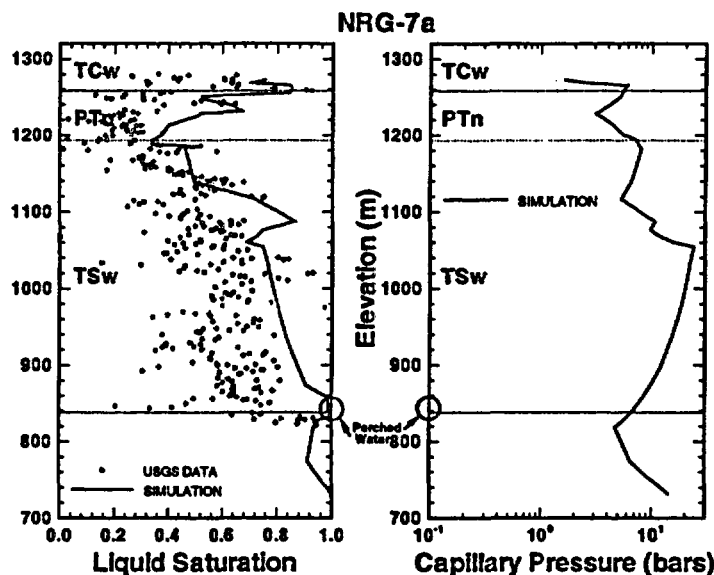


Figure 8.6.2
 Comparisons of the simulated and observed saturations of borehole NRG-7a using parameter set #1 and infiltration of 0.1 mm/yr; (a) comparisons with saturation, (b) capillary pressure.

Figure 8.6.2 and the other results (Figures not given here) show that the simulated saturations are in a fair agreement with the observed values. The simulated saturation profiles are a little "wetter" than observed data. This may be due to the quality of the measured data; there are indications that the sample cores taken from the borehole were not handled properly, which decreases saturations (Personal Communication, USGS, L. Flint, 1996).

8.6.3 Comparisons with SD-7 Data

Borehole SD-7 is located near the southwest corner of the ESF, just west of the Ghost Dance fault (Figure 8.3.1). The offset in the geologic layering due to the fault is estimated to be on the order of tens of meters. A perched water body was found in the portion of the zeolitic Calico Hills tuff of the CHnz unit. An example of the comparison is shown in Figure 8.6.3 for borehole SD-7. It shows that the matches of the simulated and observed saturations and water potentials are good. For the upper three geological units, i.e., TCw, PTn, and TSw, the four sets of parameters and infiltration rates all results in good match with the observed data. However, the match with saturations in the CHnv units is not very good when using parameter set #1, or parameter set #3. Figures 8.6.3, using parameter set #4, gives a better fit with saturations in this unit, specially in the vitric layers above and below the perched water location, which is indicated by the circle in the figure.

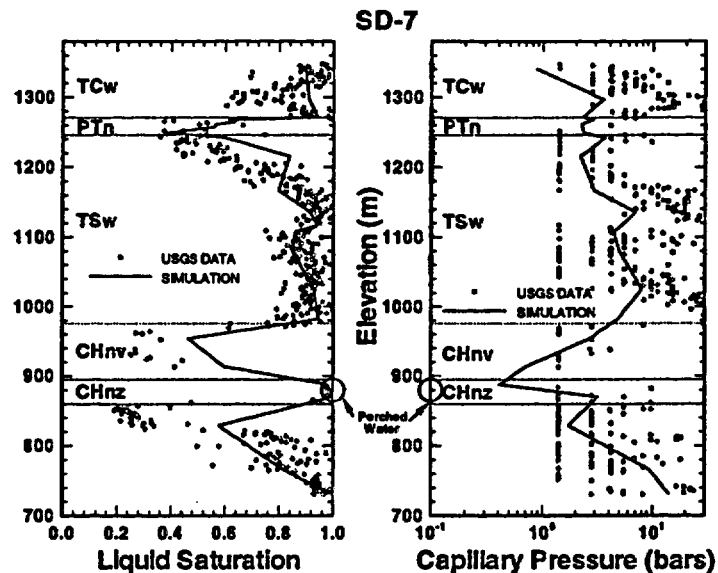


Figure 8.6.3
 Comparisons of the simulated and observed saturations and water potentials of borehole SD-7 using parameter set #4 and infiltration map #2; (a) comparisons with saturation, (b) comparisons with capillary pressure.

Different from all the other perched water boreholes discussed in this report, the perched-water body found in SD-7 is located within the Calico Hills zeolitic unit, in the middle of the CHn, rather than at the bottom of the welded tuff layer of the Topopah Spring unit. As shown in Figures 8.6.3, the perched-water location is reproduced well, and the resulting analysis indicates that use of parameter sets #1, #3 or #4 will better match the perched-water from the borehole. In these three comparisons, much higher saturation and lower capillary pressure values are obtained in the model results.

8.6.4 Comparisons with SD-9 Data

Borehole SD-9 is located adjacent to Drill Hole Wash (Figure 8.3.1) with a surface elevation of 1,302 m and has a total depth of 678 m. The perched water was found at a depth of 413 m, about 3 m above the lower nonlithophysal/vitrophyre contact in the Topopah Spring Tuff. The perched water zone was near the upper contact of the basal vitrophyre of the Topopah Spring Tuff in highly fractured, welded tuff underlain by less-fractured, non-welded tuff.

Figure 8.6.4 shows that the comparisons of the observed saturations and the modeled simulations. Also the results using the other three sets of parameters are similar to those in Figure 8.6.4. The figure indicates a good match for this borehole for all the geological units, except at the interface between the TSw and CHn units. At this interface, the observed saturations are as low as 40 - 50%, but the model gives values that are higher at 90% or more. The reason for

this disagreement may be the rock properties used for this layer. Since this zone is at the perched elevation, as shown in the figure, all the parameter sets were estimated to match the perched water of the borehole by the ITOUGH2 code (Chapter 3, Bandurraga et al.). Therefore, the model results are forced to produce higher saturations at this location. The other reason is the use of the coarse grid in the model, which leads to loss of resolution at the interfaces.

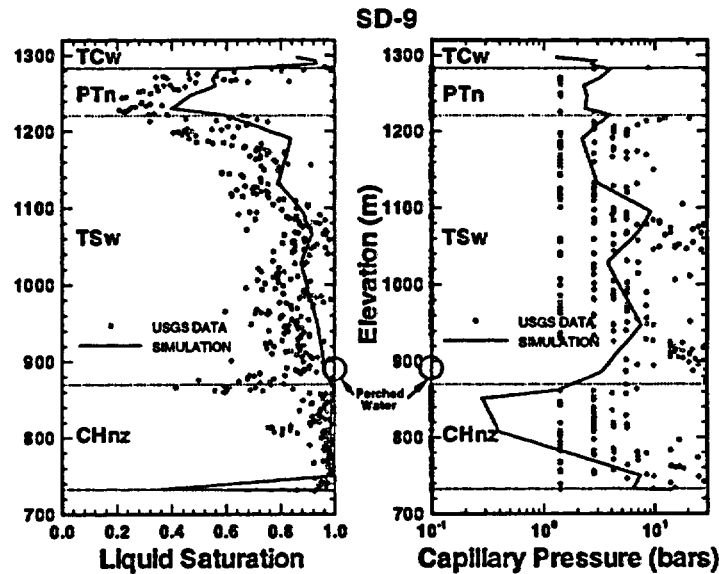


Figure 8.6.4
Comparisons of the simulated and observed saturations and water potentials of borehole SD-9 using parameter set #4 and infiltration map #2; (a) comparisons with saturation, (b) comparisons with capillary pressure.

It is interesting to note that there is a spike in the simulated saturation profiles, near the bottom of the model grid, or the water table. This is due to the presence of a thin layer of the Prow Pass vitric unit that is found there. In terms of matching the perched water location, Figure 8.6.4 using parameter set # 4 and map #2 infiltration rates gives the best fit for both saturation and capillary pressure profiles.

8.6.5
Comparisons with SD-12
Data

Borehole SD-12 is located near the center of the site-scale model (Figure 8.3.1), between the potential repository and the Exploratory Study Facilities (ESF). The borehole is at a surface elevation of 1,324 m and has a total depth of 660 m. The example simulation comparison results using are shown in Figure 8.6.5 for borehole SD-12. The figure gives comparisons only for saturations, since no water potential data are available for this borehole.

The match of the simulated salutations with the observed values is very reasonable for all the units, as shown in Figures 8.6.5, in particular, for the TSw

unit. In the PTn, the model predicted a lower saturation zone which is a little "thinner" than the observations. In the CHn, the two lower saturation spikes are reproduced well by the all the plots for the altered vitric zones, however, the model predictions are relatively "wetter" than the observed saturations there.

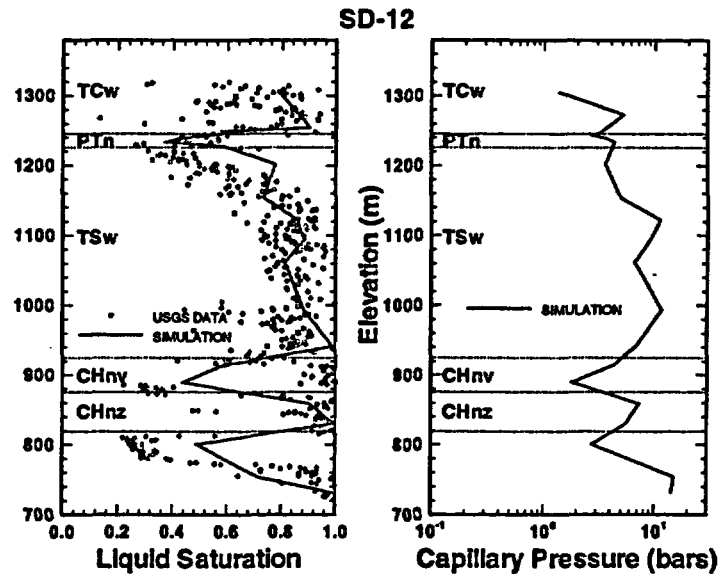


Figure 8.6.5
Comparisons of the simulated and observed saturations and water potentials of borehole SD-12 using parameter set #1 and infiltration of 0.1 mm/yr; (a) comparisons with saturation, (b) comparisons with capillary pressure.

8.6.6
Comparisons with UZ#16
Data

Borehole UZ#16 is located east of the potential repository, near the center of the ESF loop (Figure 8.3.1). UZ#16 is at a surface elevation of 1,219 m and has a total depth of 514 m. The simulation and comparison results using parameter set #4 are shown in Figure 8.6.6 for borehole UZ#16. The figure also gives comparisons only for saturations, since no measured water potential data are available for this borehole.

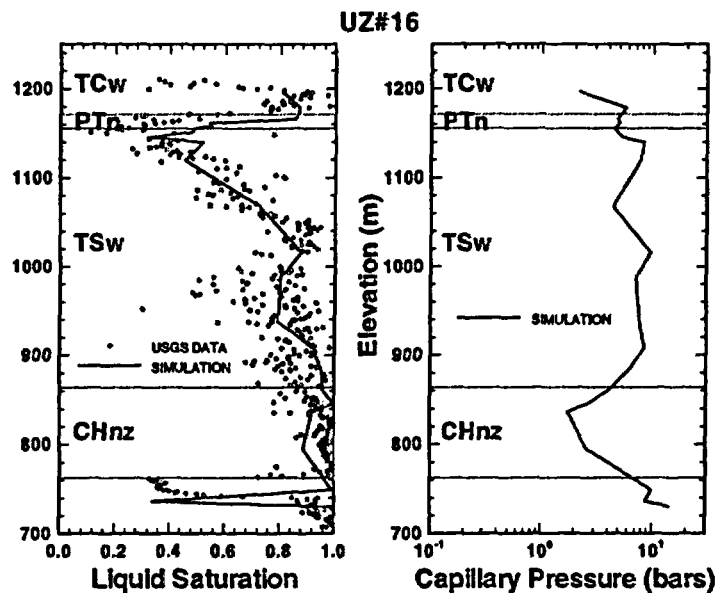


Figure 8.6.6
 Comparisons of the simulated and observed saturations of borehole UZ#16 using parameter set #4 and infiltration map #2; (a) comparisons with saturation, (b) capillary pressure.

Figure 8.6.6 shows that the overall agreement of the simulated and measured saturation profiles at the location of UZ#16 is good, for all the units. Good agreement was observed for the other sets of parameters also. The match is very good for the lower saturation spike at the bottom of the model domain, which correspond to the unaltered layer of the Prow Pass Tuff in the CHn unit. The comparisons in the zeolitic units of the CHn show relatively large disagreement, because the model predicted values are a little “drier” than the observations. But the simulation results of Figure 8.6.6 using parameter set #4 and infiltration map #2 present a good fit in this zeolitic zone.

8.6.7
 Comparisons with NRG-6
 Data

Borehole NRG-6 is also located within the ESF loop (Figure 8.3.1), south-east of borehole NRG-7a and SD-9. NRG-6 has a surface elevation of 1,247 m and a total depth of 335 m. The example simulation and comparison results for borehole NRG-6 shown in Figure 8.6.7. There is no measured water potential data available for this borehole.

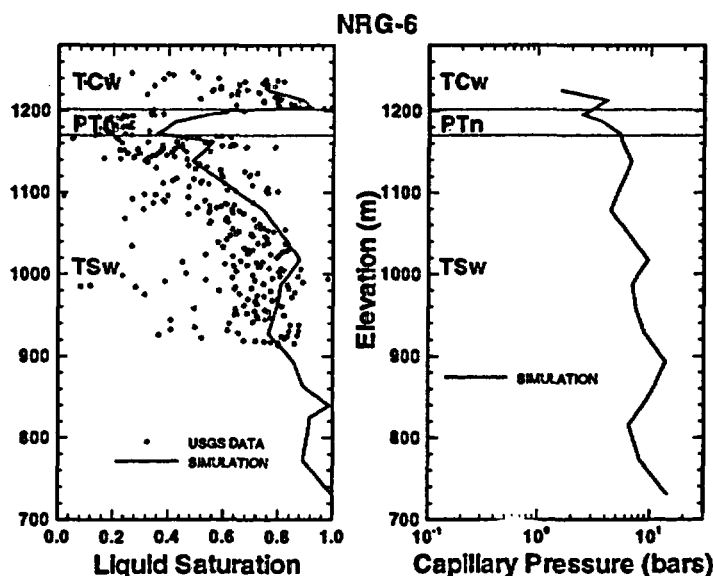


Figure 8.6.7 Comparisons of the simulated and observed saturations of borehole NRG-6 using parameter set #1 and infiltration of 01. mm/yr; (a) comparisons with saturation, (b) capillary pressure.

Figure 8.6.7 shows that the overall agreement of the simulated and measured saturation profiles at the location of NRG-6 is good, for all the units. However, the simulated saturations are a little “wetter” than the observations for this borehole. As discussed for NRG-7a borehole, the “wet” simulation results may be actually due to the quality of the sample measurement, because of mishandling the core samples (Private Comm., L. Flint, USGS, 1996).

8.7 Effects of Rock Property Variations on Moisture and Heat Flow

The effects of rock properties and their variations on moisture and heat flow and distributions within the mountain can be investigated using 2-D contour maps and 3-D plots. In this section, both 2-D and 3-D plots are used to analyze moisture flow fields and their spatial distributions, and to discuss lateral diversion issues.

8.7.1 Lateral Moisture Movement and Distribution in Selected 2-D Vertical Cross Sections

Figure 8.7.1 shows the location of four vertical cross sections, used to study moisture flow and distributions along these cross sections. The four vertical cross sections are selected to intersect boreholes UZ-14 and SD-7, from west to east, and south to north, respectively. All of the plots discussed in this Chapter are extracted from and based on 3-D simulation results.

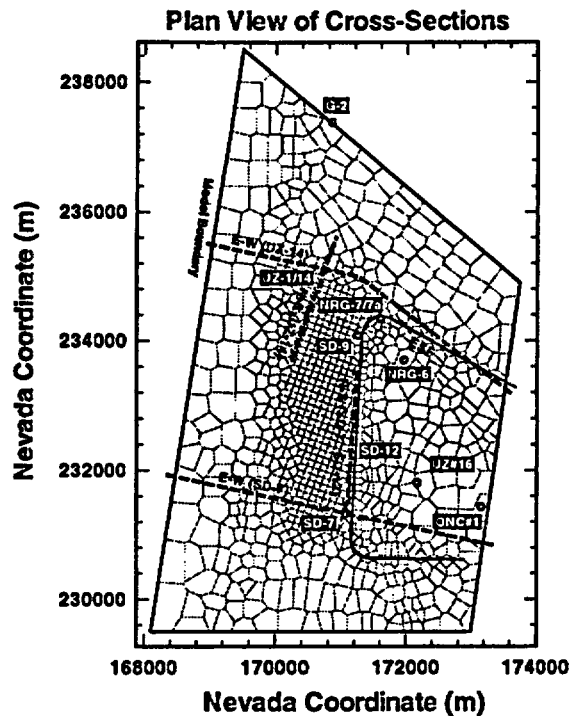


Figure 8.7.1
Location and plan view of four vertical cross sections and associated boreholes.

8.7.1.1
Near Boreholes UZ-1/14

Figures 8.7.2 to 8.7.5 show the simulated flow velocity fields and liquid saturations along the vertical, west-east cross section W-E (UZ-1/14). The simulations use the four different sets of parameters and the corresponding infiltration rates. It is obvious from the figures that there exist significant differences in the lateral moisture movement predicted by the different sets of parameters and infiltration rates.

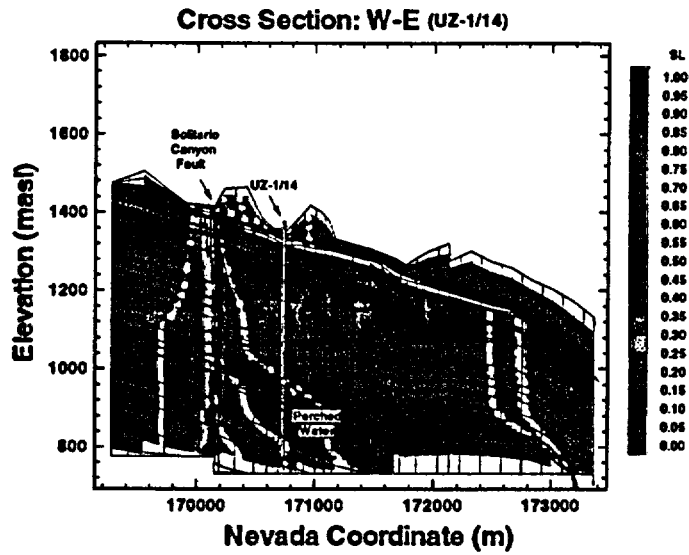


Figure 8.7.2
Velocity fields and liquid saturations along the West-East cross section crossing UZ-1/14, simulated using parameter set #1 and infiltration of 0.1 mm/yr.

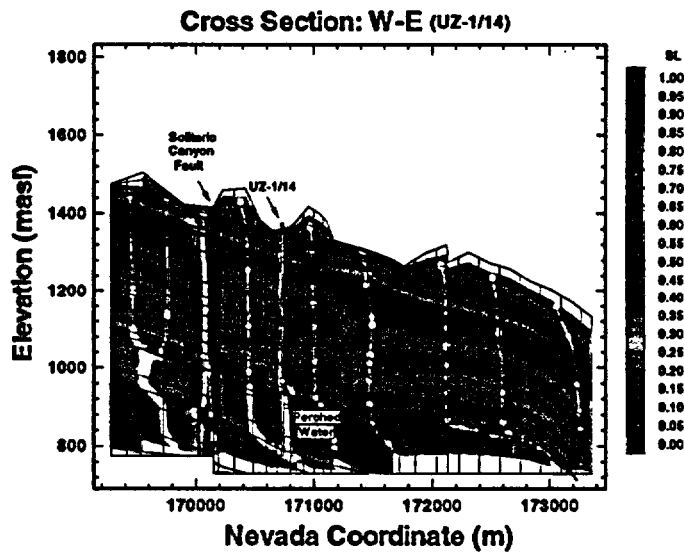


Figure 8.7.3
Velocity fields and liquid saturations along the West-East cross section crossing UZ-1/14, simulated using parameter set #2 and infiltration of 0.1 mm/yr.

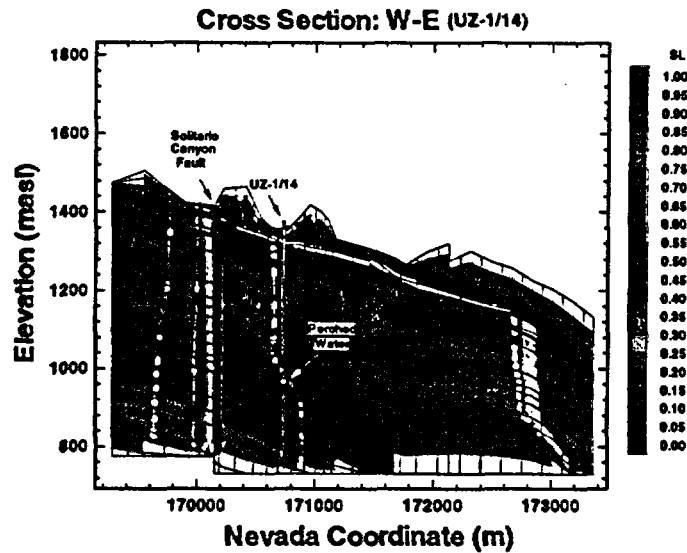


Figure 8.7.4
Velocity fields and liquid saturations along the West-East cross section crossing UZ-1/14, simulated using parameter set #3 and infiltration map #1.

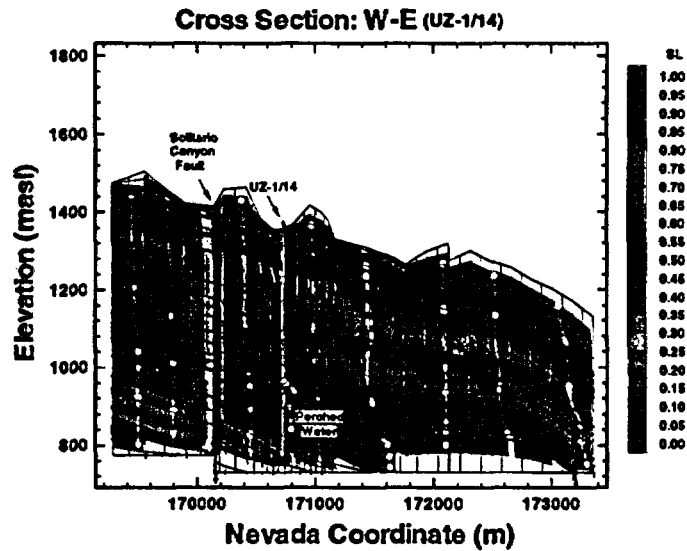


Figure 8.7.5
Velocity fields and liquid saturations along the West-East cross section crossing UZ-1/14, simulated using parameter set #4 and infiltration map #2.

The velocity field, particle traveling paths and saturation contours, shown in Figure 8.7.2, are simulated using parameter set # 1 and a uniform infiltration rate of 0.1 mm/yr. Figure 8.7.2 shows significant lateral moisture flow in the west-east cross section both along the PTn and above the zeolitic units of the

CHnz, especially within the PTn. Figure 8.7.2 indicates that almost all the infiltration has been diverted laterally across three kilometers to the east in the PTn along the cross section, starting from the Solitario Canyon fault. At about one kilometer from the eastern model boundary, flow lines become vertical. This is because there is a relatively highly saturated zone along the lateral east-flow horizons, and the capillary force gradients there force the flow toward the west or downward. The turning points of flow directions near the eastern model boundary, as shown in Figure 8.7.2 or 8.7.4, also correspond to a sudden change in slopes of geological layers. We are currently investigating this.

Along the top of the zeolitic units in the CHn, as shown in Figure 8.7.2, water is diverted to the east for about one kilometer. On Figure 8.7.2, the higher saturations are noticed for these zeolitic layers of CHnz, which match the perched water location in boreholes UZ-1/14.

Figure 8.7.3 presents the simulations using parameter set #2 and 0.1 mm/yr infiltration, and shows a very different picture, with respect with the lateral diversion of moisture flow through the PTn. The water particles, released from the ground surface, go straight down across the PTn until reaching the zeolitic layers in the CHn. Along the top surface of the zeolitic units in the CHn, the figure indicates significant lateral flow, moisture traveling hundreds of meters toward the east. The simulation (Figure 8.7.3) that is relatively "dry" at the perched water location from this simulation.

Figure 8.7.4 also shows significant lateral movement in the PTn, and the results are simulated using parameter set #3 and infiltration map #1. Figure 8.7.4 indicates that similarly to Figure 8.7.2, almost all the recharge, from the Solitario Canyon fault to east, has been diverted, in the PTn, laterally traveling three kilometers to the east along the cross section to about one kilometer from the eastern model boundary. For the same reason as in Figure 8.7.2, downward flow occurs there.

Flow path lines, as shown in Figure 8.7.4, in the CHn unit indicate that there is little lateral flow in this unit, at about 200 meters near borehole UZ-1/14. The figure also shows an extensive water body with high saturation near the perched water location.

Figure 8.7.5 shows the simulation results using parameter set #4 and infiltration map #2. It indicates that there is very little lateral flow in both PTn and CHn units, and flow is mostly straight down to the water table. Figure 8.7.5 is based on the highest infiltration rates (map #2) used in this study, with an average of 4.4 mm/yr over the model domain. The results of the simulated moisture movement indicate that higher infiltration promotes vertical flow, relative to lateral movement. Figure 8.7.5 also shows a large high saturation body around the perched water location of borehole UZ-1/14.

The moisture flow and its distribution in the south-north direction, along cross section: S-N (UZ-1/14), are shown in Figures 8.7.6 to 8.7.9. The cross section location is shown in Figure 8.7.1. The simulations are using the four different sets of parameters and the corresponding infiltration rates, respectively. Compared with the results in the west-east cross section of Figures 8.7.2 to 8.7.5, the lateral flow in the south-north direction in the vicinity of UZ-1/14 is relatively small in the PTn, because of the smaller slopes of the layers in the south-north direction.

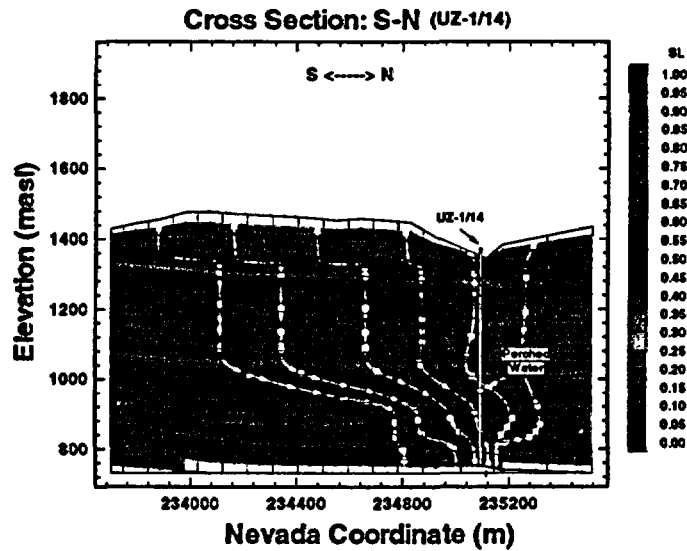


Figure 8.7.6 Velocity fields and liquid saturations along the South-North cross section crossing UZ-1/14, simulated using parameter set #1 and infiltration of 0.1 mm/yr.

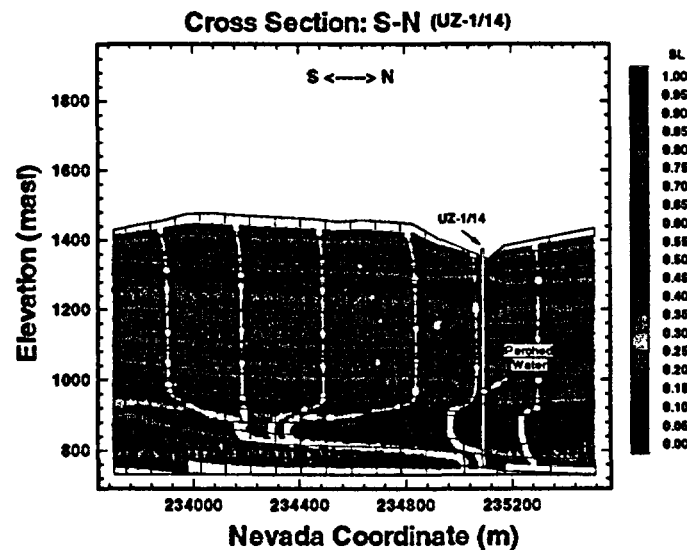


Figure 8.7.7 Velocity fields and liquid saturations along the South-North cross section crossing UZ-1/14, simulated using parameter set #2 and infiltration of 0.1 mm/yr.

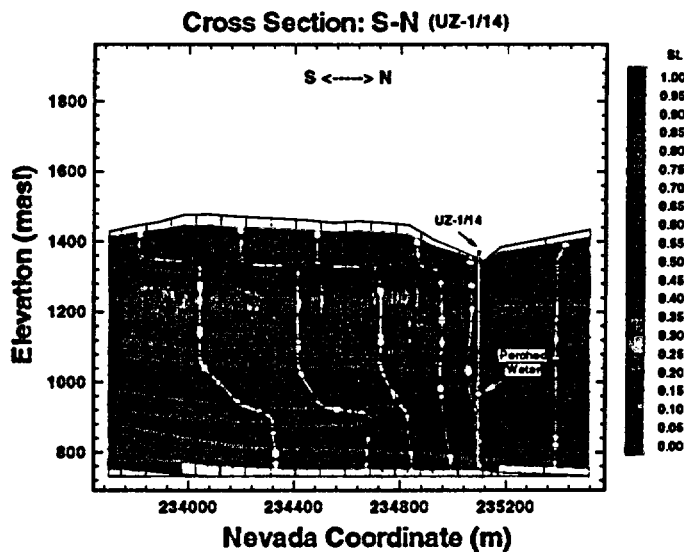


Figure 8.7.8
Velocity fields and liquid saturations along the South-North cross section crossing UZ-1/14, simulated using parameter set #3 and infiltration map #1.

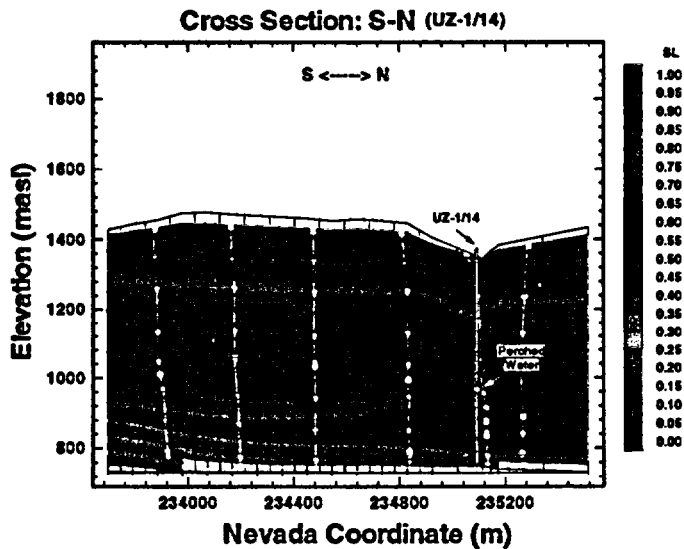


Figure 8.7.9
Velocity fields and liquid saturations along the South-North cross section crossing UZ-1/14, simulated using parameter set #4 and infiltration map #2.

Figure 8.7.6 shows about 100-300 meters lateral flow in the PTn unit, along the south-north cross section when using parameter set #1 and 0.1 mm/yr infiltration. However, substantial lateral movement can be seen in the CHn unit from south to north up to 700 meters. Figure 8.7.7 uses also 0.1 mm/yr infiltration, with parameter set #2. The picture is similar to that in the west-east direc-

tion (Figure 8.7.3). i.e., the only lateral flow occurs within the CHn, and flow is around the zeolitic unit. There is significant south-north flow, as shown in Figure 8.7.7, over a distance of more than 500 meters in the southern part of the cross section, under the repository horizon.

Using parameter set # 3 and infiltration map #1 in the model, Figure 8.7.8 shows moderate lateral moisture flow in the PTn for about 100 - 300 meters. The lateral movement and direction are similar to those shown in Figure 8.7.6. The lateral diversion within the CHn is also moderate, up to 300 meters to the north in the southern part of the cross section.

Figure 8.7.9 depicts the simulation results using parameter set #4 and infiltration map #2. The figure indicates that there is hardly any lateral flow along the south-north direction. It agrees with what is shown in Figure 8.7.5 under the same model condition.

8.7.1.2
Near Borehole SD-7

The simulated flow velocity fields and saturations along the west-east cross section: W-E (SD-7) are shown in Figures 8.7.10 to 8.7.13. The simulations use the same four sets of parameters. The lateral diversion in the vicinity of SD-7 is much smaller in the PTn than in the west-east cross section near UZ-1/14. This may be due to the PTn unit, which is much thinner near SD-7 than that near UZ-1/14. However, Figures 8.7.10 - 8.7.13 show that significant lateral diversions occur only in the CHn.

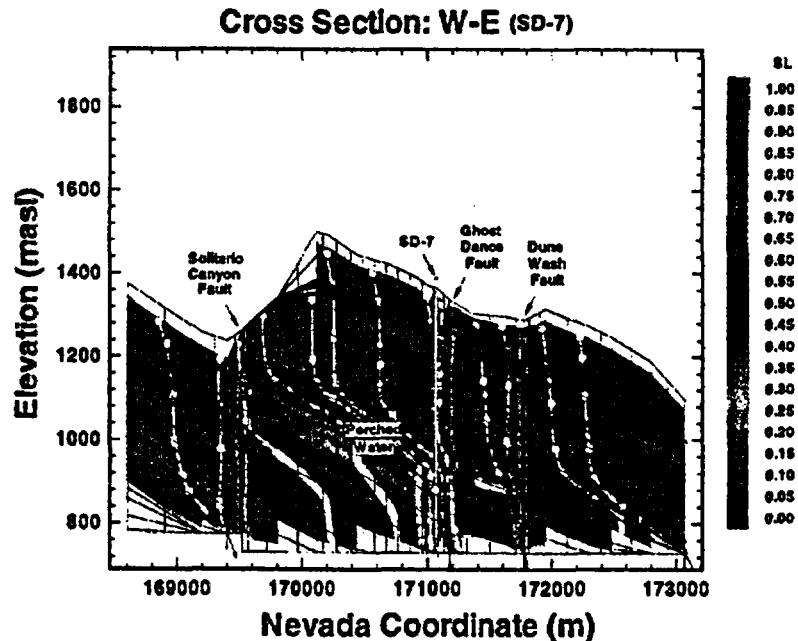


Figure 8.7.10
Velocity fields and liquid saturations along the West-East cross section crossing SD-7, simulated using parameter set #1 and infiltration of 0.1 mm/yr.

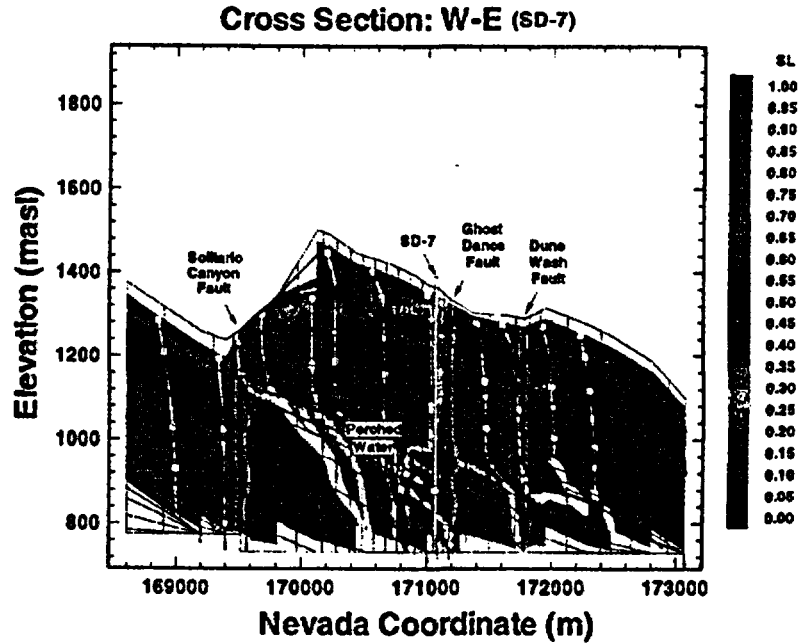


Figure 8.7.11
Velocity fields and liquid saturations along the West-East cross section crossing SD-7, simulated using parameter set #2 and infiltration of 0.1 mm/yr.

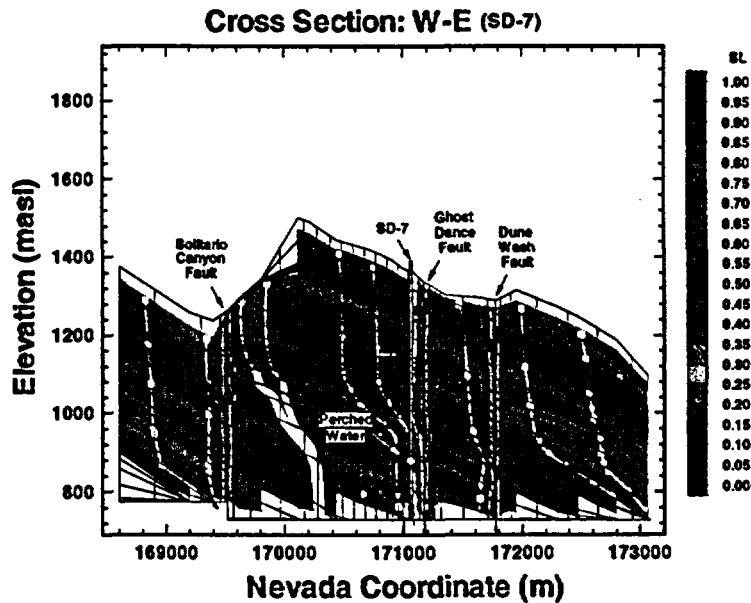


Figure 8.7.12
Velocity fields and liquid saturations along the West-East cross section crossing SD-7, simulated using parameter set #3 and infiltration map #1.

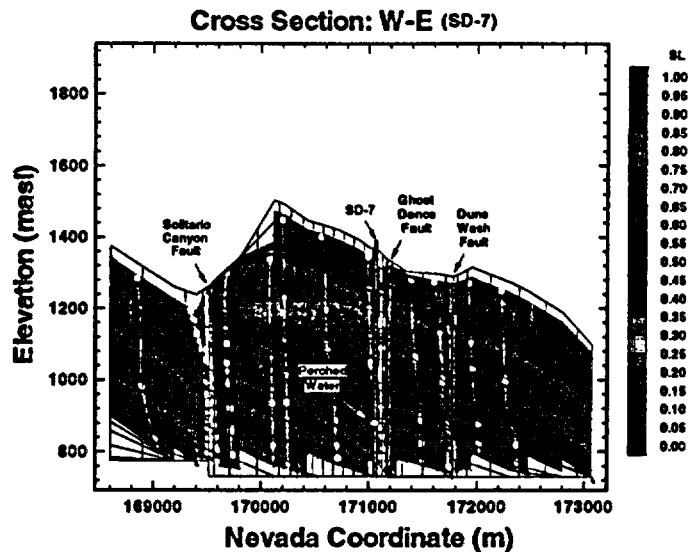


Figure 8.7.13

Velocity fields and liquid saturations along the West-East cross section crossing SD-7, simulated using parameter set #4 and infiltration map #2.

Figures 8.7.10, 8.7.11, and 8.7.12 show the results of simulations using parameter sets #1, #2 and #3, respectively. They all indicate that there is large lateral flow in the CHn between the Solitario Canyon and Ghost Dance faults, with lateral diversion of 100 to 1,000. Figures 8.7.10 and 8.7.12 also show higher saturations along the base of TCw, indicating a capillary barrier along the interface. Also, as shown in these figures, east of the Ghost Dance fault, the diverted moisture tends to flow to the Bow Ridge fault along the cross section.

Similar to the flow shown the UZ-1/14 W-E cross-section, the model using parameter set #4 and infiltration map #2 gives results showing little lateral diversion in all the units (Figure 8.7.13).

Figures 8.7.14 to 8.7.16 show the results along the south-north direction in the vicinity of SD-7. Figure 8.7.14 indicates that lateral diversions of moisture occur only in the top portion, a vitric layer, of the CHn unit, between SD-7 and SD-12. The total travel distance is about 500 meters to the north along this vitric layer.

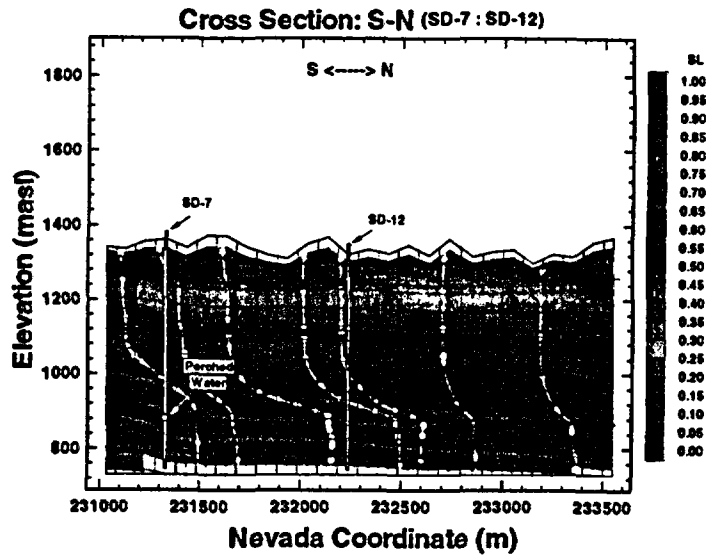


Figure 8.7.14
Velocity fields and liquid saturations along the South-North cross section crossing SD-7, simulated using parameter set #1 and infiltration of 0.1 mm/yr.

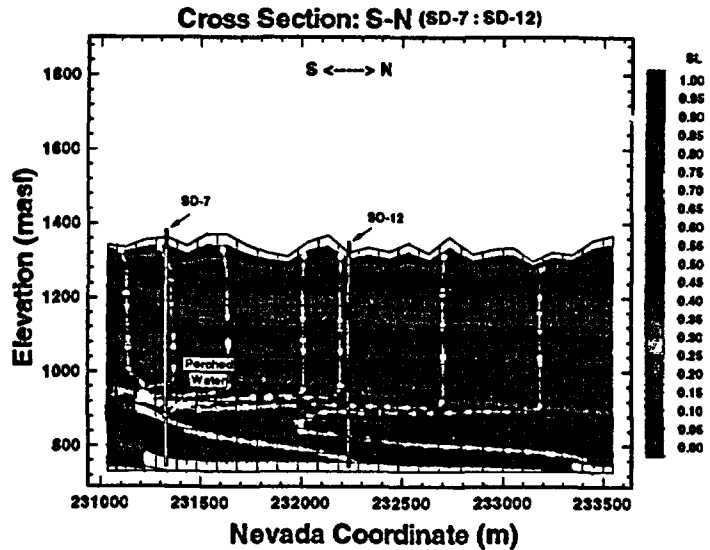


Figure 8.7.15
Velocity fields and liquid saturations along the South-North cross section crossing SD-7, simulated using parameter set #2 and infiltration of 0.1 mm/yr.

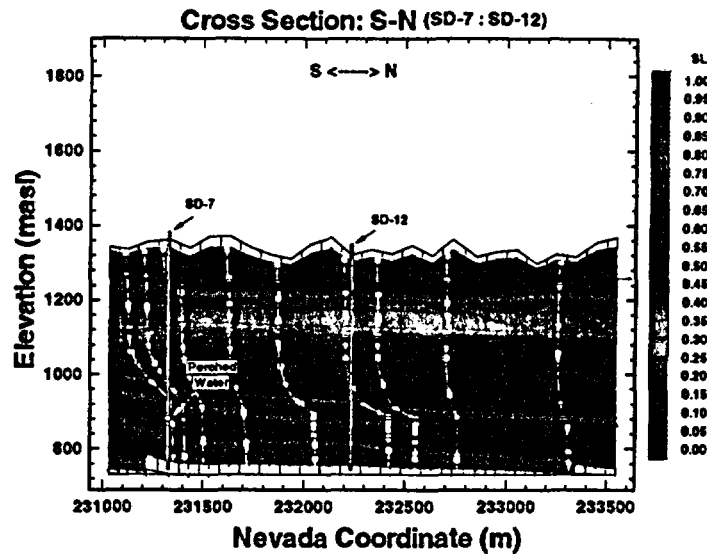


Figure 8.7.16
Velocity fields and liquid saturations along the South-North cross section crossing SD-7, simulated using parameter set #3 and infiltration map #1.

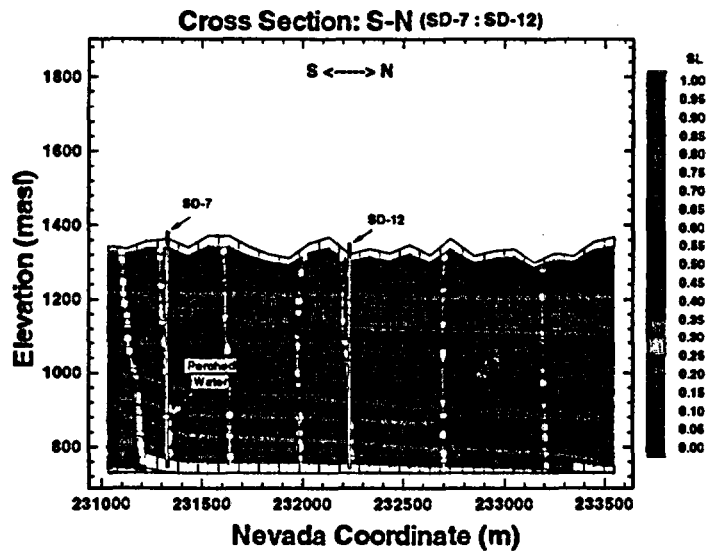


Figure 8.7.17
Velocity fields and liquid saturations along the South-North cross section crossing SD-7, simulated using parameter set #4 and infiltration map #2.

Figure 8.7.15 shows a different lateral diversion in which flow is towards the south, along the vitric layer of the top of the CH pattern. The simulation results are based on parameter set #2 and 0.1 mm/yr infiltration. All the other results in Figures 8.7.14, 8.7.16, and 8.7.17 indicate that the water is diverted to the north along the same top vitric unit of the same cross section. It is very

interesting, as shown in Figure 8.7.15, to note that water is moving to the south in the upper vitric layer and then flows back to the north, once it is past the zeolitic, or crosses a thin zeolitic layer near SD-7. Further analysis shows that the significant lateral flow along the vitric layers is due to large capillary pressure gradients, which overcome gravity forces along the dipping layer to the north. It can be seen from Figure 8.7.15 that it gets "drier" in the south end of the cross section than in the north in the top vitric unit, and this indicates that the flow direction is determined by capillary forces.

Figure 8.7.16 shows a small lateral moisture movement within the CHn, with a distance of about 100 - 200 meters. Again, Figure 8.7.17, which uses parameter set #4 and infiltration map #2, results in little lateral diversions in any units of the formation.

In summary, this study indicates that there are significant effects of rock properties and infiltration rates on lateral moisture flow in the unsaturated zone of Yucca Mountain. The PTn unit may divert water thousands of meters laterally to the east at certain locations of the mountain, and the extent of the simulated lateral movement within the PTn depends mainly on the rock properties, infiltration rates, and conceptual geological model. The lateral diversion of water flow in the unsaturated zone at Yucca Mountain is a complex phenomenon, as indicated by the 3-D modeling results. However, the key factors that have been observed to affect water lateral movement within the mountain the most are "capillary barrier" effects (Oldenburg and Pruess, 1993) and infiltration rates applied on the ground surface. This is especially true for the PTn unit, as shown in the figures discussed in this section. Permeability in the PTn unit is several orders of magnitude higher than that for the unit (TCw) above or the unit (TSw) below, but the capillary forces or the air entry pressures are not much different (See Tables 8.5.1 - 8.5.4 for the 4 sets of parameters). Therefore, a very "dry" zone may be created along the PTn, compared with those in the layers above and below from all the simulations. Thus a strong capillary barrier effect is expected across the PTn. The capillary effects change with the contrasts in moisture contents of the PTn and the adjacent units, which are directly related to the infiltration rates on the ground surface. Once a layer with strong capillary forces overlies a low capillarity layer and the vertical capillary gradients for upward water flow are large enough to overcome the gravity forces, the water flow only occurs in the lateral direction. This explains why there is hardly any lateral movement in the PTn when an infiltration rate is larger than 1 mm/yr from the modeling results.

In addition to large lateral flow in the PTn unit observed in some of the simulations, substantial lateral diversions also occur around the zeolitic units in the CHn formation. The strong moisture lateral movement in the CHnz unit, predicted in the 3-D simulation, is consistent with the thermal analysis results in Chapter 9 (Bodvarsson et al.). The lateral movement within the CHn unit tends

to divert water east to the Bow Ridge fault, along the dipping slopes of the zeolitic units.

8.7.2
3-D Lateral Moisture
Distributions and Movement

The moisture movement and distribution within the mountain can be seen more intuitively using 3-D plots. In this section, we present some of the 3-D simulation results using 3-D perspective pictures for saturations and velocity components in different directions.

The 3-D plots of saturations, simulated using parameters set #1 and #4, 0.1 mm/yr and map #2 infiltration rates, respectively, are shown Figures 8.7.18 and 8.7.19. It should be mentioned that the figures, such as Figures 8.7.19 and 8.7.20, which show the simulation results at the repository horizon, are based on the information of the model layer that represents the repository. The model layer for the repository is relatively flat only in the area of the repository, and its elevation and thickness vary outside the repository.

Figures 8.7.18 and 8.7.19 indicate a very non-uniform, but similar distribution of liquid saturations at the repository horizon. Along the four faults, Solitario Canyon, Iron Ridge, Ghost Dance and Abandoned Wash, and Dune Wash faults, very "dry" unsaturated zones are shown on the figures. In the case of lower infiltration, 0.1 mm/yr, Figure 8.7.18 shows an average saturation ranging from 0.4 to 0.6 at the potential repository between the Solitario Canyon fault and boreholes SD-7, SD-12, and SD-9. For a higher infiltration rate of map #2, Figure 8.7.19 gives a slightly higher saturations, ranging from 0.5 to 0.7 at the repository level.

Water Saturation at Repository Horizon

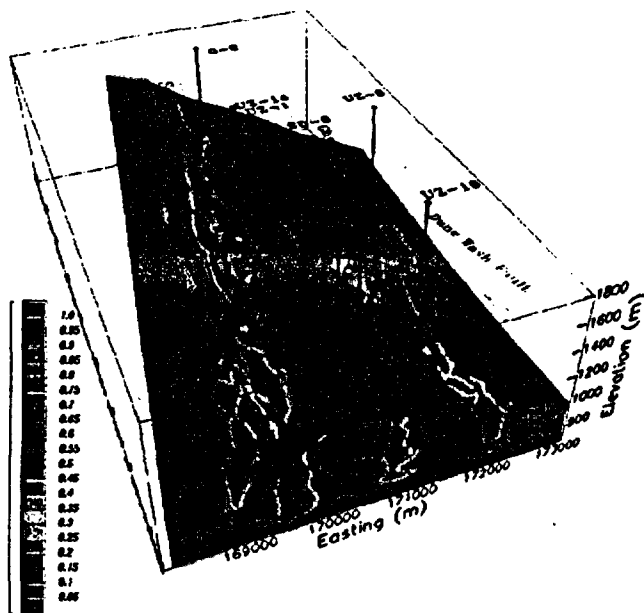


Figure 8.7.18
Saturations at the repository horizon and below, simulated using parameter set #1 and infiltration of 0.1 mm/yr.

Water Saturation at Repository Horizon

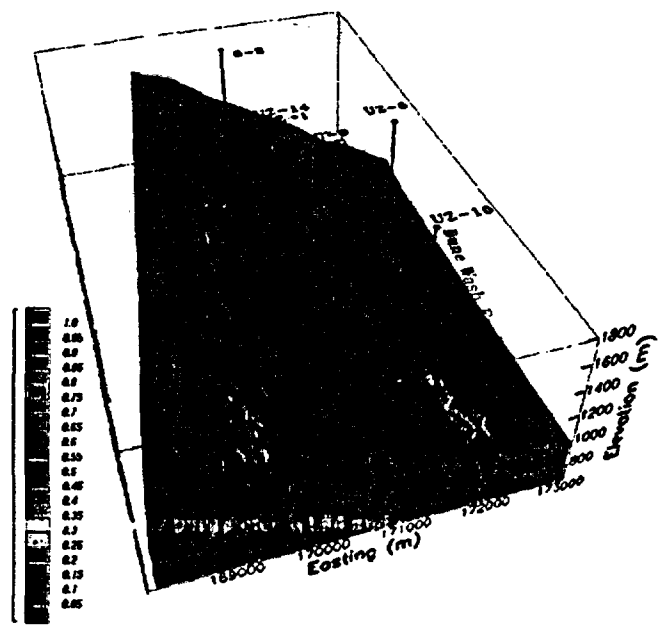


Figure 8.7.19
Saturations at the repository horizon and below, simulated using parameter set #4 and infiltration map #2.

Figure 8.7.20 shows a 3-D profile of saturations, with a volume cut along the west-east section, crossing UZ-1/14, then to the south, crossing SD-9, SD-12, and SD-7. The figure shows clearly certain high saturation zones on both sides of the Solitario canyon fault, and along the south-north cut section. The latter corresponds to the lower part of the TSw, west of the Ghost Dance fault, and the zeolitic units in the CHn.

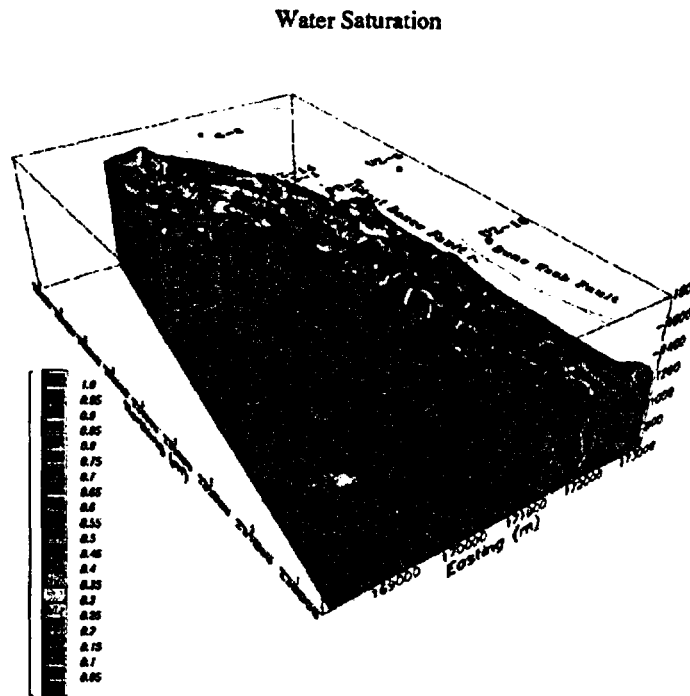


Figure 8.7.20
Saturations at the repository horizon and below, simulated using parameter set #4 and infiltration map #2.

The lateral diversions of moisture flow by the PTn can be seen using 3-D plots of velocity components in different directions. We also use the simulation results from parameter sets #1 and # 4, since these two sets of parameters produce very different lateral movement along the PTn, as discussed above. The three velocity components of flow fields simulated using parameter set #1 and #4 are shown in Figures 8.7.21 to 8.7.26, respectively. In these figures, units of scales in legends denote mass fluxes in terms of mm/yr for comparison with infiltration rates imposed on the top surface boundary

Figure 8.7.21 shows the west-east lateral mass fluxes at the middle of the PTn. On this figure and others showing west-east flow components, positive "values" or red colors indicate flow to the east directions, and the negative "values" or blue colors show west-bound flow. Figure 8.7.21 shows very large lateral flow from west to east within the PTn in the northern part of the model domain on both sides of the Solitario Canyon fault, especially near the bore-

holes UZ-1/14 and SD-9, on the order of 2 mm/yr. This result is consistent with the 2-D cross section analysis, as shown in Figure 8.7.2. Figure 8.7.21 indicates clearly that the lateral moisture flow within the PTn is dominantly from west to east, because slopes or dips of geological layers mostly are along the west-east direction.

West-East Mass Flux at Middle of PTn

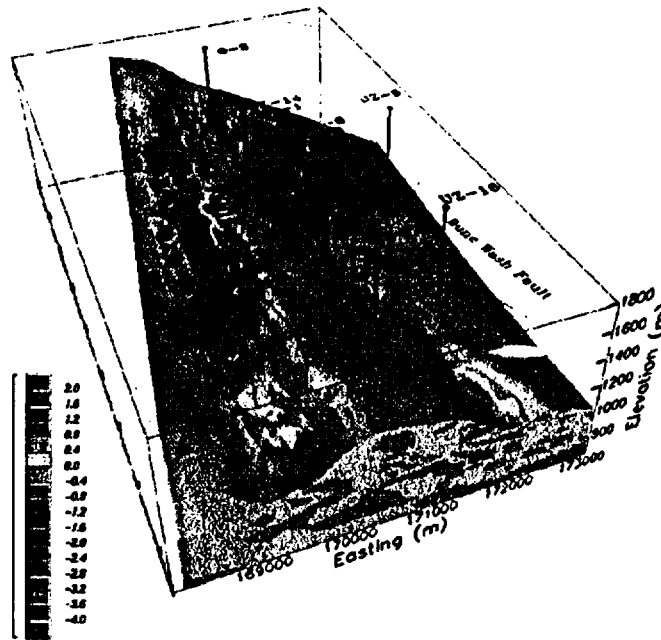


Figure 8.7.21
Velocity components in the west-east direction at the middle of the PTn, and below, simulated using parameter set #1 and infiltration of 0.1 mm/yr.

Figures 8.7.22 and 8.7.23 shows south-north and vertical components of moisture flow within the PTn, respectively. On Figure 8.7.22 or other south-north flow component plots, positive values or red color indicate south-bound flow, and negative values or blue colors show flow to north. On vertical flow maps, such as Figure 8.7.23, negative values denote downward flow. The simulation results in Figure 8.7.22 shows that there is very small lateral movement in the south-north direction in most of the PTn unit, except in the northern part of the domain, where significant north-bound flow occurs west of the Solitario Canyon fault and at the north-east corner of the model.

The vertical flow, as shown in Figure 8.7.23, indicates very non-uniform percolation fluxes crossing the PTn, even though a uniform surface infiltration rate, 0.1 mm/yr is used in this case. An averaged flux value of 0.1 to 0.2 above the repository can be seen from Figure 8.7.23, but in the northern part of the

domain, west of the Solitario Canyon fault and around the north-east corner of the model, significantly higher vertical fluxes, at about 4 mm/yr, are obtained in the simulation. This is due to the huge lateral diversion of flow toward these areas, as shown in Figures 8.7.21 and 8.7.22.

South-North Mass Flux at Middle of PTn

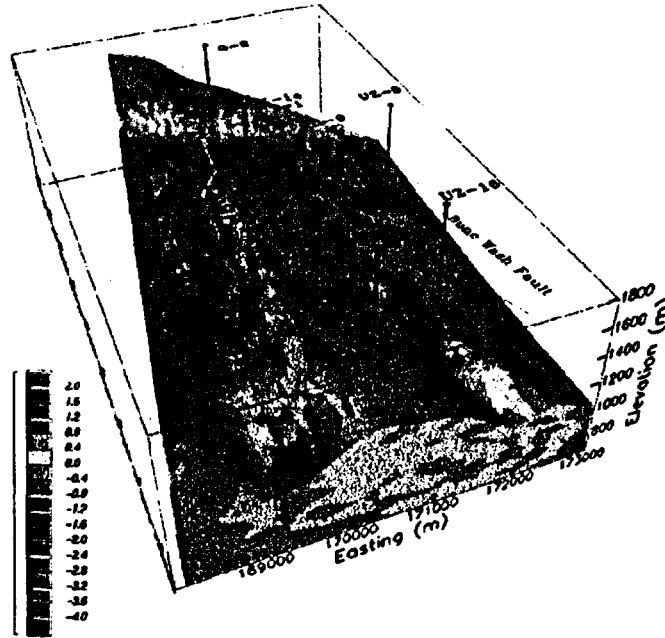


Figure 8.7.22
Velocity components in the south-north direction at the middle of the PTn, and below, simulated using parameter set #1 and infiltration of 0.1 mm/yr.

Vertical Mass Flux at Middle of PTn

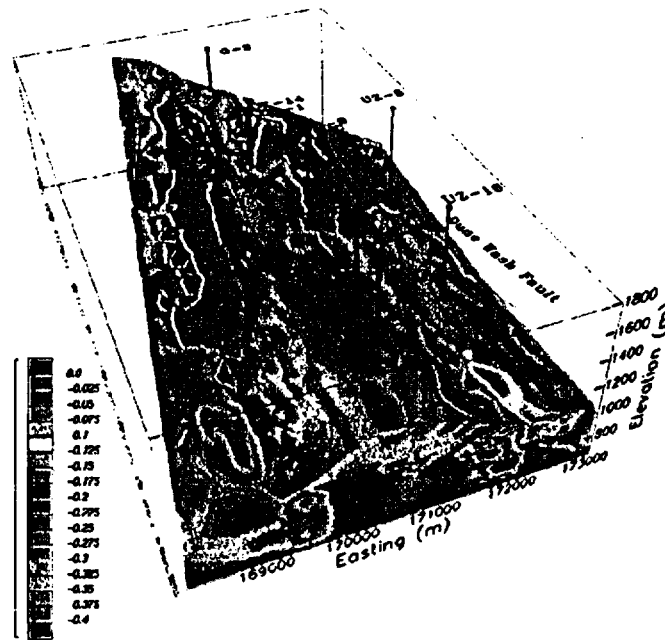


Figure 8.7.23

Velocity components in the vertical direction at the middle of the PTn, and below, simulated using parameter set #1 and infiltration of 0.1 mm/yr.

Similar to the previous three figures, Figures 8.7.24 to 8.7.26 show large lateral flow from west to east (Figure 8.7.24), indicated by the red colored zones, and relatively small diversions in the south-north direction (Figure 8.7.25). However, much higher vertical fluxes, at about 4 mm/yr, occur in the northern and middle parts of the domain through the PTn in Figure 8.7.26. But the ratios of lateral to vertical flow are very different in the areas near UZ-1/14 from the two simulation results. In the case of 0.1 mm/yr infiltration (Figures 8.7.21 - 8.7.23), the ratio of lateral/vertical components is $2.0/0.4 = 5$, but for infiltration map #2 (Figures 8.7.23 - 8.7.26), the ratio is $2.0/4.0 = 0.5$. Therefore, the lateral flow is dominating in the first case, and the vertical flow is much larger than lateral diversion when using the infiltration map #2 with parameter set # 4.

West-East Mass Flux at Middle of PTn

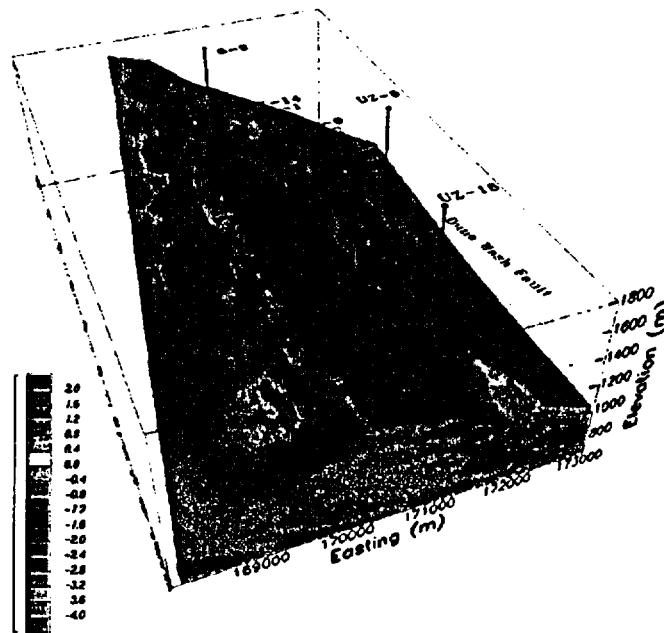


Figure 8.7.24 Velocity components in the west-east direction at the middle of the PTn, and below, simulated using parameter set #4 and infiltration map #2.

South-North Mass Flux at Middle of PTn

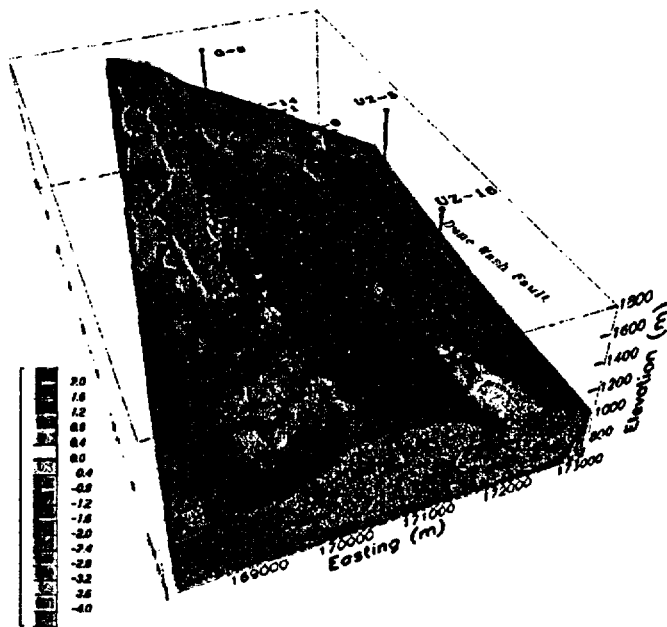


Figure 8.7.25 Velocity components in the south-north direction at the middle of the PTn, and below, simulated using parameter set #4 and infiltration map #2.

Vertical Mass Flux at Middle of PTn

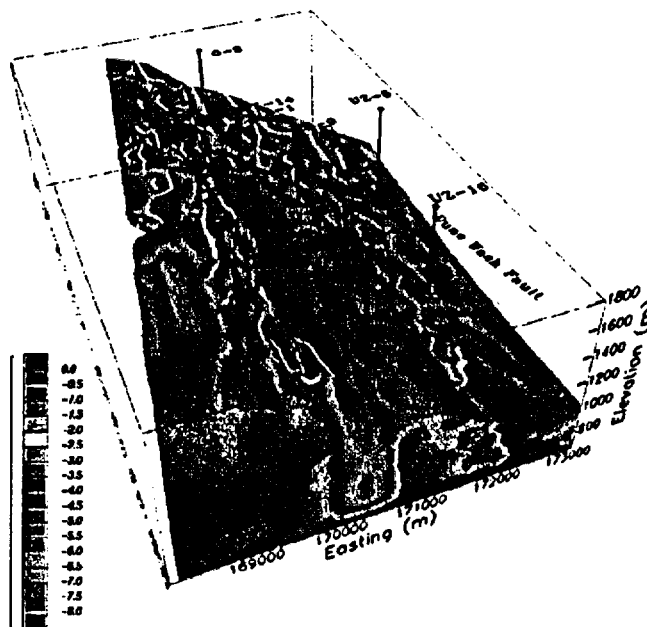


Figure 8.7.26

Velocity components in the vertical direction at the middle of the PTn, and below, simulated using parameter set #4 and infiltration map #2.

In summary, the 3-D plots of the two simulations indicate that very different percolation fluxes and lateral movement in the PTn are obtained when using different infiltration maps and rock properties. The higher infiltration rates tends to promote more vertical flow than lateral movement in the PTn unit. The percolation fluxes across the PTn unit are mainly from the lateral diversion in the lower infiltration case studied. The flux pattern follows the surface infiltration pattern when using infiltration map #2.

**8.7.3
Ambient Geothermal
Conditions and Heat Flow at
Repository Horizon**

The temperature distributions within the mountain, simulated by the four sets of rock properties and infiltration rates, are similar, and therefore, we present only one 3-D temperature plot (Figure 8.7.27). The volume cut at the south-west part of the model, as shown in Figure 8.7.27, indicates that temperature is at about 25 degree-C at the repository level.

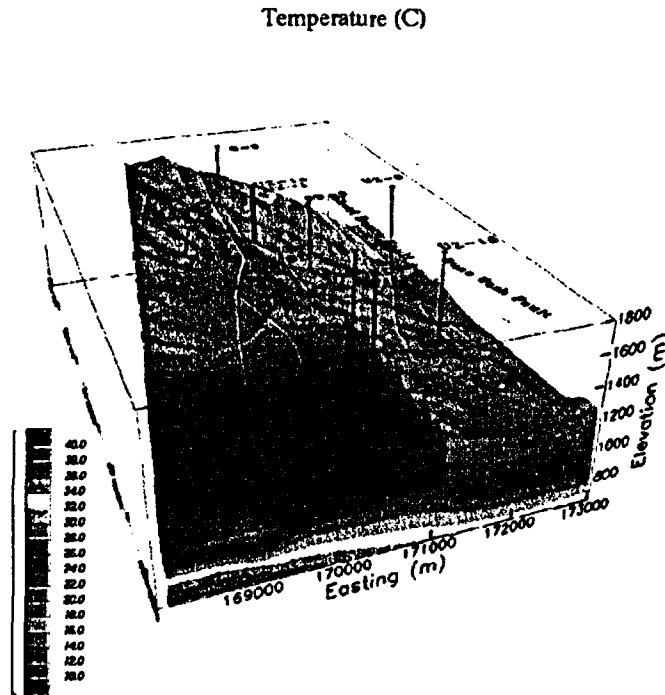


Figure 8.7.27
 3-D temperature distributions in the unsaturated zone of Yucca Mountain, simulated using parameter set #4 and infiltration map #2.

A vertical heat flow map, showing heat flux in W/m^2 at the repository horizon is shown in Figure 8.7.28. All the simulations conducted produce a heat flow pattern at the repository horizon similar to that shown in Figure 8.7.28. The averaged heat flow value is about 30 to 40 mW/m^2 , which is consistent with the estimation by Sass et al. (1988). The figures show that the highest heat flow occurs at the south-west corner of the model, where the ground surface elevation is the lowest, and the water table temperatures are the highest (Section 8.3.3). Few blue spots on the heat flow maps correspond to the low upward heat flow rates, which correlate with the higher percolation fluxes in these areas. The convection heat transfer by percolation is always downwards, therefore, as expected, the total upwards heat flow is the combined result of heat conduction and convection by liquid and vapor, and it becomes lower where the percolation flux is high. Detailed analysis of percolation fluxes from temperature data are given in Chapter 9 (Bodvarsson et al.).

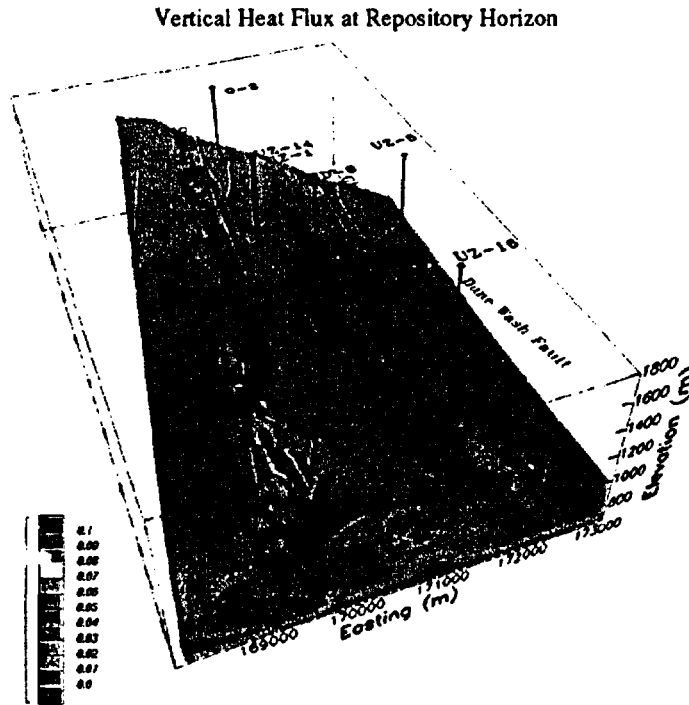


Figure 8.7.28
Vertical heat flow map at repository horizon of the unsaturated zone of Yucca Mountain, simulated using parameter set #4 and infiltration map #2.

8.8 Effects of Fault Properties

Three sets of fault properties, as summarized in Section 8.5.6, have been used in this Chapter to investigate effects of these fault properties on moisture flow in the unsaturated zone of Yucca Mountain. The fault properties were based on the previous modeling studies (Wittwer et al., 1995; and Ahlers et al., 1995 a and b) at LBNL, and the recent pneumatic analysis results (Ahlers et al., 1996). The major faults incorporated into the site-scale model are shown in Figure 8.3.1, which include the Solitario Canyon, Iron Ridge, Ghost Dance and Abandoned Wash, and Dune Wash faults. The Bow Ridge fault is treated as a boundary condition along the eastern boundary of the model domain.

The faults are represented in the model as vertical zones with consideration of stratigraphic offsets, connections to adjacent gridlayers, and variable thickness. In addition, fracture and matrix flow within fault zones are treated using the ECM approximation, instead of a single continuum porous medium, as in the previous study (Wittwer et al., 1993 and 1995).

Three-Dimensional Model Calibration and 'Sensitivity Studies

The purpose of this section is to present sensitivity analyses of effects of fault properties on 3-D moisture flow within Yucca Mountain. The representative values of fault rock properties used in the sensitivity study are listed in Table 8.5.6, 8.5.7 and 8.5.8 for property sets of fault #1, fault #2, and fault #3, respectively, in Section 8.5.6.

8.8.1 W-E Cross Section at SD-7

The fault #1 properties, listed in Table 8.5.6, use a set of uniform fault rock parameters for all the incorporated faults, and this set of fault properties has been used in most of the simulations reported this Chapter. The effects of fault properties on moisture flow can be seen clearly from the west-east vertical cross sections, as shown in Figures 8.8.1 to 8.8.4. The moisture flow and roles played by the three major faults, the Solitario Canyon, Ghost Dance and Dune Wash faults, along the west-east (SD-7) cross section (Figure 8.7.1), are displayed in these figures. The simulations for these figures are based on fault #1 properties, and parameter sets #1 to #4 with the corresponding infiltration rates, respectively.

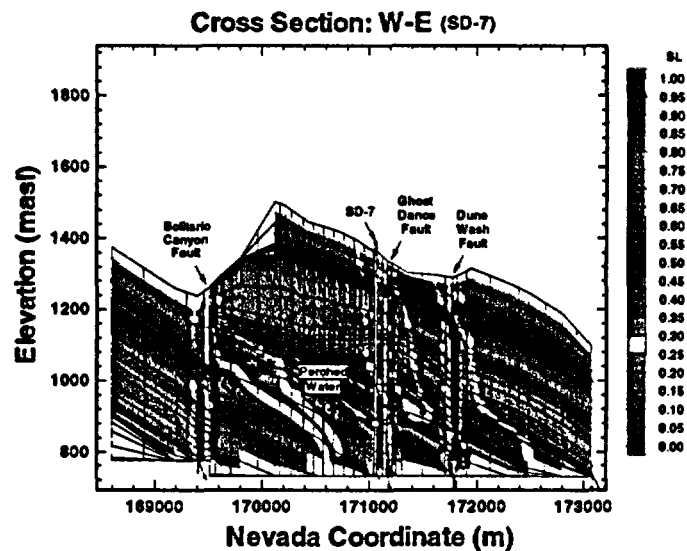


Figure 8.8.1
Moisture movement and distributions along the West-East cross section crossing SD-7, Solitario Canyon, Ghost Dance and Dune Wash faults, simulated using fault #1 properties, parameter set #1 and infiltration of 0.1 mm/yr.

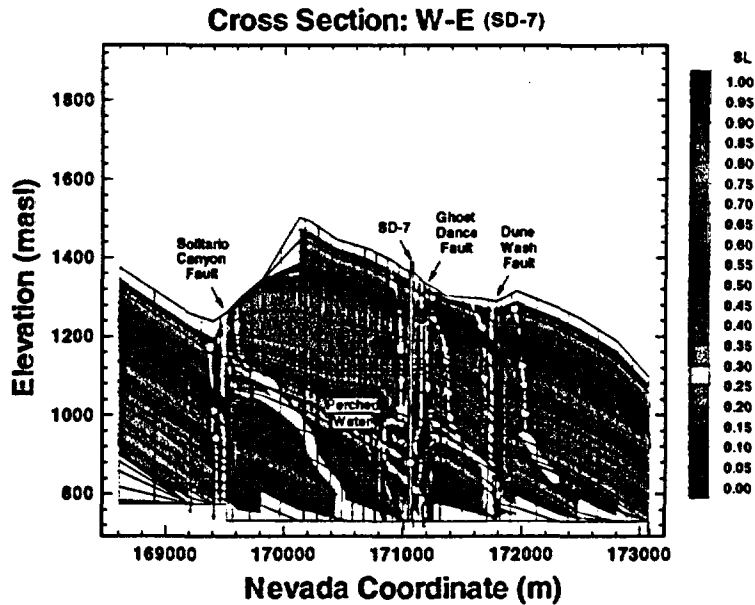


Figure 8.8.2
Moisture movement and distributions along the West-East cross section crossing SD-7, Solitario Canyon, Ghost Dance and Dune Wash faults, simulated using fault #1 properties, parameter set #2 and infiltration of 0.1 mm/yr.

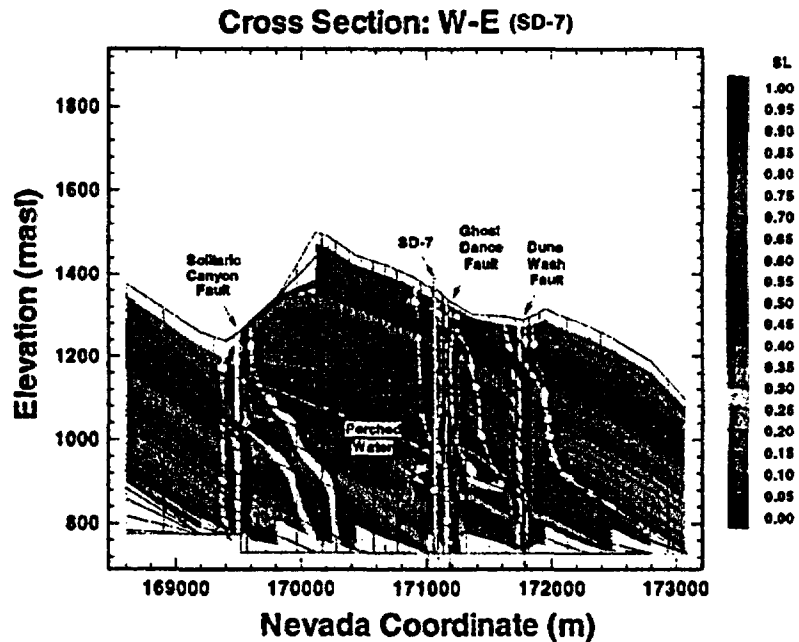


Figure 8.8.3
Moisture movement and distributions along the West-East cross section crossing SD-7, Solitario Canyon, Ghost Dance and Dune Wash faults, simulated using fault #1 properties, parameter set #3 and infiltration map #1.

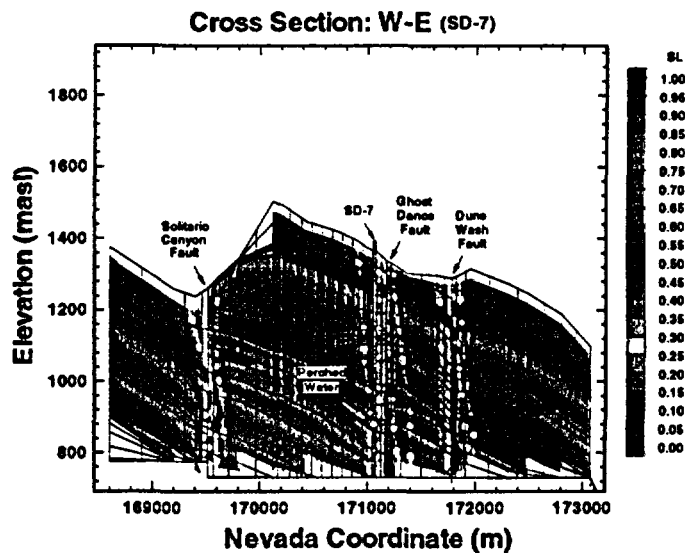


Figure 8.8.4
Moisture movement and distributions along the West-East cross section crossing SD-7, Solitario Canyon, Ghost Dance and Dune Wash faults, simulated using fault #1 properties, parameter set #4 and infiltration map #2.

Figures 8.8.1 to 8.8.4 show that the three south-north faults (the Solitario Canyon, Ghost Dance, and Dune Wash) all act as a capillary barrier to the lateral moisture flow along this cross section. The faults stay relatively "dry" with saturations of 10 - 20% when using this set of fault properties. The figures also indicates that the vertical flow paths near the faults are mainly parallel to the faults. However the moisture flow may cross or leave the faults laterally at several locations, as indicated in the four figures. Flow leaves or crosses the Solitario Canyon and Dune Wash faults at the interfaces between TCw and PTn, and moves towards the east. In these locations large offsets exist, and the PTn units on both sides of the faults are completely separated, while the TCw and the TSw formations are connected through fault zones.

Along part of the Ghost Dance fault, the vertical flow is also diverted laterally to the east near the interface of the TSw and CHn, due to high saturation zones on both sides of the fault, as shown in Figures 8.8.1, 8.8.3 and 8.8.4.

Figure 8.8.5 shows the simulation results using fault #2 properties and parameter set #1 with a uniform infiltration of 0.1 mm/yr. As discussed in Section 8.5, the only difference between fault #2 and fault #1 properties is in absolute fracture permeability. Fault #2 properties use four different fracture permeabilities for the four vertical geological units of faults, respectively, instead of a uniform fracture permeability as in fault #1 properties. The fracture permeability values are derived from the pneumatic analysis (Ahlers et al.,

1996). A comparison of Figures 8.8.5 and 8.8.1 indicates that very similar results are obtained using fault #1 and fault #2 properties. The only noticeable difference in predicting moisture flow using these two sets of fault properties is in the Dune Wash fault, at the middle of CHn, where Figure 8.8.5 shows a flow path line crossing the fault. This is because a much lower fracture permeability value of 10 md is used for the faults within the CHn unit in fault #2. Overall, Figure 8.8.5 and 8.8.1 show that differences in absolute fracture permeability of fault zones have little effects on moisture flow near faults.

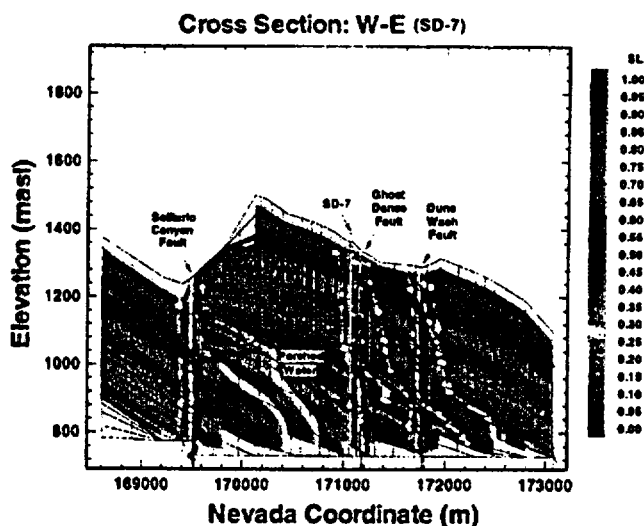


Figure 8.8.5
Moisture movement and distributions along the West-East cross section crossing SD-7, Solitario Canyon, Ghost Dance and Dune Wash faults, simulated using fault #2 properties, parameter set #1 and 0.1 mm/yr infiltration.

Figure 8.8.6 shows the flow along the same west-east cross section, and the simulation results are based on all the rock properties (parameter set #4), as used for Figure 8.8.4, except that fault #3 replaces fault #1 properties (Figure 8.8.4). Fault #3 properties are different from the set of fault #1 not only in fracture permeability, but also in moisture retention functions for fault zones. As shown in Table 8.5.8, much stronger capillary suction are provided by the fault #3 properties, which were selected from van Genuchten parameters estimated in parameter set #4 for corresponding units.

A comparison of Figures 8.8.6 and 8.8.4 indicates that there is a significant difference in saturations along the faults. Figure 8.8.6 gives much "wetter" conditions at or near faults, with saturation values between 40 to 80%. This is due to the higher capillary suction within the matrix material of faults. As a result, faults shown in Figure 8.8.6 do not act as capillary barriers anymore. Instead, the faults with fault #3 properties and higher infiltration map #2 behave as a conduit for nearby moisture flow because of relatively higher permeability and strong capillary pressure forces along the faults.

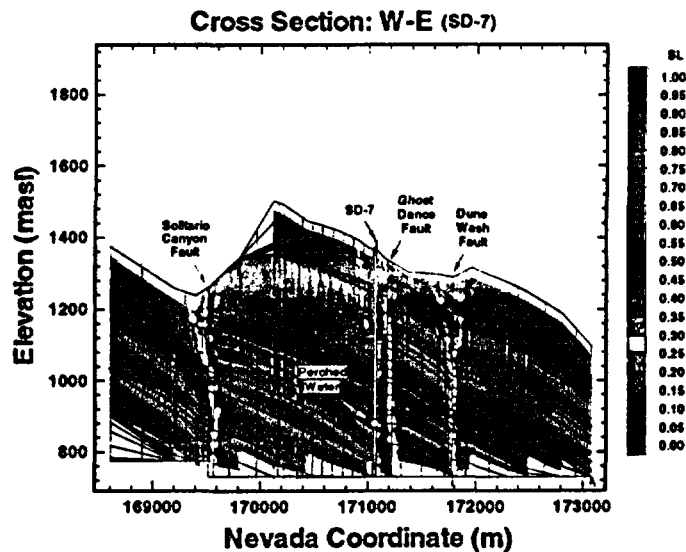


Figure 8.8.6
Moisture movement and distributions along the West-East cross section crossing SD-7, Solitario Canyon, Ghost Dance and Dune Wash faults, simulated using fault #3 properties, parameter set #4 and infiltration map #2.

8.8.2
W-E Cross Section at UZ-1/
14

For the west-east cross section of UZ-1/14 (Figure 8.7.1), Figures 8.8.7 and 8.8.8 show very similar moisture flow fields and liquid saturation contours when using fault #1 and #2 properties, with the same infiltration and rock parameter set. The Solitario Canyon faults on the two figures are both "dry", acting as a capillary barrier to lateral moisture flow. However, a flow path leaves the fault, and is diverted to the east at near the interface of the TSw and CHn units (Figure 8.8.8), using the fault #2 properties, for the same reasons discussed previously.

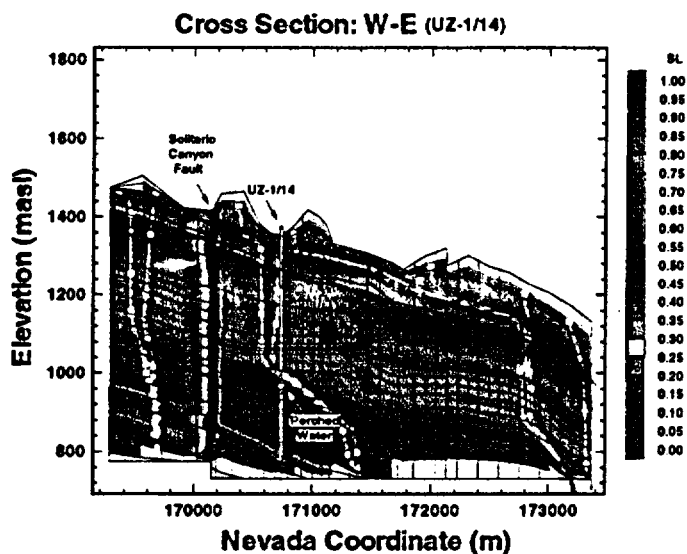


Figure 8.8.7
Moisture movement and distributions along the West-East cross section crossing UZ-1/14 and Solitario Canyon fault, simulated using fault #1 properties, parameter set #1 and infiltration of 0.1 mm/yr.

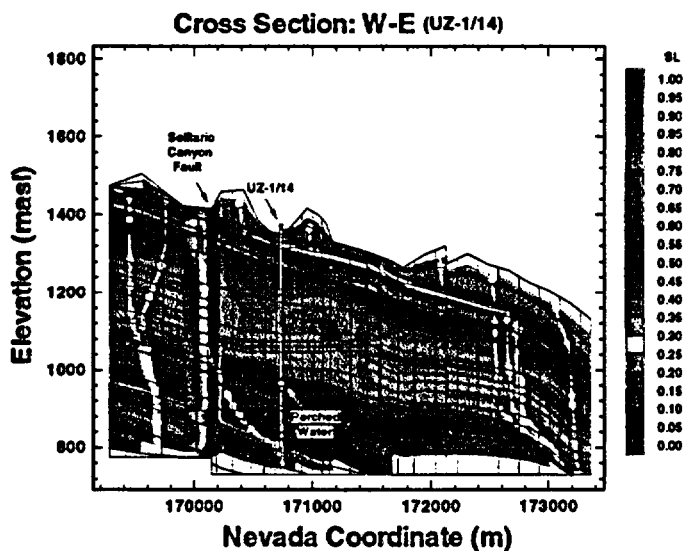


Figure 8.8.8
Moisture movement and distributions along the West-East cross section crossing UZ-1/14 and Solitario Canyon fault, simulated using fault #2 properties, parameter set #1 and infiltration of 0.1 mm/yr.

Figures 8.8.9. and 8.8.10 show a comparison of the simulation results using the fault #1 and #3 properties, and infiltration map #2 and rock parameter set #4, respectively. Similar to the W-E cross section of SD-7, Faults #1 and #3 with

parameter set # 4 and high infiltration rates of map #2 result in very different predictions on the role of faults. Figure 8.8.9 shows that the Solitario Canyon fault is very "dry", and acts as a capillary barrier, while Figure 8.8.10 indicates a very "wet" fault that carries water down to the water table.

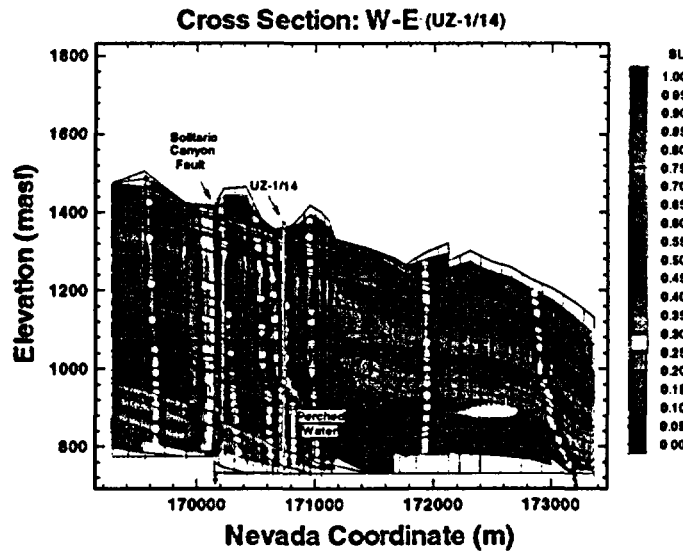


Figure 8.8.9
Moisture movement and distributions along the West-East cross section crossing UZ-1/14 and Solitario Canyon fault, simulated using fault #1 properties, parameter set #4 and infiltration map #2

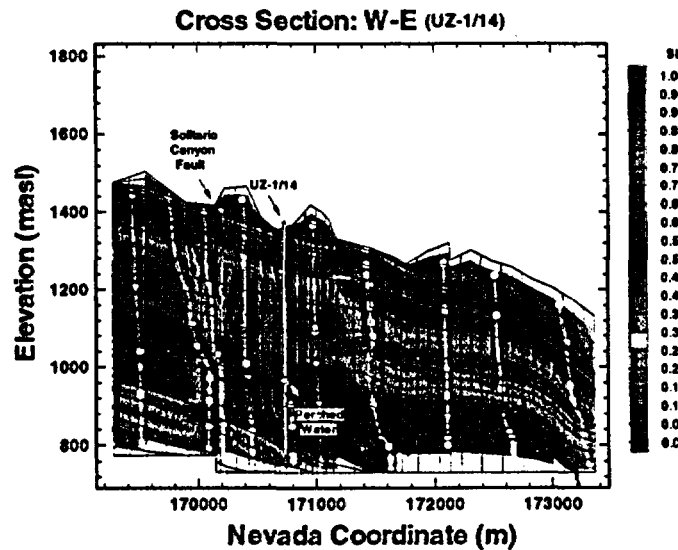


Figure 8.8.10
Moisture movement and distributions along the West-East cross section crossing UZ-1/14 and Solitario Canyon fault, simulated using fault #3 properties, parameter set #4 and infiltration map #2.

8.8.3
Groundwater Travel Times

The water ages estimated from perched water samples from UZ-14 and SD-7, based on ^{14}C data (Rousseau et al., 1996; Luckey, 1995), could give us an independent check of the water traveling times simulated in our model calibration and sensitivity studies. It was estimated that the ages of perched water from boreholes UZ-14 varied between 5,150 and 11,000 years old (Rousseau et al., 1996). The perched water of SD-7 may be 3,000 to 7,000 years old (Yang et al., 1996). The data on the SD-7 perched water age are in the process of being qualified by the USGS.

Using the 3-D modeling results of this Chapter and a particle tracking scheme, we can also estimate the ages of the water at the perched water locations. Near UZ-1/14, total time for water to travel from the surface to the perched level is about 5,000 - 10,000 years, for the simulations based on the different parameter sets, but high infiltration scenarios, and fault #1 or #3 properties. These estimated water ages is consistent with the 5,150 to 11,000 years by the geochemistry data.

Using the higher infiltration rates, the ages of the perched water at SD-7 can be estimated at about 5,000 to 12,000 years, which is somewhat consistent with the isotopic ages of 3,000 to 7,000 years. Perched water issues are discussed in Chapter 7 (Wu et al., 1996) of this report.

8.9 **3-D Dual-Permeability Model**

As part of model sensitivity analyses described in this report, a three-dimensional dual-permeability model has been developed and is presented in this section. The dual-permeability model is an alternate conceptual model that can be used to study fracture/matrix flow phenomena at Yucca Mountain. It is a built-in option in the TOUGH2 code and has been qualified for use in the Yucca Mountain Project. The details of the dual-permeability approach can be found in Pruess and Narasimhan (1985) and Pruess (1983, 1991).

8.9.1
Dual-Permeability Model
Grid and Parameters

The dual-permeability model discussed in this section extends over the entire 3-D model domain and grid (Figure 8.3.1). The dual-permeability grid was derived using the 3-D grid shown in Figure 8.3.1 as a primary grid. All the connection information, such as fracture-fracture, fracture-matrix, and matrix-matrix connecting areas and distances, were calculated using the MINC approach (Pruess, 1983). We did not reduce the connection areas between fracture and matrix elements as done by Ho et al. (1995). The fracture system in the unsaturated zone of the mountain is subdivided into four zones, which corresponds to the hydrogeologic units, TCw, PTn, TSw and CHn, respectively. The properties of the fractures for the four units are taken from TSPA-93 (Wilson et al., 1994), as listed in Table 8.9.1. Since few fractures through going exist in the PTn unit, the effects of fractures on moisture flow in the PTn are ignored in this

study, and the PTn formation is treated as a single porous medium. Also, the fracture/matrix flow in the fault zones, shown in Figure 8.3.1, is treated using the ECM approach. This may be a reasonable assumption, because matrix block sizes are smaller within fault zones than in fractured rocks outside, and the ECM equilibrium condition is better satisfied in the fault zones.

Table 8.9.1
The fracture porosity, aperture and spacing data used for the dual-permeability simulations (Wilson et al., 1994).

Unit	Porosity	Aperture (m)	Spacing (m)
TCw	1.38e-3	0.181e-3	.618
PTn	4.12e-3	0.206e-3	2.22
TSw	2.75e-3	0.180e-3	.740
CHn	9.98e-4	0.179e-3	1.618

In the dual-permeability simulations, parameter set # 4, for matrix and fractures, and infiltration map #2 are used, as listed in Table 8.5.4. The same boundary conditions and specifications, as described in Section 8.3, are used here. However, the water infiltration on the ground surface was only added into the fracture elements at the top boundary, and isothermal conditions were assumed to exist under two-phase flow conditions.

8.9.2
Comparisons with the ECM Results

A systematic study is presented in this section for comparing the results using the dual-permeability and ECM approaches on the large scale, 3-D, site-scale model. The simulation results are compared using liquid saturations and capillary pressure of fracture and matrix, obtained using both methods. Comparisons are also made with the observed matrix saturation data from several boreholes. The measured saturation data are from 7 boreholes UZ-14, UZ-16, NRG-6, NRG-7a, SD-7, SD-9, and SD-12, collected by the USGS (OCRWM, DOE, 1995).

We present the results of simulations and comparisons only for borehole SD-7, because for all the other boreholes, almost the same results are obtained. Figures 8.9.1 and 8.9.2 show the comparisons of vertical saturation and capillary pressure profiles in the matrix and fractures for borehole SD-7, including observations (if available) and simulated values using the dual-permeability and ECM approaches. It should be mentioned that the saturations in the PTn unit, shown in the figures, are for matrix only, since this unit is treated as a single continuum porous medium. The same saturations are also used in plots of fracture saturations for producing continuous curves vertically.

Figure 8.9.1 shows that almost identical results of both matrix saturations and capillary pressures are obtained from the two modeling approaches. The only differences between the two solutions may be noticed in the TCw unit, or

along the interfaces between PTn and TCw or TSw. The reasons for this minor difference are due to the conceptual model used, rather than the modeling approaches. First, in the dual-permeability simulation the water infiltration is injected into fractures only on the top boundary, while the ECM model puts the infiltration into both fracture and matrix systems. Secondly, in the dual-permeability model the top and the bottom gridlayers in the PTn unit are connected vertically only to the fracture elements in the TCw or the TSw, while the ECM model connects to both fractures and matrix. Therefore, there are discontinuities in matrix vertical connections across these interfaces. As can be seen from these figures, in the dual-permeability model water cannot flow into the PTn directly from matrix at the bottom of the TCw, and it must go through the fractures. As a result, matrix saturations simulated from the dual-permeability model are higher, or capillary pressures are lower at this interface than those in the ECM simulations.

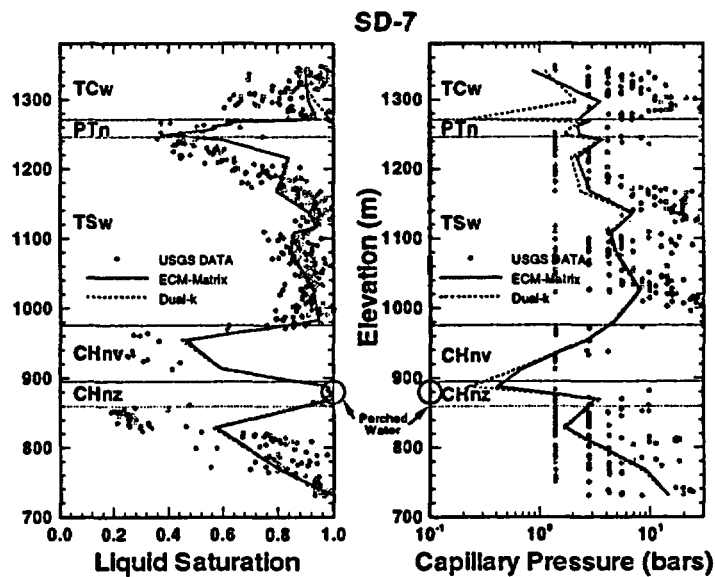


Figure 8.9.1
Comparisons of the observed and simulated saturations and capillary pressures using dual-permeability and ECM approaches at borehole SD-7 with parameter set #4 and infiltration map #2; (a) matrix saturation, (b) matrix capillary pressure.

A comparison of simulated fracture saturations at borehole SD-7 is shown in Figure 8.9.2, and the results are from the dual-permeability and the ECM approaches, respectively. Again the two solutions for fracture saturations are in good agreement under the three-dimensional flow condition. Also comparisons of fracture saturations obtained from the two modeling approaches have been made for the other boreholes, and they all match well, as shown in Figure 8.9.2.

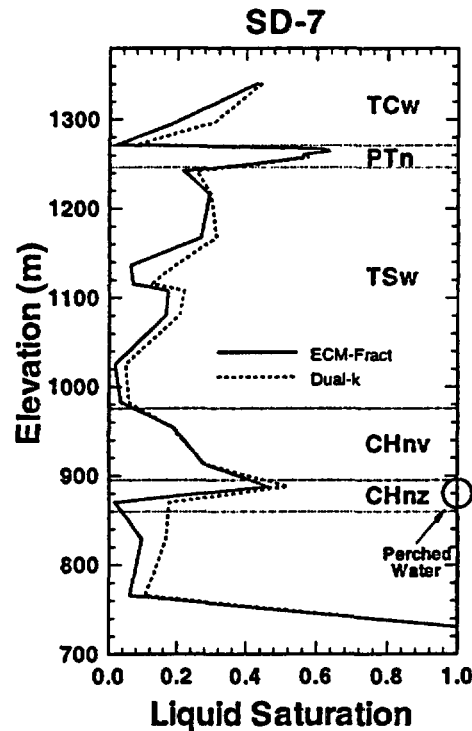


Figure 8.9.2
Comparisons of the observed and simulated fracture saturations using dual-permeability and ECM approaches at borehole SD-7 with parameter set #4 and Infiltration map #2

8.9.3
Effects of Climate Changes
Using High-Pulse Infiltration

In this section, a high-pulse infiltration scenario (climate change) is proposed using a much larger infiltration rate, i.e., three times higher than the averaged value used for infiltration map #2, or 13.2 mm/yr over the model domain. The use of such a high infiltration rate is reasonable according to Sheryl Morris of DOE (Personal Comm., 1996). The high-pulse infiltration rate is assumed for possible higher infiltration condition in the future due to climate changes. The initial condition for this high-pulse infiltration simulation is the steady-state condition generated by the previous dual-k run using the map #2 infiltration and parameter set #4. The infiltration rate is increased by a factor of three when the high-pulse simulation started.

The effects of high-pulse infiltration and transient simulations are analyzed using 2-D plots of moisture content and velocity distributions along the west-east vertical cross section crossing UZ-14 (Figure 8.7.1). The simulation results are shown in Figures 8.9.3 to 8.9.10 for simulation times of 100, 1,000, 30,000, and 100,000 years, respectively. The same scaling factors for the velocity vectors are used for matrix and fracture in all the figures.

Three-Dimensional Model Calibration and 'Sensitivity Studies

Figures 8.9.3 and 8.9.4 show liquid saturations and velocity fields after 100 years for the matrix and fractures. As can be seen in these two figures, the high infiltration front has only moved down to the middle of the PTn unit. But along the Solitario Canyon fault, the water front has passed the PTn and entered the TSw.

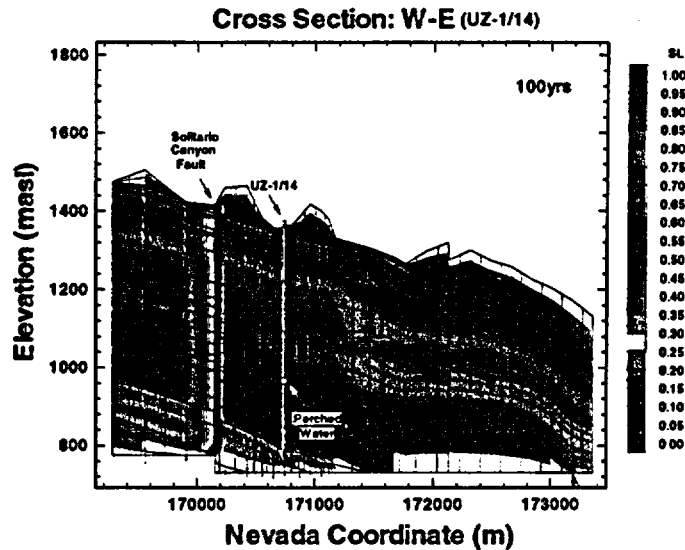


Figure 8.9.3
Matrix liquid saturations and velocity fields after 100 years along the West-East cross section crossing UZ-1/14, simulated using a dual-permeability approach and high-pulse infiltration rate.

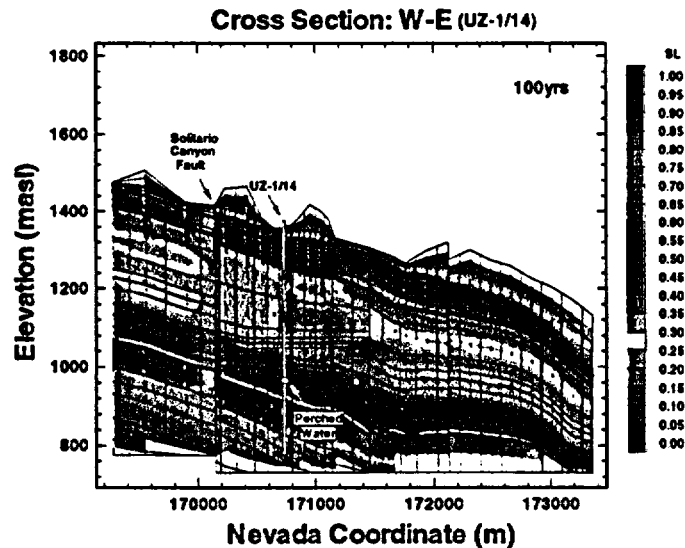


Figure 8.9.4
Fracture liquid saturations and velocity fields in 100 years along the West-East cross section crossing UZ-1/14, simulated using a dual-permeability approach and high-pulse infiltration rate.

Figures 8.9.5 and 8.9.6 show a much deeper penetration of the water front in both the fracture and the matrix systems, after 1,000 years. Figure 8.9.6 indicates (when compared with Figure 8.9.4 at 100 years) that the front already reaches the water table in the west half of the cross section through fractures in 1,000 years. The water flowing through the matrix also enters the CHn unit in 1,000 years, and reaches the water near the eastern boundary. Both of the figures show that the Solitario Canyon fault acts as a major flow pathway for rapid downward water movement. A comparison of Figures 8.9.5 and 8.9.3 show that the matrix in most of the cross section are much "wetter" at 1,000 years than at 100 years, as should be expected under the assumed infiltration condition.

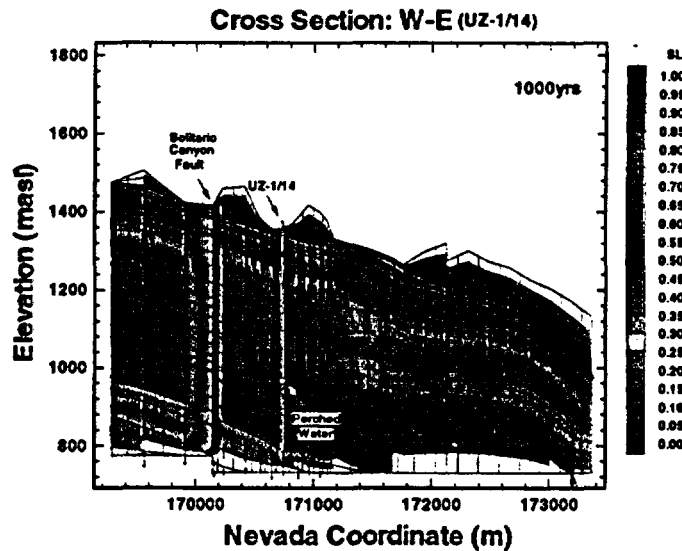


Figure 8.9.5
Matrix liquid saturations and velocity fields in 1,000 years along the West-East cross section crossing UZ-1/14, simulated using a dual-permeability approach and high-pulse infiltration rate.

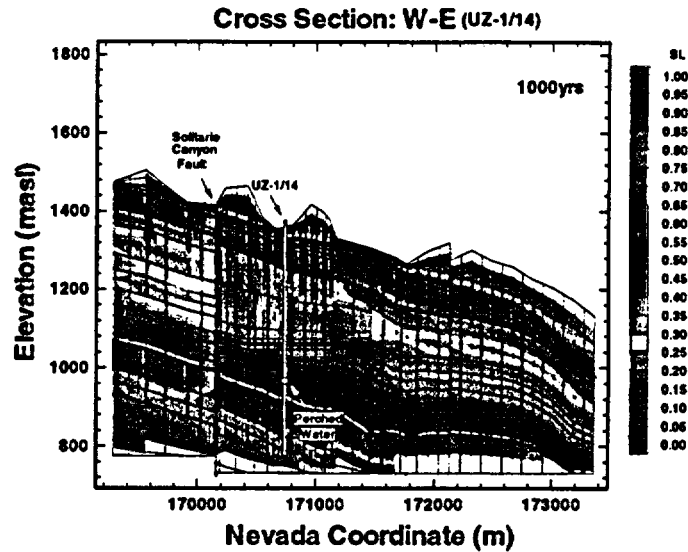


Figure 8.9.6
Fracture liquid saturations and velocity fields in 1,000 years along the West-East cross section crossing UZ-1/14, simulated using a dual-permeability approach and high-pulse infiltration rate.

After 30,000 years, higher flow velocities can be seen everywhere in both fractures and matrix, as shown in Figures 8.9.7 and 8.9.8, and both systems are somewhat "wetter" than after 1,000 years.

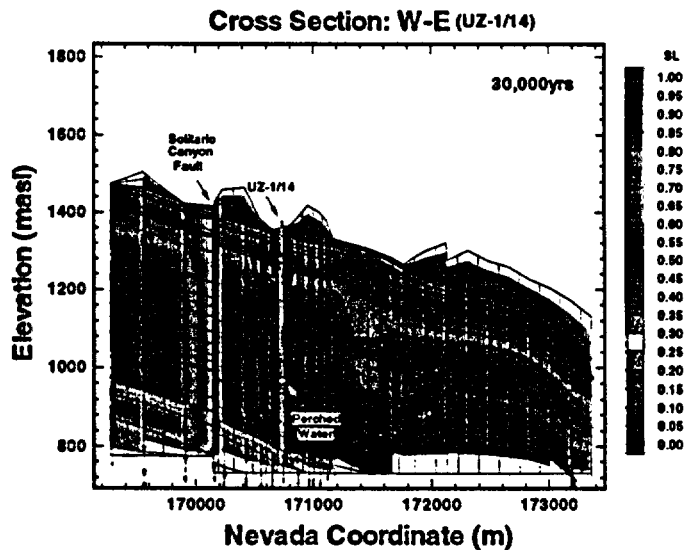


Figure 8.9.7
Matrix liquid saturations and velocity fields in 30,000 years along the West-East cross section crossing UZ-1/14, simulated using a dual-permeability approach and high-pulse infiltration rate.

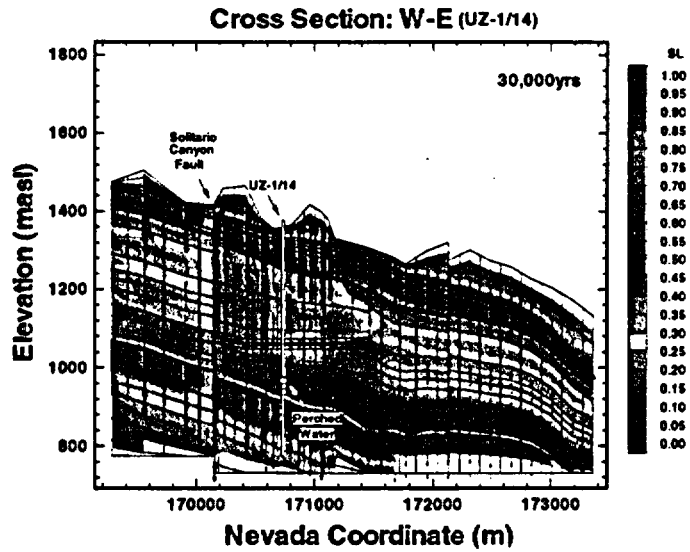


Figure 8.9.8

Fracture liquid saturations and velocity fields at 30,000 years along the West-East cross section crossing UZ-1/14, simulated using a dual-permeability approach and high-pulse infiltration rate.

After 100,000 years, Figures 8.9.9 and 8.9.10 show that there is little difference, for both saturation and velocity distributions, in the cross section, from those observed after 30,000 years. Therefore, the system reaches a steady-state after approximately 30,000 years under the high-pulse infiltration conditions.

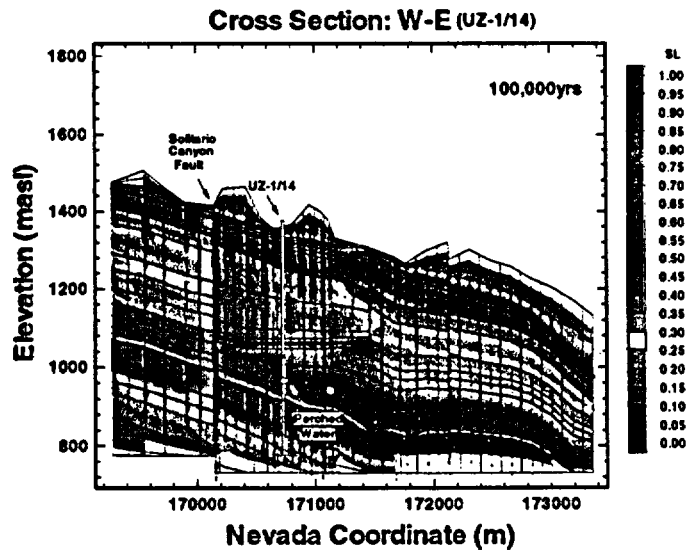


Figure 8.9.9

Matrix saturations and velocity fields in 100,000 years along the West-East cross section crossing UZ-1/14, simulated using a dual-permeability approach and high-pulse infiltration rate.

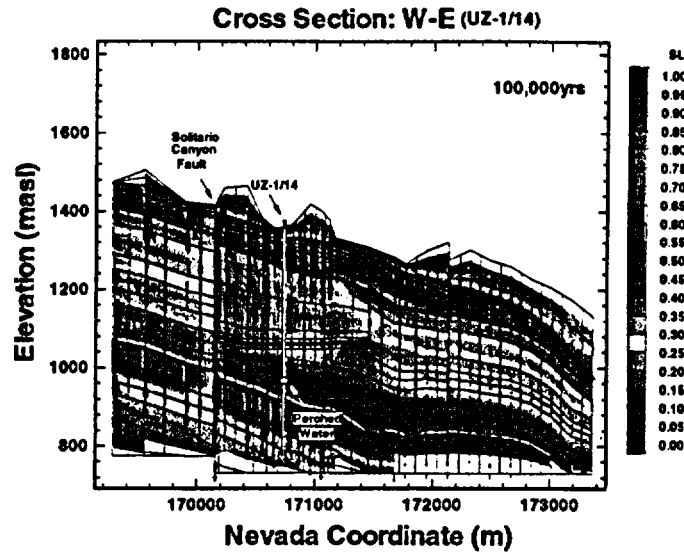


Figure 8.9.10
Fracture liquid saturations and velocity fields in 100,000 years along the West-East cross section crossing UZ-1/14, simulated using a dual-permeability approach and high-pulse infiltration rate.

8.10 Simulations of Percolation Fluxes

The percolation fluxes at the repository horizon and the water table recharge maps are simulated using the 4 sets of parameters and the ECM and dual-permeability approaches. The results are presented and analyzed in this section. Among all the important factors which affect the repository performance, the percolation fluxes through the unsaturated zone of the mountain are the most critical for PA calculations, because spatial and temporal variations in percolation fluxes affect:

- (a) water flow into drifts;
- (b) corrosion environment in the canisters;
- (c) waste mobilization; and
- (d) waste migration to the saturated zone.

8.10.1 Percolation Fluxes at Repository Horizon

As part of the output of the sensitivity studies, the percolation fluxes at repository horizons and recharge maps at the water table were calculated, as shown in Figures 8.10.1 - 8.10.6. In these figures, the unit of mass fluxes is converted to mm/yr, as used for infiltration, and the "negative" values denote

downwards flow. All the percolation maps at the repository horizon (Figures 8.10.1 to 8.10.6) show very non-uniform flux distributions.

Figure 8.10.1 shows that the percolation fluxes near the repository area is about 0.05 to 0.1 mm/yr, which is close to the infiltration rate, 0.1 mm/yr used in this simulation. The dark blue spots on the figure indicate higher percolation fluxes, or preferential flow pathways at the repository horizon. These fast flow pathways can be easily identified on the figure.

Vertical Mass Flux at Repository Horizon

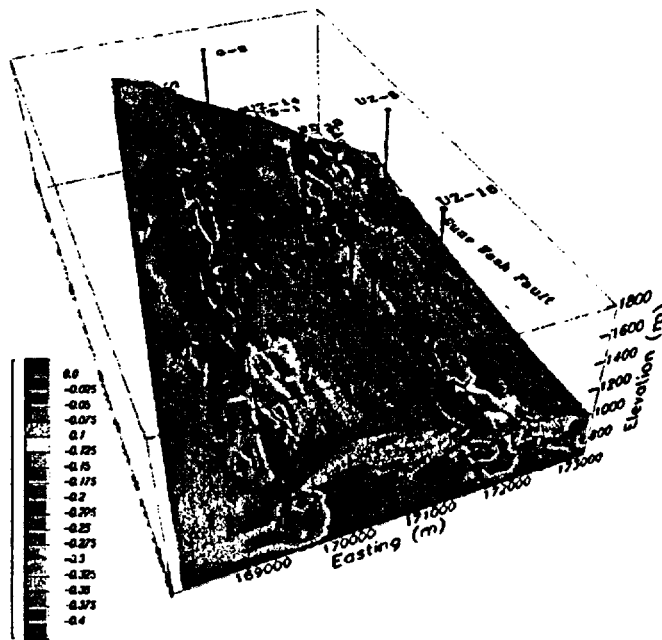


Figure 8.10.1

Percolation fluxes at the repository horizon, simulated using the ECM model, parameter set #1 and uniform infiltration rate of 0.1 mm/yr.

Vertical Mass Flux at Repository Horizon

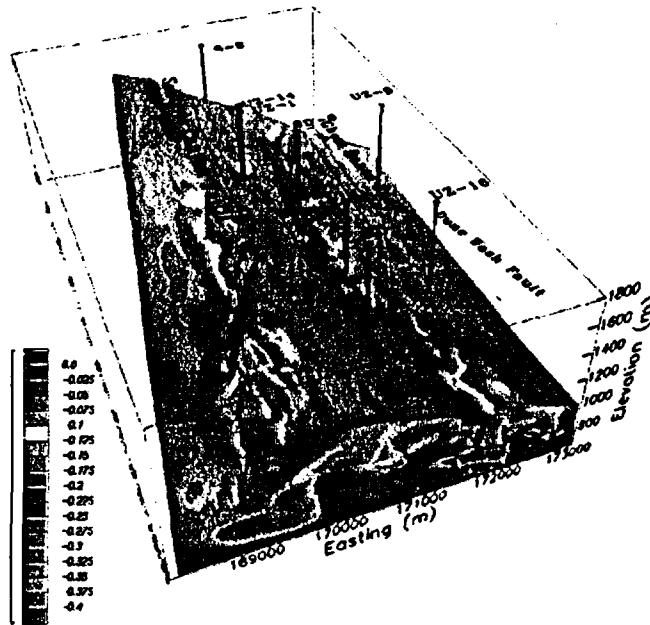


Figure 8.10.2 Percolation fluxes at the repository horizon, simulated using the ECM model, parameter set #2 and uniform infiltration rate of 0.1 mm/yr.

Vertical Mass Flux at Repository Horizon

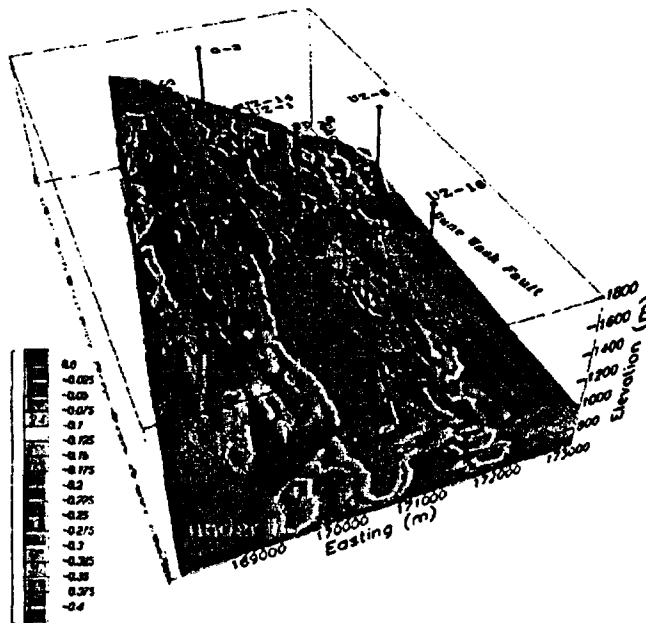


Figure 8.10.3 Percolation fluxes at the repository horizon, simulated using the ECM model, parameter set #3 and infiltration map #1.

Vertical Mass Flux at Repository Horizon

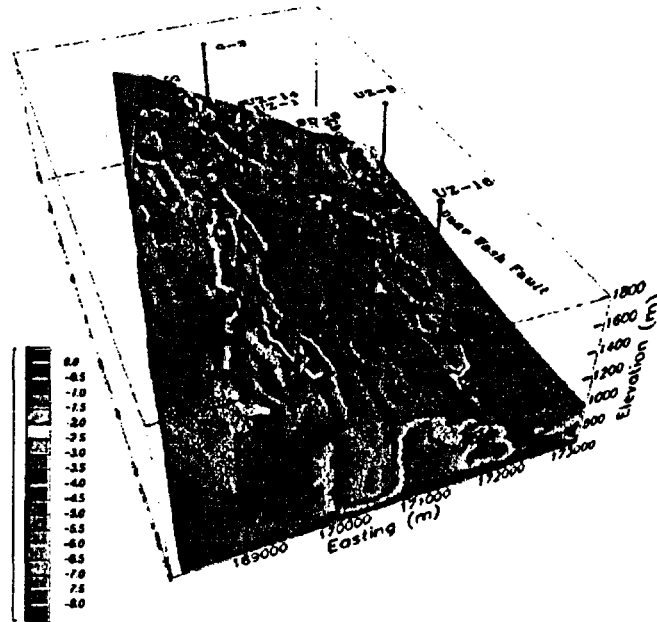


Figure 8.10.4 Percolation fluxes at the repository horizon, simulated using the ECM model, parameter set #4 and infiltration map #2.

Vertical Fracture Mass Flux at Repository Horizon

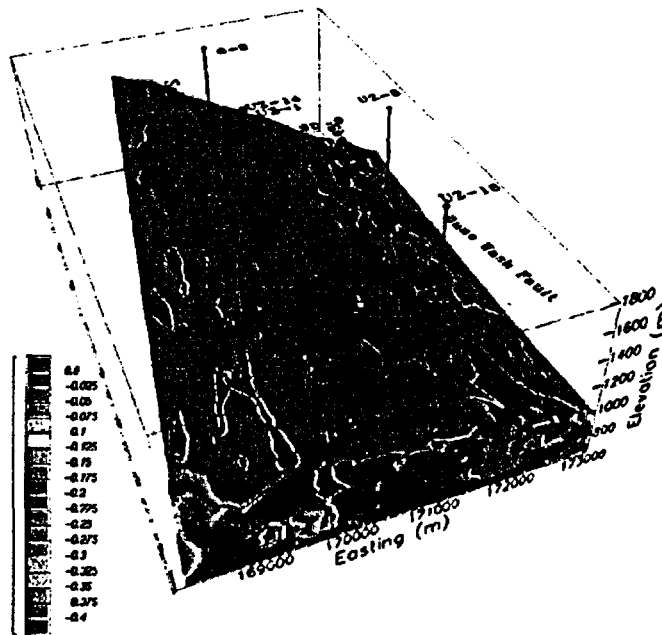


Figure 8.10.5 Fracture percolation fluxes at the repository horizon, simulated using the dual-permeability model, parameter set #4 and infiltration map #2.

Vertical Matrix Mass Flux at Repository Horizon

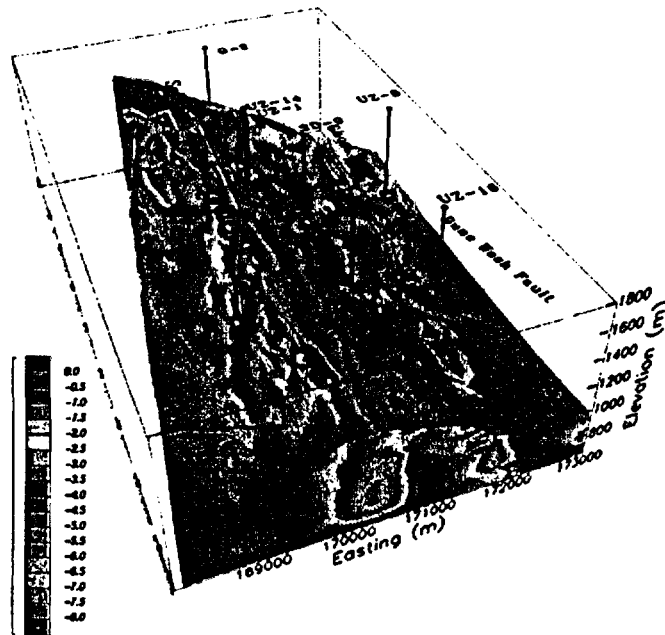


Figure 8.10.6

Matrix percolation fluxes at the repository horizon, simulated using the dual-permeability model, parameter set #4 and infiltration map #2.

The percolation fluxes in Figure 8.10.2 shows a more uniform distribution than in Figure 8.10.1, even though in both cases the uniform infiltration rate is 0.1 mm/yr. A few light blue spots on Figure 8.10.2 identifies the fast flow paths through the repository horizon, but velocities are less than in the case shown in Figure 8.10.1.

Figure 8.10.3 shows very non-uniform percolation fluxes. The average value of vertical mass fluxes near the repository area is about 0.1 to 0.15 mm/yr, which is lower than the average infiltration from map #1. Also, a few dark blue areas indicate the fast flow pathways.

Figure 8.10.4 shows relatively high percolation fluxes, because of the use of the higher infiltration map #2. In most parts of the repository level, the vertical mass fluxes are from 2 to 6 mm/yr, which bound the average surface infiltration of 4.4 mm/yr from infiltration map #2.

Figures 8.10.5 and 8.10.6 show fracture and matrix percolation fluxes, respectively. It is interesting to note that the fracture flow components are very uniform at the repository level, with an average value of 0.4 mm/yr, except for several red spots, indicating lower fluxes. Compared with the fracture flow (Figure 8.10.5), matrix percolation fluxes of Figure 8.10.6 shows a much higher

mass flow, especially along the mountain ridge and at the north-west corner of the model, which correspond to the higher surface infiltration (Figure 8.4.2). The percolation flux through the matrix near the repository ranges from 3 - 8 mm/yr. Also Figures 8.10.6 (dual-k) and 8.10.4 (ECM) show a very similar matrix flow pattern, except that the ECM predictions of higher flux zones are relatively larger in the north-west part of the model domain and along the mountain ridge where infiltration is higher.

A comparison of Figures 8.10.5 and 8.10.6 indicates that at the repository level fracture flow contributes less than 10% of the total percolation flux. This partitioning in matrix and fracture percolation fluxes at the repository level is due to the higher matrix permeability used for the simulations (Figures 8.10.4 to 8.10.6). The matrix permeability used for the repository layer in these simulations is $4.23 \times 10^{-16} \text{ m}^2$ (See Table 8.5.4, parameter set #4, for unit tsw35 for the repository parameters). This high matrix permeability value was estimated by the ITOUGH2 code in order to match the measured liquid saturation profiles layer from the boreholes under the high infiltration rate map #2. Based on the USGS data, the average value of matrix permeability in the TSw at the repository is on an order of $1.0 \times 10^{-18} \text{ m}^2$, which corresponds to a maximum matrix flow of about 0.3 mm/yr. Examination of the other simulation results using parameter sets # 1 to #3 indicates a large variation in the fracture and matrix percolation fluxes at the repository level. The fracture flow percentage varies from 20% to 70% of the total liquid fluxes through the repository.

The matrix permeability is highly variable at the repository areas of the TSw unit. This study shows that the matrix permeability values have significant effects on the partitioning of fracture and matrix flow at the repository level. Different fracture and matrix fluxes at the repository may directly impact the total influx into the drifts and the waste isolation strategy as well. Therefore, further studies are needed for accurately determining the matrix and fracture properties and their spatial distribution around the repository.

8.10.2
Water Recharge Maps at the
Water Table

The water recharge maps at the level of the water table are shown in Figures 8.10.7 to 8.10.12. Also in these figures, the unit of mass fluxes of the figures is converted to mm/yr, to compare with the surface infiltration, and "negative" values mean downward flow. The recharge maps at the water table (Figures 8.10.7 to 8.10.12) show a more non-uniform pattern than the repository percolation fluxes, discussed above. This may be due to the much longer flow pathways to the water table than to the repository level, therefore there are more effects of formation heterogeneity on the flow directions.

Figures 8.10.7 and 8.10.8 show a similar recharge map at the water table, even though the percolation fluxes at repository level are quite different (Figures 8.10.1 and 8.10.2). The fast flow pathways to the water table are indicated by the dark blue spots on the two figures.

Figure 8.10.9 shows two higher recharge zones, with 0.4 mm/yr, along the west of the Solitario Canyon fault from south to north, and along the cross section between SD-7, SD-12 and the northern boundary. In the rest of the model domain, very low fluxes (<0.1 mm/yr) are noticed, which are due to lateral diversions for this case.

A much higher recharge rates can be seen in Figure 8.10.10, but the recharge map follows the infiltration pattern (Figure 8.4.2). This indicates that little lateral diversions occur under this modeling scenario.

Vertical Mass Flux at Water Table

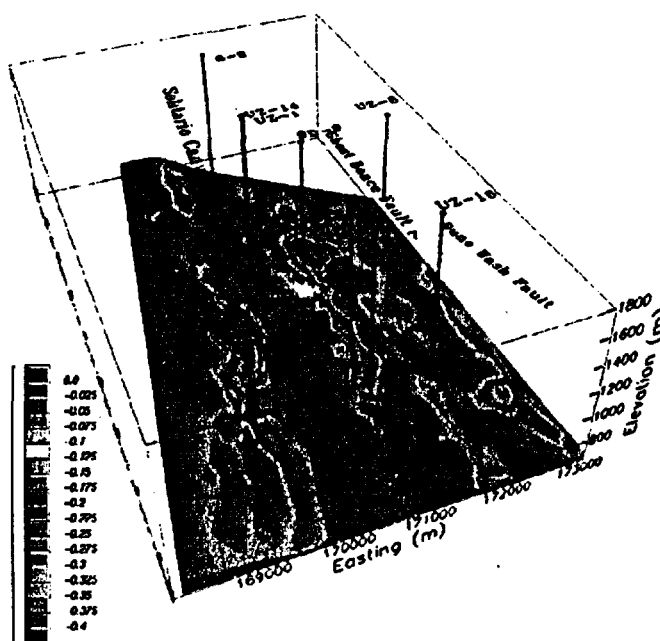


Figure 8.10.7
Recharge map at the water table, simulated using the ECM model, parameter set #1 and uniform infiltration rate of 0.1 mm/yr.

Vertical Mass Flux at Water Table

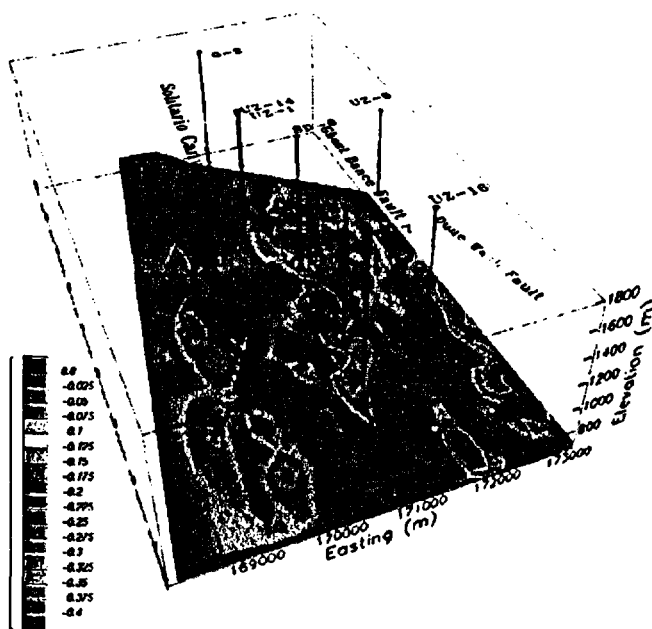


Figure 8.10.8 Recharge map at the water table, simulated using the ECM model, parameter set #2 and uniform infiltration rate of 0.1 mm/yr.

Vertical Mass Flux at Water Table

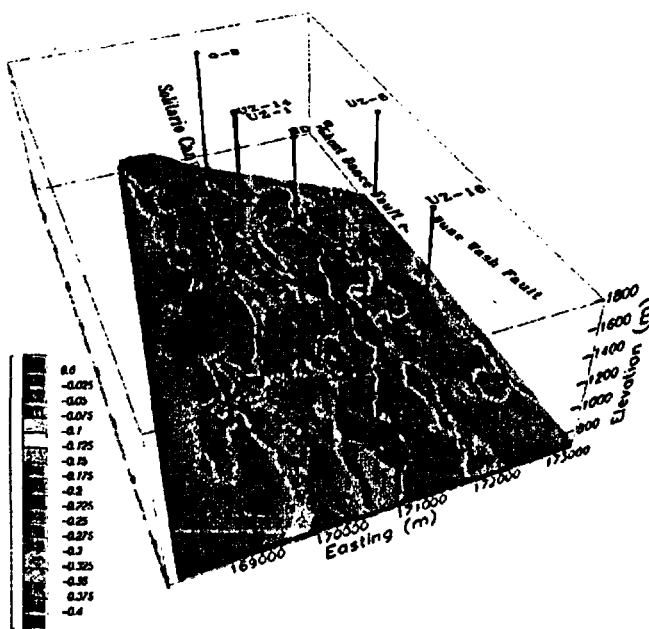


Figure 8.10.9 Recharge map at the water table, simulated using the ECM model, parameter set #3 and infiltration map #1.

Vertical Mass Flux at Water Table

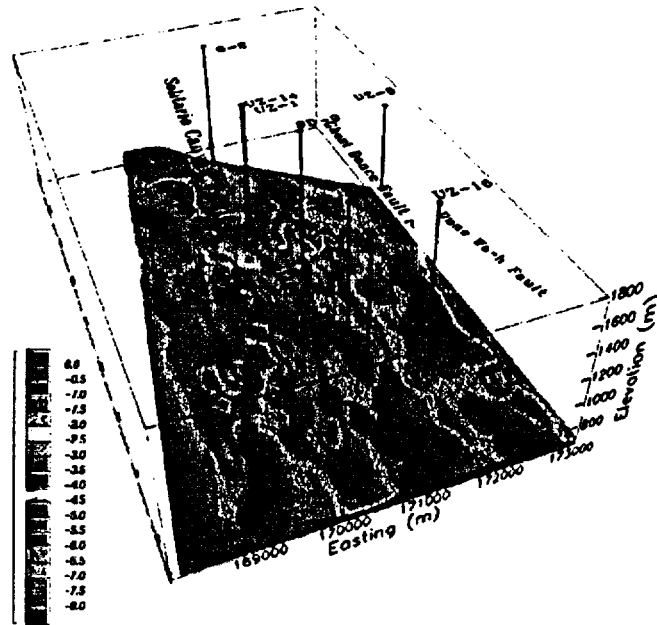


Figure 8.10.10 Recharge map at the water table, simulated using the ECM model, parameter set #4 and infiltration map #2.

Vertical Fracture Mass Flux at Water Table

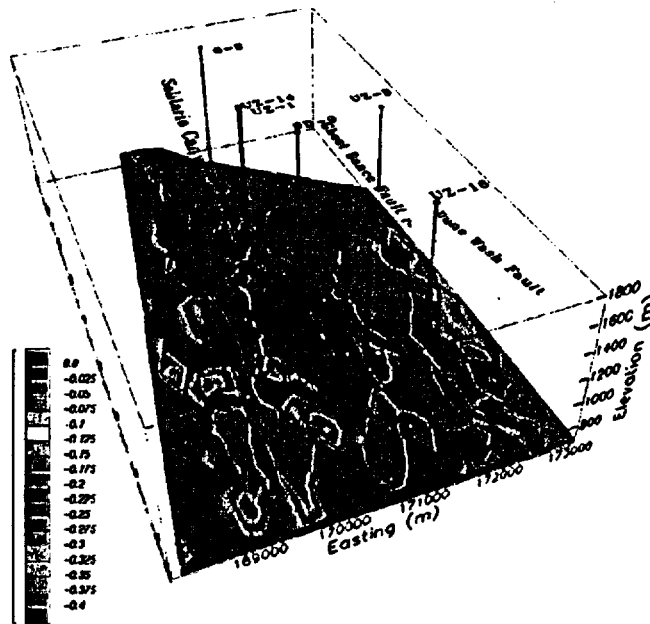


Figure 8.10.11 Recharge map at the water table, simulated using the dual-permeability model, parameter set #4 and infiltration map #2.

Vertical Matrix Mass Flux at Water Table

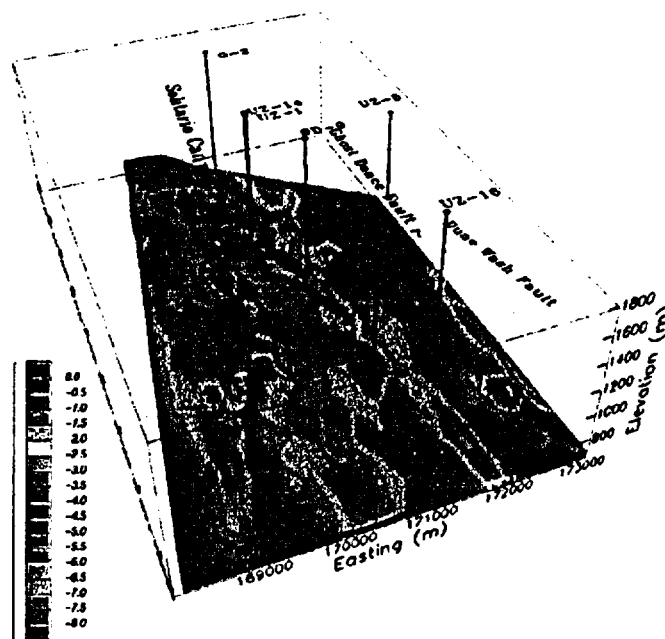


Figure 8.10.12
Recharge map at the water table, simulated using the dual-permeability model, parameter set #4 and infiltration map #2.

Figures 8.10.11 and 8.10.12 show the recharge maps through fracture and matrix for the dual-permeability model, respectively, at the water table. The fracture flow map is very different than the percolation map at the repository level (Figure 8.10.5). As shown in Figure 8.10.11, higher fracture flow fluxes at the water table occur along the major faults, in the eastern part of the model domain. This indicates that fracture flow has been diverted substantially to the east when passing through the CHn unit.

The recharge map through matrix (Figure 8.10.12) shows a good correlation with infiltration map #2 (Figure 8.4.2). This suggests that there is little lateral movement occurring when the water flows through all the unsaturated zones. Also, Figures 8.10.11 and 8.10.12 indicate that fracture flow contributes less than 10% to the total recharge to the water table, i.e., 90% of recharge is from flow through matrix-matrix connections. The two maps in Figures 8.10.10 and 8.10.12 are very similar, and this indicates the ECM and the dual-permeability approaches give similar predictions on water table recharge rates.

8.11 Summary, Conclusions and Recommendations

**8.11.1
Summary**

A systematic study of 3-D model calibrations and sensitivity analyses is reported in this Chapter. The model calibration efforts summarized in this Chapter were performed using field data on saturation and water potential, gas flow, geothermal condition and heat flow, perched water, and environmental isotopes. The sensitivity studies were conducted to assess the effects of parameter variations, infiltration rate changes, and numerical modeling approaches. Fracture/matrix interactions in welded and unwelded tuffs of the unsaturated zone were treated using the generalized ECM and the dual-permeability approach for treating fracture/matrix flow.

In this study, we have conducted a series of three-dimensional modeling simulations to calibrate the 3-D site-scale model to predict the moisture and heat flow and distribution at the Yucca Mountain site. Four sets of rock properties for fracture and matrix, and three sets of properties for faults were used in the model calibration and sensitivity studies. Several three-dimensional models which incorporate the observed moisture and geothermal data were developed. All these models were based on the current 3-D site-scale model grid.

Three different infiltration maps have been incorporated into the site-scale model, which include both uniform and spatially distributed infiltration rates. In addition, we have also conducted a series of sensitivity analysis of the effects of fault and rock properties on lateral and vertical moisture movement through the mountain. The fault properties used in our analyses are derived from pneumatic data analysis, laboratory results for the formation unit, and assumed values.

**8.11.2
Conclusions**

From the systematic model calibrations and sensitivity analyses of the 3-D, site-scale, unsaturated zone model of Yucca Mountain described in this Chapter, we conclude:

- The moisture distributions predicted by the 3-D model match well with observed water saturation profiles, and are in reasonable agreement with observed water potential data.
- The 3-D model predicted zones of high water saturations at the locations of observed perched water bodies encountered at the boreholes.
- There are significant effects of rock properties and infiltration rates on lateral moisture flow. The PTn unit may divert water thousands of meters laterally toward the east at certain locations at the mountain, depending on the rock properties and infiltration rates used in the simulation. Also large lateral diversions occur around the zeolitic zones in the CHn formation.

Three-Dimensional Model Calibration and 'Sensitivity Studies

- The controlling factors for the simulated lateral moisture movement in the unsaturated zone are contrasts in capillary pressure forces across interfaces between different grid layers, or capillary barrier effects. The contrasts in capillary forces are affected by heterogeneous rock properties and infiltration rates for given model conditions.
- The three-dimensional saturation distributions simulated by the models at repository horizon are in good agreement with observations from several boreholes.
- The heat flow through the unsaturated zone simulated by the models is also in reasonable match with field measurements.
- Sensitivity studies of three sets of fault properties and associated simulation results indicate that the major faults, as incorporated in the models, act as capillary barriers to lateral flow at low infiltration rates (0.1 mm/yr), and as a conduit or a drain pipe under high infiltration rates of several mm/yr with fault properties used in the studies.
- Lateral flow across faults may occur near the interfaces between the zeolitic units and the TSw or the vitric units, where high water saturated zones are built up in the surrounding zeolitic layers.
- By analyzing water flow down through fractures and matrix from the model results, we could also match the ages of the perched water reasonably well at the locations near boreholes UZ-1/14, and SD-7.
- The dual-permeability and the ECM approaches give almost identical simulation results in terms of predicted matrix and fracture saturations, moisture tensions and total percolation fluxes at the repository horizon under steady-state, three-dimensional flow conditions in the entire site-scale model.
- Percolation fluxes at the repository horizon and recharge maps at the water table are very non-uniformly distributed. They are affected by the surface infiltration rates, heterogeneity of rock property and faults. The predicted repository percolation flux and water table recharge maps indicate that several possible flow pathways may exist.
- The percentage of fracture and matrix flow in the total percolation flux at the repository is highly variable, and is mainly affected by matrix permeability used in the model for the repository horizon formation.

The conclusions above are based on Q data and were obtained from the simulation results using the Q computer codes, TOUGH2, and ITOUGH.

8.11.3
Recommendations

The 3-D model simulations and sensitivity studies reported in this Chapter constitute an important step in understanding fluid and heat flow within the Yucca Mountain. This study provides much confidence in the 3-D site-scale unsaturated zone model for incorporating all the available observed field data and for investigating the mountain's behavior. However, there are still a considerable number of uncertainties in our understanding of the hydrogeological system of Yucca Mountain, especially regarding percolation flux within the mountain. The major uncertainties we are still facing are (1) accuracy in estimated current, past and future net water infiltration rates over the mountain; (2) quantitative description of the heterogeneity in welded and non-welded tuffs, their flow properties and their detailed spatial distributions within the mountain; (3) insufficient field studies, especially on faults and on possible lateral moisture diversion in the PTn formation and in the CHn unit, where the zeolitic zones may play an important role in diverting moisture flow to water table.

Future modeling studies of fluid and heat flow and distribution at Yucca Mountain are advised to focus on (1) incorporating distributed matrix/fracture rock properties; (2) developing updated and accurate geological models for different hydrogeologic units; (3) conducting further comprehensive studies to determine percolation fluxes using field observations of saturation, moisture tension and temperature data, combined with direct and inverse modeling analysis; (4) performing comparative studies of model predictions and field observations regarding percolation fluxes, saturations, and moisture tensions and lateral movement; and (5) investigating effects of faults, thermal loading and air circulation on moisture movement within the mountain.

8.12 *References*

Ahlers C.F., C. Shan, C. Haukwa, A.B.J. Cohen, and G.S. Bodvarsson, Calibration and prediction of pneumatic response at Yucca Mountain, Nevada using the unsaturated zone flow model, Yucca Mountain Project Milestone OB12M, 1996.

Ahlers, C.F., T.M. Bandurraga, G.S. Bodvarsson, G. Chen, S. Finsterle, and Y.S. Wu, Performance analysis of the LBNL/USGS three-dimensional unsaturated zone site-scale model, Yucca Mountain Project Milestone 3GLM105M, Lawrence Berkeley National Laboratory, Berkeley, CA, 1995a.

Ahlers, C.F., T.M. Bandurraga, G.S. Bodvarsson, G. Chen, S. Finsterle, and Y.S. Wu, Summary of model calibration and sensitivity studies using the LBNL/USGS three-dimensional unsaturated zone site-scale model, Yucca Mountain Project Milestone 3GLM107M, Lawrence Berkeley Laboratory, Berkeley, CA, 1995b.

ACCN: MOL.19960208.0091-0097
DTN: LB092995312293.001 (Non-Q)

Three-Dimensional Model Calibration and 'Sensitivity Studies

Buesch, D.C., R.W. Spengler, T. C. Moyer, and J.K Geslin, Revised stratigraphic nomenclature and macroscopic identification of lithostratigraphic units of the Paintbrush Group exposed at Yucca Mountain, Nevada, U.S. Geological Survey Report OFR 94-469, U.S. Geological Survey, Denver, CO, 1995.

DTN: GS931208314211.049 (Q)

DOE, Reference Information Base (RIB), Yucca Mountain Site Characterization Project, 1993

Finsterle, S., ITOUGH2 User's Guide, Version 2.2, Lawrence Berkeley Laboratory, Research Report LBL-34581, UC-600, Lawrence Berkeley Laboratory, Berkeley, CA, 1993.

ACCN: MOL.19941026.0075

Flint, L., Permeability Data for UZ-16 and SD-9, 1995.

DTN: GS950608312231.006

Flint, L.E., and A.L. Flint, Spacial distribution of potential near surface moisture flux at Yucca Mountain, Proceedings of the Fifth International Conference on High Level Radioactive Waste Management, Las Vegas, NV, pp. 2352-58, U.S. Geological Survey, Lakewood, CO, 1995.

DTN: GS940108312212.005 (Non-Q)

Flint, L., Personal communication, 1996.

Flint, A.L., E.L. Flint, and J.A. Hevesi, Conceptual and numerical model of infiltration for the Yucca Mountain area, Nevada, U. S. Geological Survey, Water-Resources Investigation Report-96, Denver, Colorado, 1996.

Fridrich, C.J., W.W. Dudley Jr., and J.S. Stuckless, Hydrogeologic analysis of the unsaturated-zone ground-water system under Yucca Mountain, Nevada, Journal of Hydrology, v. 154, pp.133, 1994.

ACCN: MOL.19940811.0102

Hevesi, J.A., and A.L. Flint, Geostatistical model for estimating precipitation and recharge in the Yucca Mountain Region, Nevada-California, U. S. Geological Survey, Water-Resources Investigation Report, Denver, Colorado, 1995.

DTN: GS960108312111.001 (Non-Q)

Ho, C.K., S.J. Altman, and B.W. Arnold, Alternative Conceptual Models and Codes for Unsaturated Flow in Fractured Tuff: Preliminary Assessments for GWTT-95, Yucca Mountain Site Characterization Project Report, SAND95-1456, September 1995.

Hudson, D.B., and A. L. Flint, Estimation of shallow infiltration and presence of potential fast pathways for shallow infiltration in the Yucca Mountain area, Nevada, U.S. Geological Survey, Water Resources Investigations Report, Denver, CO, 1995 (in review.)

DTN: GS960508312212.006 (Non-Q)

Three-Dimensional Model Calibration and 'Sensitivity Studies

International Formulation Committee, A formulation of the thermodynamic properties of ordinary water substance, IFC Secretariat, DÄsseldorf, Germany, 1967.

ACCN: NNA.19890918.0501

Lu, N., and E.M. Kwicklis, A preliminary, two-dimensional numerical model for gas circulation around UZ6s, Yucca Mountain, Nevada, U.S. Geological Survey, Lakewood, CO, 1995.

Luckey, R.R., Perched water testing - USW SD-7, Personal communication, March, 1995.

OCRWM/DOE, Technical Data Catalog, Yucca Mountain Site Characterization Project, 1995.

Oldenburg, C.M., and K. Pruess, On numerical modeling of capillary barriers, *Water Resources Res.*, 29(4), pp. 1045-1055, 1993.

Pruess, K., TOUGH2 - a general-purpose numerical simulator for multiphase fluid and heat flow, Lawrence Berkeley Laboratory Report LBL-29400, Lawrence Berkeley Laboratory, Berkeley, CA, 1991.

ACCN: NNA.19940202.0088

Pruess, K., J.S.Y. Wang, and Y.W. Tsang, On thermohydrologic conditions near high-level nuclear wastes emplaced in partially saturated fractured tuff, Part I. Simulation studies with explicit consideration of fracture effects, *Water Resources Res.*, 26(6), pp.1235-1248, 1990a.

ACCN: NNA.19910328.0073

Pruess, K., J.S.Y. Wang, and Y.W. Tsang, On the thermohydrologic conditions near high-level nuclear wastes emplaced in partially saturated fractured tuff, part 2. Effective continuum approximation, *Water Resources Res.*, 26(6), pp.1249-1261, 1990b.

Pruess, K., and T.N. Narasimhan, A practical method for modeling fluid and heat flow in fractured porous media, *Soc. Pet. Eng. J.*, 25, pp. 14-26, 1985.

ACCN: NNA.19910307.0185

Pruess K., A. Simmons, Y.S. Wu, and G. Moridis, TOUGH2 Software Qualification, Lawrence Berkeley National Laboratory, Berkeley, Ca, February, 1996.

Pruess, K., GMINC - A mesh generator for flow simulations in fractured reservoirs, Lawrence Berkeley National Laboratory Report LBL-15227, Lawrence Berkeley National Laboratory, Berkeley, California, 1983a.

ACCN: NNA.19910307.0134

Rousseau J.P., C.L. Loskot, J. Kume, M. Kurzmack, N.D. Brain, K. Thomas, A.J. Greengard, In-situ borehole instrumentation and monitoring data for USW NRG-7a and USW NRG-6, Yucca Mountain, Nye County, Nevada, 1995.

Three-Dimensional Model Calibration and 'Sensitivity Studies

Rousseau, J.P., E.M. Kwicklis, and D.C. Gillies, Hydrogeology of the unsaturated zone, North Ramp Area of the Exploratory Studies Facility, Yucca Mountain, U. S. Geological Survey Water-Resources Investigation, U. S. Geological Survey, Denver, CO, 1996.

Rousseau, J.P., Data transmittal of pneumatic pressure records from 10/24/1994 through 3/31/1996 for boreholes UE-25 UZ#5, USW NRG-6, USW NRG-7a, USW SD-12, and USW UZ-7a, Yucca Mountain, Nevada, U. S. Geological Survey, 1996.

DTN: GS950508312232.004 Q

DTN: GS960308312232.001 Q

Sass, J.H., Lachenbruch, A.H., Dudley, W.W., Jr., Priest, S.S., and Munroe, R.J., Temperature, thermal conductivity, and heat flow near Yucca Mountain, Nevada: some tectonic and hydrologic implications, U.S. Geological Survey Open-File Report 87-649, U.S. Geological Survey, 1988.

ACCN: NNA.19890123.0010

DTN: GS950408318523.001 (Non-Q)

Wilson, M.L., J.H. Gauthier, R.W. Barnard, G.E. Barr, H.A. Dockery, E. Dunn, R.R. Eaton, D.C. Guerin, N. Lu, M.J. Martinez, R. Nilson, C.A. Rautman, T.H. Robey, B. Ross, E.E. Ryder, A.R. Schenker, S.A. Shannon, L.H. Skinner, W.G. Halsey, J.D. Gansemer, L.C. Lewis, A.D. Lamont, I.R. Triay, A. Meijer, and D.E. Morris, Total-system performance assessment for Yucca Mountain - SNL second iteration (TSPA-1993), Sandia National Laboratories Report SAND93-2675, UC-814, Sandia National Laboratories, Albuquerque, NM, 1994.

ACCN: NNA19940112.0123

Wittwer, C., G. Chen, G.S. Bodvarsson, M. Chornack, A. Flint, L. Flint, E. Kwicklis, and R. Spengler, Preliminary development of the LBL/USGS three-dimensional site-scale model of Yucca Mountain, Nevada, Lawrence Berkeley National Laboratory Report LBL-37356, UC-814, Lawrence Berkeley National Laboratory, Berkeley, CA, 1995.

Wittwer, G., G. Chen, and G.S. Bodvarsson, Studies of the role of fault zones on fluid flow using the site-scale numerical model of Yucca Mountain, Proceedings of the Fourth International High Level Radioactive Waste Management Conference, Las Vegas, pp.667-674, 1993.

ACCN: NNA.19931129.0085

DTN: GS930308312293.002 (Non-Q)

Wu, Y. S., S. Finsterle, P. Frazer, and A. Simmons, Software qualification for ITOUGH2 and various equation-of-state (EOS) modules and auxiliary modules for TOUGH2 and ITOUGH2, Report Lawrence Berkeley National Laboratory, Berkeley, CA, August 1996 (draft).

Three-Dimensional Model Calibration and 'Sensitivity Studies

Yang, I. C., G.W. Rattray, and P. Yu, Interpretations of chemical and isotopic data from boreholes in the unsaturated-zone at Yucca Mountain, Nevada, U. S. Geological Survey Water-Resources Investigation Report-96-4058, U. S. Geological Survey, Denver, Colorado, 1996.

TEMPERATURE AND HEAT FLOW ANALYSIS

G. S. Bodvarsson, Y.S. Wu, and S. Finsterle

August 1996

9.1 Introduction

The three-dimensional site-scale model, developed by Lawrence Berkeley National Laboratory (LBNL) in collaboration with the U.S. Geological Survey (USGS), has primarily been used for studies of isothermal moisture movement within the unsaturated zone at Yucca Mountain (Wittwer et al. 1995; Ahlers et al. 1995a; Ahlers et al. 1995b). However, under natural hydrologic and thermal conditions, both liquid and gas (air and vapor) flow in the unsaturated zone of Yucca Mountain is affected by ambient temperature changes, geothermal gradients, atmospheric and water table conditions. Thermal and hydrological regimes are closely related due to the effects of coupling between thermal, density, and atmospheric conditions on air circulation through the mountain (Weeks, 1987; Lu and Kwicklis, 1995).

In addition to effects of natural thermal conditions, heat will also be generated as a result of emplacing high level nuclear waste in the unsaturated zone. The thermal loading from the waste repository will significantly affect the pre- and post waste emplacement performance of the repository. Quantitative evaluation of thermo-hydrologic and thermal loading effects on the performance of the potential high-level nuclear waste repository at Yucca Mountain is essential in conducting site characterization, performance assessment studies, and repository and engineering barrier design. Thus, there is a need to incorporate observed temperature and heat flow data of Yucca Mountain into the three-dimensional, site-scale model in order to enhance the capability for modeling thermal effects.

Sass et al. (1988) examined temperature data from various boreholes at Yucca Mountain. They suggested that the temperature profiles from the boreholes were primarily conductive and did not exhibit a significant convective component. They identified two processes that would explain deviations from conductive behavior. One relates to infiltrating water and the heat consumption caused by the warming of the water as it percolates through the unsaturated zone from the ground surface to the water table. The other involved the possibility of gas flow from deeper areas of the unsaturated zone to shallower areas carrying water vapor that condenses at shallow depths and releases the latent heat. This conceptual model is considered less likely given our current understanding of heat flow properties at Yucca Mountain.

Ahlers et al. (1995) performed conductive heat transfer analysis using the available temperature and heat flow data from the Yucca Mountain site for 25 geologic and hydrologic boreholes (Sass et al., 1988). These temperature logs sug-

gested that geothermal gradients in the unsaturated zone are primarily conductive and range between 15°C/km to 60°C/km. The measured temperature data (Sass et al., 1988), the rock thermal conductivities (Nimick, 1989, 1990; DOE (RIB), 1993; and Rautman, 1995), and the rock thermal capacities (DOE (RIB), 1993) were incorporated into the present three-dimensional site-scale model to simulate thermal effects and to account for the ambient hydro-thermal conditions of the repository. A parameter estimation study was also conducted for calibrating thermal conductivities using an inverse modeling code, ITOUGH2 (Finsterle, 1993) and 1-D submodels. This work is briefly summarized in this chapter.

In the main part of this chapter, we investigate the effects of percolating water from infiltration on the temperature conditions and gradients that exist within the unsaturated zone. Model calculations using ITOUGH2 are used to examine the importance of this process using qualified data from recent boreholes. The results of these analyses are augmented by additional temperature data from non-qualified (non-Q) data from older boreholes (Sass et al. 1988). Finally, summary comments and recommendations are given.

9.2 QA Status of Data and Software Used in this Chapter

The temperature data from older boreholes given by Sass et al. (1988) are non qualified (non-Q). Temperature data from boreholes UZ-4, UZ-5, UZ-7a, NRG-6, NRG-7a, and SD-12 are qualified (Q-data) or will be qualified when the data have been submitted to and approved by the Technical Database. Table 9.2.1 gives the appropriate data tracking numbers for the data that are already qualified. The computer software used in this chapter is fully qualified. The ITOUGH2 code qualification is documented in a LBNL report entitled "Software Qualification of ITOUGH2 and various TOUGH2 and ITOUGH2 Equations of State Modules and Auxiliary Modules" by Y.S. Wu, S. Finsterle, P. Fraiser, C.F. Ahlers and A. Simmons (1996).

Table 9.2.1 Qualified temperature data and corresponding data tracking numbers.			
Hole	Investigator	Organization	Data Tracking Number
UZ-4	Rousseau	USGS	9/96: GS960308312232.001
UZ-5	Rousseau	USGS	9/96: GS960308312232.001
UZ-7a	Rousseau	USGS	9/96: GS960308312232.001
NRG-6	Rousseau	USGS	9/96: GS960308312232.001
NRG-7a	Rousseau	USGS	9/96: GS960308312232.001
SD-12	Rousseau	USGS	9/96: GS960308312232.001

9.3 *Temperature and Heat Flow Data*

9.3.1
Temperature Data

Temperature data observed from 35 test boreholes near Yucca Mountain were reported by Sass et al. (1988), and repeated temperature logs were obtained from 18 of these boreholes. We selected 25 boreholes which included all the boreholes with measured temperature data within or near the site-scale model area. The selected borehole location map and the plan view of the model surface area of the site-scale model are shown in Figure 9.3.1, and the coordinates and borehole completion information for the 25 boreholes are given in Table 9.3.1.

Table 9.3.1 also gives the same information for some of the recently drilled boreholes at Yucca Mountain. These include boreholes UZ-4, UZ-5, UZ-7a, NRG-6, NRG-7, and SD-12. The temperature data from these boreholes are qualified (Q data).

The temperature data for most of these boreholes were digitized from the original plots given in the report by Sass et al. (1988). For the recent wells, the temperature data were obtained from J. Rousseau of USGS (see data tracking numbers in Table 9.2.1). Sass et al. (1988) studied these data and concluded that temperature gradients in the unsaturated zone appear primarily conductive and range between 15°C/km to 60°C/km within the study area. Figures 9.3.2-9.3.7 present the observed borehole temperature profiles, showing generally near-linear profiles in the unsaturated zone.

Temperature and Heat Flow Analysis

Table 9.3.1 Location, elevation, and completion information for the selected boreholes					
Source: Yucca Mountain Site Characterization Project, Site Atlas Supplement, October 1993					
Boreholes	Coordinates		Surface Elevation	Total Depth	Water Level
	North (m)	East (m)	(m)	(m)	Depth (m)
UE-25 a#1	-233142	172623	1199	762	469
UE-25 a#4	-234078	172051	1250	152	—
UE-25 a#5	-233768	172137	1236	148	—
UE-25 a#6	-233446	172060	1235	152	—
UE-25 a#7	-233553	172355	1221	305	—
UE-25 b#1	-233246	172644	1201	1220	470
USW G-1	-234848	170993	1325	1829	572
USW G-2	-237386	170842	1554	1831	525
USW G-3	-229447	170226	1480	1533	750
USW G-4	-233418	171627	1270	915	540
USW H-1	-234774	171410	1303	1829	572
USW H-3	-230594	170216	1483	1219	751
USW H-4	-232149	171880	1249	1219	518
USW H-5	-233670	170355	1479	1219	703
USW H-6	-232653	168882	1302	1220	526
USW WT-1	-229801	171828	1202	515	471
USW WT-2	-231849	171274	1301	628	571
UE-25 WT#4	-234242	173139	1167	482	438
UE-25 WT#6	-237920	172067	1313	383	279
USW WT-7	-230298	168826	1197	491	421
USW WT-10	-228225	168646	1123	431	348
UE-25 WT#16	-236043	173856	1210	521	472
UE-25 WT#17	-228118	172581	1124	443	395
UE-25 WT#18	-235052	172168	1336	623	605
USW UZ-1	-235085	170759	1349	387	—
UE-25 UZ#4	-234305	172559	122.5	111.7	—
UE-25 UZ#5	-234267	172558	1204.5	110.6	—
USW UZ-7a	-231845	171397	1288.6	234.2	—
UE-25 NRG-6	-233698	171964	1247.5	335.3	—
UE-25 NRG-7a	-234355	171598	1282.2	461.3	—
USW SD-12	-232244	171177	1323.68	659.6	593.7

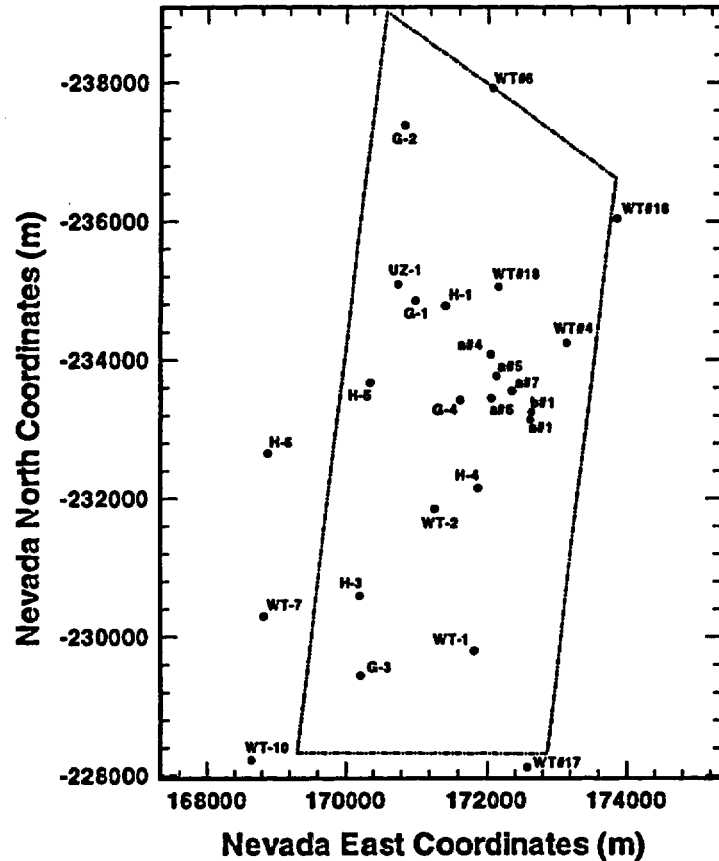


Figure 9.3.1
Map of borehole locations used for the conduction study and the study area of the site-scale model.

Figures 9.3.2 - 9.3.3 show the temperature profiles from a series of boreholes UE-25 a#1, a#4, a#5, a#6, a#7 and b#1. Four shallow boreholes of this series, UE-25 a#1, a#4, a#5 and a#7, were drilled within the main drainage of Drill Hole Wash and were believed to have been affected by vertical and lateral movements of fluids. As shown in Figure 9.3.2 - 9.3.3, there exist irregularities and contrasts in thermal gradient that could not be attributed to heat conduction and may be associated with convection heat transfer by vertical and lateral movements of fluids within the upper part of the unsaturated zone in Drill Hole Wash. Borehole UE-25 b#1 (Figure 9.3.3) is near the main surface drainage of Drill Hole Wash, and also shows some degree of disturbance to the temperature field in the unsaturated zone. Between 300 - 600 m elevation, which is below the water table, the profile is nearly isothermal and suggests that very strong

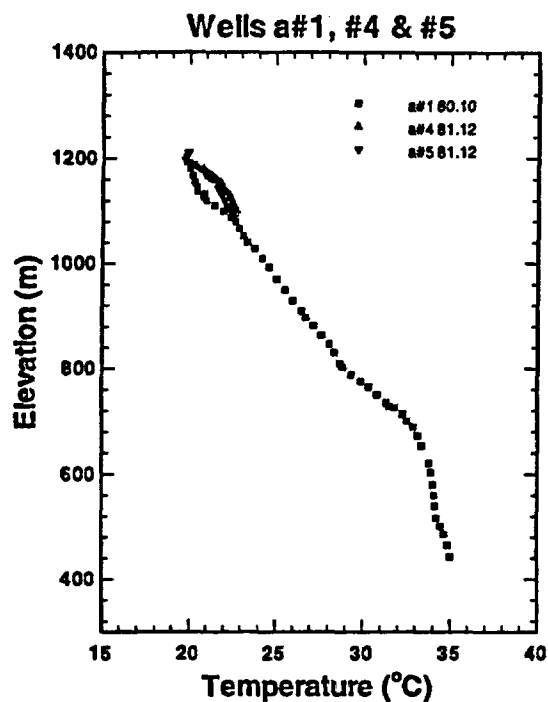


Figure 9.3.2
Observed temperature profiles for UE-25: a#1, a#4 and a#5. Data from Sass et al. (1988).

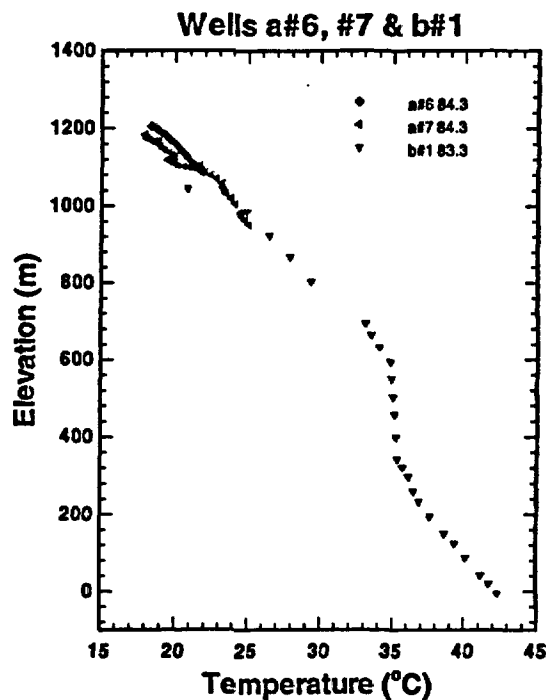


Figure 9.3.3
Observed temperature profiles for UE-25: a#6, a#7 and b#. Data from Sass et al. (1988).

heat convection is occurring. Below 200 m elevation, the profile is linear with a gradient of about 23°C/km, suggesting conductive heat flow. It should be noted that the water table is located at an elevation of approximately 730 meters above sea level for most of the boreholes considered.

The temperature profiles from the "G" series boreholes, USW G-1, G-2, G-3 and G-4, are shown in Figure 9.3.4. These boreholes were drilled primarily to obtain geologic data, although considerable hydrologic and thermal information has been obtained from them. The temperature profile for G-2 shows downflow at elevations between 900-700 m.a.s.l., and this has been analyzed by Czarniecki et al. (1994) and Sass (1996).

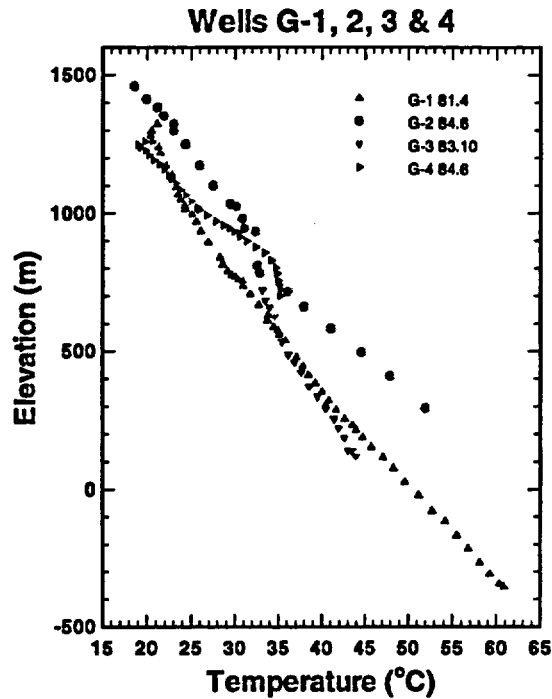


Figure 9.3.4
Observed temperature profiles for G-series boreholes, USW G-1, G-2, G-3 and G-4. Data from Sass et al. (1988).

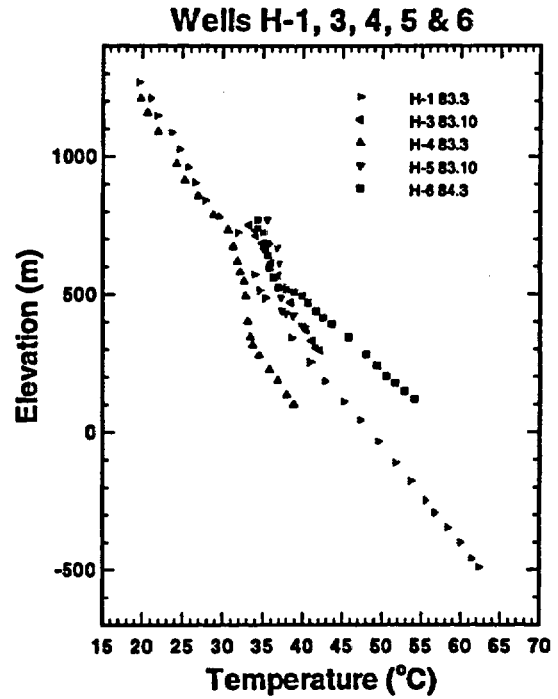


Figure 9.3.5
Observed temperature profiles for H-series boreholes, USW H-1, H-2, H-3 and H-4. Data from Sass et al. (1988).

Figure 9.3.5 shows the temperature profiles from the "H" series boreholes, USW H-1, H-3, H-4, H-5, and H-6. These boreholes were drilled primarily for hydrologic studies. The temperature behavior is similar to that of the "G" series.

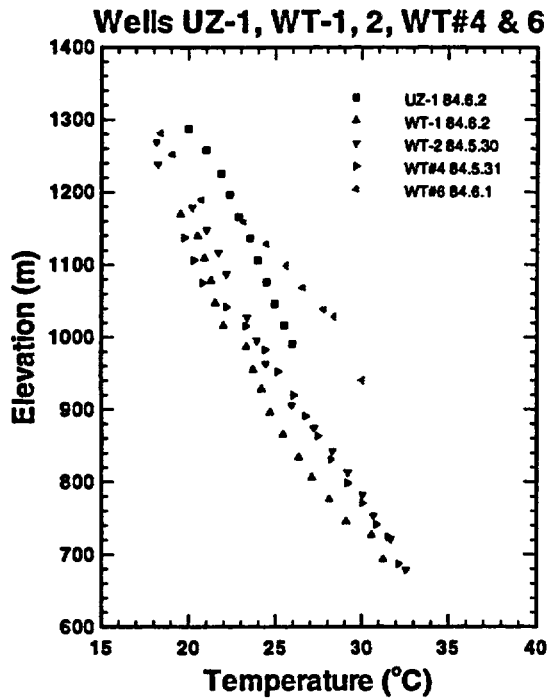


Figure 9.3.6
Observed temperature profiles for USW UZ-1, WT-1, WT-2, WT#4 and WT#6. Data from Sass et al. (1988).

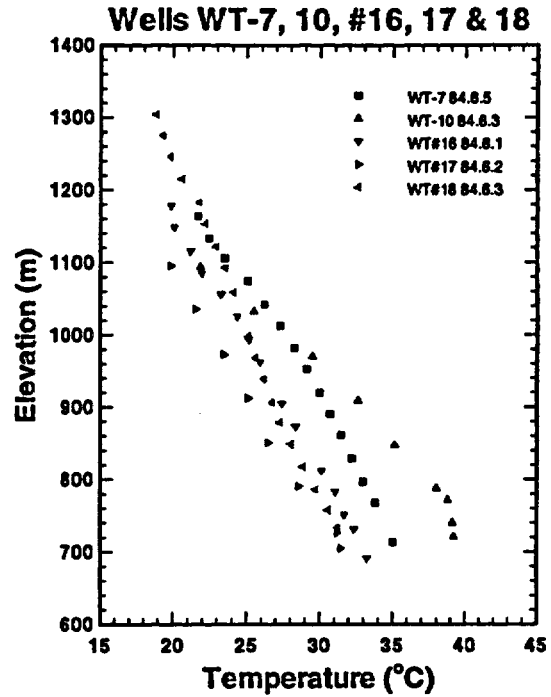


Figure 9.3.7
Observed temperature profiles for USW WT-7, WT-10, WT#16, WT#17 and WT#18. Data from Sass et al. (1988).

Figures 9.3.6 and 9.3.7 present the measured temperatures for the "WT" series and UZ-1 holes. These boreholes are primarily for engineering studies of the unsaturated zone and water table. The thermal gradients, as shown in Figures 9.3.6 and 9.3.7, vary from about 20°C/km to 60°C/km in the unsaturated zone.

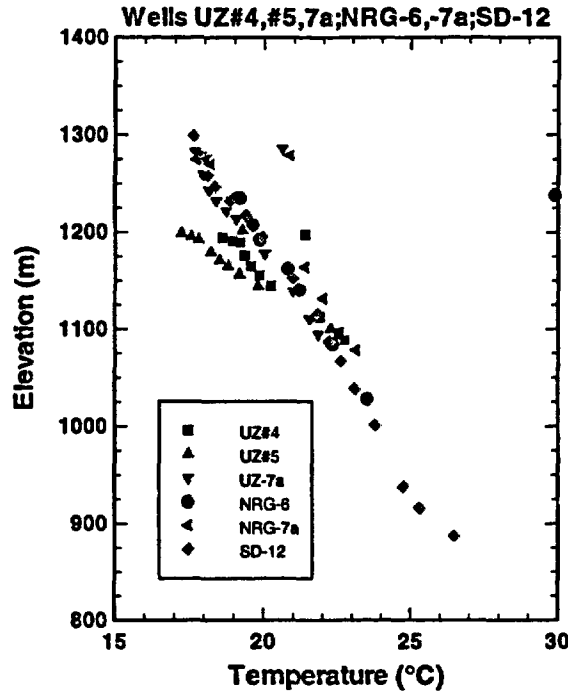


Figure 9.3.8
Observed temperature profiles for UZ-4, UZ-5, UZ-7a, SD-12, NRG-6 and NRG-7a. Data from Rousseau et al. (1996) and unpublished data by Rousseau of USGS.

Figure 9.3.8 shows the measured stable temperatures in boreholes UZ-4, UZ-5, UZ-7a, NRG-6, NRG-7 and SD-12. These temperature data are generally much more accurate than those from Sass et al. (1988) because these holes were instrumented with long term monitoring equipment. The data reported in Sass et al. (1988) were measured in gas filled or liquid filled boreholes. This can very significantly affect the temperature measurements in various ways primarily due to internal well flows. The data shown in figure 9.3.8 are, however, similar to the rest of the holes. This provides some indication that the data in Sass et al. (1988) are of sufficient quality to generate useful scientific, although not qualified conclusions.

9.3.2
Heat Flow Data

Sass et al. (1988) estimated the conductive heat flow at the Yucca Mountain site based on the temperature surveys and thermal conductivity measurement in both the saturated and the unsaturated zones. They found that heat flows in the unsaturated zone vary in a systematic fashion, both geographically and as a function of the unsaturated zone thickness. The average heat flow from the unsaturated zone is about 41 mW/m^2 (see Figure 9.3.9). In comparison, the limited temperature data available for the saturated zone indicates an average heat flux of some 50 mW/m^2 (Sass et al., 1988; Rousseau et al., 1996).

Temperature and Heat Flow Analysis

The site-scale model study area is near the southern boundary of a regional heat flow anomaly, the Eureka Low. As indicated by Sass et al. (1988), average heat flow in the Eureka Low is about half that for the adjacent regions. Fridrich et al. (1994) suggests two related interpretations for the heat flow anomaly under Yucca Mountain. First, part of the anomaly results from cool underflow in the deep carbonate aquifer. Second, the correspondence of the northern limit of the heat-flow anomaly to the steep potentiometric gradient to the north suggests that the effective northern limit of the deep carbonate aquifer, and by inference, the zone of downwelling fluid, may coincide with the large lateral potentiometric gradient under Yucca Mountain. The heat flow values within the general site scale model domain range between about 35–45 mW/m², as shown in Figure 9.3.9. The contours of the figure show low heat flow in the central portion and increasing heat flow away from the center of the site-scale model area. It should be noted that the data shown in Figure 9.3.9 do not include qualified data from the recently drilled boreholes.

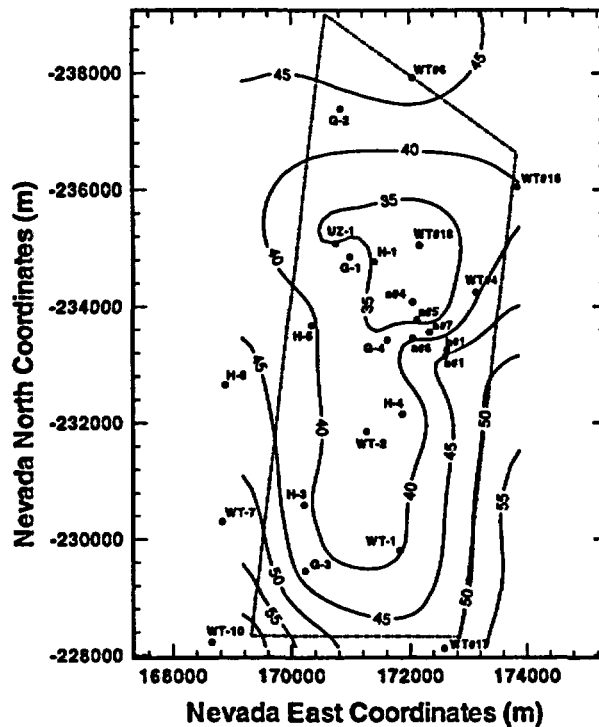


Figure 9.3.9
Heat flow distribution in the unsaturated zone (mW/m²) taken from Sass et al. (1988).

9.4 Heat Conduction Analysis

9.4.1 Model Description

In the heat conduction analysis of the temperature data, we only use the borehole data from Sass et al. (1988). At the time this work was performed, LBNL had not received the more recent qualified temperature data. The data from Sass et al. (1988) are sufficient for the intended use of this analysis which is to investigate to what extent heat conduction can explain the available data. The next section of this chapter investigates how a combined convection/conduction analysis fits all of the available data.

At the locations of the 25 boreholes used in this work, we extracted the appropriate 1-dimensional columns from the UZ model. These columns contain the proper geological information including layering, dipping, and other data. They also contain the correct ground surface elevations (topography) and the location of the water table.

9.4.2 Model Parameters And Boundary Conditions

Model parameter specifications, rock properties and boundary conditions were specified following the framework of the site-scale model (Wittwer et al., 1995; Ahlers et al., 1995). The additional parameters and conditions for simulating thermal effects are presented in this section. Spatially varying constant temperatures were specified at the bottom of the model. The temperature values were taken and interpolated from the borehole temperature data reported by Sass et al. (1988).

Constant temperatures at the upper model boundary (ground surface) were specified with an averaged value of about 18°C, which was derived from extrapolation of the shallow temperature data to the ground surface.

Porosity, rock grain density, thermal conductivities, and rock specific heat used in the model are described in Ahlers et al. (1995).

We have also used a thermal conductivity model, recently developed by Rautman (1995a, 1995b). This model correlates thermal conductivity as a function of porosity, temperature and saturation at the Yucca Mountain site. Thermal conductivity is one of the key heat transfer properties and a controlling factor for conductive heat flow around the repository area. In an effort to look at the response and sensitivity of the model temperature fields to the thermal conductivity data, and to best estimate the thermal conductivity values for the different rock types, we have performed a parameter estimation study using the inverse modeling code, ITOUGH2 (Finsterle, 1993). The ITOUGH2 code solves the inversion problem of a TOUGH2 simulation to estimate model parameters by an automatic model calibration and optimization procedure. The ITOUGH2 simulations were carried out using the observed temperature logs of the selected 25 boreholes to identify and estimate an optimum thermal conductivity set for the site-scale model. As discussed in Chapter 4 (Wu et al.) and in an

accompanying software QA document (Wu et al., 1996), the ITOUGH2 code is qualified.

**9.4.3
Simulation And Comparison**

The measured temperature data were compared with the three-dimensional simulation results for boreholes within and near the model area. For rock thermal conductivities, the tabulated data in RIB, Rautman's model (1995b), and ITOUGH2 (optimized) values were used in the simulations. The simulated temperature profiles are plotted for boreholes H-3 and H-5 in Figures 9.4.1 and 9.4.2, as dashed, solid and dotted curves for RIB, Rautman's model, and the ITOUGH2 estimated (Fitted) parameters, respectively. The observed temperature data are represented by symbols in the figures with the logging dates specified. These plots just show examples of the matches obtained; the reader is referred to Ahlers et al. (1995) for detailed descriptions of all of the matches with the available borehole temperature data.

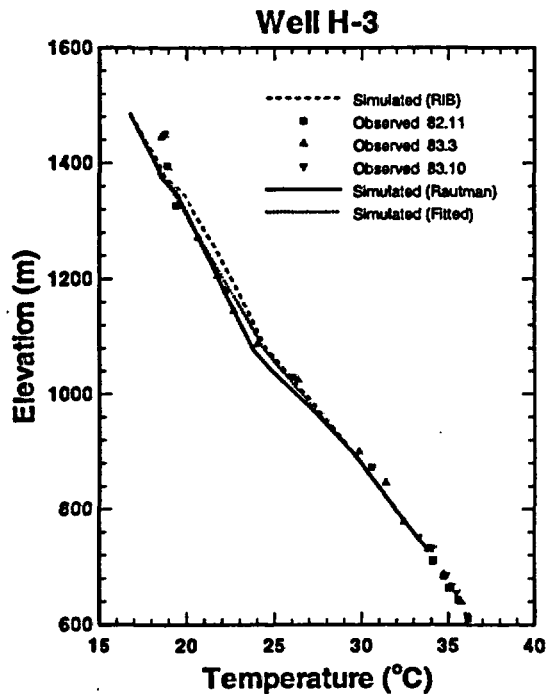


Figure 9.4.1
Comparison between measured temperature data for well H-3 (Sass et al., 1988) and various ITOUGH2 optimized profiles.

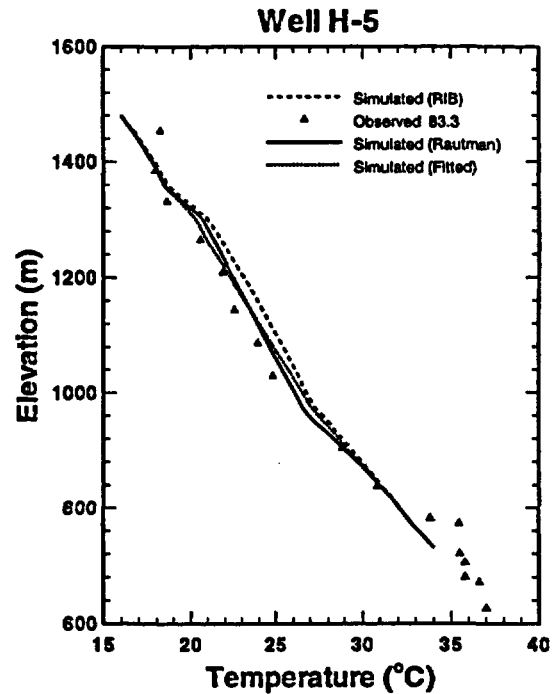


Figure 9.4.2
Comparison between measured temperature data for well H-5 (Sass et al., 1988) and various ITOUGH2 optimized profiles.

Figure 9.4.3 shows observed temperature data for borehole H-3 and calculated values for comparison. It is clear that all of the thermal conductivity models match the data reasonably well, but the Rautman thermal conductivity model does the best. This was actually the case for most of the borehole data

(Ahlers et al., 1995). The rather steep temperature gradient in the Topopah Springs Unit (elevation between 1350 and 1100 m.a.s.l.) is matched by ITOUGH2 using heat thermal conductivities than the values measured. As suggested in the next section, conductive heat transfer cannot fully explain the observed temperature data for many boreholes at Yucca Mountain, perhaps because of a significant amount of water percolating through the unsaturated zone and absorbing some of the heat flux rising from depth.

Figure 9.4.2 shows another example. In this case, we examine borehole H-5, which is located close to the crest of Yucca Mountain, as is the previous borehole, H-3 (see Figures 9.3.1 and 9.5.1). The temperature data from this borehole are also matched reasonably well by the ITOUGH2 conductivity model. A close examination shows that the rather low gradient in temperature in the Topopah Spring Unit is not well matched, perhaps again due to the lack of percolating water in the model used. Temperature in deeper formations show some scatter, perhaps due to measurement errors.

In general, almost all of the temperature data from the 25 boreholes selected from Sass et al. (1988) are matched reasonably well with the conduction-only model. Certain features as derived above are not really explained by such a model and perhaps require a more general conduction/convection model developed in the next section. However, there is also uncertainty about the quality of temperature data from gas and liquid filled boreholes.

9.5 Analysis of Temperature Data Using a Coupled Conduction/Convection Model

The heat conduction analysis performed in the last section did reasonably well in explaining the trends of the temperature data but there were still some significant differences. For many of the wells, the observed temperature gradient in some of the units including Topopah Springs and Calico Hills were less than that obtained by the model. The ITOUGH2 code tried to obtain better matches by increasing thermal conductivities, thereby allowing for the same heat flux using a smaller temperature gradient. As thermal conductivity data are fairly accurate one does not expect that significant errors in thermal conductivity or spatial variability of thermal conductivity exists within the units. An alternative explanation for these smaller temperature gradients is percolating water through the unsaturated zone. In order for this water to increase in temperature from the average surface temperature of 19°C to temperatures around 30°C, some energy must be utilized. Significant downflow percolation will affect the temperature gradients within the unsaturated zone considerably, as pointed out by Sass et al. (1988) and Rousseau et al. (1996).

The percolation flux through the unsaturated zone is believed to be the most important parameter for performance assessment and TSPA calculations

for the Yucca Mountain site. The percolation flux affects the amount of flow into drifts, the number of canisters that may be affected, the waste mobilization issue, and the transport of the radionuclides to the water table. As the spatial and temporal variability of the percolation flux is difficult to measure directly, it must be determined or bounded by indirect methods such as modeling of moisture tension, saturation, and environmental isotope data. If temperature data can be of use in determining or bounding the value of percolation flux, this would be of great importance, and much needed. In the following analysis we start by using the available qualified temperature data to investigate the percolation flux and then proceed to add non-qualified data as collaborative evidence.

9.5.1 Percolation Flux Analysis Using Qualified Temperature Data

The boreholes with qualified temperature data include UZ-4, UZ-5, UZ-7a, NRG-6, NRG-7a, and SD-12. The data from these boreholes were collected by J. Rousseau and others at USGS (see data tracking numbers from Table 9.2.1). The temperature data from these boreholes are of very good quality as the boreholes were instrumented with long term monitoring equipment. The temperature data are shown to be relatively stable and should accurately reflect the actual temperature conditions within the unsaturated zone. Figure 9.3.8 shows all of the temperature data and indicates that most of the boreholes extend only to shallow regions of the unsaturated zone. The only borehole that goes entirely through the TSw is borehole SD-12. The rest of the boreholes basically go through the Paintbrush Unit and perhaps just to the top part of the Topopah Springs Unit. However, the data from boreholes UZ-7a, NRG-6, NRG-7a and SD-12 allow for reasonable determination of the temperature gradient within the Topopah Springs Unit. The values obtained are about 17°C per kilometer for boreholes UZ-7a and SD-12, and about 21°C per kilometer for boreholes NRG-6 and NRG-7a.

In order to convert temperature gradients into estimates of percolation flux, one must assume a conceptual model. A reasonable model is one that assumes that the heat flux E through the unsaturated zone is the sum of the conductive upward heat flow and the downward energy flux due to percolating water. In this case the following equation can be derived:

$$E = \lambda \cdot \nabla T - q_l \cdot \rho_l \cdot c_l \cdot \Delta T \quad (9.5.1)$$

Here, $\lambda = 1.73 \text{ W/m/}^\circ\text{C}$ is heat conductivity, q_l is the volumetric liquid flow rate, $\rho_l = 1000 \text{ kg/m}^3$ is water density, $c_l = 4187 \text{ J/kg/}^\circ\text{C}$ is the specific heat of liquid water, $\Delta T = 14 \text{ }^\circ\text{C}$ is the temperature change the downwardly percolating water undergoes as it moves from the surface to the water table.

The above values for the thermal conductivity and the water density and specific heat are reasonable averages from measurements on cores (data on thermal conductivity taken from RIB; DOE 1993) and from the equation of state for water.

In order to calculate the percolation flux (q_j), one needs an estimate for the average heat flux E through the region penetrated by the above boreholes. Sass et al. (1988) reviewed all of the data available at that time and concluded that the heat flux through the unsaturated zone varied from 30-60 mW/m² (see Section 9.3.2). When they used the temperature data from the unsaturated zone, they obtained values around 41 mW/m². However, it should be noted that this heat flux is derived from temperature gradients in the Topopah Springs assuming only conduction and neglecting the convective component. Sass et al. (1988) also estimated the heat flux from temperature data taken from the saturated zone and arrived at an average value of some 50 mW/m². As this estimate is independent of the unsaturated zone temperature gradient, it may be more reasonable for our analysis of percolation flux.

If one uses a heat flux of $E=50$ mW/m² (in equation 9.6.1), one can derive a percolation flux of about 10 mm/yr for the areas around boreholes SD-12 and UZ-7a, and a percolation flux of about 7 mm/yr for areas around boreholes NRG-6 and NRG-7a. These are fairly large percolation flux values, but they agree reasonable well with the range of infiltration values given by A. Flint in his latest infiltration map (Flint et al., 1996). They present infiltration values that range from almost no infiltration rate to about 12 mm/yr. Flint et al. (1996) estimate an average infiltration rate in the repository area of some 4-5 m/yr based on 8 years of monitoring data. These estimates therefore represent infiltration values for the current climate. If one assumes that heat flux through the unsaturated zone is 40 mW/m², one can calculate an effective percolation flux of 6 mm/yr for the area around SD-21 and UZ-7a, and 2 mm/yr for boreholes NRG-6 and NRG-7a. Again, these are values that are in the range of the infiltration rates estimated by Flint et al. (1996). Also, temperature analysis of shallow boreholes UZ-4 and UZ-5 performed by Rousseau et al. (1996) show infiltration rates of 5-15 mm/yr which is consistent with the above analysis and results.

In summary, all of the temperature data from the recently drilled boreholes, UZ-4, UZ-5, UZ-7a, NRG-6, NRG-7a, and SD-12 indicate very significant percolation of water through the unsaturated zone at Yucca Mountain. Given the importance of the percolation flux parameter, these results are very significant and should be verified by further temperature measurements and other indirect analysis. They should also be verified using the full three-dimensional UZ model.

9.5.2 Percolation Flux Analysis Using Non-Qualified and Qualified Temperature Data

Similar analysis to the one performed in the last section can be done using both qualified and non-qualified data. In addition to the 7 boreholes that have qualified data, we use the additional 25 boreholes from Sass et al. (1988) that have non-qualified data. The borehole locations used in the analysis are shown on the topographic map in Figure 9.5.1. This figure shows that most of the boreholes are located in washes and very few along ridge tops. The data from these boreholes may therefore be biased and not representative of the average conditions within the mountain. The approach taken was to estimate the

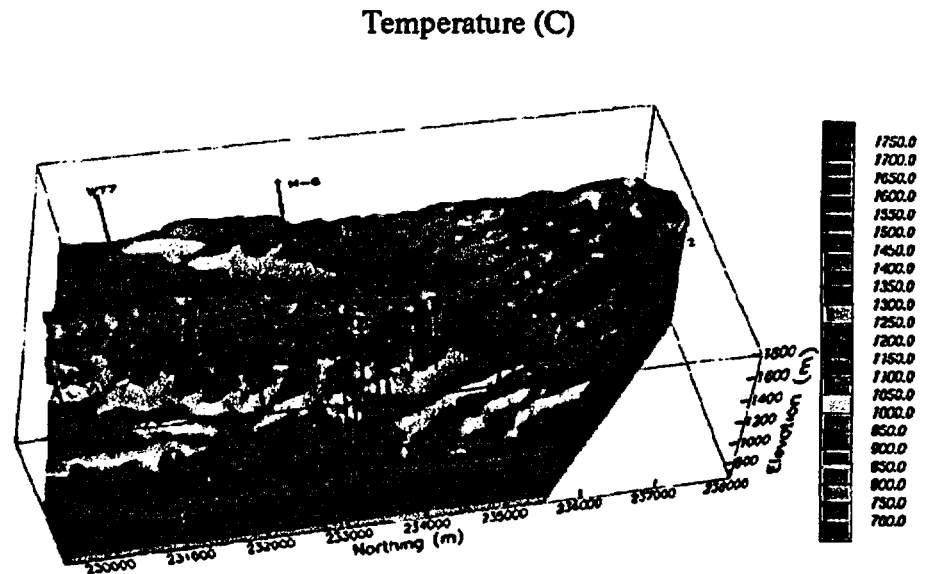


Figure 9.5.1
Locations of boreholes used in the coupled convection/conduction analysis superimposed on an elevation contour map.

temperature gradients in the Topopah Springs Unit for all of the boreholes and contour the results as shown in Figure 9.5.2.

The figure shows remarkably consistent patterns with large areas within the unsaturated zone where similar temperature gradients are found. The lowest temperature gradients are found along the crest of Yucca Mountain and towards the Ghost Dance Fault. These temperature gradients are on the order of 16-18 °C per kilometer. Another area with similar low temperature gradients is found in the vicinity of boreholes UZ-1, G-1, H-1 and UT-18. Almost the entire repository region is estimated to have a low temperature gradient in the Topopah Springs unit thereby suggesting a fairly large percolation flux on the order of 5-12 mm/yr depending upon the assumed geothermal heat flux. In the area between the Ghost Dance Fault and the Bow Ridge Fault considerably higher temperature gradients are found, generally increasing towards Bow Ridge Fault. The estimated percolation fluxes in this area are in the neighborhood of some 0-6 mm/yr, but this again depends on the assumed heat flux through the unsaturated zone. It should be noted that the contour map shown in Figure 9.5.2 is very approximate and ignores major structural features. One may argue that the main low temperature gradient area in Figure 9.5.2 should extend between the Solitario Canyon fault and the Calico Hills fault.

Temperature and Heat Flow Analysis

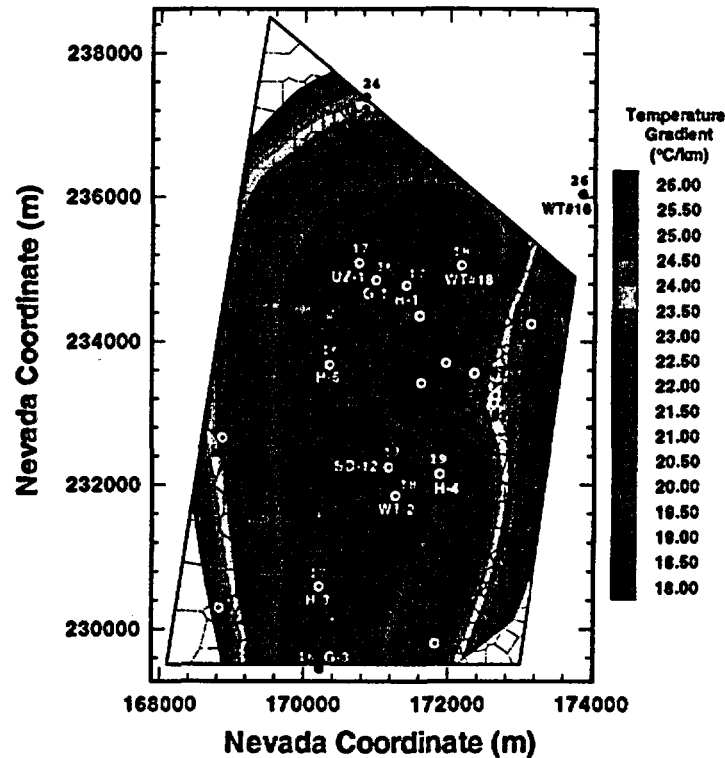


Figure 9.5.2

Temperature gradient contour map for the Topopah Springs Unit based on qualified and non-qualified temperature data for the boreholes shown. The temperature data were collected by Sass et al. (1988) and Rousseau et al. (1996).

The above analysis and the temperature gradient data shown in Figure 9.5.2 are in some agreement with the latest infiltration map prepared by A. Flint et al. (1996). Flint et al. (1996) estimated the largest infiltration rate at the crest of Yucca Mountain with different degrees of reductions towards the east and the west. Their zone of large infiltration is much thinner areally than the one suggested by the data in Figure 9.5.2., but one must remember that direct comparison between infiltration rates at the ground surface and percolation flux at the repository region is not possible. We must also note that variable infiltration between areas of sideslope areas with thick alluvium and areas on top of ridges is not considered here. Most of the wells in the present analysis are located in or near washes and these may have substantially different average infiltration and percolation than the entire area considering all surface process and features (see Figure 9.5.1). Flint et al. (1996) conclude that most infiltration occurs near crests and sideslopes whereas the temperature analysis by Rousseau et al. (1996) suggests highest infiltration in channels of washes. It is therefore not clear if the present estimates for percolation flux may be high or low for the entire repository region.



Figure 9.5.3

Spatial distribution of percolation flux at the repository horizon using Flint et al. (1996) infiltration map. (Figure is taken from Chapter 8, Wu et al.).

A useful insight may be gained from the 3-D simulations presented in Chapter 8 (Wu et al., 1996). Figure 9.5.3 shows the computed percolation flux at the repository level using the latest infiltration map by Flint et al. (1996) and the latest matrix and fracture properties given in Chapter 3 (Bandurraga et al., 1996). Comparison between Figures 9.5.2 and 9.5.3 shows that they are very similar in terms of areas of high and low percolation fluxes. If we were to assume an average heat flux of about 45 mW/m^2 , the average value between the heat flux for the saturated zone and the unsaturated zone, the numerical values in both flux maps of Figures 9.5.2 and 9.5.3 would be very similar. We conclude that the average flux through the repository in the TSw is on the order of 5 mm/yr.

Although there are definite trends in the temperature gradients as shown in Figure 9.5.2, there is one borehole that exhibits an interesting temperature profile. Borehole UZ-7a is drilled through the Ghost Dance Fault and actually resides within the fault for hundreds of meters. This borehole only penetrates about 120 meters of the Topopah Springs units. Temperature data from this borehole has been measured by J. Rousseau of USGS. A temperature gradient of about 18°C/km is found in the bottom 50 meters of the borehole and this gradient is given in Figure 9.5.2. This temperature gradient is found below the elevation at which the borehole exits the Ghost Dance Fault. In the top 70 meters of the Topopah Spring, where the borehole resides within the fault zone, a tem-

perature gradient of about $26^{\circ}\text{C}/\text{km}$ is measured. If these temperature gradients are used in equation 9.5.1, one obtains about $1\text{ mm}/\text{yr}$ percolation through the Ghost Dance Fault, but on the order of $5\text{ mm}/\text{yr}$ in the rock mass adjacent to the fault. However, this analysis of the data may be in error because of the very limited available data set. For example, it can be argued that temperature gradients in the top 100 meters of a unit are not reliable as they reflect temperatures and gradients of the adjacent unit, especially if the thermal conductivities of the two units are quite different, which is the case with the Paintbrush unit and the Topopah Springs unit.

9.6.3 Percolation Flux Through the Calico Hills Using Non- Qualified Data

Similar analysis was performed using the temperature data from the Calico Hills Unit. Only the non-qualified data were used since very limited qualified temperature data are available. Again, we use the 25 boreholes from Sass et al. (1988). Figure 9.5.4 shows the temperature gradient in the Calico Hills in the region of interest. The figure shows that the temperature gradient in the Calico Hills is much larger than that of the Topopah Springs Unit because of the much lower effective thermal conductivity of the Calico Hills Unit. The temperature gradients in the Calico Hills Unit vary from about 28 to over $40^{\circ}\text{C}/\text{km}$. There is one anomalous temperature gradient value of $24^{\circ}\text{C}/\text{km}$ for borehole H-3 and another one of $38^{\circ}/\text{km}$ for borehole H-1. The thermal conductivity of the Calico Hills Unit varies considerably depending on the vitric or zeolitic nature of the formation as well as the degree of welding and the degree of water saturation. A relatively low effective thermal conductivity estimate would be $1.2\text{ W}/\text{m}^{\circ}\text{C}$ (RIB; DOE 1993). If this value is adopted and heat flux of $50\text{ mW}/\text{m}^2$ is assumed, one can calculate a percolation flux of $7\text{ mm}/\text{yr}$ through most of the Calico Hills Unit. If the same value of thermal conductivity is assumed and a heat flux of $40\text{ mW}/\text{m}^2$ is used, an effective percolation flux of about $2\text{ mm}/\text{yr}$ can be computed. In general, the low temperature gradient area basically covers the entire repository area.

Temperature and Heat Flow Analysis

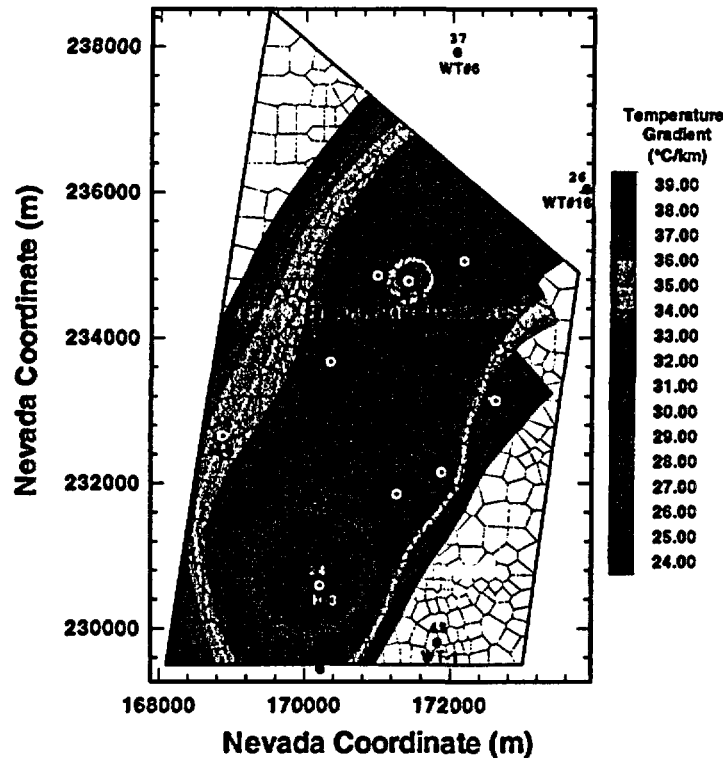


Figure 9.5.4

Approximate temperature gradient contour map for the Calico Hills Unit based on qualified and non-qualified temperature data for the boreholes shown. Temperature data were taken from Sass et al. (1988).

It is interesting to note that although the above percolation flux values are quite substantial, they are less than those estimated through the TSw. One possible explanation of this is lateral flow on top of the zeolites in the CHn as hypothesized in our conceptual model discussion in Chapter 1 (Bodvarsson et al., 1996). The suggested lateral flow above the zeolite is an important conceptualization because of the potential for retardation if the water actually flows through the zeolitic rock (Robinson et al., 1995). Other supporting evidence for this is the fact that H-3 has the lowest temperature gradient in the CHn, and H-3 is close to the region where there is a hole in the zeolites of the CHn, therefore allowing fluid to percolate freely through the unit (see Chapter 1; Bodvarsson, et al., 1996). Also, borehole H-1 has the highest temperature gradient and this borehole only has zeolitic rocks in the Calico Hills unit.

9.6.4 Combined Numerical Analysis of Temperature Gradients in TSw and CHn Using Both Qualified and Non-Qualified Data

The ITOUGH2 computer code was used to estimate percolation flux using all of the temperature data from the 7 qualified wells and the 25 boreholes from Sass et al. (1988). In these simulations, the thermal conductivities of all units were fixed using the values discussed in Ahlers et al. (1995), but the infiltration flux at the ground surface and the percolation flux through the units were estimated. The results showed very comparable percolation flux values to what can be inferred from Figure 9.5.3 and 9.5.4 when the data in these figure are averaged. Since these simulations were conducted using a 1-dimensional model for each one of the boreholes, the infiltration rate at the top, the percolation flux through TSw and the percolation flux through CHn were all assumed to be equal. As Figures 9.5.2 and 9.5.3 and the analysis above have shown, the percolation flux through the TSw seems to be higher than that through the CHn due to lateral flow perhaps around the zeolitic zones. The ITOUGH matches with the data therefore represent an average percolation flux for the two units and probably do not reflect the actual, more complex 2-D and 3-D flow patterns within the unsaturated zone.

Further analysis will be conducted during FY97 that will consist of ITOUGH2 temperature inversions above the CHn using temperature data from all units and then a separate analysis for temperature inversion within the CHn. These analyses will also take into account in more detail the different thermal conductivity variations within all units of the unsaturated zone. Then the results will be applied to the entire 3-D model and the temperature data and gradients from all of the boreholes will be matched simultaneously.

9.7 Concluding Remarks

Lawrence Berkeley National Laboratory (LBNL), in cooperation with USGS, is developing and enhancing the three-dimensional site-scale numerical model of the unsaturated zone at Yucca Mountain. In this chapter, preliminary work on incorporating temperature and thermal conditions into the model is described.

Qualified temperature data from seven boreholes and non-qualified data from twenty-five boreholes are used. Conduction analysis of the data show good matches with temperatures for most of the boreholes and that the thermal conductivity model by Rautman et al. (1995) best explains the data (Ahlers et al., 1995). ITOUGH2 optimization of thermal conductivities generally tends to increase values to obtain a smaller temperature gradient within the Topopah Springs Unit. This is believed to be an artifact of the conduction-only model used as water percolating through the mountain affects the temperature gradient. All of the above conclusions are non-qualified (non-Q) but are believed to be scientifically valid.

A coupled convection/conduction model was also used to analyze the temperature data, and in particular for the purpose of estimating the percolation flux through the mountain. Qualified data from boreholes UZ-7a and SD-12 suggest a percolation flux of some 5 to 10 mm/yr depending upon the assumed heat flux. Qualified data from boreholes NRG-6 and NRG-7a suggest percolation flux of around 2-6 mm/yr, again depending upon the assumed heat flux. These percolation flux values are in reasonable agreement with the recently developed infiltration map (Flint et al., 1996).

The qualified data set from the seven boreholes is augmented by twenty-five non-qualified temperature profiles from boreholes predicted by Sass et al. (1988). The coupled conduction/convection model was applied to all of the available data in order to develop an appropriate percolation map for the proposed repository region. The results show that there are very consistent trends in the temperature gradient data throughout the mountain. Assuming reasonable heat flux values one obtains a percolation flux through the repository horizon in the Topopah Springs Unit of some 5 to 10 mm/yr. We believe that the flux is probably closer to 5 mm/yr given the nature of the assumptions and approximations used. These results are consistent with the computer generated percolation flux map of the repository horizon that results from three-dimensional numerical simulations using the unsaturated-zone model. Analysis of temperatures of the Calico Hills and deeper units show, in general, less of a percolation flux, suggesting lateral flow above the unit, perhaps due to the low permeability zeolites.

It should be emphasized that the analysis presented here is preliminary and needs to be verified by a careful selection of thermal conductivities and heat flow, and a more realistic model. Alternative processes that can explain the temperature data, such as vapor condensation, should be evaluated.

9.8 References

Ahlers C.F., T.M. Bandurraga, G.S. Bodvarsson, G. Chen, S. Finsterle, and Y.S. Wu, Performance analysis of the LBNL/USGS three-dimensional unsaturated zone site-scale model, Lawrence Berkeley National Laboratory, 1995a.

Ahlers C.F., T.M. Bandurraga, G.S. Bodvarsson, G. Chen, S. Finsterle, and Y.S. Wu, Summary of model calibration and sensitivity studies using the LBNL/USGS three-dimensional unsaturated zone site-scale model, Lawrence Berkeley National Laboratory, 1995b.

ACCN: MOL.19960208.0091-0097

DTN: LB092995312293.001

Temperature and Heat Flow Analysis

- Czarnecki J.B., G.M. O'Brien, P.H. Nelson, Is there Perched Water Under Yucca Mountain in borehole USW G27, EOS, Transactions, American Geophysical Union, 1994 Fall Meeting, Vol.75, NO.44, Supplement, November, 1994
ACCN: MOL.19950131.0438
- DOE, Reference Information Base (RIB), Yucca Mountain Site Characterization Project, 1993
- Finsterle S., ITOUGH2 User's Guide Version 2.2, Lawrence Berkeley National Laboratory Report LBNL-34581, Lawrence Berkeley National Laboratory, Berkeley, CA, 1993.
ACCN: MOL.19941026.0075
- Flint A.L., J.A. Hevesi, and L.E. Flint, Conceptual and numerical model of infiltration for the Yucca Mountain area, Nevada, U. S. Geological Survey Water Resources Investigation Report, U. S. Geological Survey, Denver, CO, 1996.
- Fridrich C.J., Dudley, W.W., Jr., and Stuckless, J.S., Hydrogeologic analysis of the unsaturated-zone ground-water system under Yucca Mountain, Nevada, Journal of Hydrology, V. 154, p.133, 1994.
- Lu N, and E. M. Kwicklis, A preliminary, two-dimensional numerical model for gas circulation around UZ6s, Yucca Mountain, Nevada, U.S. Geological Survey, Lakewood, CO, 1995.
- Nimick F. B., Thermal-conductivity data for tuffs from the unsaturated zone at Yucca Mountain, Nevada, Sandia National Laboratory Report SAND88-0642, UC-70, Sandia National Laboratory, Albuquerque, NM, 1989.
ACCN: NNA.19900328.0105
- Nimick F. B., The thermal conductivity of seven thermal/mechanical units at Yucca Mountain, Nevada, Sandia National Laboratory Report, SAND88-1387, UC-814, Sandia National Laboratory, Albuquerque, NM, 1990.
ACCN: NNA.19891107.0078
- Rautman C.A., Modeling spatial heterogeneity of thermal conductivity using a surrogate property, Proceedings of the Sixth Annual International Conference on High-Level Radioactive Waste Management, Las Vegas, NV, pp.83-84, 1995a.
ACCN: MOL.19950321.0080
- Rautman C.A., Preliminary geostatistical modeling of thermal conductivity for a cross section of Yucca Mountain, Nevada, Sandia National Laboratory Report, SAND 94-2283, WC-814, Sandia National Laboratory, Albuquerque, NM, 1995b.
DTN: SNSAND94228300.000 (Non-Q)
- Robinson B.A., A.V. Wolfsberg, G.A. Zyvoloski, and C.W. Gable, An unsaturated zone flow and transport model of Yucca Mountain, LA-Milestone 3468 (Draft), 1995.

Temperature and Heat Flow Analysis

- Rousseau J.P., E.M. Kwicklis, and D.C. Gillies, Hydrogeology of the unsaturated zone, North Ramp Area of the Exploratory Studies Facility, Yucca Mountain, U. S. Geological Survey Water-Resources Investigation, U. S. Geological Survey, Denver, CO, 1996.
- Sass J.H., Significance of the temperature profile in USW-G2 and its evolution with time, manuscript in prep, update May, 1996.
- Sass J.H., Lachenbruch, A.H., Dudley, W.W., Jr., Priest, S.S., and Munroe, R.J., Temperature, thermal conductivity, and heat flow near Yucca Mountain, Nevada: some tectonic and hydrologic implications, U.S. Geological Survey Open-File Report 87-649, U.S. Geological Survey, 1988.
ACCN: NNA.19890123.0010
DTN: GS950408318523.001 (Non-Q)
- Weeks E.P., Effect of topography on gas flow in unsaturated fractured rock: concepts and observations, flow and transport through unsaturated fractured rock, (D.D. Evans and T.J. Nicholson, Eds.), Geophysical Monograph 42, American Geophysical Union, Washington, D.C., pp.165-170, 1987.
ACCN: HQS.19880517.3214
- Wittwer C., G. Chen, G.S. Bodvarsson, M. Chornack, A. Flint, L. Flint, E. Kwicklis, and R. Spengler, Preliminary development of the LBL/USGS three-dimensional site-scale model of Yucca Mountain, Nevada, Lawrence Berkeley National Laboratory Report LBL-37356, UC-814, Lawrence Berkeley National Laboratory, Berkeley, CA, 1995.
- Wu. Y.S., S. Finsterle, P. Frazer, and A. Simmons, Software qualification for ITOUGH2 and various equation-of-state (EOS) modules and auxiliary modules for TOUGH2 and ITOUGH2, Report Lawrence Berkeley National Laboratory, Berkeley, CA, August 1996 (draft).

**PRELIMINARY CONCEPTUAL MODEL
OF FLOW PATHWAYS
BASED ON ^{36}Cl AND OTHER
ENVIRONMENTAL ISOTOPES**

J. Fairley and E. Sonnenthal

August 1996

10.1 Introduction

10.1.1 Objective of work

The objective of this chapter is to produce a preliminary conceptual model of flow pathways in the unsaturated zone based on ^{36}Cl and other environmental isotopes. The model is checked for consistency against results of other UZ model calibration parameters (e.g., see chapter 11 on percolation flux; Sonnenthal et al., and ch. 14 on fractures; Simmons et al.) The model is then used to predict which areas yet to be encountered in the ESF may provide additional evidence of fast flow paths and accordingly to devise an appropriate sampling and testing program that will allow not only better characterization of fast paths but also a greater understanding of flux at the repository horizon. Particular aspects of this prediction are the effects of fault inclination and infiltration pulses on fluid spreading which are treated in section 10.6.

An understanding of flow pathways as indicated by environmental isotopes was already being incorporated into the unsaturated zone site-scale flow model when DOE requested that this aspect of the flow model receive greater emphasis because of concerns over the detection of bomb-pulse concentration of ^{36}Cl in the ESF. DOE requested that predictions be made as to where the Project can expect to find bomb-pulse concentrations in the remainder of the ESF that has not been excavated and in other areas of Yucca Mountain. Experience with field tracer tests at Raymond Quarry, the C-holes, and in international programs (Grimsel laboratory, Stripa, etc.) has shown the difficulty of predicting where tracers will be found. Prediction of breakthrough has the greatest confidence in saturated sedimentary systems; in unsaturated rock the difficulty increases greatly and becomes even more difficult when the system is fractured, both of which are the case at Yucca Mountain. Compounding the challenge is the Project's very limited knowledge of the hydrologic characteristics of major faults and their role as flow pathways. However, without diversion of resources, we were able to combine insights gained from previous investigations of environmental isotopes (discussed above) with constraints of parameters of the UZ flow model, explained in other chapters of this report, to produce a preliminary flow model that incorporates environmental isotopes. Although the results presented here are preliminary and will be refined for the fully calibrated model in June 1997, the accelerated effort to incorporate environmental isotopes into the flow model has begun by testing conceptual models to improve our understanding of flow pathways in the unsaturated zone and will lead to a better focus for the FY97 model development.

Quality Assurance Pedigree of Data: The environmental isotope data in this chapter were taken from unqualified sources (non-Q) in published literature. Material properties were taken from chapter 3 of this report (Bandurraga et al.). See chapter 3 for detail of QA status. The Effective Continuum Model (ECM) module and radionuclide transport modules of TOUGH2 used in the numerical modeling of this chapter are presently being qualified in conjunction with this report (Wu et al., 1996). TOUGH2 Version 1.11 was qualified in February 1996 (Pruess et al., 1996).

Prediction of occurrence of ^{36}Cl at the repository horizon has two aspects: 1) the problem of getting a pulse through the Paintbrush non-welded hydrogeologic unit (PTn), and 2) spreading in the Topopah Spring welded unit (TSw) at the repository horizon. Section 10.2 evaluates conceptual models for getting a pulse of the water through the PTn and Section 10.3 considers both the effect of inclination of faults and the effect of a transient pulse carrying ^{36}Cl through the repository horizon.

10.1.2 Background

Environmental isotopes are stable isotopes that are produced either in the atmosphere, in surface and ground waters, or *in situ* in rock, soil, and alluvium. Because environmental isotopes fractionate in nature, their concentrations change as a function of temperature, pressure, and source region. The concentrations of some environmental isotopes relative to their background ratios can therefore be utilized to obtain information about source regions, climatic conditions, mixing of different reservoirs, and residence time in a particular reservoir. A special class of environmental isotope tracer includes those from anthropogenic sources (i.e., nuclear testing), such as ^{36}Cl , ^{129}I , ^3H , ^{99}Tc , ^{243}Pu , and ^{137}Cs . As tracers these have been useful in evaluating flow pathways from the surface through the unsaturated zone at Yucca Mountain. Because of their occurrence at Yucca Mountain, ^{36}Cl and ^3H concentrations, in particular, provide important insights into fast pathways in the unsaturated zone.

Although environmental isotopes are very good tracers of pathways, past events, and indicators of residence times in rock or water, they have limitations. A common misconception is that concentrations of environmental isotopes can be used to determine percolation flux to the horizon where they are found. For example, they can show that a pulse of water deposited material in a fracture lining at some period in time, but not how much water passed that location. Furthermore, the mere detection of a tracer such as ^{36}Cl at repository depth tells nothing about the significance of its occurrence in a performance sense, i.e., the level of concentration of the isotope that would lead to estimates of detrimental performance with respect to flow pathways. Nonetheless, in spite of their limitations, environmental isotopes provide a useful tool for calibration of the site-scale unsaturated zone flow model because they provide an additional line of evidence for testing consistency of conceptual and numerical models with observations. It is for the purpose of model calibration that we discuss issues

Preliminary Conceptual Model of Flow Pathways based on ^{36}Cl and Other Environmental Isotopes

related to environmental isotopes with emphasis on their confirmation of fast flow pathways through the unsaturated zone.

10.1.3

^{36}Cl : Measurements, Assumptions, Caveats

^{36}Cl is produced by a number of sources which can be grouped into atmospheric sources and *in situ* production. Atmospheric sources include natural sources and anthropogenic sources, such as global fallout and local Nevada Test Site (NTS) activities. ^{36}Cl is produced naturally in the atmosphere by reaction of cosmic rays with ^{40}Ar , ^{36}Ar , and ^{36}Cl . ^{36}Cl has a half-life of 308,000 years and residence time in the stratosphere on the order of months to years (Fabryka-Martin et al., 1993). Atmospheric sources dominate in waters older than 40 years and have concentration ratios of 500 ($^{36}\text{Cl}/\text{Cl} \times 10^{-15}$) in present-day waters but have been as high as 1500×10^{-15} over the past half million years. Anthropogenic sources dominate in young waters and reach values at Yucca Mountain as high as peak global fallout ($200,000 \times 10^{-15}$; Fabryka-Martin and Wolfsberg, presentation to NWTRB, 1996).

In rocks and minerals near the surface, ^{36}Cl is produced *in situ* by reaction of cosmic rays with ^{39}K , ^{40}Ca , and ^{35}Cl . This is termed spallation. The concentration of ^{36}Cl from this source is variable and depends on the age of exposure of rocks and minerals (with longer exposure times having higher ratios) as well as on their elemental composition. This source is thought to be of negligible importance at Yucca Mountain in comparison to the amount produced by atmospheric sources. Fabryka-Martin and others (1996) considered $^{36}\text{Cl}/\text{Cl}$ ratios in excess of 1500×10^{-15} to be indicative of bomb-pulse. It remains to be seen whether sufficient Cl can be mobilized from Cl at the surface to produce bomb-pulse ratios observed at depth. ^{36}Cl can also be produced *in situ* in deep subsurface rocks and ocean waters through neutron capture by ^{35}Cl . The estimated value at Yucca Mountain contributed by this source is 20-30 ($^{36}\text{Cl}/\text{Cl} \times 10^{-15}$) and is of little significance.

The meteoric $^{36}\text{Cl}/\text{Cl}$ ratio is a result of two variable processes: cosmogenic production rate of ^{36}Cl in the atmosphere, and deposition rates of stable Cl. Production of ^{36}Cl in the atmosphere is a function of atmospheric cosmic-ray intensity, which is inversely proportional to temporal variations in the earth's geomagnetic field intensity. Based on reconstructions of the paleomagnetic field intensity, ^{36}Cl production was perhaps double its present rate for much of the past 500 Ky (Fabryka-Martin et al., 1996). Variations in the stable Cl deposition rate are more difficult to reconstruct. These variations are a product of changing meteorologic patterns and changing source regions. It is assumed that the Cl deposition rate has varied $\pm 25\%$ relative to its present rate of 106 mg Cl/m²yr (Fabryka-Martin et al., 1993).

^{36}Cl is analyzed by collecting Cl leached from one to a few kilograms of broken rock, followed by filtering and precipitation as silver chloride (AgCl). After purification, the AgCl separate is analyzed by accelerator mass spectrometry (AMS). Analytical measurement and sample contamination are not usually

Preliminary Conceptual Model of Flow Pathways based on ^{36}Cl and Other Environmental Isotopes

sources of error. However, the rock is a possible source of contamination. Tuff contains Cl that can be released during reaming of the bit during drilling operations or during crushing in the laboratory. Rock Cl has lower $^{36}\text{Cl}/\text{Cl}$ ratios than background ratios, which would dilute the observed $^{36}\text{Cl}/\text{Cl}$ ratio. Since the $^{36}\text{Cl}/\text{Cl}$ ratio is inversely proportional to residence time or apparent age, this would indicate longer residence times. This explains why measured $^{36}\text{Cl}/\text{Cl}$ ratios for borehole samples are systematically lower than values for ESF samples (Fabryka-Martin et al., 1993; Liu et al., 1995) because the method of sample collection in the ESF does not pulverize the rock.

^{36}Cl dating tends to indicate greater ages than ^{14}C methods by an order of magnitude (Liu et al., 1995). Uncorrected ^{14}C ages for pore water from the unsaturated zone and for perched water at Yucca Mountain have ranged from modern to 10 Ky (Yang, 1994; Yang et al., 1996) whereas uncorrected ^{36}Cl based ages have ranged from modern to 700 Ky (Fabryka-Martin et al., 1993). The apparent discrepancies may be attributed to one of the following reasons (Liu et al., 1995): 1) different transport mechanisms for carbon and chloride; 2) different magnitudes and timing of bomb-pulse signals; 3) mixing of waters from different flow paths with different apparent ages; and 4) inadequate methods for correcting for the effect of sample contamination by carbon or chloride from sources other than that in the infiltrating water. By adjustments using the Cl/Br ratio, measured $^{36}\text{Cl}/\text{Cl}$ ratios in rock samples are corrected for dilution of the meteoric component by rock Cl before calculating residence times from these data. However, the Cl/Br ratio itself is a source of uncertainty because the ratio varies in soils, alluvium, ground water and rock, and because of analytical difficulties in measuring extremely low Br concentrations.

10.1.4 Unsaturated Zone (UZ) Flow Model Calibration

Calibration of the unsaturated zone flow model relies on many different observations that are folded into conceptual models which balance the mass of gas, water, and energy. The conceptual models are then tested by numerical models which account for all of the observations. The preferred choice among alternate conceptual models is the one that most rigorously accounts for all of the data and observations. The calibration process involves testing each type of data or observation in the numerical model and then matching it to other observations. For example, the conceptual model of water flow must first account for the location and volume of perched water and then for perched water age (see ch. 7 of this volume; Wu et al.). Saturation and moisture tension from wells must be calibrated (see chapter 8 of this volume; Wu et al.). Next the concentration of environmental isotopes in wells and in the ESF must be accounted for (this chapter) along with fracture coating ages for their indication of flow pathways and residence times (see chapter 14 of this volume; Simmons et al.). ESF moisture balance must be considered to determine the degree of relative humidity and whether evaporation is occurring in fractures. Finally, data and observations from the Ghost Dance and other faults must be examined with respect to their influence on all of the above parameters. Similar types of cali-

Preliminary Conceptual Model of Flow Pathways based on ^{36}Cl and Other Environmental Isotopes

bration are done for the gas flow and heat transfer components of the unsaturated zone flow model.

Calibration of all of these components into one model is an ambitious undertaking. With the goal of producing a fully calibrated model which utilizes all available Yucca Mountain data for these parameters by June of 1997, we have accelerated efforts this year by incorporating as much information as possible. Although the results presented here are preliminary and will undoubtedly be refined as additional site characterization data become available, the calibration achieved for this 1996 model has given us a significant head start toward the final model.

10.1.5 Changes in the UZ Flow Model Based on Environmental Isotopes

The preferred conceptual flow model until recently at Yucca Mountain allowed for spatially variable flow and infiltration but was dominated by matrix flow (Montazer and Wilson, 1984). However, through site characterization data gathered since the mid-1980's from drill holes and from the Exploratory Studies Facility (ESF), it has become increasingly evident that flow along fast preferential pathways through fractures is a significant and perhaps the dominant flow regime in the unsaturated zone. Several lines of evidence point to the existence of fast flow pathways at Yucca Mountain. One of the most compelling lines is the existence and composition of perched water that is younger and different in composition from saturated zone water. Furthermore, in several locations perched water has been contaminated with polymer from drilling operations that reflects a recent infiltration pulse. A second important line of evidence is from environmental tracer tests such as ^{36}Cl and ^3H , and a third is derived from age dates of fracture-lining materials.

Wang and others (1993) investigated fast flow pathways at Rainier Mesa as a possible analog to wetter conditions at Yucca Mountain and encouraged the characterization of fast pathways through the Calico Hills unit based on their predictions. Yang (1992) identified fast pathways indicated by ^{14}C ages, ^3H , and major ion chemistry in UZ-16 and UZ-14 and in boreholes UZ-4 and UZ-5. Fabryka-Martin and others (1993) and Liu and others (1995) found evidence of bomb-pulse ^{36}Cl in boreholes UZ-14 and UZ-16 and in numerous neutron holes. In 1996 detailed studies in the area of the North Ramp of the ESF that included pneumatic and hydrologic property data as well as isotopic and geochemical data (Rousseau et al., 1996) provided supporting demonstration of the significance of fast pathways at Yucca Mountain. Their report was issued closely in time to reports on two other corroborating studies which synthesized geochemical and isotopic data: Yang and others (1996) interpreted chemical and isotopic data $\delta^3\text{H}$, ^{14}C , $\delta^{18}\text{O}$, and $\delta^{87}\text{Sr}$ from boreholes at Yucca Mountain, and Fabryka-Martin and others (1996) presented results of an extensive sampling, both systematic and feature-based that provided evidence of ^{36}Cl with bomb-pulse signature at the repository horizon in the ESF in areas of through-going faults that served as preferential fast flow paths.

Preliminary Conceptual Model of Flow Pathways based on ^{36}Cl and Other Environmental Isotopes

10.1.5.1 Perched Water

Perched water has been encountered at the base of the Topopah Spring Tuff, just above the contact between the lower nonlithophysal zone and the crystal-poor vitric zone, and in the top of the nonwelded to partially welded tuffs of the Calico Hills Formation in boreholes USW UZ-1, USW UZ-14, NRG-7a and SD-9 near the North Ramp. It was also found in UZ-16 and in SD-7 (see Figure 10.1.5.1.1). Major ion chemistry of this perched water is very similar to that of Calico Hills Formation pore water, a sodium-carbonate or sodium-bicarbonate type (Rousseau et al., 1996). The chloride concentration of the perched water, however (6×10^{-15} mg/l), is much lower than the chloride concentration of pore water obtained from the same interval (87.5 mg/l), indicating very little contribution of water from the matrix of the overlying rocks. Stable isotope data for $\delta^{18}\text{O}$ and deuterium (δD) are consistent with rapid, fracture infiltration with little or no evaporation. All samples represent the time period since last glaciation and are heavier in isotopic composition than saturated zone water (Benson and Klieforth, 1989). After correction of apparent ages for dissolution of older caliche by infiltrating water, the age of perched water was estimated to be 4000-7000 years, an age that is much younger than any that could be derived using a matrix-to-matrix percolation model (Rousseau et al., 1996). In UZ-14 water ^{14}C values from the top 300 feet ranging from 70-95% modern carbon are similar to values for the Calico Hills Formation pore water, which are between 70-96% modern carbon at depths of 1400-1714 feet (Yang, 1992).

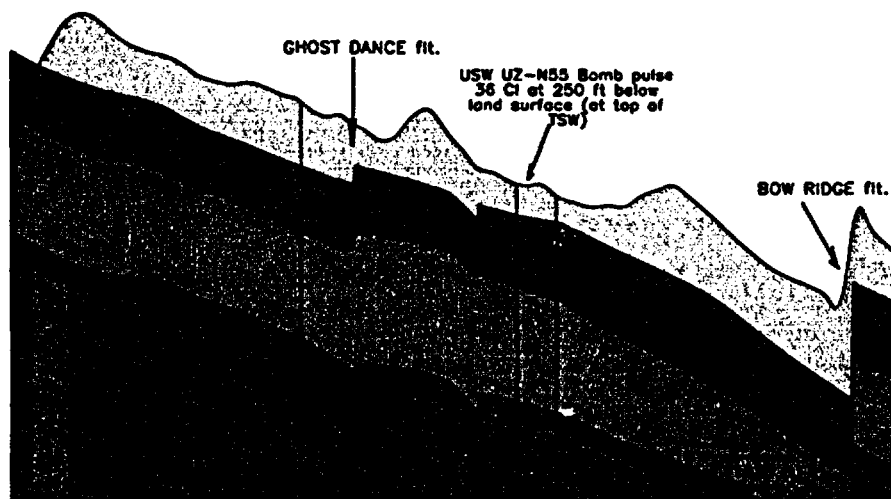


Figure 10.1.5.1.1
Cross-section of Yucca Mountain between Ghost Dance fault and Bow Ridge fault showing location of perched water at SD-7, location of bomb-pulse ^{36}Cl in neutron hole UZN-55 and location of bomb-pulse tritium in UZ-16

Even further evidence for rapid infiltration along fractures to depth is found in $\delta^{87}\text{Sr}$ signatures. The $\delta^{87}\text{Sr}$ signature of the perched water is +4.46%.

Preliminary Conceptual Model of Flow Pathways based on ^{36}Cl and Other Environmental Isotopes

This is similar to that for pedogenic calcite ($\delta^{87}\text{Sr}$ of +4.4%) and calcite fracture fillings in the Yucca Mountain area, but dissimilar to that of the Topopah Spring Tuff [$\delta^{87}\text{Sr}$ of +1.5% to +9.6%; (Peterman and Stuckless, 1993)]. Saturated zone water has $\delta^{87}\text{Sr}$ values of +1.0 to +3.3%. These data indicate that perched water probably obtained its isotopic signature from dissolution of shallow surficial calcite during infiltration or during downward percolation through fractures (Marshall et al., 1993).

10.1.5.2 Locations of Indicators

Tritium concentrations were below detection limits (4 tritium units) at the same five locations in the ESF where bomb-pulse ^{36}Cl was found (Yang, presentation to NWTRB, 1996; see Figure 10.1.5.2.1). Greater than 30 tritium units (TU) is considered bomb-pulse. In Alcove 3 (where ^{36}Cl was not measured), tritium concentrations ranged from $6-12 \pm 4$ TU. In the Calico Hills Formation in UZ-16 concentrations of more than 100TU were detected (Yang et al., 1996). In Bow Ridge Fault gouge 40 m below ground surface and in UZ-N55 cuttings from a depth of 53 m, ^{99}Tc was detected. At these two locations, bomb-pulse ^{36}Cl was also detected (see Figure 10.1.5.1.1). In summary, bomb-pulse nuclides that behave in a chemically similar manner to ^{36}Cl , such as ^3H and ^{99}Tc (i.e., are not retarded in the flow system) are also detected at elevated levels some distance below the surface and confirm the existence of fast flow paths at least to those depths.

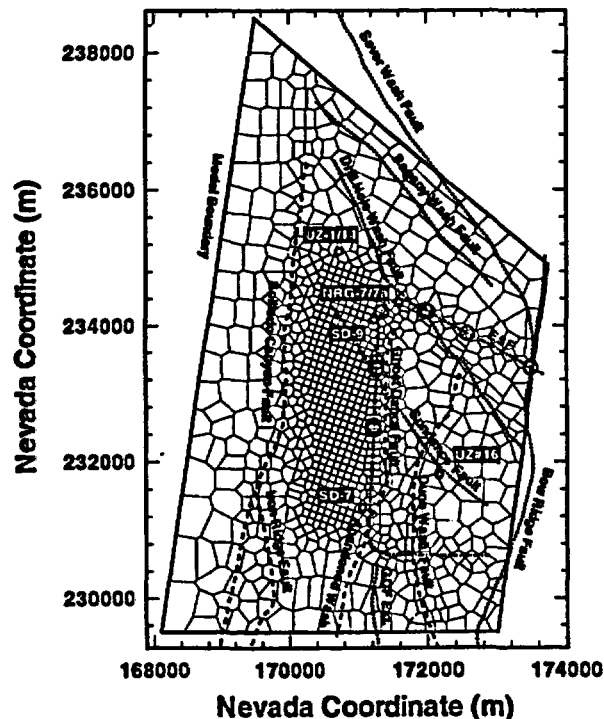


Figure 10.1.5.2.1: Map of UZ model showing model grid, trace of major faults, trace of ESF and boreholes where perched water was detected. Circles indicate locations where bomb-pulse concentrations of ^{36}Cl were found in the ESF.

Elevated tritium concentrations of pore water at several locations provide evidence for rapid, shallow fracture flow through the TCw and the PTn. Tritium profiles across these units indicated pore-water age inversions with older water overlying younger water. At one location age inversions were observed to a depth of 245 feet, just below the PTn-Topopah Spring contact (Rousseau et al., 1996). (Tritium concentration in UZ#4 ranges from 0-45 TU with a peak concentration at 150 feet; UZ#5 has a peak concentration of 75 TU at 105 feet; NRG-6 shows a peak of 30-150 TU broadly distributed from 175-245 feet) (Rousseau et al., 1996). Given the short half-life of tritium (12.5 years), the infiltration must have occurred within the last forty years.

**10.1.5.3
Corroborating Evidence of
Fast Paths**

Although bomb-pulse ^{36}Cl signatures at the repository horizon appear to be clear indicators of fast paths, greater confidence will be gained by evaluating lines of corroborating evidence, as well as examining contributions from other sources that could influence the signature and reconstruction of the past ^{36}Cl signal in the atmosphere. Other lines of evidence include: 1) surface calcite as an additional source of ^{36}Cl ; 2) examination of field relations and mineralogic textures, i.e. fluxes as estimated by fracture coatings and age dating of those coatings by U-series and ^{14}C methods [see chapter 14 of this volume; Simmons et al.]; 3) correlation of age dates with net infiltration estimates; and 4) measurement of other bomb-pulse nuclides such as ^3H , ^{137}Cs , ^{243}Pu , ^{99}Tc and ^{129}I .

Results of dating fracture coatings using ^{14}C and U-series dating are currently more in keeping with hypotheses of slow flux over long time periods (Paces, 1996) than with fast pathways. This supports hypotheses of several flow systems at Yucca Mountain, matrix flow, flow in fractures, flow in fractures/structural features, with some rapid and some very slow. The current distribution of U-series ages is quite broad, with a peak around 100-175 Ky and the youngest age at 37 Ky. Based on the concept of "continuous deposition", Paces (1996) estimated flux in "slow" fractures to be about 1×10^{-4} mm/yr. More extensive testing of models of calcite deposition and how they provide insights into flux estimates are needed.

10.2 Conceptual Model Development

The stratigraphy of Yucca Mountain is characterized by an alternating sequence of welded and non-welded ash flow and airfall tuff deposits (see Figure 10.1.1). The welded tuffs are characterized by low matrix porosities and permeabilities, but have high fracture densities. The non-welded tuffs have low fracture densities but relatively higher matrix porosities and permeabilities. All of the units were subject to varying degrees of alteration to clays and zeolites, which lowered their permeabilities in affected areas. Within the framework of this heterogeneous hydrogeologic system, three key factors affect flux at the proposed repository horizon: 1) variable patterns of near-surface infiltra-

tion, 2) spatial variability of flow through the Paintbrush Tuff non-welded unit (PTn), and 3) spatially variable material properties at the repository horizon.

Infiltration due to precipitation is variable, both spatially and temporally. Currently, estimates of net infiltration into the Tiva Canyon welded unit (TCw) vary spatially from 0 to 14 mm/yr (Flint et al., in review). Due to orographic effects, more precipitation falls at higher elevations on Yucca Mountain, and to the north of the site. A greater fraction of precipitation falling on sideslopes and ridges, as opposed to alluvial channels and terraces, will become net infiltration (Flint, et al., 1994). Borehole studies have shown that infiltration processes are temporally variable, as well. Infiltration appears to move downward in episodic, transient pulses after rainfall events (Flint et al., 1994). These infiltration pulses can transit the extensively fractured TCw relatively quickly, as evidenced by apparent age inversions of water in the TCw and PTn.

Infiltration into the PTn is complex because fractures transmitting flux from the TCw generally terminate at the top of the PTn. Apparently few fractures cross all of the non-welded layers in the unit (Rousseau et al., 1996). Flow patterns within the PTn are affected by the microstructure and dip of layers, small zones of alteration, and variability in permeability distribution in the unit. Existing fractures in the PTn make uncertain contributions to flux through the unit, as a result of permeability alterations arising from fracture coatings (see chapter 14, this volume). Because of its high porosity and high storativity, travel times through the matrix of the PTn are great. Flow penetrating the TCw may be diverted laterally either at the top or within the PTn, but the extent and volume of this flow is poorly understood, and as more information is obtained, lateral diversion of flow appears to be less significant than originally thought (Rousseau et al., 1996). The PTn unit is also transected by numerous faults that may act as both as conduits and barriers to subsurface fluid flow.

The most important aspect of quantifying percolation flux at the potential repository horizon in the TSw unit is net infiltration. It is expected that the flux varies spatially and temporally in response to climatic changes and heterogeneity within the flow system. The ages of fracture- and lithophysal-cavity-filling materials within the TSw indicate that these materials were deposited by water percolating downward over hundreds of thousands of years. For the unfractured rock matrix of the TCw unit, TSw unit, and unaltered CHn unit, measured hydraulic conductivities are very small. Therefore, the rock matrix of these units would only be able to transmit water at an average velocity on the order of a fraction of a millimeter per year. Based on these properties and the net infiltration rates discussed above, flow through the rock matrix would require at least several thousand years to reach the potential repository horizon from the ground surface. Matrix saturation and water potential data from boreholes are consistent with these relatively low fluxes (<1mm/yr; Rousseau et al., 1996).

Current conceptual models for the hydrologic system at Yucca Mountain recognize that fractures and through-going faults may be conduits for episodic, rapid, gravity-driven flow of water into and through the unsaturated zone. Montazer and Wilson (1984) stated that: "...nonuniform infiltration periodically produces moderately intense fluxes..." and "...pulses of infiltration may cause rapid percolation down through the Tiva Canyon welded unit and into the Paintbrush nonwelded unit." (Montazer and Wilson, 1984, p. 51). Evidence obtained from several studies at Yucca Mountain has established that water entering fractures in exposures of the highly fractured TCw unit at land surface following infrequent, intense storms is a major, if not the principal means, by which infiltration moves into the deep unsaturated zone. The largely unfractured and nonwelded PTn unit is considered likely to impede the downward flow of water that may be transmitted through the overlying TCw unit. Water entering the PTn unit is believed to be dispersed by imbibition into and diffusion through the rock matrix, and also may be diverted laterally along the eastward dipping beds of the unit. In this circumstance, the PTn unit may be a barrier to downward water flow that would restrict the movement of water into the underlying TSw unit. The absence of visible water inflow to the ESF from the enclosing rock mass and the results of apparent age determinations on fracture and cavity infilling materials in the TSw unit along the ESF main drift provide new evidence that the average downward water flux from the overlying PTn unit into and through the TSw unit is very low, as would be expected if the PTn is a flow barrier. Observations of localized occurrences of bomb-pulse ^{36}Cl in the ESF, however, imply that if the PTn is a barrier, it is not a uniformly continuous barrier to downward flow but is breached locally by pathways capable of rapid flow through the unit and into the underlying TSw unit.

For the present study, three conceptual models were examined that could account for rapid flow pathways through the PTn. Hypotheses examined included:

- A. **Matrix:** High saturations at the TCw/PTn contact create locally high hydraulic gradients, resulting in fast transport of ^{36}Cl through the matrix of the PTn. Once through the PTn, flow enters fractures in the TSw and migrates rapidly to depth (see Figure 10.2.1a);
- B. **Fracture:** Steady-state infiltration rates and rock properties are conducive to transport of bomb-pulse ^{36}Cl along continuous, high permeability fracture pathways (see Figure 10.2.1b);
- C. **Fault:** Transport of ^{36}Cl occurs as a result of rapidly transient pulses of infiltration along through-going structural pathways (see Figure 10.2.1c).

Preliminary Conceptual Model of Flow Pathways based on ^{36}Cl and Other Environmental Isotopes

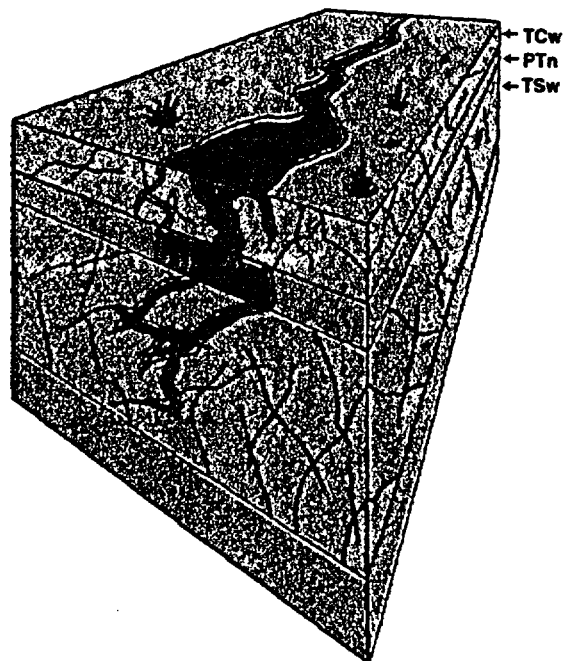


Figure 10.2.1a

Hypothesis "A". This figure illustrates the conceptual model of fast pathway flow in which locally high saturations (shown in this figure as resulting from surface runoff) raise the unsaturated conductivity of the PTn unit to near its saturated value, resulting in fast transport of ^{36}Cl through the matrix of the PTn. Once through the PTn, flow enters fractures in the TSw and migrates rapidly to depth.

Preliminary Conceptual Model of Flow Pathways based on ^{36}Cl and Other Environmental Isotopes

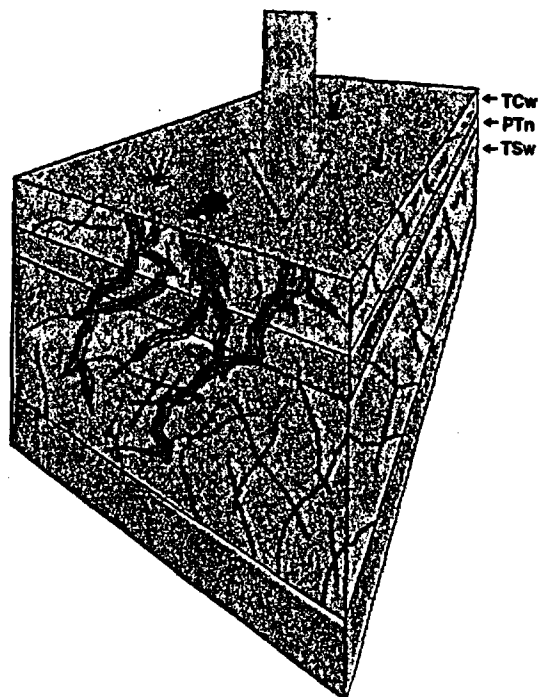


Figure 10.2.1b: Hypothesis "B". This conceptual model of fast pathway flow proposes that ambient (steady state) infiltration finds conditions conducive to flow through high permeability fracture networks in the PTn.

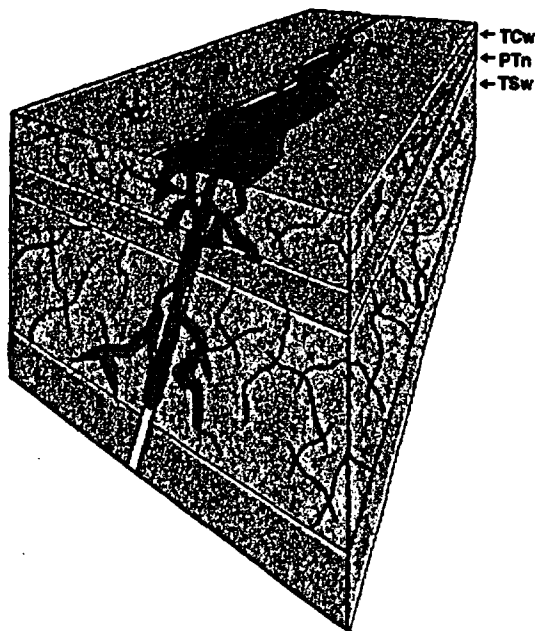


Figure 10.2.1c: Hypothesis "C". This illustration presents the hypothesis that transport of ^{36}Cl occurs as result of rapidly transient pulses of infiltration along existing structural pathways of high conductivity, such as faults, which transect the PTn at discreet locations.

Preliminary Conceptual Model of Flow Pathways based on ^{36}Cl and Other Environmental Isotopes

A simple order of magnitude analysis was used to examine the reasonableness of hypothesis "A". If the average drained porosity is taken to be 0.15, the average vertical permeability of the PTn is probably on the order of $2\text{E-}13\text{m}^2$ (Ahlers, et al, 1996). Assuming a saturated thickness of 50 m for the PTn, a unit gradient, and evaluating the properties of water at 27°C , Darcy's law yields a travel time through the PTn of 40 days. Although this travel time is well within the range expected for fast pathway flow, this estimate is valid for *saturated* conditions. Deviation from saturation will cause a reduction in effective permeability, with a commensurate increase in travel times. For example, using the van Genuchten (1980) equation to relate saturation and relative permeability (with $m=0.163$, and a saturation of 0.5 for the PTn) yields a travel time of about 27,000 years. Clearly, for this conceptual model to remain valid, saturations must locally remain near 1.0 in the area of a fast pathway. Such high saturations of the PTn have not been observed to date in surface based boreholes or in the ESF. Furthermore, in order to maintain locally saturated conditions in the PTn, fluxes must be on the order of meters per year, and must persist for the duration of transit time (1 to 50 years). Since matrix saturation and water potential data from boreholes are consistent with low fluxes ($<1\text{mm/yr}$; Rousseau et al., 1996) and support the conclusions of long travel times through the matrix of the PTn, this model was dismissed.

In hypothesis "B" the PTn is continuously fractured for its entire thickness, and flow through the PTn is controlled by the permeability of the fracture(s) and the equilibrium established between the fractures and the matrix. This conceptual model was tested by Fabryka-Martin et al. (1996) for modeling fast pathway transport of ^{36}Cl . Many of the objections of hypothesis "A" are removed by hypothesis "B". Under saturated conditions (the lower bound on travel time) a fracture network with an effective permeability of 10^{-12}m^2 (effective hydraulic aperture = 0.004 mm) will conduct water through the PTn unit in a matter of minutes (subject to assumptions stated in the preceding paragraph). As in the analysis presented for hypothesis "A", travel times through the PTn under unsaturated conditions are much longer than for saturated conditions; however, even for very low saturations travel times through the PTn for the hypothetical 10^{-12}m^2 fracture remain within the 50-year time-frame for the transport of bomb-pulse ^{36}Cl . Our simulations qualitatively corroborated those conducted by Fabryka-Martin et al. (1996) which concluded that ^{36}Cl generated during above-ground nuclear testing could arrive at the proposed repository horizon in 50 years under hypothesis "B".

Hypothesis "B" offers a plausible theory for the transport of ^{36}Cl to the level of the ESF. Unfortunately, evaluation of the results of this conceptual model are not completely consistent with field evidence. Observations of lateral "spreading" of ^{36}Cl in the host rock appear to be indicative of rapidly transient infiltration (Chapter 4, this volume). Although spreading would be expected of both steady-state and transient infiltration, lateral movement away from the fast pathway would presumably be dominated by diffusion for steady-state fluxes,

leading to lateral travel times in excess of those indicated by environmental isotopes. In addition, relatively low (as compared to a large, rapidly transient flux, as is proposed in hypothesis "C"), steady state fluxes assumed are more consistent with a "well-mixed flow" model of ^{36}Cl transport; however, modeling of tritium concentrations in UE25 UZ-16 by the United States Geologic Survey appears to support a piston-flow model of transport. Yang, et al., (1996) caution that no hydrologic system exhibits pure mixing- or piston-behavior, but nevertheless found their observations to be consistent with a piston-flow model.

In spite of this difficulty, hypothesis "B" cannot be entirely discounted. It remains a useful conceptual model for studying the effects of geologic and hydrologic parameters on the transport of ^{36}Cl , and for establishing bounds on flux and travel times. In order to investigate a conceptual model more consistent with field evidence, however, hypothesis "C" was chosen as the preferred conceptual model for this study.

Montazer and Wilson (1984) generally perceived transient fracture flow as ending at or in the PTn hydrogeologic unit, resulting in saturation build-up and lateral flow along the TCw/PTn contact. Early investigations of the effects of transient pulses on flux travel times at Yucca Mountain by Wang and Narasimhan (1986) found that small pulses were generally attenuated in the TCw, while larger pulses penetrated progressively deeper into the PTn. For the largest pulse case (12,500mm/yr for 0.2 years), the investigators found that the moisture front penetrated the upper part of the TSw unit in about 1,000 years after the application of the pulse. In this case the PTn unit was treated as a composite medium with no implicit fracturing (fracture and matrix properties of the welded units were treated as a multiple interacting continuum). However, Buscheck and others (1991) and Nitao and others (1992) demonstrated through simulations that under certain conditions episodic fracture flow could transit the PTn with much shorter travel times. These investigators used a discrete fracture model and ponded conditions at the entrance to fractures of varying aperture (from 0.01 to 1.0 mm) to demonstrate the possibility of fast pathway flow at Yucca Mountain. The predicted travel times were strongly dependent on the assumed aperture of the fracture. For the assumed hydrologic properties, the 1.0 mm fracture was found to transmit infiltration to the level of the ESF in times on the order of 14 days, while flow through smaller fractures generally became matrix-dominated in the PTn. Other investigators working in the area of non-equilibrium fracture flow have obtained qualitatively similar results (see Zimmerman and Bodvarsson, 1995, 1996). Although the cited studies represent extreme conditions (i.e., ponded conditions at the fracture entrance), they provide modeling evidence that rapidly transient flow to the level of the ESF in less than 50 years is possible.

Field evidence also supports the feasibility of transient pulses reaching the level of the ESF. As mentioned in section 10.1, perched water encountered in USW UZ-14 was found to be contaminated with drilling polymer. In this case, a

pulse of infiltration generated by drilling operations at USW G-1 migrated several hundred meters laterally and vertically, within a few years. Although the infiltrating pulse was large (about 8,700,000 liters; Burger and Scofield, 1995), it demonstrates the possibility of transmitting episodic pulses through the unsaturated zone.

Due to the rapidly transient nature of the flow field inherent in hypothesis "C", analysis of this conceptual model is not amenable to simple analytical arguments such as were used for hypothesis "A". In addition, the difficulties in demonstrating the validity of one hypothesis over another are great. Rather than attempting a rigorous fast pathway model at a specific location at Yucca Mountain, we have chosen to use a very simple schematic model to examine the plausibility of hypothesis "C". This model is only the first step in incorporating environmental isotopes into a realistic model representative of actual site conditions. The details of these simulations are the subject of the following section.

10.3 Numerical Hypothesis Testing

10.3.1 Approach

The plausibility of the preferred conceptual model was tested numerically using the modular integrated-finite difference code TOUGH2 (Pruess, 1987, 1991). The grid for the schematic fast pathways model consisted of a two-dimensional mesh of 15×62 (930) blocks, thirty of which were boundary elements, fifteen representing the water table, and fifteen representing the land surface, not including the effects of alluvium or topography (see figure 10.3.1.1; both boundaries were considered to be at constant temperature, pressure, and saturation. Properties were assigned to the grid-blocks based on the most recent material property inversions from the unsaturated zone site-scale model (see chapter 3 of this volume) and were designed to be representative of the Yucca Mountain site. The properties assigned included both fracture and matrix properties (dual continuum) for the Tiva Canyon, Topapah Spring, and Calico Hills hydrogeologic units. Properties assigned to the Paintbrush non-welded units consisted of matrix properties only (single continuum), reflecting the predominantly unfractured character of the PTn as observed in the ESF. The cross-cutting fault was also modeled as a single continuum. The grid was locally refined near the fault to allow accurate computation of saturations and capillary pressures in rapidly transient simulations.

Preliminary Conceptual Model of Flow Pathways based on ^{36}Cl and Other Environmental Isotopes

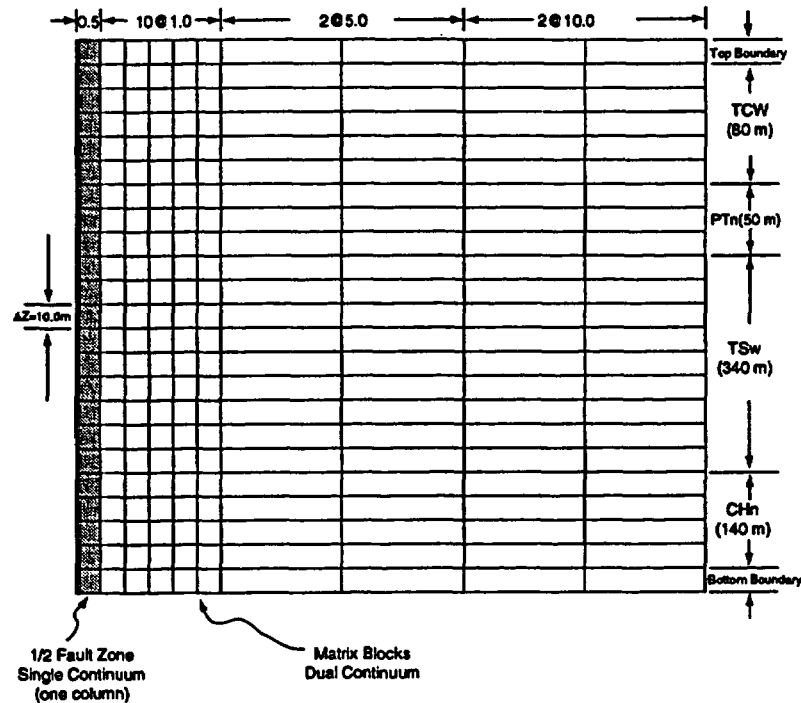


Figure 10.3.1.1

Representation of grid for schematic fast pathways model. The fault zone is modeled as a rubbleized zone of high permeability occupying a single column of blocks (shaded area). All other blocks are combination matrix/fracture blocks represented by the equivalent continuum method (chapter 3, this volume). The bottom boundary is placed at the water table; the top boundary is at the land surface, exclusive of topography and alluvium (both boundaries are constant saturation, temperature, and pressure). The right-hand boundary is a no-flow boundary condition, while the left side of the grid is a symmetry boundary through the center of the fault zone (one-half of the fault zone is modeled explicitly). All dimensions are in meters. Drawing not to scale; some gridblocks are omitted for clarity.

To represent a fast pathway as proposed in the preferred conceptual model, the hydrogeologic units were transected by a fault, whose properties were systematically varied. As mentioned in section 10.2, some information about fault permeabilities has recently become available as a result of pneumatic monitoring by the United States Geological Survey (Rousseau, et al., 1996), and analysis of pneumatic data by Lawrence Berkeley National Laboratory (Ahlers, et al., 1996); however, most fault properties have remained poorly constrained. In light of this uncertainty, the properties assigned to the fault blocks in the present model represent "generic" fault properties rather than those associated with a specific fault. The fault was intended to represent a narrow rubbleized zone of high permeability; effective single fracture apertures were calculated using the cubic law for ease of comparison. van Genuchten (1980) alpha parameters were approximated from capillary theory using the method of Wang and Narasimhan (1985) (see Figure 10.3.1.2), while porosities were calculated by dividing the effective fracture aperture by the grid block width. Properties for

the fault were assumed to be independent of depth, with the exception of horizontal permeabilities. Horizontal permeabilities in the fault were set equal to the fracture permeability of adjacent grid blocks, to simulate mass flux out of the fault at a rate proportional to the bulk permeability of the surrounding geologic material.

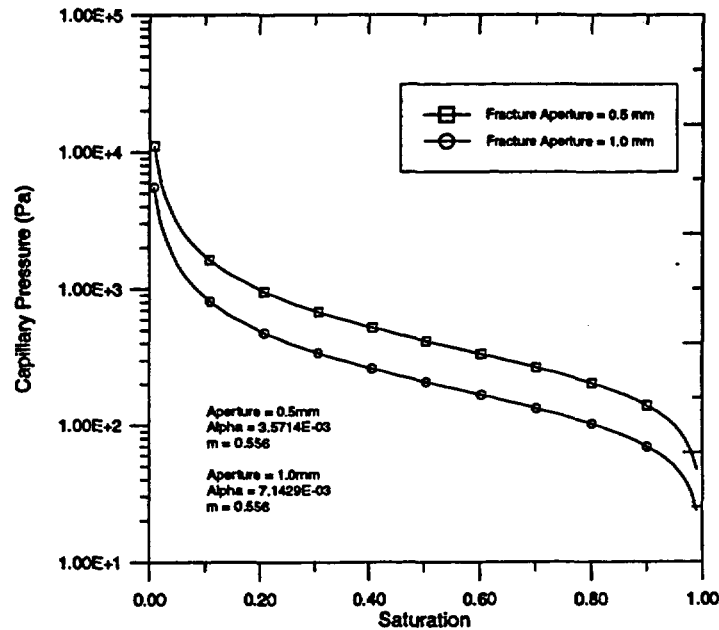


Figure 10.3.1.2
Characteristic curves for two simulated fault zones. Fault apertures shown are effective hydraulic apertures as calculated from the cubic law for comparison purposes.

10.3.2 Methods and Results

The primary modeling objective of the first part of the study was to demonstrate the plausibility of the hypothesis that transport of ^{36}Cl through the PTn occurs as a result of rapidly transient pulses of infiltration along existing structural pathways. A secondary objective was to expand on investigations initiated by Fabryka-Martin, et al. (1996) as to what parameters might influence the transportation of ^{36}Cl to depth. To this end, simulations were conducted using two values of infiltration flux (0.1 mm/yr and 1.0 mm/yr) and two values of fracture permeability (effective hydraulic apertures of 0.5 mm and 1.0 mm), as well as several different sizes of transient infiltration pulses. These parameters and their associated values were chosen after a review of other modeling studies conducted in the area of fast pathway analysis, most notably those by Wang and Narasimhan (1986), Buscheck, et al. (1991), Nitao et al. (1992), and Fabryka-Martin et al. (1996). To evaluate the effect of different geologic conditions, PTn thicknesses of 20, 50 and 100 m were modeled. The 20 and 50 m thicknesses of PTn were chosen to approximately bracket measured thicknesses as reported by

Moyer et al. (1995), while the 100 m thickness established an extreme case for comparison purposes.

A standard methodology was followed for each case modeled: a grid with appropriate material property assignments was run to steady state under the assumed ambient infiltration. After the model was equilibrated, an infiltration pulse was applied to the fault element blocks for a period of one week (during this time, the non-fault blocks continued to receive infiltration at the ambient rate). The size of the pulses varied from a 2600 mm/yr to 26000 mm/yr (5 to 50 cm/wk), consistent in rate, but of shorter duration than pulses used by Wang and Narasimhan (1996), and smaller than those that would be expected from a ponded infiltration boundary condition (see section 10.4 for a discussion of the pulse sizes selected). This was followed by a recovery period of 50 years. A low concentration of a non-reactive tracer was added to all infiltration from the initiation of the pulse to the end of the recovery period, at which time the concentrations of tracer in the column were examined to determine the depth of penetration and spread of the infiltration pulse. The transport calculations were made using a radionuclide transport module written for the TOUGH2 code (Wu, et al., in press). The transport module is capable of simulating transport with dispersion (transverse and longitudinal), diffusion, decay, and adsorption; however, for the purposes of this study dispersion was neglected. Due to the short time of the simulations (50 years) as compared to the half-life of ^{36}Cl (308,000 years), radioactive decay was assumed to be negligible, as was retardation (^{36}Cl was assumed to act as a perfect tracer). The diffusion coefficient of ^{36}Cl in water was approximated as $1.0\text{E}-10\text{m}^2/\text{s}$. Although numerical dispersion is known to be a concern with transport modeling using finite difference schemes, it was felt that for an order of magnitude study, given the parameter uncertainties inherent in the geologic materials, this would be a second order effect that could be neglected.

Saturation and capillary pressure curves for the steady-state profiles responded appropriately to variations in infiltration rate and fault permeability. Greater fault permeability and lower infiltration rates dry the column slightly and cause a modest increase in capillary suction (capillary pressures become more negative), while lower fault permeability and higher infiltration rates have the opposite effect. The steady-state saturations and capillary pressure curves maintain an acceptable approximation of site conditions for all cases used in this study.

Figure 10.3.2.1 shows the effect of varying pulse size on tracer concentrations in the simulated fault. Concentrations represented in this plot (as in all plots, unless otherwise noted) are for a time 50 years after the beginning of pulse application. For the three cases shown, nominal infiltration rate, effective fault aperture, and PTn thickness were all held constant at 0.1 mm/yr, 1.0 mm, and 50 m, respectively.

Preliminary Conceptual Model of Flow Pathways based on ³⁶Cl and Other Environmental Isotopes

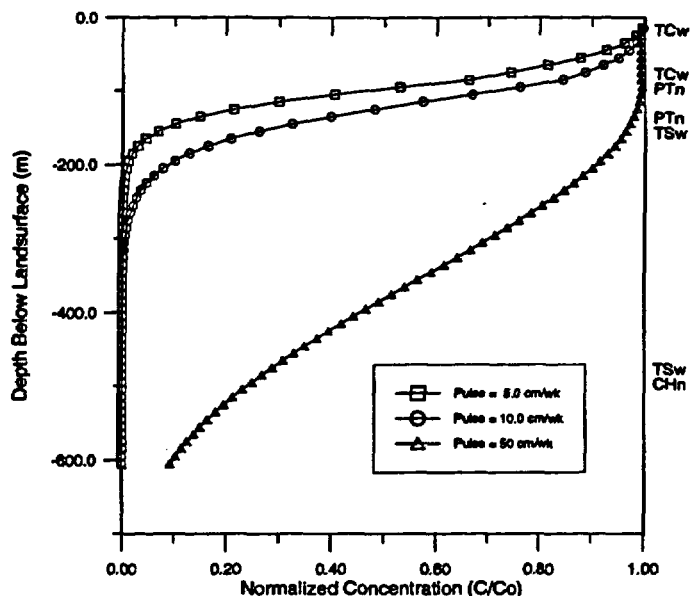


Figure 10.3.2.1

Normalized concentrations of tracer as a function of depth below landsurface. The three pulses shown span one order of magnitude in size, ranging from 5.0cm/wk to 50cm/wk. The infiltration pulses were applied at the specified rate for one week, after which time the model was allowed to recover at ambient infiltration. The values of concentration shown are taken from a simulated high permeability pathway, fifty years after the initiation of the pulse.

As expected, concentration of arriving tracer at all depths is directly proportional to pulse size. For the two smaller pulses (5 cm/wk and 10 cm/wk), normalized concentrations at the level of the ESF are on the order of 1% (0.01 of input concentration). For the largest pulse, 50 cm/wk, concentrations at the ESF are greater than 60% of input concentration. Furthermore, it can be seen from the figure that, for the 50 cm/wk pulse, concentrations arriving at the water table (610m below land surface) are on the order of 10%, indicating travel times of less than 50 years from the land surface to the saturated zone.

The effects of different fault permeabilities (Figure 10.3.2.2) and infiltration rates (Figure 10.3.2.3) are also illustrated. For the cases illustrated in Figure 10.3.2.2, infiltration (0.1 mm/yr), PTn thickness (50 m), and pulse size (10 cm/wk) were all held constant. Effective fault aperture was varied by a factor of two, from 0.5 mm to 1.0 mm, a variation that spans the critical aperture size as noted in the studies of Buscheck et al., (1991) and Nitao et al., (1992). Similarly, pulse size (10 cm/wk), fault aperture (1.0 mm), and PTn thickness (50 m) were held constant for the cases shown in Figure 10.3.2.3, while the nominal infiltration rate was varied by an order of magnitude (0.1 mm/yr vs. 1.0 mm/yr).

Preliminary Conceptual Model of Flow Pathways based on ^{36}Cl and Other Environmental Isotopes

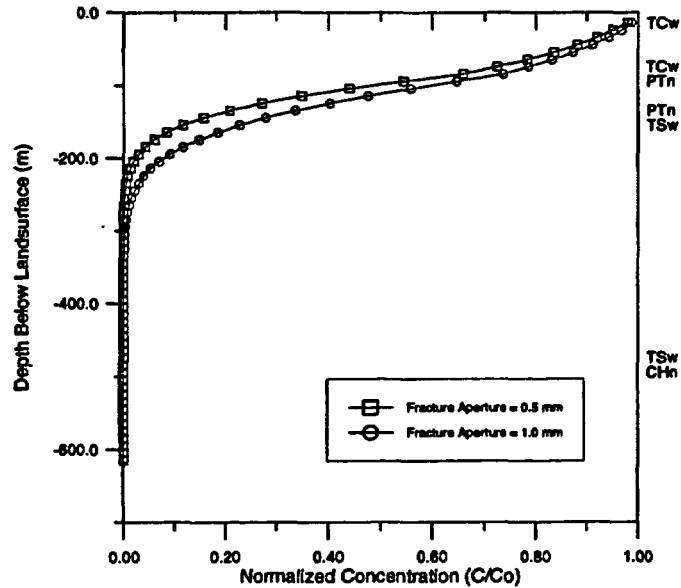


Figure 10.3.2.2
Normalized concentrations of two different effective fault apertures: 0.5mm and 1.0mm. Infiltration pulses shown are 10cm/wk.

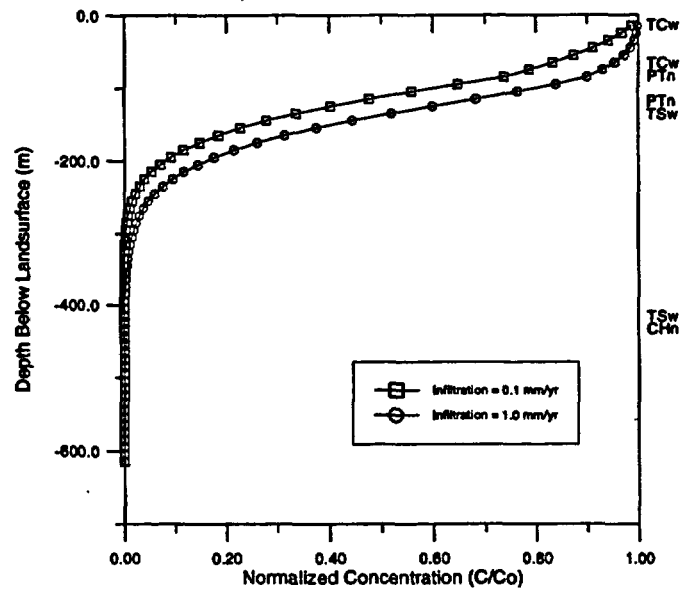


Figure 10.3.2.3
Normalized concentrations of tracer in a simulated fault zone as a function of depth below land surface. Infiltration rates shown are 0.1mm/yr and 1.0mm/yr, for a pulse size of 10cm/wk.

Preliminary Conceptual Model of Flow Pathways based on ^{36}Cl and Other Environmental Isotopes

In the cases presented in Figures 10.3.2.2 and 10.3.2.3, changes in concentrations of tracer arriving at the ESF in fifty years for the different cases were consistent with current thinking on fast pathways. An increase in the nominal infiltration rate resulted in a slightly more saturated column, decreasing capillary suction in the matrix and more rapid travel times to the level of the ESF (figure 10.3.2.3). A similar trend is apparent in Figure 10.3.2.2; as fault permeability is increased, the arrival time of the tracer is decreased. The effect of different thicknesses of PTn on tracer concentrations, however, was unexpected. Figures 10.3.2.4 and 10.3.2.5 show variations in arrival concentrations of tracer as a function of pulse size and PTn thickness. For the cases shown, infiltration and equivalent fault aperture are held constant at 0.1 mm/yr and 1.0 mm, respectively, while pulse size is varied from 5 cm/wk (figure 10.3.2.4) and 50 cm/wk (figure 10.3.2.5). For each figure, the thickness of the PTn was assigned values of 20, 50, and 100 m. As mentioned in section 10.2, the thickness of the PTn is believed to vary between approximately 20 and 50 meters; the 100 meter case was included to provide an extreme scenario for comparison purposes. Results of the sensitivity analysis, as shown in these figures, are discussed in the next section.

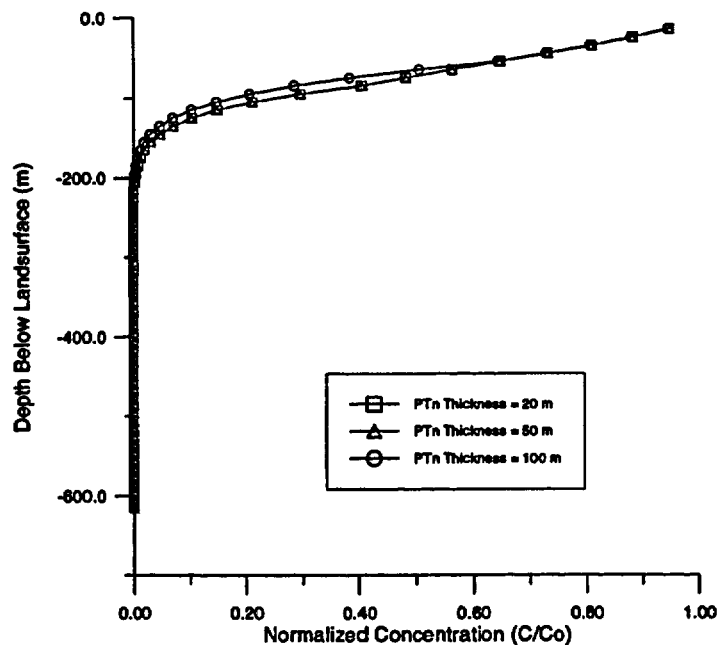


Figure 10.3.2.4

Effect of PTn thickness on arrival concentrations of tracer at depth. Three thicknesses of PTn are shown: 20m, 50m, and 100m. Pulse size is 5.0cm/wk, effective fault aperture is 1.0mm. Thicknesses of 20 to 50m are generally representative of those found at the Yucca Mountain site; the 100m case is included as an extreme condition for comparison purposes.

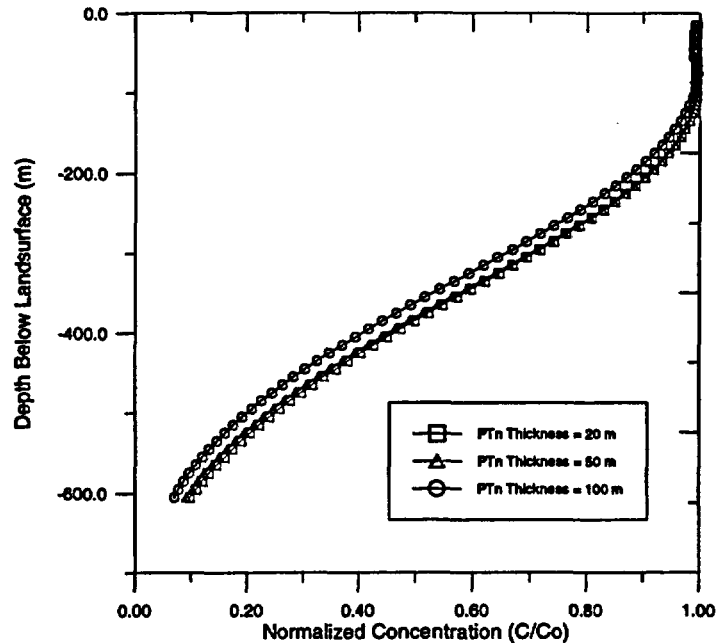


Figure 10.3.2.5

Effect of PTn thickness on arrival concentrations of tracer as a function of depth, for a pulse size of 50cm/wk, and an effective fault aperture of 1.0mm.

10.4 Discussion of Results

To a varying degree, all factors tested in the numerical simulations affected the ability of infiltration pulses to penetrate to the depth of the ESF, particularly within the fifty year time-frame for bomb-pulse ^{36}Cl . System response to variation of parameters in each case was consistent with expectations based on prior experience and literature review. The sensitivity of the system to the parameters tested, however, was somewhat unexpected.

Previous investigators of fast pathways have generally assumed ponded boundary conditions at the fracture entrance [Buscheck, et al. (1991); Zimmerman, et al. (1996)]. Although this assumption is useful, the large fluxes associated with such a condition are probably not a reasonable approximation of field conditions. Results of the present study indicate that episodic fast pathway flow can occur with fluxes of a much smaller magnitude. Of those sensitivities evaluated in this study, the single most important factor in determining the concentration of tracer arriving at the horizon of the ESF is the volume of the infiltration pulse. In light of this sensitivity to pulse volume, an important question is whether the pulses used in these simulations are of a reasonable magnitude.

Preliminary Conceptual Model of Flow Pathways based on ^{36}Cl and Other Environmental Isotopes

Although net infiltration is one of the most important parameters to be determined at Yucca Mountain, it is also one of the most difficult to measure. Estimates of net infiltration vary from slightly negative (net loss of moisture from the mountain) to about 10 mm/yr. Measurement of net infiltration is complicated by the heterogeneity of the Yucca Mountain site, among other factors. Recent estimates (Flint, et al., in review), show infiltration varying from zero to 14 mm/yr, depending locally on slope aspect, thickness of alluvial cover, extent of fracturing in the bedrock, and other factors (Figure 10.4.1). Unfortunately, a one-to-one correlation between temporally averaged estimates of infiltration and the size of rapidly transient pulses is not possible; however most, if not all, of the same considerations used by Flint, et al., (in review) to estimate net infiltration can be applied to pulse infiltration. In particular, the extent of fracturing at the tuff/alluvial contact and the thickness of overlying alluvium are important in determining the magnitude of infiltration pulse that could be generated by a storm event, or a series of storm events.

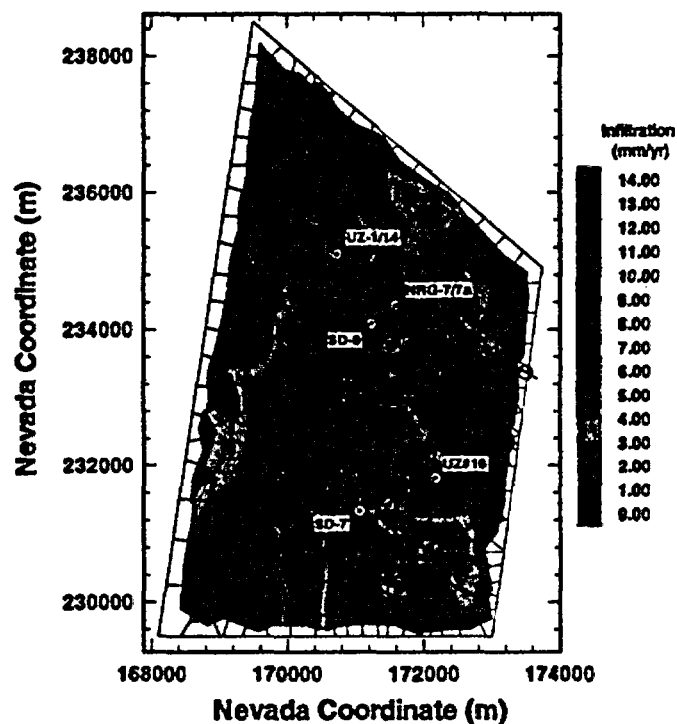


Figure 10.4.1

Map of near-surface infiltration, showing the Exploratory Studies Facility. Locations of bomb-pulse levels of ^{36}Cl are marked as open circles. SOURCE: United States Geological Survey (Flint et al., in review).

Preliminary Conceptual Model of Flow Pathways based on ^{36}Cl and Other Environmental Isotopes

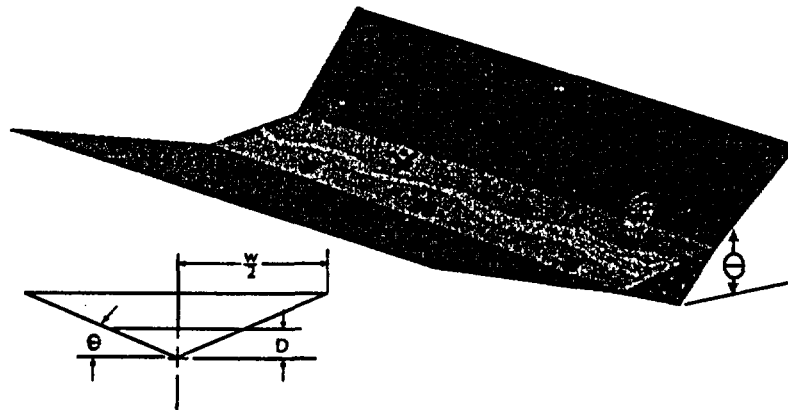


Figure 10.4.2

Width of watershed basin needed to generate an infiltration pulse. By geometry, the basin width needed to generate an infiltration pulse is:

$$w_p = (D^2\phi + V_p \tan\theta)/P\tan\phi$$

where D is the thickness of alluvial cover at the center of the wash, P is the volume of precipitation per event, per area, ϕ is the porosity of the alluvium, and θ is the angle of inclination of the sides. The analysis neglects storage along the sidewalls and losses to evapotranspiration.

A simple geometric analysis can be used to illustrate the important factors in estimating infiltration (Figure 10.4.2). The width of basin (w_s) necessary to capture sufficient precipitation from a single event (P = volume of precipitation/area) to saturate a thickness of alluvium lying in the bottom of the basin (thickness at the center of the basin = D) assuming a geometrically regular basin with sides inclined at some angle θ and porosity in the alluvium ϕ is:

$$w_s = D^2\phi/P\tan\theta \quad (10.1)$$

assuming no evapotranspiration or storage along the sidewalls. To transmit an additional pulse of infiltration, of volume V_p , through the alluvium requires a basin width $w_p > w_s$, where:

$$w_p = (D^2\phi + V_p \tan\theta)/P\tan\theta \quad (10.2)$$

Replacing the independent variables with values of $D = 0.5\text{m}$, $\phi = 0.40$, $\theta = 15^\circ$, $V_p = 0.5\text{m}^3/\text{m}$ (the maximum used in the simulations), and $P = 0.02\text{m}$ (2 cm/hr for one hour of precipitation, a reasonable value for a summer thunderstorm event) yields a basin width of 44 m. The major assumption of this analysis is that no storage of precipitation occurs along the sidewall. This is perhaps not overly conservative if the soil cover is thin, as it is on many ridges and side-slopes of the site (Flint et al., 1994), and the bedrock is fractured in conjunction with a fault zone. Some field evidence supports the supposition that zones of fracturing associated with faults at Yucca Mountain may be wide near the sur-

face and taper with depth to a single feature or narrow zone near the PTn (W. Day, presentation to Nuclear Waste Technical Review Board, 1996). If this is the case, zones of fracturing associated with faults may by-pass soil cover and act to concentrate precipitation from large storm events and channel it to preferential pathways through the PTn.

Although the simple geometric analysis above indicates that pulses equivalent to those used in this study could, in theory, be generated at Yucca Mountain, the value of w_p will change for different independent parameters. In particular, w_p is especially sensitive to the depth of alluvium D , the only variable to which w_p has a functional dependence based on the square power. This is in agreement with the findings of other investigators, who have found that the deepest penetration of precipitation generally occurs where soils are thin (ridges and sideslopes), while the shallowest infiltration is beneath thick alluvium in the bottoms of washes (Flint et al., 1994).

Patterns of ^{36}Cl deposition in near-surface boreholes also support a sensitive dependence between alluvial thickness and depth of penetration of an infiltration front. Unpublished results from ^{36}Cl analyses of cuttings from UZN-series boreholes (unsaturated zone boreholes for neutron moisture logging) indicate that areas of thick alluvial cover act to store infiltration, returning it to the atmosphere at a later time. For example, UZ-N54, which is located on an alluvial terrace with approximately 10 m of alluvium overlying bedrock, shows bomb-pulse concentrations of ^{36}Cl at depths of up to 3 m, while in UZ-N53, on a side-slope with about 15 cm of alluvial cover, bomb-pulse levels of ^{36}Cl can be found to depths greater than 60 m. Another borehole located in this same area, UZ-N55, where alluvial cover is on the order of 30 cm thick, demonstrates probable bomb-pulse ratios of ^{36}Cl to a depth of 80 m (250'), at the top of the TSw unit (see Figure 10.1.3.1.1). In the case of UZ-N55, transport through the PTn is believed to be associated with a fault zone, in agreement with the preferred conceptual model of this paper. Thus, field evidence as well as modeling results indicate that the most likely areas for development of fast pathways are in washes with thin alluvial cover which are transected by faults and prone to flooding.

Next to the size of the infiltration pulse, the numerical simulations show that fracture aperture is important in determining the depth of penetration of an infiltrating pulse of water. This is also in agreement with the results of other investigators. Buscheck et al. (1991) and Nitao et al. (1992), found the time for flow through a fracture to transit a unit (T) to be inversely proportional to the sixth power of fracture aperture ($T \sim b^{-6}$), assuming the validity of the cubic law (which the investigators note may not be applicable in all circumstances, but is illustrative).

While our study does show the PTn to have a role in attenuating infiltration pulses, the model is much less sensitive to PTn thickness than to the size of the

infiltrating pulse or the effective fault aperture. Figures 10.3.2.4 and 10.3.2.5 illustrate this point. In these figures it can be seen that, for the two sizes of infiltration pulses shown in the graphs, tracer concentration arrivals at depth are only weakly dependent on the thickness of the PTn. The same is true for ambient infiltration flux rate. It was originally hypothesized that greater infiltration flux would result in higher matrix saturations, which would in turn weaken capillary suction in the matrix and lead to more rapid transmission of pulses and higher concentrations of tracer at depth. Although these conditions are present (see figure 10.3.2.3), their effects are much less pronounced than expected. These results arise from the characteristic curves used for the fault properties. As discussed in section 10.3.1, fault characteristic properties were calculated from capillary theory, idealizing the rubbleized fault zone as a single fracture of equivalent effective hydraulic properties. One of the difficulties with this approach is the inability to make direct inferences from modeling results to field observations. As has been discussed several times in this report, the characteristic curves and other properties (e.g., porosity) necessary for accurate modeling of flow in the fault zones at Yucca Mountain are presently unknown. The current study demonstrates only that the transport of ^{36}Cl as a result of transient pulse infiltration is *plausible*, given reasonable assumptions. Before accurate, site specific modeling of fast pathways can be undertaken these important properties must be better constrained.

10.5 Locations of Fast Pathways

Our results indicate that in order for flow to occur along fast pathways, the following necessary conditions must be met:

- 1) A continuous, high-permeability pathway to depth, and
- 2) A means of focusing infiltration flux to the pathway.

The first condition implies an association between tectonic features and fast pathways. Faults cross-cut existing strata (as opposed to syngenetic fractures, such as cooling joint, which are generally strata-bound), and therefore represent features which could provide a "continuous, high-permeability pathway to depth". In fact, a strong correlation appears between elevated levels of ^{36}Cl and the presence of faulting. Of the five feature-based areas in the ESF which returned bomb-pulse ^{36}Cl ratios (some consisting of multiple samples), three are directly associated with mapped faults (four samples near the ESF station 2+00 were associated with the Bow Ridge fault, four samples between stations 18+90 to 19+50 were associated with the Drill Hole Wash fault, and six samples were near the Sundance fault, between stations 34+00 and 36+00), while the remaining two areas are close enough to known faults that a correlation is probable (a sample from station 12+44 is near the western edge of the imbricate fault zone, and a sample from station 26+79 is close to the surface expression of an

unnamed fault). Conversely, none of the systematic samples demonstrated bomb-pulse ^{36}Cl . The *existence* of a continuous-to-depth feature is not sufficient to provide a fast pathway, however. In addition to being continuous, the potential fast pathway must also have a *high permeability*. Historically, little data on the hydrologic properties of Yucca Mountain faults have been available, but recent analyses have provided some information on these critical parameters.

Utilizing data on barometrically-forced pressure fluctuations from instrumented boreholes at Yucca Mountain, Ahlers, et al. (1996) were able to infer properties for several faults in the vicinity of the ESF. By making reasonable assumptions, they calculated gas relative permeabilities in faulted sections of the TSw on the order of $1 - 20 \times 10^{-12} \text{ m}^2$, and through the PTn on the order of $0.2 \times 10^{-12} \text{ m}^2$. Although these values are somewhat small for non-equilibrium fracture flow (a $20 \times 10^{-12} \text{ m}^2$ fracture would have an effective hydraulic aperture of 0.02 mm), they represent areal averages of permeability over hundreds of meters. In addition, because the permeabilities inferred are *gas* permeabilities, it is possible that locally high saturations in the faults could mask liquid permeabilities which are higher than those measured for gases. Given the heterogeneous nature of Yucca Mountain, the existence of areas of permeability sufficient to sustain episodic fracture flow within faults is a reasonable assumption.

The second necessary condition may be satisfied in channels of washes that transect the site. As discussed in section 10.4, Flint et al. (1994) found that the depth of penetration of an infiltration front was inversely proportional to the thickness of the alluvial cover. They found that: "...when surface flow is negligible, the deepest infiltration was found in the ridgetops, and the shallowest infiltration was observed in the washes...". Following significant runoff events, however, they noted: "...large volumes of water often infiltrated more than 5 meters into the soil in the washes..." (Flint et al., 1994). These observations suggest that the most likely point of origin for infiltration pulses is the bottoms of washes that are subject to flash flooding and have alluvial cover thickness of (much) less than 5 m. As discussed in the preceding section, the basin size necessary to generate a pulse of infiltration is directly proportional to the square of the thickness of alluvial cover (among other factors). Thick alluvium tends to store potential infiltration and return it to the atmosphere by evapotranspiration. An absence of alluvium would seem to be ideal for generating an infiltration pulse; however, without the ability to store some water at the surface, the duration of the event may be too short to generate the necessary pulse of infiltration. A thin alluvial cover will moderate the infiltration pulse, but also act to sustain flux into the high-permeability pathway. The presence of fault splays, which may act to concentrate runoff and funnel it to a through-going structural feature, will also increase the likelihood of fast pathway formation.

From this discussion we can select candidate areas for fast pathways. A candidate area will be in an active wash with thin alluvial cover, preferably

Preliminary Conceptual Model of Flow Pathways based on ^{36}Cl and Other Environmental Isotopes

with a large basin area to collect runoff. In addition, the candidate area will be in close proximity to a high permeability fault zone. With the exception of bomb-pulse ^{36}Cl associated with the Bow Ridge fault (four samples near ESF station 2+00), all known detections of bomb-pulse ^{36}Cl are located near active washes (see Figure 10.5.1). Bomb-pulse ^{36}Cl detections associated with the Bow Ridge fault are not believed to be representative because their occurrence in the ESF is above the PTn hydrostratigraphic unit. The Drillhole Wash fault ^{36}Cl detections (ESF stations 18+90 to 19+50) are located proximal to thicker areas of alluvium (4-5m); however, this wash is known to flood, and is so marked on the "Flood Potential of Fortymile Wash" map (U.S. DOE, 1995). This increases the probability that at times in the recent past sufficient moisture was available to saturate the alluvium and generate an infiltration pulse in spite of the relatively thick alluvial cover in this wash. The other ^{36}Cl detections (ESF stations 12+44, 26+79, and 34+00 to 36+00, as well as recent detections at stations 43+63 and 44+20) are all located in areas of thin alluvial cover, beneath the upper regions of washes whose lower regions are known to be flood prone (U.S. DOE, 1995). The association of the known bomb-pulse ^{36}Cl occurrences with faults has already been discussed.

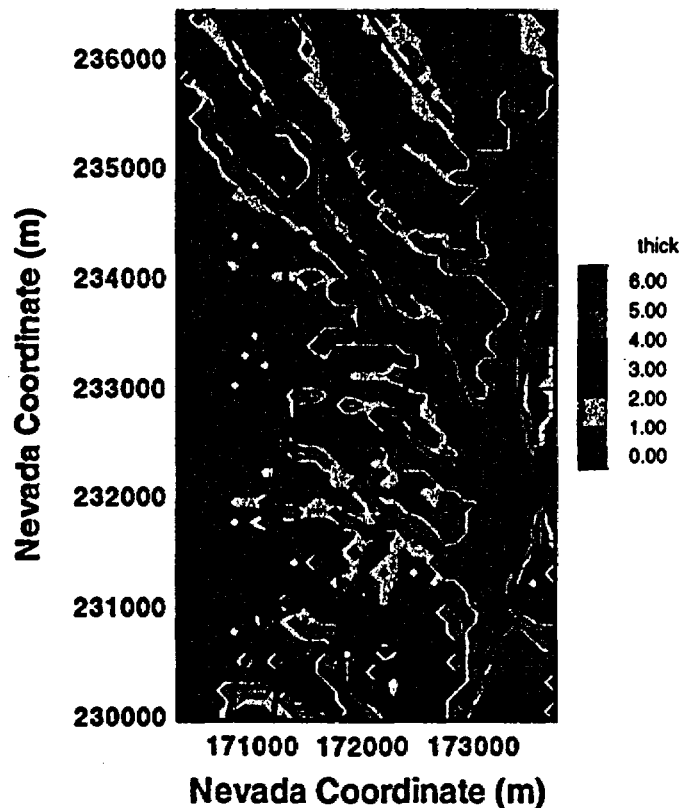


Figure 10.5.1
Map of alluvial thickness at the Yucca Mountain site, showing the Exploratory Studies Facility and major faults. Open red circles denote locations of known bomb-pulse ^{36}Cl samples; filled red circles show approximate locations of candidate areas for bomb-pulse ^{36}Cl .

Based on these considerations, we chose four candidate areas that will be intersected by the ESF as likely zones for the detection of bomb-pulse levels of ^{36}Cl . These areas are noted on Figure 10.5.2, and are located near ESF stations 50+00, 55+00, 57+00 to 61+00, and station 68+00. The first three of these locations are beneath upper regions of washes whose lower regions are prone to flooding (U.S. DOE, 1995), in areas of thin alluvial cover (Flint et al, in review), and proximal to the surface trace of the Ghost Dance fault (Day, et al., in review). The fourth is beneath a similarly flood-prone wash, in close proximity to the Dune Wash fault (Day, et al., in review).

These "predictions" should be viewed with some caution. In particular, the numerical simulations indicate the most important properties with respect to fast pathways are those of the fault or fracture zone. Although the candidate sites were chosen by determining areas most conducive to fast pathway formation, properties of the fault zones in these candidate areas are not well constrained. Pneumatic data from UZ-7a indicates that the Ghost Dance fault is a high permeability pathway in the area of ESF station 50+00 (see chapter 6 of this volume); however, as mentioned earlier, fault permeabilities determined from pneumatic data represent averages over relatively large spatial scales. There is, therefore, no guarantee that a high permeability pathway will intersect the alignment of the ESF in the area of the candidate sites. In addition, we expect lateral spreading of flux along the trace of the fault (as appears to be the case along the main test level of the ESF) to be more significant than spreading perpendicular to the fault. Testing along the south ramp of the ESF, therefore, may be less likely to encounter bomb-pulse isotopes than testing along the main test level. These factors are effects of the innate heterogeneity of Yucca Mountain, which makes any predictions of fast pathway locations extremely difficult. It is worth mentioning that, even in the saturated zone, the prediction of tracer tests in fractured, heterogeneous geologic media is very difficult. These difficulties are amplified by orders of magnitude in the unsaturated zone. Nevertheless, in our view, the candidate sites described above offer the highest probability for the detection of fast pathways, and should be considered for detailed sampling for ^{36}Cl as well as other environmental tracers.

10.6 Fluid Spreading Near Faults

The last few sections have dealt mainly with the problem of ^{36}Cl transport through the PTn unit, based on the distribution of bomb-pulse occurrences within the ESF. Additional data show a significant areal spread of bomb-pulse ^{36}Cl up to 150 m from the fault or high permeability feature. The areal spread of fluids away from faults experiencing higher infiltration fluxes and mechanisms for the spread of bomb-pulse ^{36}Cl are identified and numerically simulated in the last few sections of this chapter.

We start by assuming that at a given location bomb-pulse ^{36}Cl will rapidly migrate through the PTn, based on the analysis in the preceding section. Therefore, we developed a model that considers solely the TSw unit below the PTn, corresponding to the top boundary condition and the Calico Hills zeolitic unit serving as the bottom boundary condition. Then we introduce water with ^{36}Cl at the top boundary as a point source and simulate the spreading through the TSw so that the main fault provides the transport through the PTn as well as into the surrounding fractured rocks.

Some parameters and processes believed to be important for the spreading of ^{36}Cl are: the point source strengths and duration (pulse vs. steady-state), the fault properties and those of the surrounding rocks and the inclination of the fault. These are briefly investigated in the following sections.

**10.6.1
Conceptual Model**

**10.6.1.1
Role of Fracture and Matrix
Permeabilities**

The highly welded TSw tuff has very low matrix permeabilities and thus the bulk of any short time-scale flow must occur predominantly through the fracture network. In the middle nonlithophysal unit Topopah Spring Tuff, there are three near vertical fracture sets (N35E - 80°NW, N55W - 83°SW, and a weak set having an orientation N22E - 80°NW) and a shallow dipping set (N105W - 20°SW; see chapter 14 and references therein; Simmons et al., 1996). For this two-dimensional model we assume that the permeability field can be described by a vertical fracture set and a horizontal set with permeabilities based on those determined by pneumatic testing (Ahlers et al., 1996). These permeabilities are in general agreement with calculations using the infinite parallel plate model (cubic law) with fracture apertures from Wilson (1993) and the fracture densities observed in the ESF near the location of the submodel and North Ghost Dance Fault Alcove (Day and Beason, 1996). The fault is also described by the fracture and the matrix properties. Flow in the fractures and matrix are treated using the equivalent continuum method (ECM).

Preliminary Conceptual Model of Flow Pathways based on ³⁶Cl and Other Environmental Isotopes

Table 10.1
Fault (F-1, F-2, and F-3) and Rock (R) Permeabilities, Porosities, and van Genuchten Parameters (all data from Wu et al., 1996 and Wu, pers comm.; ϕ_m of F-1 here modified from 0.30 to 0.05).

No.	Unit	k_m (m ²)	$k_{f,h}$ (m ²)	$k_{f,v}$ (m ²)	α_m (Pa ⁻¹)	α_f (Pa ⁻¹)	m_m	m_f	ϕ_m	ϕ_f
F-1	Tsw	1.e-13	2.e-11	2.e-11	0.61e-4	1.00e-3	0.229	0.226	0.05	0.001
	CHn	1.e-13	1.e-14	1.e-14	0.61e-4	1.00e-3	0.223	0.227	0.05	0.001
F-2	Tsw	1.e-13	2.e-11	2.e-11	0.24e-5	1.08e-2	0.229	0.226	0.30	0.001
	CHn	1.e-13	1.e-14	1.e-14	0.98e-4	1.00e-3	0.223	0.227	0.30	0.001
F-3	Tsw	1.e-13	2.e-11	2.e-11	0.61e-4	1.00e-3	0.500	0.500	0.30	0.001
	CHn	1.e-13	1.e-14	1.e-14	0.61e-4	1.00e-3	0.500	0.500	0.30	0.001
R	Tsw32	1.e-20	2.e-12	1.e-11	1.56e-5	1.17e-3	0.251	0.250	0.001	0.001

κ_m = matrix permeability
 $\alpha_m, m_m, \alpha_f, m_f$ = matrix, fracture van Genuchten parameters
 $\kappa_{f,h}$ = horizontal fracture permeability
 ϕ_m, ϕ_f = matrix and fracture porosities
 $\kappa_{f,v}$ = vertical fracture permeability

Three sets of fault parameters (F-1, F-2, and F-3) developed for the UZ model were implemented for steady-state simulations (Table 10.1; see chapter 9: Wu et al., 1996). The latter authors developed fault parameters for each unit through which the fault traversed, hence in Table 10.1 parameters are given for the matrix and fracture components of the fault in each unit (here the Tsw and CHn). The rock adjacent to the fault is denoted by "R" and is represented by one subunit of the Topopah Spring Unit (Tsw32). The properties of Tsw32 were taken from 0.1 mm ITOUGH2 inversions (chapter 3: Bandurraga et al., 1996). The matrix porosity was set to a nominal 0.001, so that the effects of fracture-driven flow could be evaluated. Fracture permeabilities are based on results of pneumatic tests in the fault and surrounding rocks (Ahlers et al., 1996). The vertical fracture permeability in the rock adjacent to the fault is 20 times higher than the horizontal fracture permeability, and thus this will be a strong control on the transport out of the fault. The matrix permeability of the fault is set fairly high (10-13 m²) to account for the presence of microfractures not represented by the larger-scale fracture network. For the same reason, matrix porosities are set to the relatively high value of 0.30 in fault sets 2 and 3. The aim of this work is not to justify the values developed by Wu et al. (1996), but to investigate their effect on fluid saturations and fluxes at a smaller spatial scale than the UZ model.

10.6.1.2
Role of Fracture and Matrix van Genuchten Parameters on Spreading and Fluxes

Two seemingly disparate aspects of the behavior of fluids traversing faults are important to evaluating fluxes experienced by the repository. Measurements in the ESF have shown that the fractures in faults have low moisture contents (Y. Tsang, pers. comm.) compared to the unfractured rock from boreholes at the same depth. However, faults may also act as pathways for rapid fluid transport

after episodes of increased shallow infiltration. This section provides further sensitivity tests for the relative saturations and fluxes between faults and adjacent units at a scale an order of magnitude smaller than the UZ model.

The van Genuchten parameters chosen for the fractures and matrix control, to a large extent, the liquid distributions in the fault and in the surrounding rocks. Within the fault, the stronger capillary suction of the matrix will tend to keep fractures dry and the matrix at a higher liquid saturation. Differences between the properties of the fractures and matrix of the adjacent rocks and those of the fault will control the exchange between the fault and its surroundings. Therefore, the differences in the parameters (Table 10.1) have the effect of changing the suction between the fracture and matrix and differences in the exponent affects the rate of change of the capillary pressure with changing effective saturation. The properties of fracture surfaces (i.e., mineral coatings) may also limit the uptake of fluid by the matrix adjacent to a fracture (Thoma et al., 1992; Tokunaga and Wan, 1996), although this effect is not treated in this work.

In order to assess the degree of spreading from a fault, we set up several steady-state simulations of different infiltration rates in the fault. The assumption is that a fault may have a higher infiltration flux at the base of the PTn than at the surface, because of the strong lateral migration of water in the PTn (see Chapter 11: Sonnenthal et al., 1996; Chapter 8: Wu et al., 1996), or that surface water in drainage basins may flow rapidly down through fractures in the TCw and the PTn, as described in previous sections. We assume that this flux is constant and localized in the fault and the remainder of the TSw top receives a uniform 0.1 mm/yr infiltration flux. We do not know the flux carried by faults either at steady-state or under transient conditions, and thus we have used some of the same values used for surface infiltration pulses in previous sections. The steady-state results do not address the nonlinear effects on capillary pressures caused by pulses of high infiltration, and therefore in the last section we describe a simple two-dimensional simulation of a transient pulse of fluid carrying a ^{36}Cl tracer directed into the fault.

**10.6.2
Model Description and
Assumptions**

**10.6.2.1
Model Dimensions and
Numerical Grid**

A two-dimensional E-W vertical section of the UZ three-dimensional submodel (chapter 11: Sonnenthal et al., 1996) was used for the simulations in this study. It is 160 m wide (E-W), the approximate bounds of the Ghost Dance Fault (GDF) and the ESF and approximately 400 m thick, from the base of the PTn to the base of the second Calico Hills zeolitic unit (CH2zc). Although the dips and thicknesses were retained from the UZ submodel, the rock properties were set everywhere to that of the TSw32 unit, so that the effects of rock properties and

Preliminary Conceptual Model of Flow Pathways based on ^{36}Cl and Other Environmental Isotopes

fault inclination could be treated separately from layer differences. In contrast to the submodel which did not include fault properties at the location of the GDF, the two-dimensional model uses fault properties from the UZ model.

The two-dimensional grid has a uniform horizontal spacing of 10 m (16 grid elements) and a variable vertical spacing (12 elements plus top and bottom boundary elements). The fault is defined as a single column of 10 m wide grid elements at the eastern boundary of the domain. Although the grid is relatively coarse, the small problem size allowed a large number of simulations to be run as sensitivity studies. For better resolution of the concentration fronts a much finer mesh would be necessary. Although this would affect the position of the concentration front, this numerical dispersion is much less than the differences in spreading produced by the changes in fault and matrix parameters we tested.

10.6.2.2 Codes and Specific Routines Employed

Simulations were performed using the TOUGH2 code (Pruess, 1987; 1991). Gas pressure and saturations were solved using the EOS3 routine of TOUGH2 (Pruess, 1991).

10.6.2.3 Initial and Boundary Conditions

Steady-state simulations were performed under isothermal conditions ($T = 25\text{ }^\circ\text{C}$) with no-flux side boundaries. The lower boundary was set to practically full liquid saturation ($SL = 0.999$) and $P_{\text{gas}} = 92\text{ kPa}$. Transient flow was solved using the steady-state results as initial conditions. The initial concentration of ^{36}Cl was set to zero everywhere, and its decay constant assumed zero over the time period of interest (50 years). It was assumed that no reaction or adsorption of ^{36}Cl took place (i.e., zero retardation). Specific conditions for each simulation are described in the appropriate sections.

10.6.3 Results of Simulations

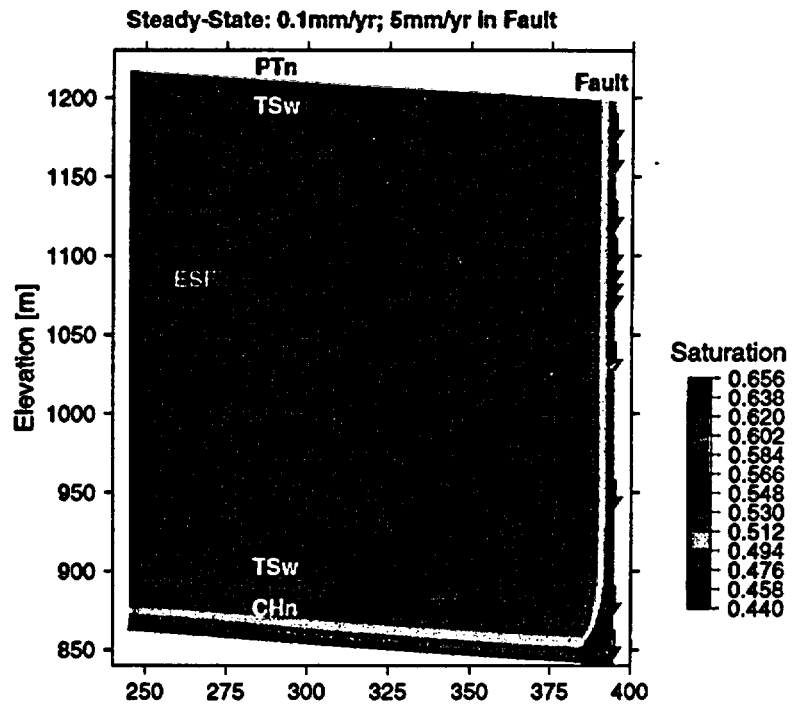
A series of simulations was performed as sensitivity tests of the effects of different fracture and matrix wetting parameters, fault orientation, and infiltration pulses on the spatial spreading of fluxes around a fault. In all cases the total liquid saturation of the rock is plotted (fracture plus matrix). Because the parameters for the rock adjacent to the fault were modified to allow the fracture properties to be emphasized, the liquid saturations are lower than the actual values at this level. However, the relationships between infiltration rates and distance of spreading and the effects of differing fault properties on the partitioning of fluid between the fault and its surroundings should be generally valid.

10.6.3.1 Effects of Fault Fracture and Matrix Wetting Parameters on Steady-State Fluxes

Steady-state liquid saturations (combined matrix and fracture) and flux vectors are shown for 5 and 10 mm/yr infiltration fluxes into the fault element (Figures 10.6.1a and 10.6.1b), using the first set of fault properties in Table 10.1. In both cases the fault has a higher liquid saturation than the surrounding rock, and the adjacent rock has a higher saturation than the rock at a distance from

Preliminary Conceptual Model of Flow Pathways based on ^{36}Cl and Other Environmental Isotopes

the fault. As expected, the spreading increases with increasing flux and with depth, where it eventually merges with the capillary fringe above the lower saturated boundary. Near the top of the TSw, there is very little spreading. Although some spreading is observed in the saturations, most of the flux is transmitted through the fault, as can be seen from the vertical and constant length flux vectors in the fault.



Preliminary Conceptual Model of Flow Pathways based on ^{36}Cl and Other Environmental Isotopes

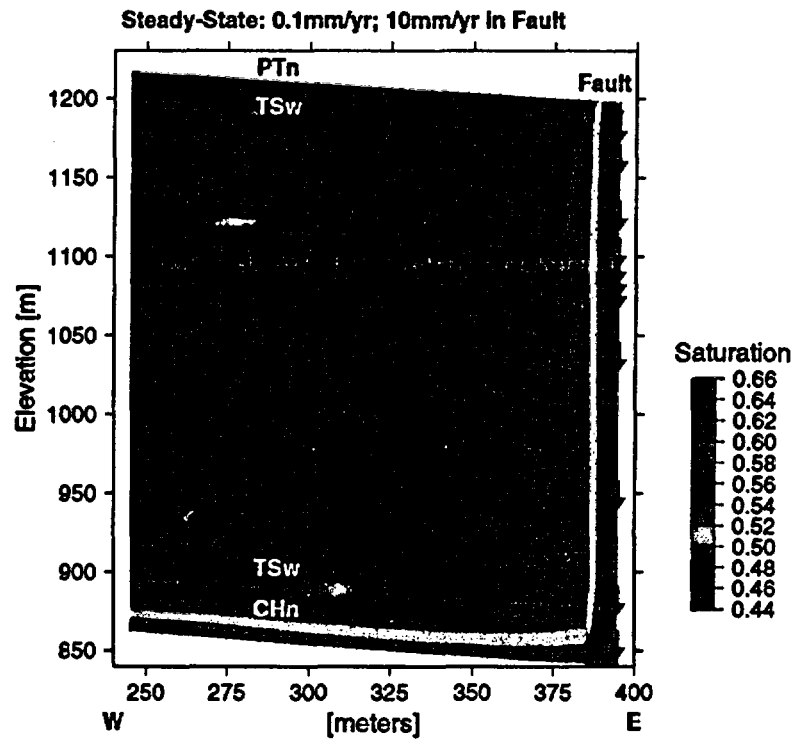


Figure 10.6.1b

Figures 10.6.1a, b

Steady-state saturations and flux vectors for a 5.0 mm/yr infiltration rate (a) and a 10 mm/yr infiltration rate (b) into the fault for fault property set 1. The adjacent rock surface is given a 0.1 mm/yr infiltration rate. High saturations near the lower boundary result from the saturated boundary condition. Here the fault has attained a higher saturation than the adjacent rock, which also is wetter than the rock away from the fault. Flux vector sizes are scaled to the maximum flux, which for the steady-steady vertical fault simulations is close to the applied infiltration rate at the fault, because much of the flow is confined to the fault.

Results from the second fault property set (Figure 10.6.2) show a fairly dry fault (saturation ~ 0.05) and the adjacent rock has a lower saturation than at a distance. In this case, the matrix in the fault plays an important role, as it effectively drains the fractures in the adjacent rock and the fractures in the fault. Hence, there is no spreading of fluid out of the fault. Fluid distributions are also virtually unchanged from the infiltration rate of 5 mm/yr to 10 mm/yr.

Preliminary Conceptual Model of Flow Pathways based on ^{36}Cl and Other Environmental Isotopes

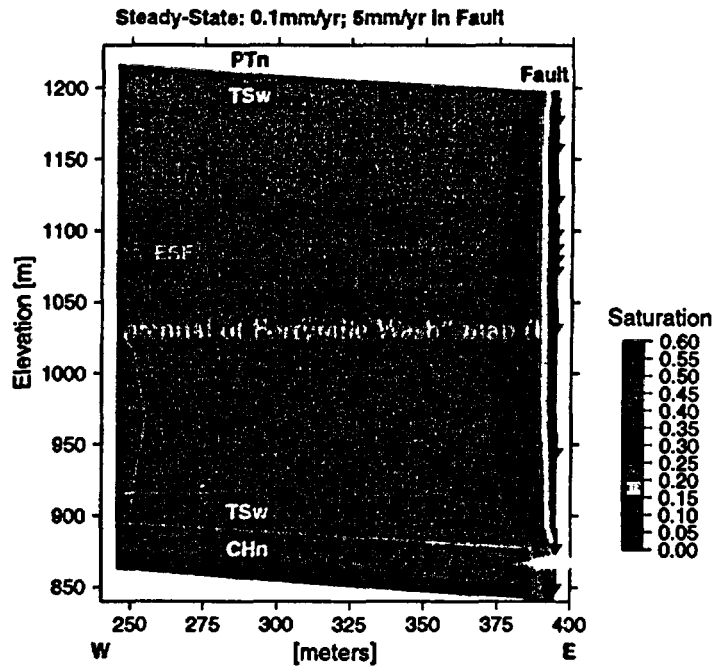


Figure 10.6.2a

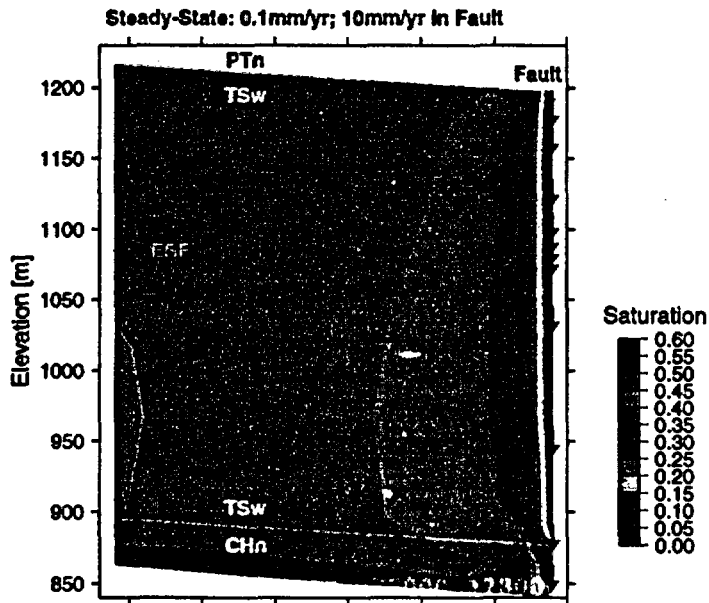


Figure 10.6.2b

Figures 10.6.2 a, b
Steady-state saturations and flux vectors for a 5.0 mm/yr infiltration rate (a) and a 10 mm/yr infiltration rate (b) into the fault for fault property set 2. The adjacent rock surface is given a 0.1 mm/yr infiltration rate.

Preliminary Conceptual Model of Flow Pathways based on ^{36}Cl and Other Environmental Isotopes

Steady-state saturations and flux vectors for the third set of fault properties are plotted in Figure 10.6.3. The fault has a very low saturation and there is also higher saturation in the adjacent rock, indicating migration of fluid out of the fault. The proportion of fluid leaving the fault is quite small, because the flux vector magnitudes do not diminish noticeably with depth. At the infiltration rate of 10 mm/yr in the fault the spreading of higher saturations is also significantly greater than that of the simulation having an infiltration rate of 5 mm/yr.

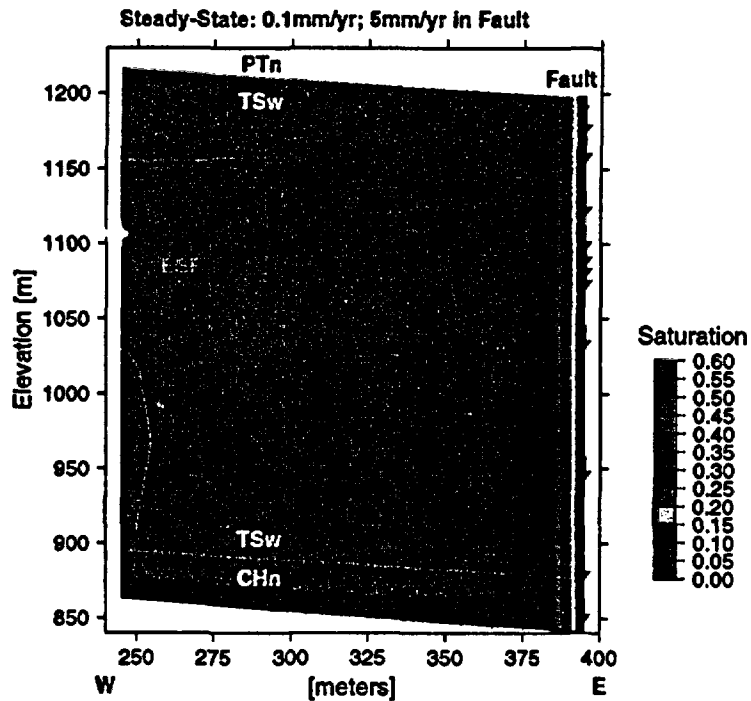


Figure 10.6.3a

Preliminary Conceptual Model of Flow Pathways based on ^{36}Cl and Other Environmental Isotopes

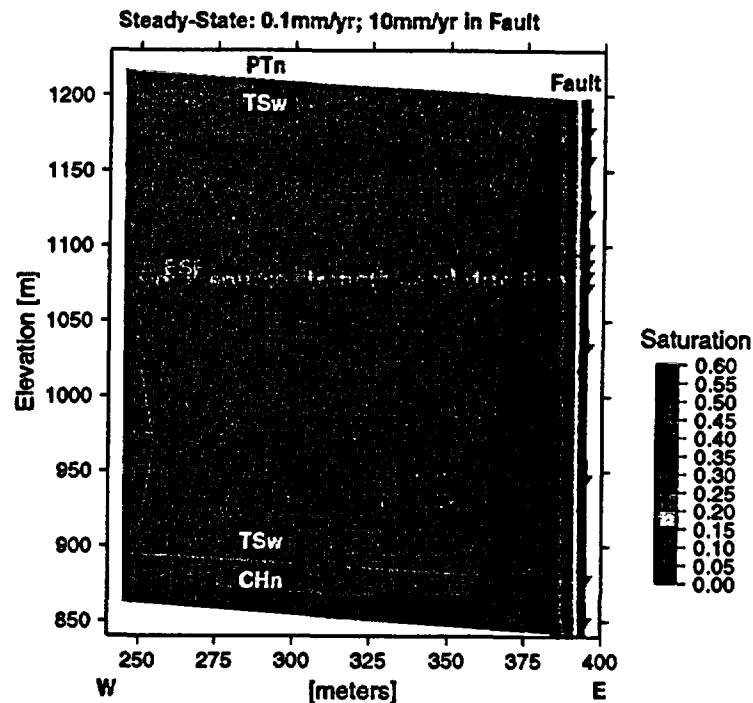


Figure 10.6.3.b

Figures 10.6.3 a, b

Steady-state saturations and flux vectors for a 5.0 mm/yr infiltration rate (a) and a 10 mm/yr infiltration rate (b) into the fault for fault property set 3. The adjacent rock surface is given a 0.1 mm/yr infiltration rate.

Saturations as a function of distance from the fault are plotted in Figure 10.6.4 at the level of the repository (~ 1085 m) for the 10 mm/yr fault infiltration runs previously shown. Although set 1 yields considerable spreading away from the fault, the saturations in the fault are higher than the surrounding rock. The third set of fault properties is consistent with observations of a dry fault zone and also findings of ^{36}Cl at depth associated with faults, although the near zero saturation in the fault is exceedingly low. Fault property set 2 has a somewhat higher saturation in the fault (~ 0.05) but the adjacent rock has lower saturations up to over 50 m away compared to the rock away from the fault. These marked differences show that the behavior of the system is a strong function of the parameters chosen, which when compared to measurements should allow for a refinement of the parameter sets. However, even though we have shown that the sensitivity to the parameter values is great, the study is not complete in the sense of showing that a given result is uniquely determined by a single set of parameters.

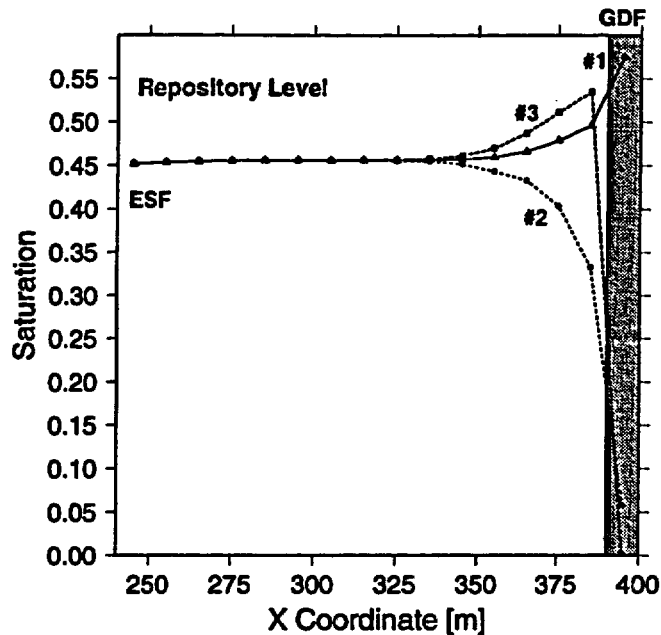


Figure 10.6.4
Steady-state saturations at the repository horizon as a function of distance from the fault for the three sets of fault parameters. The infiltration rate was 10 mm/yr into the fault and 0.1 mm/yr elsewhere.

10.6.3.2 Effects of Fault Inclination

So far the UZ model has not considered the effects of fault inclination on the fluid distribution around fault zones at depth. On a large scale (hundreds of meters to kilometers), small deviations from vertical may be less important for grid block sizes of 100 m or more. At the scale of meters to tens of meters or more the fault inclination should affect the fluid paths significantly. This is, of course, a great simplification because the fault zone will differ in thickness through its depth and also along its strike as is well documented for the Ghost Dance Fault (Rousseau et al., 1996). Changes in permeability with depth in the fault will also tend to disperse flow, in particular where units having different hydraulic conductivities and fracture and matrix properties are abutted.

An estimate of the importance of the fault inclination can be addressed simply with the model used in the previous simulations. Rotation of the gravity vector direction in the TOUGH2 input (i.e., the direction cosine) is mathematically equivalent to rotation of the spatial coordinates. In this simulation the domain was rotated so that the inclination of the fault is 80 degrees and the adjacent rock is underlying the fault. This value is the approximate inclination observed on the Ghost Dance Fault (Rousseau et al., 1996). Therefore, flow would be along the footwall faces of fractures, and thus transport out of the fault would tend to be in the underlying rock. Flow along the footwall is supported by observations of mineral coatings on fractures of the footwall faces

Preliminary Conceptual Model of Flow Pathways based on ^{36}Cl and Other Environmental Isotopes

(Paces, 1996). Because we are rotating the entire domain, the geometric relationship of the fault to the adjacent rock units is not strictly correct, in terms of the geologic model, yet it captures some of the effects that the vertical fault clearly cannot describe.

For this simulation, the third set of fault properties was chosen for two reasons. First, as was previously stated, the steady-state results are consistent with general observations of liquid saturations at Yucca Mountain. Second, in the case of the vertical fault it yields a moderate amount of spreading, so that we may expect the results obtained will be intermediate between those of the other parameter sets, which produced very different steady-state liquid distributions under the applied conditions.

Steady-state saturations and flux vectors (Figure 10.6.5) for an infiltration rate of 10 mm/yr applied to the fault show that the distance of spreading from the fault is increased by a factor of nearly 2 over the vertical fault simulation (Figure 10.6.3b). At the level of the ESF it is about 80 meters wide compared to about 50 meters away from the vertical fault (Figure 10.6.6). Saturations are also higher at the western boundary because of the no-flux condition. Another aspect of the effect of the fault inclination is that except for the upper flow vectors the predominant flow direction is still down the fault. However, inspection of the flux magnitudes (vector lengths) indicates that the flux in the fault diminishes with depth owing to a significant loss of fluid to the adjacent rock.

Preliminary Conceptual Model of Flow Pathways based on ^{36}Cl and Other Environmental Isotopes

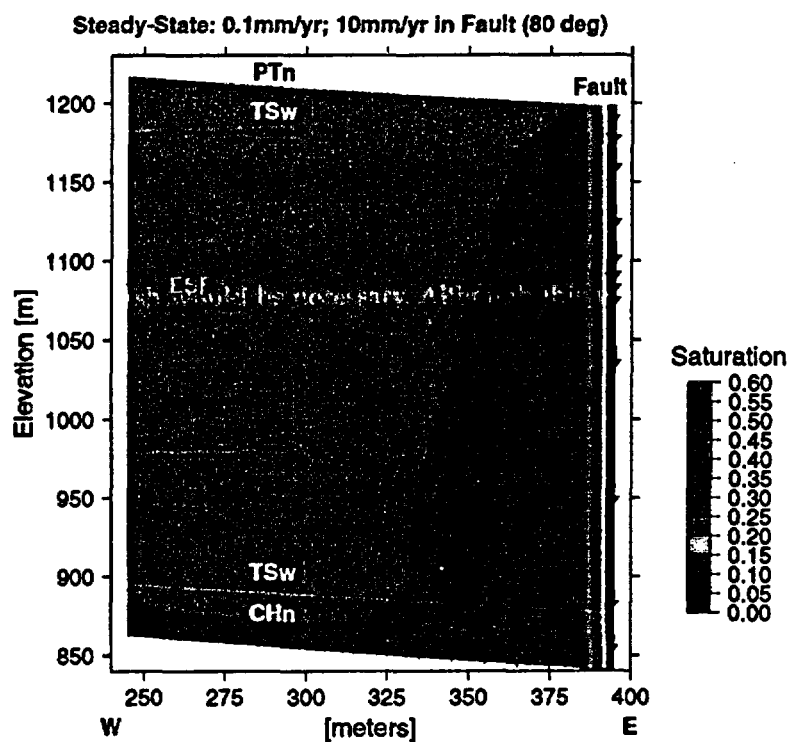


Figure 10.6.5
Steady-state saturations and flux vectors for a fault inclination of 80 degrees. The direction of the gravity vector is to the southwest. Hydraulic properties of the fault were from set 3 (Table 1). The surface infiltration rate was 0.1 mm/yr with 10 mm/yr in the fault.

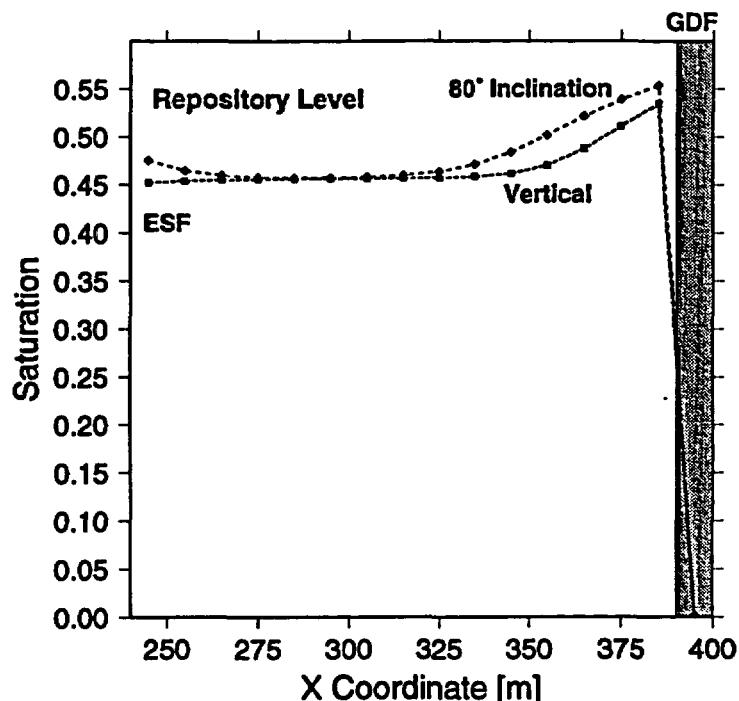


Figure 10.6.6

Steady-state saturations at the repository horizon as a function of distance from the fault for a fault inclination of 80 degrees and a vertical fault. The infiltration rate was 10 mm/yr into the fault and 0.1 mm/yr elsewhere.

Given the simple geometry of the fault, of the surrounding rock units, and the uniform rock properties, it was shown that faults will not act as merely narrow high permeability conduits or capillary barriers in the unsaturated zone. The increase in distance of spreading with increasing flux in the fault suggests that spatial measurements of moisture contents around faults may be another indicator of long term fluxes. Although the faults may be dry for extended periods of time, slow equilibration of pore fluids in the adjacent low permeability rocks would retain some of the longer time-scale average fluxes.

10.6.3.3 Transient Infiltration Pulses and ^{36}Cl Transport

The effect of a transient pulse of high infiltration through the PTn on the distribution of ^{36}Cl is considered in this section. The system is assumed to be at steady-state with a uniform infiltration rate of 0.1 mm/yr with the initial ^{36}Cl concentration equal to zero everywhere. As in the previous simulation of an inclined fault, the third set of van Genuchten parameters was used. An infiltration pulse of 10 cm was then applied over a period of one week to the fault element at the top of the TSw. A rate of 0.1 mm/yr was continued over the other surface elements. A tracer concentration (here corresponding to ^{36}Cl) of 10 ppm was added with the infiltration over the entire surface. Following this period,

Preliminary Conceptual Model of Flow Pathways based on ^{36}Cl and Other Environmental Isotopes

the infiltration was continued at 0.1 mm/yr over the entire surface, with the ^{36}Cl concentration in the infiltration water set to zero. The value of 10 ppm was chosen solely in order to provide a high enough concentration to limit the effects of numerical noise in the spatial derivatives of concentration. Because we are interested in transport for a time period (50 yrs) that is much shorter than the half-life of radioactive decay for ^{36}Cl , the decay constant was assumed to be zero. As mentioned in section 10.6.2.3 it is also assumed that there are no reactions or adsorption phenomena affecting the concentration. A typical diffusion coefficient of ions in dilute aqueous solutions ($10^{-10} \text{ m}^2\text{s}^{-1}$) and a dispersivity of 1 m (horizontal and vertical) were chosen.

Concentrations of ^{36}Cl and flux vectors are shown in Figure 10.6.7 for times of 1 week (at the end of the pulse), 1 year, 5 years and 50 years after the infiltration pulse. The high fracture permeability of the fault allowed fluid to flow rapidly downward, passing the repository horizon within months after the infiltration pulse. The initially large pulse caused some near-surface lateral spreading which was then carried down the fault and in the adjacent rock. In contrast to the steady-state results, the front of the plume narrows with depth, but is significantly wider near the top of the TSw. As in the steady-state simulations, water from the fault spread out into the surrounding rock up to over 40 meters at the level of the ESF. ^{36}Cl was also carried down through the top of the TSw by the ambient infiltration of 0.1 mm/yr, however, from this simulation it is not possible to track the position of this front, because the vertical discretization is too coarse relative to the width of the concentration anomaly and numerical dispersion has caused a spatial spread of very low concentration values. Because the horizontal discretization is on average finer and the concentration anomaly is larger because of the much greater flux in the fault, the lateral boundary of the ^{36}Cl plume is better defined than the leading edge of the concentration front. Further high-resolution models will be necessary to refine models of transport in this region.

Preliminary Conceptual Model of Flow Pathways based on ^{36}Cl and Other Environmental Isotopes

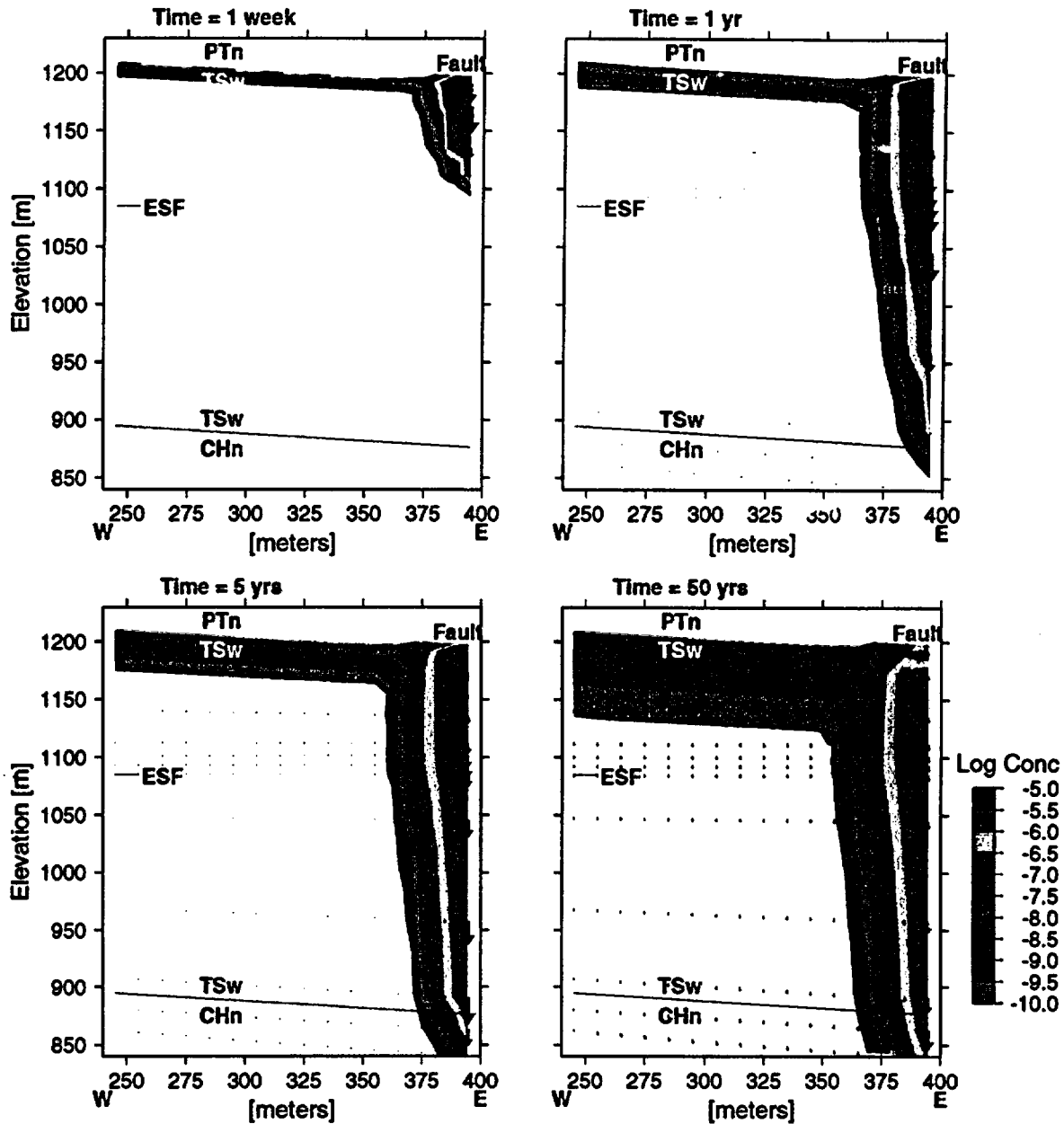


Figure 10.6.7

Concentration of ^{36}Cl after a 1 week duration infiltration pulse of 10 cm in the fault element at times of 1 week, 1 year, 5 years and 50 years. The initial condition was a steady-state infiltration flux of 0.1 mm/yr, and this flux was continued after the infiltration pulse. The adjacent rock surface received a constant infiltration of 0.1 mm/yr. The concentration of ^{36}Cl of the infiltration water in the pulse was set to 10 ppm. The flux vectors were scaled to the maximum value, so that at fifty years the pulse front had passed through the system and the flux vectors in the adjacent rock are now apparent.

10.7 Discussion

Without heterogeneous structures in the Topopah Spring Tuff or in the faults, the areal spreading of water transported by the fault is dependent on the permeability anisotropy of fracture network in the fault and surrounding rock, the fracture and matrix van Genuchten parameters, and the orientation of faults and adjacent units. For a steady-state infiltration rate of 0.1 mm/yr at the base of the PTn and rates of 5 mm/yr and 10 mm/yr in a vertical fault the relative fluxes between the fault and the surrounding rocks and their saturations were very different for the three sets of fault parameters investigated. The steady-state results using the third set of fault parameters (Table 10.1) are consistent with observations and conceptual models of fractured low-saturation fault zones with higher saturations in low permeability less fractured rocks. Assuming a vertical fault, the areal spread of fluid from the fault into the surrounding rock increases with depth and with increasing infiltration flux into the fault. A fault inclination of 80 degrees resulted in a spreading distance of nearly twice that of the vertical fault in the footwall region. The distances of spreading are about the same order of magnitude as the observed spread of bomb-pulse ^{36}Cl in the ESF. The areal distribution of fluid saturations around faults or zones of high fracture connectivity may be useful in the refinement of fault and matrix parameters, at the scale of tens of meters.

The effect of a transient infiltration pulse carrying a ^{36}Cl tracer was that the initial pulse caused a widened concentration plume which narrowed with depth. In one year the plume traveled about 250 m from the base of the PTn to the top of the CHn. Using the vertical fault assumption, the half-width of the plume (distance from the fault) was about 40 m at the level of the ESF. It is clear that transient high infiltration pulses will result in a wider area of spreading out of the fault zone than longer duration lower fluxes (yet greater long-term average fluxes).

10.8 Summary and Conclusions/Recommendations

Summary

1. Fast flow pathways exist at Yucca Mountain as indicated by the presence of bomb-pulse tritium and ^{36}Cl and, by the presence of young perched water.
2. We expect the PTn to constitute a major barrier to infiltration into the TSw, except in areas where it is breached by major through-going faults. Our preferred conceptual model, based on evaluation of these alternatives, is one in which transport of ^{36}Cl occurs as a result of rapidly transient infiltration pulses along through-going structural pathways.

Preliminary Conceptual Model of Flow Pathways based on ^{36}Cl and Other Environmental Isotopes

3. In order for flow to occur along fast pathways, a continuous, high-permeability pathway must exist to depth, and a means of focusing infiltration to the pathway must exist.
4. Formation of a fast pathway is very sensitive to the characteristics of the pathway, i.e. fault-zone permeability, pulse volume, depth of alluvial cover, and characteristic curves.
5. Four areas that will be intersected by the ESF are candidate sites for detection of bomb-pulse concentrations of ^{36}Cl . These are located near ESF stations 50+00, 55+00, 57+00 to 61+00, and station 68+00. All four are beneath upper regions of washes whose lower regions are prone to flooding, all are in areas of thin alluvial cover, and all are close to surface traces of faults.
6. Penetration of recent water into the TSw unit is indicated by bomb-pulse ^{36}Cl in fractures of the ESF. However, bomb-pulse signals by themselves are not indicative of the amount or distribution of ground water flux within the unsaturated zone. Further testing and modeling is necessary to discriminate between fast pathways along major, through-going structures such as faults, and randomly located features such as interconnected fracture networks.
7. Fast pathways alone are not detrimental to repository performance unless it can be shown that fluxes along those pathways are significant. Cumulative results of all of the ^{36}Cl sampling suggest that the fraction of bomb-pulse water at the repository horizon may be a very small fraction of total flow at this depth. Most of the ^{36}Cl was not deposited by rapid flow. Therefore, the ^{36}Cl data agree with existing conceptual models of the Yucca Mountain ground water flow system in that a small volume of ground water representing a small fraction of the total flow can travel rapidly through the unsaturated zone, especially in the vicinity of structural features that penetrate the TSw. The difference between occurrence of ^{36}Cl at the repository horizon and the significance of ^{36}Cl occurrence is a regulatory issue.

These statements are based on non-Q data but are believed to be scientifically valid.

Recommendations

1. Because of the sensitivity of fast pathway flow to fault characteristics, an increased emphasis on characterization of fault properties at the surface and in the ESF should be a high priority for the Project. Particular emphasis should be placed along the main test level with attention paid to lateral spreading along north-south trending fractures. This will allow the necessary refinement of the site-scale flow model to include variation of fault properties with depth.

2. A sampling program in the ESF should include areas near structural features, particularly those below areas that meet other criteria at the ground surface, based on predictions of location of fast pathways near faults, as described in section 10.5.
3. Determination of percolation flux should receive high priority for investigation through *in situ* field tests and confidence-building through modeling, because flux is the most important parameter needed by total system performance assessment.
4. Many lines of investigation should be pursued to further understand the significance of fast pathways to repository performance. Preliminary results regarding the bomb-pulse ^{36}Cl concentrations observed at repository depth in the TSw may be significant to the predicted long-term performance of the potential Yucca Mountain repository, but the observations should be combined with all other direct and indirect indicators of percolation flux and its distribution in space and time between fractures and matrix to provide confident estimates of these important performance parameters. ^{36}Cl observations should be one part of the investigations and continued sampling (in the ESF especially below areas of thin alluvial cover and near structural features), analysis, interpretation, and modeling to explain the ^{36}Cl distribution should be undertaken with the aim of defining the correlation, or lack thereof, of such observations with mappable structural features. If these features are randomly located and therefore cannot be detected or avoided, then determining the flux distribution in the features with confidence and the continuity of the features with depth will be important determinants in predicted overall performance of the repository over long time periods.

10.9 References

- Ahlers, C.F., T.M. Bandurraga, G.S. Bodvarsson, G.Chen, S. Finsterle, and Y.S. Wu, Summary of model calibration and sensitivity studies using the LBNL/USGS three-dimensional unsaturated zone site-scale model, Yucca Mountain Project Milestone 3GLM107M, Lawrence Berkeley Laboratory, Berkeley, CA, 1995.
ACCN: MOL.19960208.0091-0097
DTN: LB092995312293.001 (Non-Q)
- Ahlers, C.F., C. Shan. C. Haukwa, A.J.B. Cohen, and G.S. Bodvarsson, Calibration and prediction of pneumatic response at Yucca Mountain, Nevada using the LBNL/USGS three-dimensional site-scale model of the unsaturated zone, Yucca Mountain Project Milestone OB12M, Lawrence Berkeley Laboratory, Berkeley, CA, 1996.

Preliminary Conceptual Model of Flow Pathways based on ³⁶Cl and Other Environmental Isotopes

- Benson, L.V., and H. Klieforth, Stable isotopes in precipitation and ground water in the Yucca Mountain region, South Nevada: paleoclimatic implication: Geophysical Monograph 55, pp. 41-59, 1989.
- Burger, P.A., and K.M. Scofield, Perched water at Yucca Mountain – implications on the Exploratory Studies Facility, Nye County, Nevada, 26 pp., 1996.
- Buscheck, T.A., J.J. Nitao, and D.A. Chesnut, The impact of episodic nonequilibrium fracture-matrix flow on geological repository performance, American Nuclear Society FOCUS '91 Conference on Nuclear Waste Packaging, Las Vegas, NV, September 29-October 2, 1991, 1991.
- Day, W.C., C.J. Potter, D.S. Sweetkind, and R.P. Dickerson, Bedrock geologic map of the central block area, Yucca Mountain, Nevada, U.S. Geological Survey Preliminary Map (not for distribution), mapping through 4/26/96 (in review).
- Day, W.C., and S. Beason, Geologic structure at Yucca Mountain, presentation to U.S. Nuclear Waste Technical Review Board, Denver, CO, July 9-10, 1996.
- Fabryka-Martin, J.T. and A.V. Wolfsberg, Hydrologic flow paths and rates inferred from the distribution of chlorine-36 in the ESF, presentation to Nuclear Waste Technical Review Board, Denver, Colorado, July 9-10, 1996.
- Fabryka-Martin, J. T., P.R. Dixon, S. Levy, B. Liu, H.J. Turin, and A.V. Wolfsberg, Systematic sampling for chlorine-36 in the Exploratory Studies Facility, LA-CST-TIP-96-001, Milestone 3783AD, Los Alamos National Laboratory, Los Alamos, NM, 61 pp., 1996.
- Fabryka-Martin, J.T., S.J. Wightman, W.J. Murphy, M.P. Wickham, M.W. Caffee, G.J. Nimz, J.R. Southon, and P. Sharma, Distribution of chlorine-36 in the unsaturated zone at Yucca Mountain: an indicator of fast transport paths, Proceedings of FOCUS '93: Site Characterization and Model Validation, (American Nuclear Society, La Grange Park, Illinois) Las Vegas, Nevada, September 26-29, 1993, pp. 58-68, 1993.
- Flint, L.E., A.L. Flint, and J.A. Hevesi, Shallow infiltration processes in arid watersheds at Yucca Mountain, Nevada, in Proceedings of the Fifth International High Level Radioactive Waste Management Conference, (American Nuclear Society, La Grange Park, Illinois), Las Vegas, Nevada, May 22-26, 1994, pp. 2315-2322, 1994.
- Flint, A.L., J.A. Hevesi, and L.E. Flint, Conceptual and numerical model of infiltration for the Yucca Mountain area, Nevada, U.S. Geological Survey Water Resources Investigation Report 96-xxxx (in review).

Preliminary Conceptual Model of Flow Pathways based on ^{36}Cl and Other Environmental Isotopes

Liu, B., J.T. Fabryka-Martin, A.V. Wolfsberg, B. Robinson, and P. Sharma, Significance of apparent age discrepancies in water ages derived from atmospheric radionuclides at Yucca Mountain, Nevada, in *Water Resources at Risk*, W.R. Hotchkiss, J.S. Downey, E.D. Gutentag, and J.E. Moore, eds., (American Institute of Hydrology, Minneapolis, Minnesota), pp. NH-52-NH-62, 1995.

Marshall, B.D., J.F. Whelan, Z.E. Peterman, K. Futa, S.A. Mahon, and J.S. Stuckless, Isotopic studies of fracture coatings at Yucca Mountain, Nevada, USA, in *Water-Rock Interaction, Proceedings of the Seventh International Symposium on Water-Rock Interaction (WRI-7)*, Park City, Utah, July 13-18, 1992, A.A. Balkema, Rotterdam and Brookfield, Capetown, South Africa, pp. 737-740, 1992.

ACCN: NNA.19921029.0034

DTN: GS920208315215.004

Montazer, P., and W.E. Wilson, Conceptual hydrologic model of flow in the unsaturated zone, Yucca Mountain, Nevada: U.S. Geological Survey Water Resources Investigation Report 84-4345, 55 p., 1984.

Moyer, T.C., J.K. Geslin, and L.E. Flint, Stratigraphic relations and hydrologic properties of the Paintbrush Tuff (PTN) nonwelded hydrogeologic unit, Yucca Mountain, Nevada, U.S. Geological Survey Open-File Report 95-397, 164 pp., 1995.

Nitao, J.J., T.A. Buscheck, and D.A. Chesnut, The implications of episodic non-equilibrium fracture-matrix flow on site suitability and total system performance, in *Proceedings of the Third International High-Level Radioactive Waste Management Conference*, (American Nuclear Society, La Grange Park, Illinois), Las Vegas, Nevada, April 12-16, 1992, pp. 279-296, 1992

Paces, J. B., Memorandum to R.W. Craig dated February 23, 1996, concerning "Submission of Milestone 3GQH455", 1996.

DTN: GS960208315215.001 Q

Peterman, S.E. and J.S. Stuckless, Isotopic evidence of complex ground-water flow at Yucca Mountain, Nevada, in *Proceedings of the Fourth International High-Level Radioactive Waste Management Conference*, Las Vegas, Nevada, April 26-30, 1993, (American Nuclear Society, La Grange Park, Illinois), p. 1559-1566, 1993.

Pruess, K., TOUGH User's guide, Report LBL-20700, Lawrence Berkeley Laboratory, Berkeley, California and Nuclear Regulatory Commission Report NUREG/CR4645, Washington, DC., 78 pp., 1987.

Pruess, K., TOUGH2, a general-purpose numerical simulator for multiphase fluid and heat flow, Report LBL-29400, Lawrence Berkeley Laboratory, Berkeley, California, 102 pp., 1991.

Preliminary Conceptual Model of Flow Pathways based on ^{36}Cl and Other Environmental Isotopes

Pruess, K., A. Simmons, Y.S. Wu, and G. Moridis, TOUGH2 software qualification, Report LBL-38383, Lawrence Berkeley National Laboratory, Berkeley, California, 131 pp., 1996.

Rousseau, J.E., E.M. Kwicklis, and D.C. Gillies, eds., Hydrogeology of the unsaturated zone, North Ramp area of the Exploratory Studies Facility, Yucca Mountain, Nevada, U.S. Geological Survey Water Resources Investigations Report 96-xxx, 267 pp., 1996.

Thoma, S.G., D.P. Gallegos, and D.M. Smith, Impact of fracture coatings on fracture/matrix flow interactions in unsaturated, porous media, *Water Resources Research*, v. 28 (5), pp. 1357-1367, 1992.

Tokunaga, T.K. and J. Wan, Water film flow along surfaces of porous rock, Lawrence Berkeley National Laboratory, 1996 (draft).

U.S. Department of Energy, Yucca Mountain Site Characterization Project Site Atlas 1995, volume 1, prepared by EG&G Energy Measurements, 1995.

van Genuchten, M. Th., A closed-form equation for predicting the hydraulic conductivity of unsaturated soils: *Soil Science Society of America Journal*, 44, p. 892-898, 1980.

Wang, J.S.Y., N.G.W. Cook, H.A. Wollenberg, C.L. Carnahan, I. Javandel, and C.F. Tsang, Geohydrologic models of Rainier Mesa and their implications to Yucca Mountain in Proceedings of Fourth International High-Level Radioactive Waste Management Conference, (American Nuclear Society, La Grange Park, Illinois), Las Vegas, Nevada, April 26-30, 1993, pp. 675-682, 1993.

Wang, J.S.Y. and T.N. Narasimhan, Hydrologic mechanisms governing partially saturated fluid flow in fractured welded units and porous non-welded units at Yucca Mountain, Report SAND-7114, Sandia National Laboratories, Albuquerque, New Mexico, 73 pp., 1986.

Wilson, M.L., Sensitivity analyses for total system performance assessment, in Proceedings of the Fourth International High-Level Radioactive Waste Management Conference, (American Nuclear Society, La Grange Park, Illinois, Eds., v. 1, pp. 14-21), Las Vegas, Nevada, 1993.
ACCN: NNA 19930702.0013

Wilson, M.L., J.H. Gauthier, R.W. Barnard, G.E. Barr, H.A. Dockery, E. Dunn, R.R. Eaton, D.C. Guerin, N. Lu, M.J. Martinez, R. Nilson, C.A. Rautman, T.H. Robey, B. Ross, E.E. Ryder, A. R. Schenker, S.A. Shannon, L.H. Skinner, W.G. Halsey, J. Gansemer, L.C. Lewis, A. D. Lamont, I.R. Triay, A. Meijer, and D.E. Morris, Total system performance assessment for Yucca Mountain - SNL Second Iteration (TSPA-1993), Sandia National Laboratories Report SAND93-2675, Sandia National Laboratories, Albuquerque, NM, 1994.
ACCN: NNA.19940112.012

Preliminary Conceptual Model of Flow Pathways based on ³⁶Cl and Other Environmental Isotopes

Wilson, M.L., TSPA insights into impacts of climate and chlorine-36, presentation to U.S. Nuclear Waste Technical Review Board, Denver, Colorado, July 9-10, 1996.

Wu, Y.S., S. Finsterle, P. Fraser, C.F. Ahlers, and A. Simmons, Software qualification for ITOUGH2 and various equation-of-state (EOS) modules and auxiliary modules for TOUGH2 and ITOUGH2, Report LBL-xxxx, Lawrence Berkeley National Laboratory, Berkeley, CA, (draft).

Yang, I.C., Flow and transport through unsaturated rock - data from two test holes, Yucca Mountain, Nevada, in Proceedings of Third International High-Level Radioactive Waste Management Conference, (American Nuclear Society, La Grange Park, Illinois), Las Vegas, Nevada, April 12-16, 1992, pp. 732-737, 1992.

ACCN: NNA.19930112.0137

DTN: GS920908312272.011 (Non-Q)

Yang, I.C., G.W., Rattray, and P. Yu, Interpretations of chemical and isotopic data from boreholes in the unsaturated zone at Yucca Mountain, Nevada, U.S. Geological Survey Water Resources Investigations Report 96-4058, 58+ pp., 1996.

Zimmerman, R.W. and G.S. Bodvarsson, Coupling of the semi-analytical dual-porosity simulation procedure to the LBNL/USGS site-scale model of the unsaturated zone at Yucca Mountain, Yucca Mountain Project Milestone 3GLS101MM, 1996.

SUBMODEL OF PERCOLATION FLUX AT THE REPOSITORY

E. Sonnenthal, S. Finsterle, and G.S. Bodvarsson

August 1996

11.1 Introduction

Quantification of the percolation flux at different spatial scales is necessary for assessing possible interactions of meteoric water with the proposed repository at Yucca Mountain. The large-scale global flux predicted by coarsely gridded site-scale models will help determine the maximum potential for waste dissolution and transport to the saturated zone. For determination of smaller more localized fast paths and channels that form because of smaller scale heterogeneities, one must employ submodels. It is to be expected that "fast" flow will occur at all scales and the important task of quantifying these flow rates is a challenge.

The current three-dimensional UZ site-scale model has a spatial discretization on the order of 100m horizontally and 10 to 50m vertically. It is hoped that this spatial discretization is sufficient to resolve lateral and vertical fluxes to the extent warranted by the existing data set and that required by the performance assessment abstraction team. It is important to quantify to some extent the accuracy of the UZ model, both in terms of grid discretization errors and also in terms of heterogeneities at various scales. In this chapter we develop a submodel of the three-dimensional UZ model that is used to investigate grid effects and the effects of heterogeneous fracture and matrix properties.

The UZ submodel considered covers an area of 160m E-W by 100m N-S and extends from the ground surface to the water table. The grid element dimensions of the horizontal grid is 10m with a variable vertical spacing, but generally of the same order. All geological complexities, such as layering and dips, are retained from the larger scale UZ model. Thus, this model provides a much-needed link between the geologically realistic UZ model and the more abstracted smaller scale drift-scale models, such as those developed by Birkholzer and coworkers at LBNL (Birkholzer et al., 1996). It is expected that the submodel developed in this chapter will provide the boundary conditions for future work on the drift-scale models in FY97.

The 10m resolution of the submodel grid will allow us to examine the possible spatial variations in percolation fluxes at a scale an order of magnitude smaller than is possible with the current UZ model. Although we are considering only the steady-state fluid fluxes in this work it will be also be important in future studies to quantify the effects of short periods of increased precipitation resulting in transient infiltration pulses above the repository horizon.

11.2 Approach

Criteria for the selection of the submodel are based on geologic, modeling and verification considerations. Evaluation of the flow patterns, fluid fluxes, and saturations generated by three-dimensional UZ model simulations (see chapter 8; Wu et al., 1996), help in selection of the submodel site and allow for direct comparison with the submodel simulation results. Development of the submodel entails the creation of a three-dimensional grid and the assignment of hydrogeologic unit thicknesses, geometries, and rock properties. The fracture and matrix permeabilities, relative permeabilities, porosities, thermal properties, and boundary conditions must be consistent with the UZ model. We then model the steady-state fluid fluxes, temperatures, and liquid saturations using the TOUGH2 code (Pruess, 1987; 1991). To model the effect of permeability heterogeneities on the steady-state fluid fluxes, a stochastic permeability field generated by simulated annealing is used to modify the UZ model permeabilities within the submodel.

11.3 Quality Assurance Status of Data and Software Used In This Chapter

No quality-affecting work was performed in this study. Quality-affecting data was not developed in this work. The rock properties and geologic data used in the model simulations are non-Quality Assurance (Q) data. The simulation code TOUGH2 is Q. The simulating annealing code SIMAND3D is non-Q. The ITOUGH2 code is Q.

11.4 Selection of a Submodel of the UZ Model

It is important that the geologic characteristics of the submodel are representative of the repository area. The data sources from which the implemented geology and rock properties are derived (i.e., boreholes, the Exploratory Studies Facility (ESF), and drifts off the ESF; the North and South Ghost Dance Fault alcoves and the thermal alcove) should be close to the submodel area. From a modeling perspective, the local flow field near the repository horizon in the area surrounding the submodel should be predominantly vertical. This simplifies the assignment of boundary conditions imposed at the sides of the submodel, because it is then unnecessary to prescribe local horizontal fluxes.

A submodel was defined from the UZ model (Fig 11.4.1) that is bounded on the east by the Exploratory Studies Facility (ESF) and on the west by the trace of the Ghost Dance Fault (GDF). The submodel is bounded to the north by the North Ghost Dance Fault Alcove. The dimensions of this inner rectangular submodel are 160 m (E-W) by 100m (N-S) and from the top of the Tiva Canyon unit

Submodel of Percolation Flux at the Repository

(TCw) to the Prow Pass formation at the level of the water table model layer (PP3vp to PP2zp). In addition to the site's proximity to the ESF, the alcove, and the GDF, the trace of the roughly NW-trending Sundance Fault passes diagonally across the submodel domain. In further studies, the inclusion of fault properties from the Sundance Fault will allow for the evaluation of potential "fast paths", as indicated by the presence of bomb pulse ^{36}Cl (Faybeyha-martin et al., 1996) at the level of the repository. The area adjacent to the North GDF Alcove is the proposed site for the Percolation Flux Test, an array of horizontal boreholes spaced approximately 10m apart from which data will be obtained on liquid saturations, temperatures, and fluxes. There will be pneumatic data, permeabilities, temperatures, and fracture geometries and sizes from the ESF and the alcove itself, which will be compared to the submodel results.

Location of Submodel and Potential Percolation Study Area

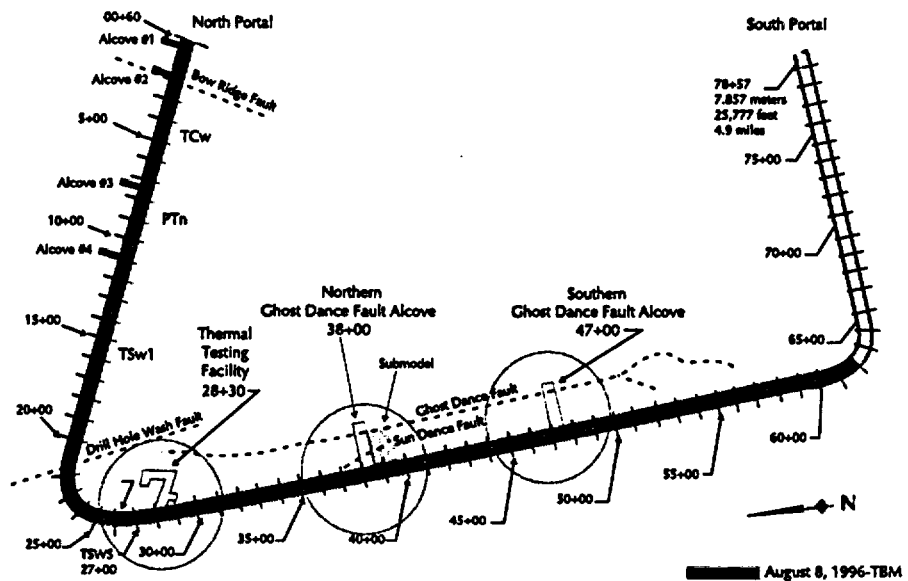


Figure 11.4.1
Map view of submodel. The Ghost Dance Fault and the projected positions of the ESF and North Ghost Dance Fault alcove are boundaries to the submodel.

11.5 Geology of the Submodel Area

An E-W cross-section of Yucca Mountain, taken in the vicinity of the submodel area, shows the hydrogeological units and offsets of the major faults (Fig. 11.5.1). The submodel area is located to the west of the Ghost Dance Fault,

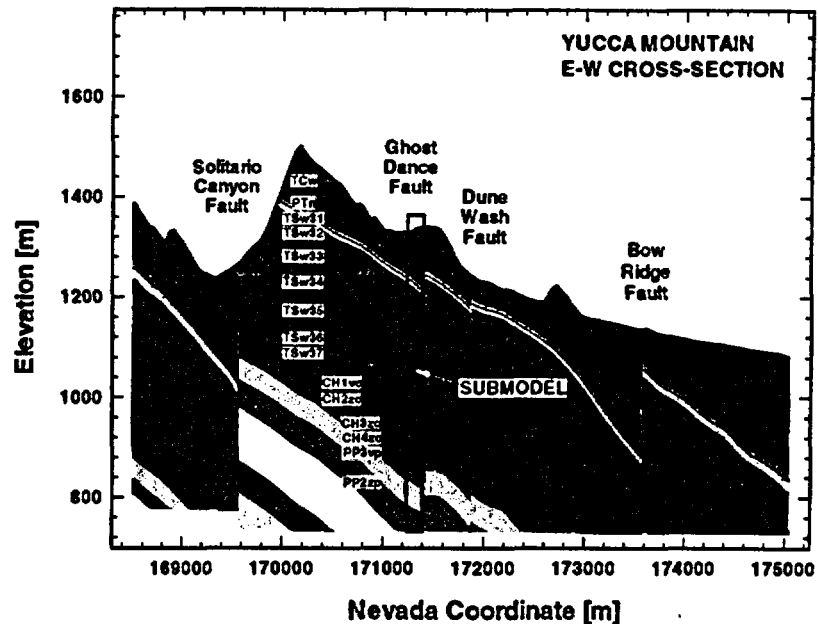


Figure 11.5.1
E-W cross-section of Yucca Mountain showing hydrogeological units and major faults. Details can be found in chapter 2 (Bandurraga et al., 1996).

which has a vertical offset of approximately 23 to 29 meters locally (see chapter 2: Bandurraga et al., 1996).

Given the small area of the submodel, the geological data obtained from the UZ model would be expected to be fairly uniform over the extent of the submodel. Although the stratigraphic relations are uniform over the submodel area, substantial variations exist in the unit thicknesses (Table 1). One notable rock property boundary is adjacent to the submodel in the region of coarse grid elements surrounding it, dividing a much less permeable zeolitized region of the CHn geologic unit (CH1zc) to the east from a vitric region (CH1vc) to the west. The trace of the NW-trending Sundance Fault zone crosses diagonally across the center of the submodel and is a normal fault, having displacements of zero to 35 feet along its 1500 ft. length (Rousseau et al., 1996). A detailed discussion of the geology, stratigraphy and hydrogeological units is presented in Chapter 2 (Bandurraga, 1996).

For reference, a range of thicknesses and vertical matrix and fracture permeabilities for the hydrogeological units present in the submodel are given in Table 11.5.1. All rock transport property (fracture and matrix permeabilities), porosities, van Genuchten parameters for fractures and matrix, and residual saturations were determined by inverse modeling of borehole data and are described in detail in Chapter 3 (Bandurraga et al., 1996).

Table 11.5.1 Typical Thicknesses and Permeabilities of Hydrogeological Units in Submodel			
Unit	Thick- ness (m)	Vertical Permeability (m^2)	
		Matrix	Fracture
TCw11	25 - 55	1.55e-18	5.23e-12
TCw12	6	1.14e-16	6.40e-12
TCw13	3	6.41e-17	5.76e-12
PTn21	3	2.40e-13	-
PTn23	3	2.30e-15	-
PTn24	5 - 6	3.26e-15	-
PTn25	10 - 16	4.41e-13	-
TSw31	3 - 4	1.62e-16	6.31e-12
TSw32	35 - 45	6.14e-15	4.22e-12
TSw33	6 - 45	9.86e-18	6.16e-12
TSw34	6 - 10	3.07e-17	4.01e-12
TSw35	60 - 71	7.51e-18	6.95e-12
TSw36	90 - 106	9.15e-17	4.01e-12
TSw37	18 - 30	3.24e-17	4.01e-12
CH1vc	25 - 30	1.57e-12	7.24e-13
CH1zc	25 - 30	5.62e-16	1.00e-13
CH2zc	13 - 19	2.03e-18	2.47e-13
CH3zc	42 - 52	2.03e-18	2.47e-13
CH4zc	17 - 20	5.47e-18	1.00e-13
PP3vp	25 - 50	1.01e-16	3.01e-14
PP2zp	0 - 10	6.11e-17	1.00e-13

11.6 The TOUGH2 Code and Equation of State Modules

The integral finite difference code TOUGH2 was used for all flow simulations presented in this chapter. Two equation of state modules were employed - EOS3 (Pruess, 1991) and EOS9 (Pruess and Antunez, 1995). For two-phase simulations (water and air) EOS3 utilizes as its primary variables P_{gas} , S_{gas} , and T , with air approximated as an ideal gas, and water properties obtained from steam table relations. EOS9 treats the gas as a passive phase ($P_{gas} = \text{constant}$) and thus the CPU time required for a steady-state solution is significantly less than for simulations using EOS3. At steady-state fluid distributions, S_L is nearly identical for both modules (for a detailed discussion see Forsyth et al., 1995). Because the solution time of the fully coupled two-phase flow problem employing EOS3 is dramatically reduced once S_L is close to its steady-state value, S_L is

first determined using EOS9. For all of the simulations reported in this chapter we used the equivalent continuum method (ECM), which treats flow in the matrix and fracture as a single continuum (see Chapter 6; Doughty et al., 1996).

11.7 Evaluation of Coarse Flows From the UZ Model

In order to justify the boundary conditions used on the submodel the steady-state fluxes surrounding it must be evaluated from simulations using the UZ model. Data from elements surrounding and incorporated within the submodel were extracted from a three-dimensional simulation (chapter 8; Wu et al., 1996) using the TOUGH2 code. Rock parameters used in this simulation were obtained by inversion using the code ITOUGH2 at an infiltration rate of 0.1 mm/year (see chapter 3; Bandurraga et al., 1996).

The region around the submodel includes nine surface elements from the site-scale model and is traversed by the nearly N-S trace of the GDF. Fluid flux vectors, plotted in three dimensions, are shown in Fig. 11.7.1 for the nine columns (each having approximately 24 layers, except the elements in the fault plane where the stratigraphy is doubled). The GDF is shown as a red plane, the approximate location based on the UZ model fault element node positions. The outline of the interior submodel domain (to be described in the following sections) is also plotted. The coordinates of the X and Y axes were shortened for plotting purposes and can be easily converted to Nevada state plane coordinates (X+171000, Y+232000). All plots shown in this chapter are referenced to this same set of coordinates.

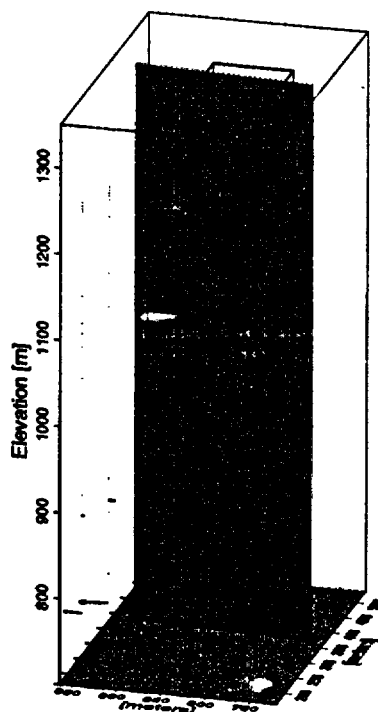


Figure 11.7.1

Liquid flux vectors from UZ model simulation in area around submodel domain. Filled circles are UZ model grid nodes projected onto the base. The red plane represents the approximate geometry of the Ghost Dance Fault, as indicated by the UZ model fault element nodes. The inner submodel domain is shown as the rectangular box. The strong lateral flow in the vitric layers CH1vc (elevation ~900m; south-trending) and PP3vp units (elevation ~790 m; north-trending) is substantially greater than in all other units.

The highest fluid fluxes are within vitric layers (UZ model hydrogeological units CH1vc and PP3vp) that overlie low permeability zeolitized layers of the Calico Hills and Prow Pass units. The upper Calico Hills vitric layer (CH1vc) lies directly below the Topopah Spring unit (TSw) and overlies a low permeability zeolitic unit (CH2zc), whereas the PP3vp layer is sandwiched between zeolitic horizons. In both of these vitric horizons the flows are nearly horizontal, trending south in the CH1vc (~890m) and north in the PP3vp unit (~775m). The flow paths follow the general direction of the strike of the contact between the western vitric portion of the CH1vc and the zeolitic zone to the east (CH1zc). The much lower permeability zeolitic zone is a barrier to flow in this region.

Because the fluid fluxes in the Topopah Spring unit are several orders of magnitude lower than in the underlying Calico Hills vitric units the latter data points were removed and the flux vectors rescaled. Flux vectors in the TSw (~900-1200m) are predominantly vertical downward and several orders of magnitude lower than in the underlying vitric units (Fig 11.7.2). There is some south-trending flow in the Tiva Canyon unit (~1275m: TCw) and the Paintbrush unit (~1200-1250m: PTn) that is not as strongly developed within the center of

Submodel of Percolation Flux at the Repository

the submodel domain. At the infiltration rate of 0.1 mm/yr liquid, fluxes for the two fault elements are relatively small and diminish downward owing to capillary suction into the surrounding matrix. The contrasts with observations of bomb pulse ^{36}Cl in water associated with faults at the repository level in the ESF (Fabryka-Martin et al., 1996).

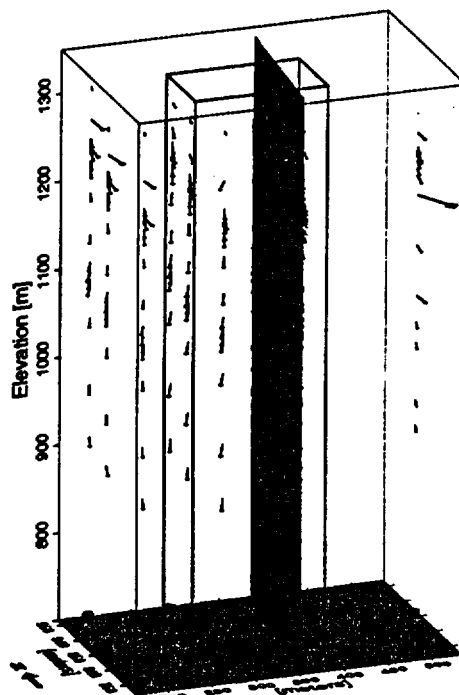


Figure 11.7.2

Renormalized liquid flux vectors for TSw, PTn, and TCw units from UZ model simulation in area around submodel domain. Strong lateral flow is evident in the PTn, while flow in the TCw and at the level of the ESF (about 1085m) is predominantly vertical. Fluxes along the fault diminish with depth, owing to the higher capillary suction of the surrounding matrix.

Normalizing the vertical flux by the infiltration rate gives an indication of the possible loss or gain of fluid through channeled infiltration. Fig 11.7.3 (a) shows a column of the normalized vertical flux components taken within the submodel domain (element 185 in the UZ model). For the entire repository horizon and (~1085m) TSw unit the ratio is approximately one, with a very sharp and substantial positive deviation in the Prow Pass vitric unit, as shown previously in the three-dimensional flux vector diagram (Fig. 11.7.1). At the approximate level of the ESF (~1085m), for a grid node within the submodel domain, the magnitude of the percolation flux is 0.155 mm/yr – about 50% higher than the infiltration rate (see section 9 below). The proportion of the vertical flux (here negative in the downward direction) to the magnitude of the flux is shown in Fig. 11.7.3 (b) for the same column. As expected the vertical component of the flux is near zero in the Prow Pass unit and also in the Calico Hills vitric unit where the flows are horizontal. Within the TSw, the ratio is nearly

Submodel of Percolation Flux at the Repository

everywhere -1.0, indicating that the flux is near vertical throughout the unit. Near the surface, in the TCw, there is also a nonvertical flux component and less so in the PTn. From the earlier three-dimensional vector flux diagram (Fig. 11.7.2) the lateral components of flow in the TCw and PTn in the submodel area are less than in the region to the west and northwest in the UZ model. Although the UZ model does not indicate a substantial impact of the lateral flows on the TSw unit, it may become important in the vicinity of a fast flow path through the PTn.

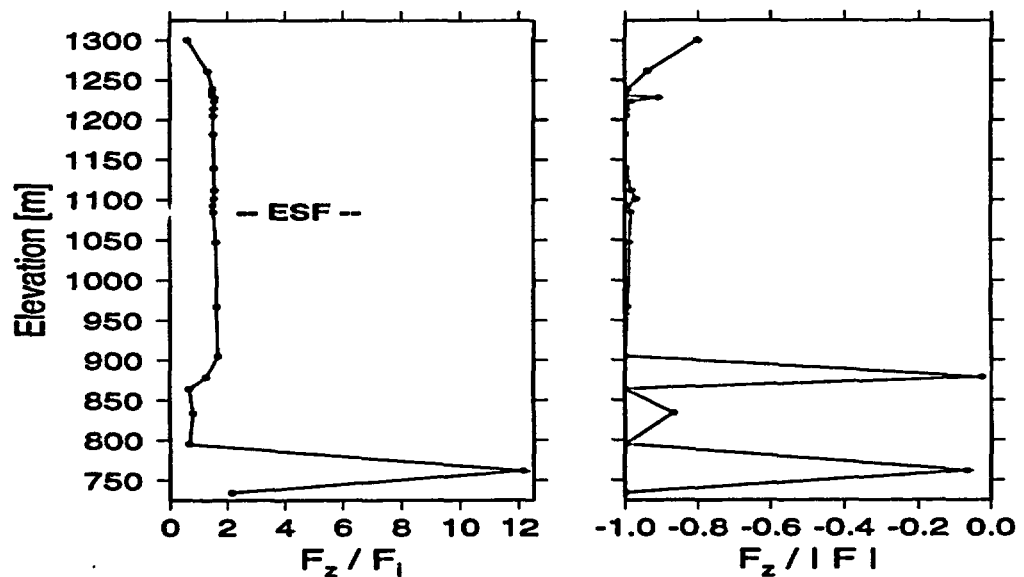


Figure 11.7.3

The vertical component of the fluid flux from element 185 in the UZ model normalized to the 0.1 mm/yr infiltration flux (a) and the magnitude of the flux (b).

In general, the mostly vertical flow paths in the UZ model at the repository level supports our choice of a submodel in this area. The nonvertical flows in the overlying PTn and TCw units suggests that we should include a larger region above the submodel domain to capture the effects of these lateral fluxes. Even with the lateral flow in the overlying units, the ratio of the percolation flux at the repository horizon to the local infiltration flux is close to one, indicating that the lateral fluxes do not substantially modify the total flux in the TSw. Because of the regional confined lateral flows in the CH1vc and PP3vp vitric units, the submodel in its present form cannot predict the larger-scale transport of fluids after passing through the base of the TSw.

11.8 Development of the UZ Submodel

11.8.1 Numerical Grid

A three-dimensional submodel of the UZ model was created with square 10 x 10 meter elements (in plan view) having dimensions of 16 elements (E-W) by 10 elements (N-S) and 24 layers (Fig. 11.8.1). The western boundary of the model is bounded by the position of the ESF and the eastern boundary is taken close to the trace of the Ghost Dance Fault. The northern boundary is approximately that of the North Ghost Dance Fault Alcove, whereas the southern boundary is set 100 meters to the south. This regular grid was then surrounded by coarse grid elements to minimize local boundary effects and to capture some of the regional nonvertical flow in the overlying PTn and TCw units. The number of grid elements is 5846, plus 250 bottom boundary elements in all simulations, and an additional 250 top elements for simulations employing the EOS3 module.

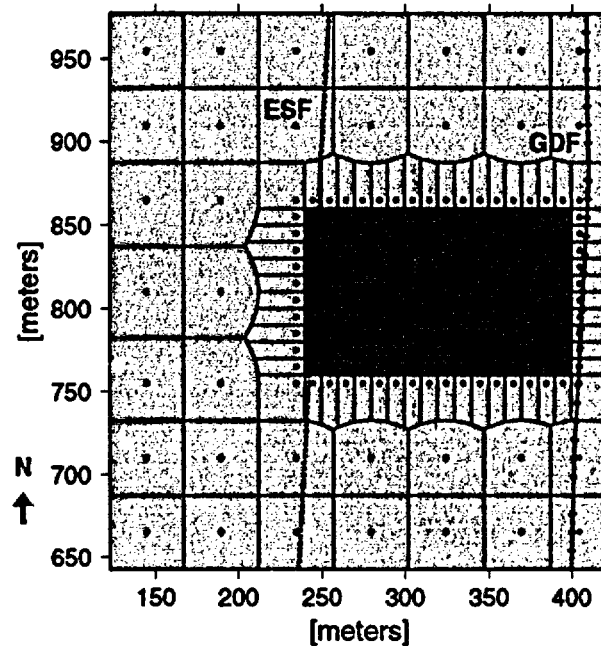


Figure 11.8.1

Plan view of submodel grid showing inner rectangular mesh and coarse outer mesh. Positions of the ESF and GDF from the UZ model are the approximate bounds to the inner submodel (blue box).

Near-surface flow in the overlying TCw unit deviates from the horizontal, apparently controlled mostly by topographic variations. Because of some regional lateral flow in the PTn, the downward fluid flow to the repository horizon in the submodel may be slightly lower than the UZ model would predict, although as we showed in the previous section this effect was not evident at this location. To account for such possible effects, and to remove the numerical

boundaries away from the submodel boundaries, coarse grid elements were added in the upstream and downstream directions (ascertained from the UZ model).

Unit thicknesses were derived from the same isopach thickness data used to generate the UZ model input data (see Table 1). Some modifications to unit designations (TSw32 and TSw33) were made because of apparent discontinuities resulting from the coarse scale of the vertical discretization relative to the X and Y internodal distances and the dip of the units. Because a boundary exists between the regions of the Calico Hills unit that are either zeolitic or vitric (CH1zc and CH1zc), the elements at the boundary were assigned based on their areal overlap. This boundary crosses the outer coarse grid region, to the west of the inner rectangular submodel domain. The lowermost unit in the western part of the submodel is PP2zp, however because of its approximately eastward dip below the water-table, on the eastern side the lowermost unit becomes PP3vp.

11.8.2 Initial and Boundary Conditions

The dominantly vertical flow in the TSw unit indicates that the lateral boundary conditions of a submodel enclosed within this zone may be set to no mass flux and free slip. For purely vertical flow this is equivalent to a condition of lateral continuity. The upper boundary condition was set to a spatially uniform and constant infiltration rate for two different cases (0.1 mm/yr and 5.0 mm/yr). The gas pressure at the surface is given an initial value of 90 kPa, which is allowed to equilibrate to a steady-state profile, assuming a fixed lower boundary gas pressure. The lower boundary condition (at the water table) was set to a constant gas pressure ($P_{\text{gas}} = 92 \text{ kPa}$) with practically full liquid saturation ($S_L = 0.999$). For simulations coupling energy conservation as well as mass conservation the surface temperature was set to a uniform and constant 17 deg. C and the temperature at the base of the submodel was set to 30 deg. C, based on UZ thermal models (chapter 9: Wu et al., 1996). The specific enthalpy of infiltration water was set to a constant 75.61 kJ/kg (chapter 9: Wu et al., 1996; chapter 12: Finsterle et al., 1996).

11.9 Numerical Simulations

In this section we describe a series of steady-state simulations employing the submodel described above. These simulations were designed to determine the local percolation fluxes at the repository horizon for constant infiltration rates and to compare these higher resolution results to those obtained from the much coarser grid UZ model. The fluxes observed in the submodel simulations using the UZ model geologic properties are then compared to simulations in which the permeabilities are modified by a stochastic field generated by simulated annealing.

11.9.1
Steady-State Liquid Fluxes, Saturations and Temperature Gradients

Steady-state simulations were performed using areally uniform infiltration rates of 0.1 and 5.0 mm/year. A rate of 0.1 mm/yr is suggested from the inverse modeling of matrix properties (see chapter 2; Bandurraga et al., 1996). The much higher value of 5.0 mm/yr is the approximate value obtained from the infiltration map of Flint et al. (1996) at the surface location above the proposed percolation flux test area. Mapped onto the UZ model grid, the infiltration rates show spatial differences of more than an order of magnitude over less than 100 meters and between neighboring grid nodes (Fig. 11.9.1). The high local variability in the infiltration rates at the scale of the submodel make any values extracted from this local data set uncertain. Therefore, simulations were performed using the two bounding rates to evaluate the likely range of percolation fluxes at the repository horizon.

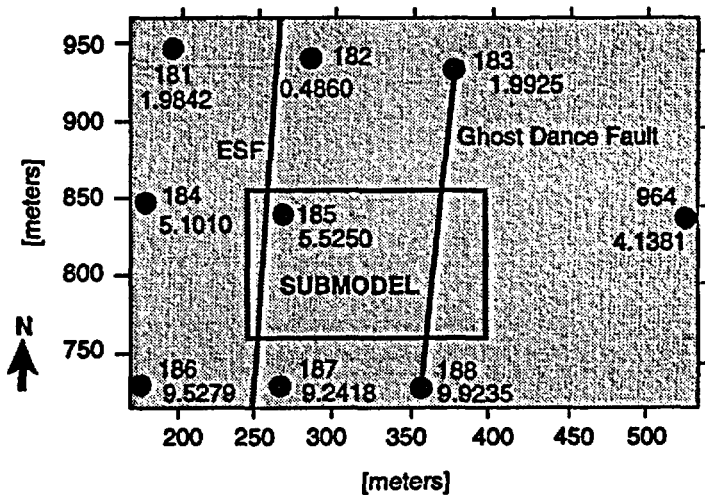


Figure 11.9.1
 Infiltration rates at UZ model grid nodes, as derived from Flint et al., (1996). Fluxes to the south of the submodel domain (inner grid) are up to 20 times higher than those to the north.

Steady-state flux vectors for the inner rectangular submodel domain are shown in Fig. 11.9.2 for an infiltration rate of 0.1 mm/yr. Very strong down-dip layer-parallel flow is pronounced in the upper PTn unit, with a maximum absolute flux of about 1.12 mm/yr, over 11 times greater than the infiltration flux. Some lateral flow is also evident in the vitric Calico Hills unit, but only about a third that observed in the PTn. Much lower fluxes are observed in the Topopah Spring unit, and some deviations from the vertical are evident at the base of the repository horizon.

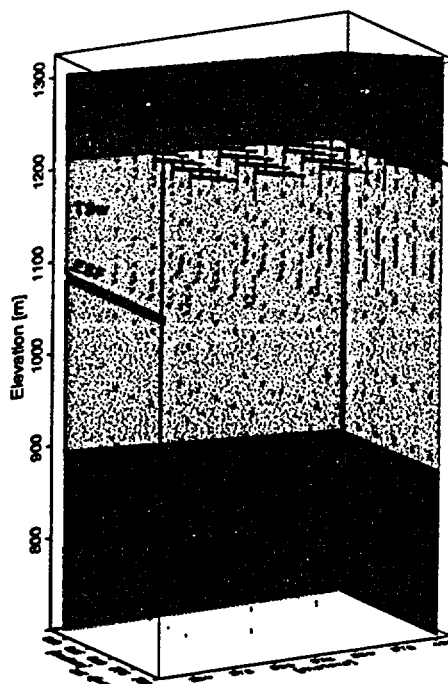


Figure 11.9.2

Steady-state fluid flux vectors for an infiltration rate of 0.1mm/yr. Strong lateral flow (maximum = 1.12 mm/yr) is evident in the PTn (elevation ~ 1230 to 1238 m).

At the eastern boundary of the submodel the flow in the PTn and below is diverted downward as a result of the no-flux condition (Fig. 11.9.3). As this is also the approximate position of the Ghost Dance Fault, and if the fault is acting as a impermeable barrier, then this boundary condition may be reasonable in the sense of the larger scale flow. However, even if the fault is acting as a barrier because of the offset of more permeable units, the high permeability of the fault would act as a better conduit than the submodel boundary conditions allow (in their present form). Alternatively, capillary suction in the rocks adjacent to the fault would keep the fault relatively dry and thus flow would be distributed preferentially in the matrix as the UZ model indicates. The offset of the PTn at the GDF is apparently complete (Fig. 11.5.1) suggesting that flow would either be diverted down the fault fractures or in the adjacent rock matrix (in contrast to the ^{36}Cl findings).

Submodel of Percolation Flux at the Repository

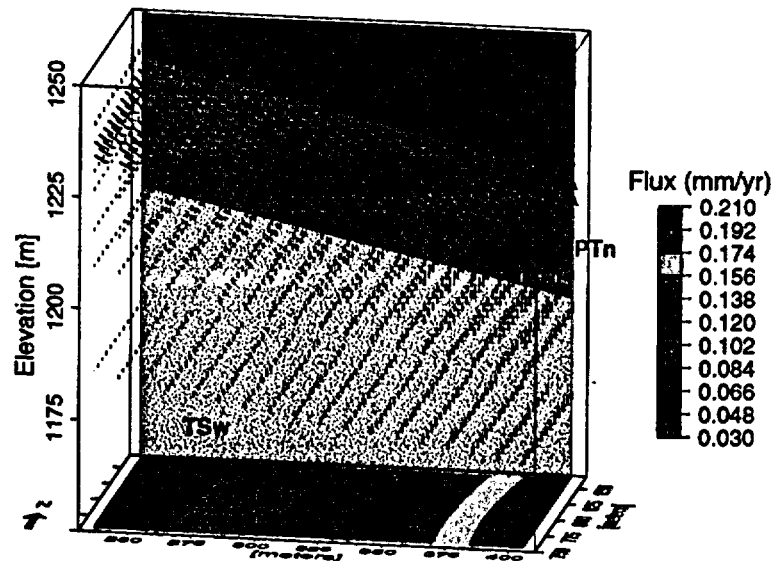


Figure 11.9.3

Flux vectors for the upper TSw layer to the bottom of the TCw unit (partial layer on east side). The strong lateral flows are in two of the thin upper PTn units. Lateral flows are directed vertically downward near the contact of the eastern boundary. Flux magnitude contours projected onto the base are of the lowermost layer (top TSw unit).

Even though the lateral fluxes in the PTn are quite high, the fluxes in the underlying TSw layers are predominantly vertical and much closer to the 0.1 mm/yr infiltration rate (Fig. 11.9.3). The flux contours shown in this figure are for the uppermost layer of the TSw (the lowermost layer in the section plotted). As the flux vectors indicate, the fluxes are much higher as the eastern boundary is approached, but only about a factor of two higher than the infiltration rate, much lower than the factor of over 11 seen in the PTn.

The major proportion of fluid is transported by the matrix, because of the low fracture porosity ($\sim 2 \times 10^{-4}$) and the typically low saturations of water in fractures. The fluid distributions are dependent on the values of the van Genuchten parameters chosen, which is treated in detail by Wu et al. (1996) (see Chapter 8, Wu, 1996).

Just above the level of the ESF, and near the top of the repository horizon (1094 m) the fluxes are also much higher adjacent to the eastern boundary, yet the effect has diminished somewhat and some local variations are evident (Fig. 11.9.4). Two factors contribute to the higher fluxes near the eastern boundary at this level. First, as was shown for the PTn and upper TSw layer, the flow is diverted downward at the eastern boundary. Second, the rock properties change at this level (TSw34 at the west and TSw33 at the east) because of the

Submodel of Percolation Flux at the Repository

eastward dip of the units. The permeability of TSw33 is about an order of magnitude higher than TSw34 and thus one would expect flow to be enhanced preferentially in the eastern zone. Liquid saturations differ across the submodel at this same level with higher values near the eastern boundary, but also at the western boundary also reflecting the combined effects of local rock property variations and flux differences (Fig. 11.9.5).

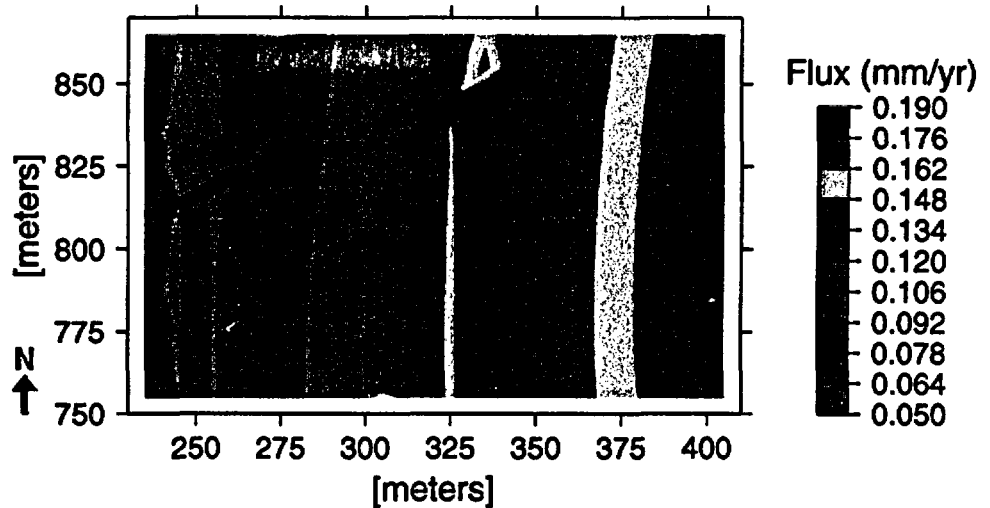


Figure 11.9.4

Contour map of the flux vector magnitudes for layer (TSw34-TSw33) at approximately the 1094 meter level, for an infiltration rate of 0.1 mm/yr.

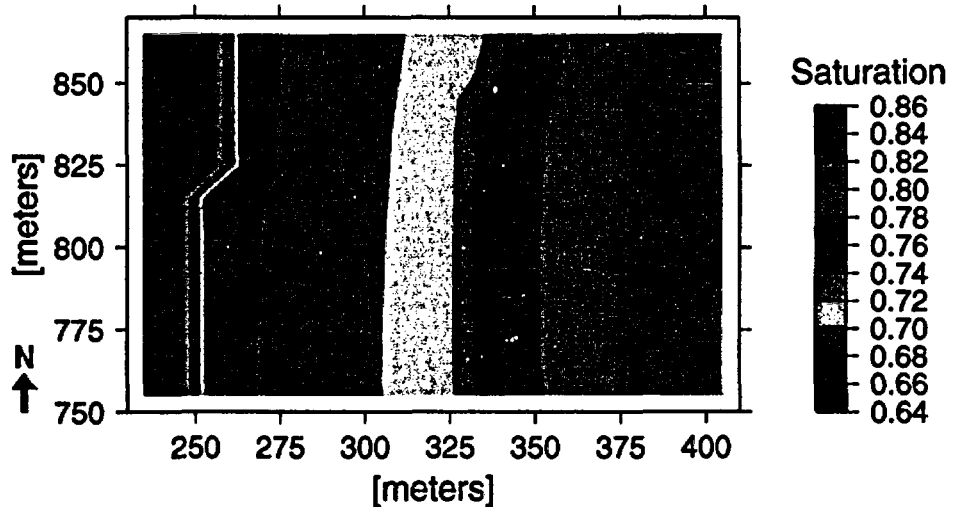


Figure 11.9.5

Contour map of liquid saturations for layer (TSw34-TSw33) at approximately the 1094 meter level, for an infiltration rate of 0.1 mm/yr.

Submodel of Percolation Flux at the Repository

Results obtained using an infiltration rate of 5.0 mm/yr exhibit similar flux patterns to the 0.1mm simulation, with some differences owing to locally higher saturations. Flux magnitude contours at same level as in Fig. 11.9.4 (~1094m) also show the higher fluxes at the eastern boundary, yet they are only about 30% higher than the infiltration rate as opposed to 90% for the 0.1 mm/yr case (Fig.11.9.6). Liquid saturations at this level (Fig. 11.9.7) are about the same for the eastern boundary as in the 0.1 mm/yr case (~ 0.80 to 0.82). At the western boundary, however, the saturation is much higher at the 5.0 mm/yr infiltration rate (0.95 compared to 0.85).

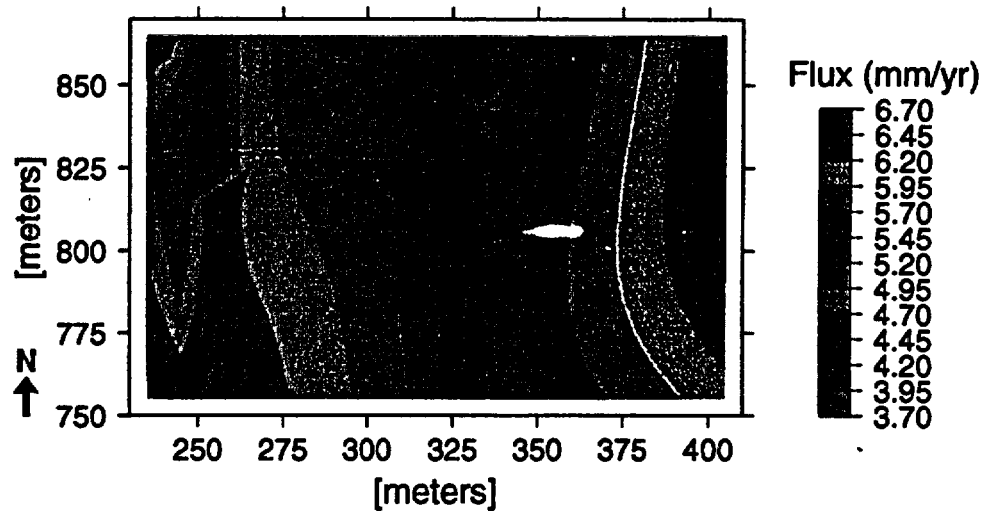


Figure 11.9.6

Contour map of the flux vector magnitudes for layer (TSw34-TSw33) at approximately the 1094 meter level, for an infiltration rate of 5.0 mm/yr.

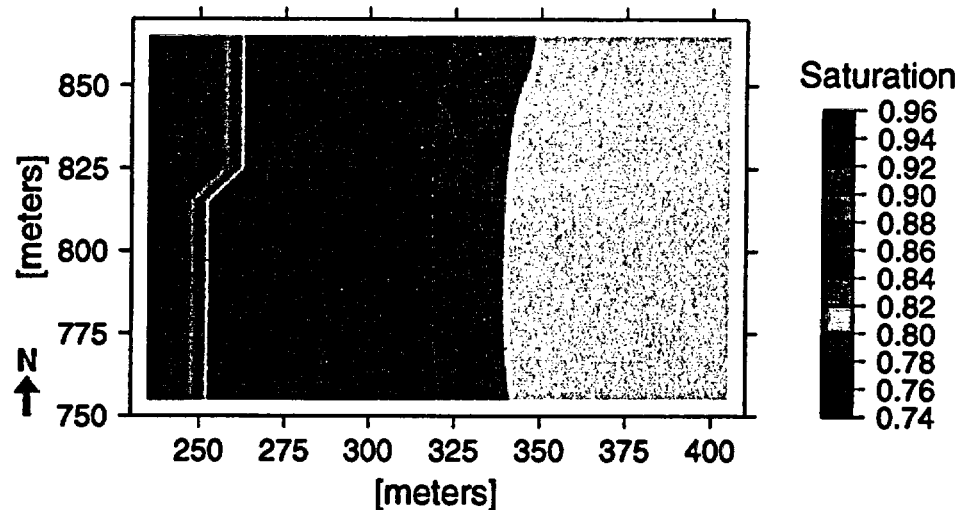


Figure 11.9.7
 Contour map of liquid saturations for layer (TSw34-TSw33) at approximately the 1094 meter level, for an infiltration rate of 5.0 mm/yr.

In addition to the higher fluid fluxes associated with an increased infiltration rate, there is also an associated thermal effect from the downward advection of cooler surface fluid. The assumed boundary conditions (approximate values from the UZ model) are 17 deg. C at the surface and 30 deg. C at the water table and the base of the simulation. Steady-state temperature profiles for infiltration rates of 0.1 mm/yr and 5.0 mm/yr are shown in Fig. 11.9.8, taken from one column in the center of the inner rectangular simulation subdomain. There is small but noticeable cooling effect at the higher infiltration rate throughout the rock column. The differences in the temperature gradients are greatest near the surface (0.1mm/yr > 5.0 mm/yr), and decrease with depth until about the 1000m level where they are same. Below this depth the 5.0 mm/yr infiltration rate profile has a larger gradient than the 0.1mm/year profile, as a result of the constant temperature lower boundary condition. At the approximate level of the ESF (1085 m) the local temperature gradient (dT/dZ) is about 0.34 deg C/km lower for the higher infiltration rate of 5.0 mm/yr (Table 11.9.1). The fluxes at this location are somewhat higher than the infiltration rate, so that in areas where the local fluxes are different (i.e., near the eastern and western boundaries) the effect would be correspondingly larger or smaller.

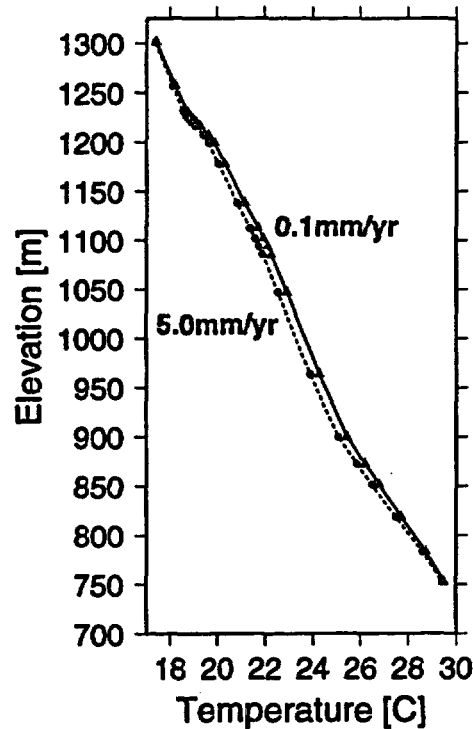


Figure 11.9.8 Steady-state temperature profiles from center of submodel domain for infiltration rates of 0.1 and 5.0 mm/yr.

Table 11.9.1 Steady-State Conditions at Repository Horizon For Differing Infiltration Rates		
	0.1 mm/yr	5.0 mm/yr
dT/dZ (deg. C/km)	17.48	17.14
Liquid Saturation	0.87	0.95
Vertical Fluid Flux (mm/yr)	0.127	5.396

Overall, the results of the steady-state submodel simulations shows that small-scale differences in fluxes can be significant, at a scale smaller than the UZ model can describe. This becomes even more significant, considering that the rock properties used in the submodel were extracted from the UZ model and do not reflect the local heterogeneities invariably present. The boundary conditions of the submodel affect the fluxes considerably, and thus the influence of the Ghost Dance and Sundance Faults on fluxes and saturations at the scale of the submodel should be investigated further. Even with these boundary effects, the fluxes at the repository horizon are predominantly vertical, in agreement with the UZ model. In the following section we can make a more detailed comparison of the UZ model and submodel at the repository horizon.

Submodel of Percolation Flux at the Repository

11.9.2 Comparison to UZ Model Results

It is useful to compare the results of the steady-state fluxes in the submodel to UZ model simulations. One element from the UZ model has its nodal position within the interior subdomain of the submodel and simulation results from this element (see chapter 8: Wu et al., 1996) are compared to the average of all nodes in the interior submodel domain (216 nodes) at the approximate level of the ESF (1085 m). Table 11.9.3 lists the temperature, water saturation, and the fluid flux for each model simulation. While there are some differences, the fluxes in the UZ model are only 12% higher than the average submodel flux, and both are higher than the infiltration rate. Given that the coarseness of the UZ model is about 10 times greater than the submodel, and the bounds of the UZ model element do not directly overlie the submodel, the values are reasonably close. The liquid saturation in the UZ model is significantly higher than in the average submodel, however comparison to the saturations near the same nodal position shows a closer match (0.85 to 0.87), compared to the submodel average of 0.82.

	UZ Model	Submodel Average
Liquid Saturation	0.91	0.82
Fluid Flux (mm/yr)	0.155	0.137

Another comparison can be made to simulations performed by Xiang et al. (1995) on a nearby column of rock, also using TOUGH2. Using three sets of rock property data (LBL, an averaged set of LBL data, and Wilson et al., 1994) they showed the water saturations, fluid velocities, and travel times at different infiltration rates. For all 3 data sets, the pore liquid velocity at about the 1085 m level was approximately 2.9×10^{-11} m/s (corresponding to 0.1 mm/yr), close to the values obtained in the submodel and UZ model simulations.

Although strong lateral flow is not observed in the CHn in the submodel simulations, the strong downdip flow in the PTn observed in the submodel is also seen in the UZ model (Chapter 9: Wu et al., 1996). Compared to the submodel, stronger lateral flow developed in the TCw unit in the UZ model, most likely a result of topographic effects and the large thickness variations in this unit.

11.9.3 Development of a 3D heterogeneous permeability field

Rock matrix heterogeneity and differences in fracture size, spacing and connectivity will lead to variations in the percolation flux at differing scales. The assessment of spatially and temporally variable fluid fluxes at a scale of tens of meters is not possible with the UZ model, because the grid elements have a horizontal length-scale of about 100 meters. Thus, the submodel can help quantify such local, but potentially significant perturbations to the flow field. Because the three-dimensional pattern of heterogeneity at the scale of our grid elements (10

x 10 meters) in the area of study is unknown, one way in which to assess the possible effects of permeability heterogeneities is to introduce stochastic variation.

Heterogeneities were imposed on the system by modification of the existing matrix and fracture permeabilities using an isotropic three-dimensional field obtained by simulated annealing (code SIMAND3D, S. Finsterle and A. Datta-Gupta, pers. comm.). Simulated annealing has previously been used for creating models of three-dimensional fracture networks (Long et al., 1991) with a final configuration close to the percolation threshold (Sahimi, 1993). Another method used to introduce small-scale stochastic heterogeneities in models of the repository horizon at Yucca Mountain is the "turning bands method" (Antunez and Pruess, 1994; Pruess and Antunez, 1995). The latter method was used to generate a distribution of fracture apertures with correlation lengths at the sub-meter scale.

Using SIMAND3D, a range of isotropic permeabilities having a standard deviation of 1.0 was generated around a hypothetical mean value (K_m) with absolute bounds three orders of magnitude around the mean. In comparison, the range of permeabilities (measured by air injection) at the repository horizon in the vicinity of the thermal alcove (TSw2) differ by three orders of magnitude over distances of a few meters (Y. Tsang, pers. comm.). Although the submodel does not have the resolution required to model heterogeneities at the scale of a few meters, it is not clear from the thermal alcove measurements whether these small-scale features do not have some larger scale connectivity or aggregation as might be expected.

The dimensions of the heterogeneities created by the simulated annealing process are controlled by the lengths over which smaller-scale variations may be correlated. The correlation lengths were set to 100 meters in the X and Y directions, and to 200 meters in the Z direction (Table 11.9.3). This choice was governed by the necessity to create heterogeneities of a plan view scale larger than a single grid element and with sufficient vertical connectivity to allow for local flow channeling. Yet the vertical connectivity was not intended to be such that the structures are continuous through the entire domain in the sense of a fault or fracture zone. The SIMAND3D code requires that the distances between vertical grid nodes are uniform. For simplicity, the vertical heterogeneities were applied directly to the nonuniform submodel grid. The end result is that correlation lengths for the vertical heterogeneities differ according to the difference in thickness between the submodel layer and 20 meter layer thickness chosen in the simulated annealing calculation. Although the correlation lengths are similar in scale to the submodel horizontal dimensions, the observed structures are typically several tens of meters in diameter, which is large enough to be properly realized using the 10m horizontal grid spacing, yet small enough such that a few full structures are observed in plan view.

Submodel of Percolation Flux at the Repository

Table 11.9.3
Spatial Parameters Used in Simulated Annealing

Coordinate	Layers	Layer Thickness	Correlation Length
X	18	10 meters	100 meters
Y	12	10 meters	100 meters
Z	24	20 meters	200 meters

Dividing the generated permeabilities (κ_s) by the hypothetical mean value (κ_m) gives the factor which was then applied to the UZ model permeabilities (κ_{UZ}) to obtain the new permeability field. Thus the modified permeability field ($\bar{\kappa}$) used in the simulations is given by:

$$\bar{\kappa} = \frac{\kappa_{st}}{\kappa_m} \kappa_{UZ} \quad (11.4.1)$$

The ratio of the vertical to horizontal permeability from the UZ model was maintained constant. The stochastic variations were generated only for the interior regular grid, so that the permeabilities of the surrounding coarse grid elements were left unchanged, thus minimizing focused nonvertical flow in the boundary elements. The contoured permeability field is shown on an E-W cross-section through the center of the submodel domain (Fig. 11.9.9) and as a horizontal slice taken close to the level of the ESF (Fig. 11.9.10). There is obvious horizontal and vertical connectivity of the generated structures, with inlayer variations of about 2 orders of magnitude higher and lower than the original permeabilities. This compares to a modification to the permeability field of about 2 orders of magnitude by Pruess and Antunez (1995).

Submodel of Percolation Flux at the Repository

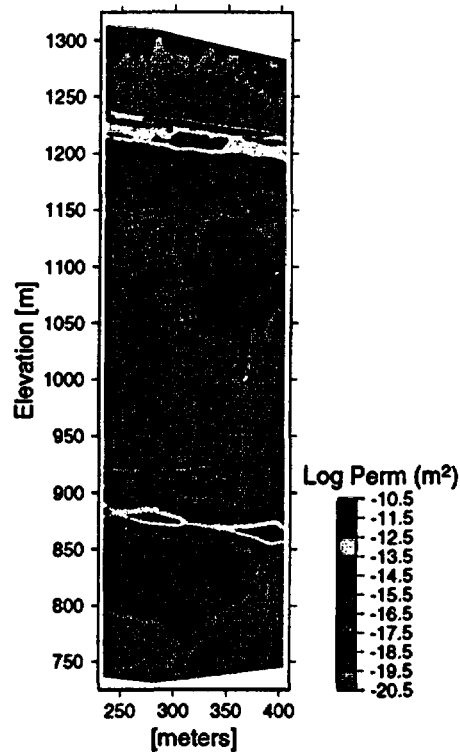


Figure 11.9.9
Permeability contours for an E-W cross-section through center of submodel domain. The variations within each layer produced by the application of the stochastic field are evident as is the initial larger variation between layers.

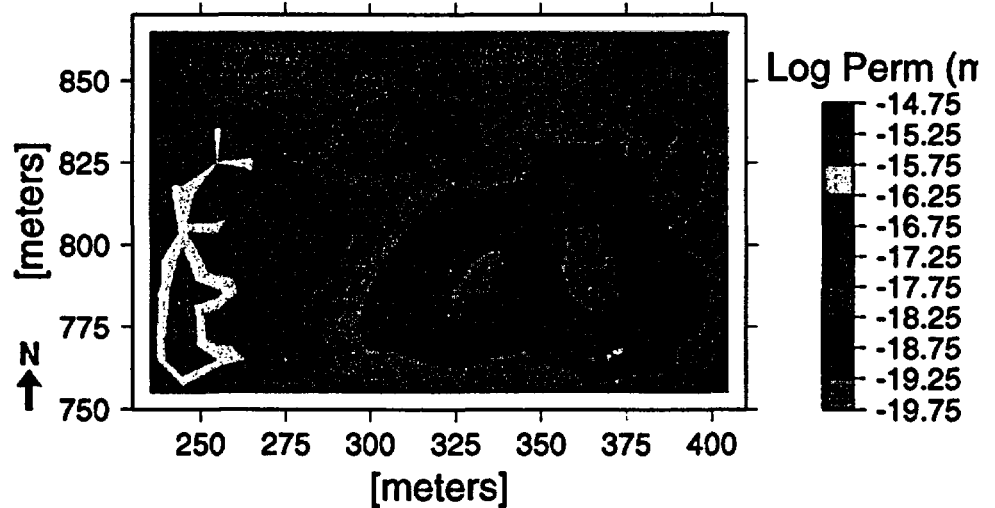


Figure 11.9.10
Permeability contours for the TSw34-TSw33 layer (approximately 1094m elevation), near the top of the repository horizon.

11.9.4 Steady state results for heterogeneous permeability field

Two simulations were performed to investigate the steady-state saturations and fluid fluxes for a locally heterogeneous permeability field generated by application of the stochastic field to the UZ model permeabilities. For these simulations a version of TOUGH2 was used which allows for the modification of the permeability at each grid element, as described by Pruess and Antunez (1995). As in the latter study, we used the equation of state module EOS9 (described in section 6). The temperature was set to isothermal conditions (25 deg. C). Simulations were performed using the same boundary conditions and rock properties as in the previous section for infiltration rates of 0.1 mm/year and 5.0 mm/year. In reality, the infiltration rates at the surface may differ spatially because of permeability variations, however given the small-scale variations in infiltration rates shown by Flint et al. (1996), a modification of the infiltration rates locally cannot be justified at this time. In addition, at the depth of the repository such local effects are likely to be minimal because of the high permeability of the overlying PTn and the subsurface equilibration of fluid potentials. For this problem, it is assumed that the fracture and matrix van Genuchten parameters are identical to the unmodified permeability field. If matrix permeability variations are related primarily to differences in matrix pore throat radii, and likewise fracture permeabilities are primarily a function of aperture, then capillary pressures would be much different. Yet, differences in fracture connectivity and densities leading to such permeability variations would not similarly affect these parameters. Air permeability tests in the TSw at the repository horizon (Y. Tsang, personal communication) have not shown a relationship between the fracture size or density and the air permeability.

Steady-state fluid flux vectors using an areally uniform infiltration rate of 0.1 mm/year show complex flow behavior in many regions of the submodel, but are especially well developed in the PTn and CHn units. Because of the large variations in fluxes and their variable orientation throughout the submodel it is instructive to examine the fluxes in a selected location. Comparison of the fluid flux contours at the level of the proposed repository (Fig. 11.9.11) show differences from the model using the unmodified permeabilities (Fig. 11.9.4). There are some localized features of higher and lower fluxes and the overall differences are greater, yet even though the permeability variations at this level vary by several orders of magnitude the highest fluxes are only about 35% higher than in the unmodified submodel. Liquid saturations (Fig. 11.9.12) are little different in the heterogeneous submodel compared to the unmodified submodel (Fig. 11.9.5). Thus, the local deviations in permeability we imposed on the system do effect the patterns of the heterogeneities but the flux magnitudes and saturations are not as strongly modified at this level. This agrees with the study of Xiang et al. (1995) which showed similar fluid velocities at the repository horizon for columns having different overlying rock properties and modeled saturations. Of course, preferential pathways in the heterogeneous model would tend to allow greater channeling of fluid during transient events of increased infiltration flux.

Submodel of Percolation Flux at the Repository

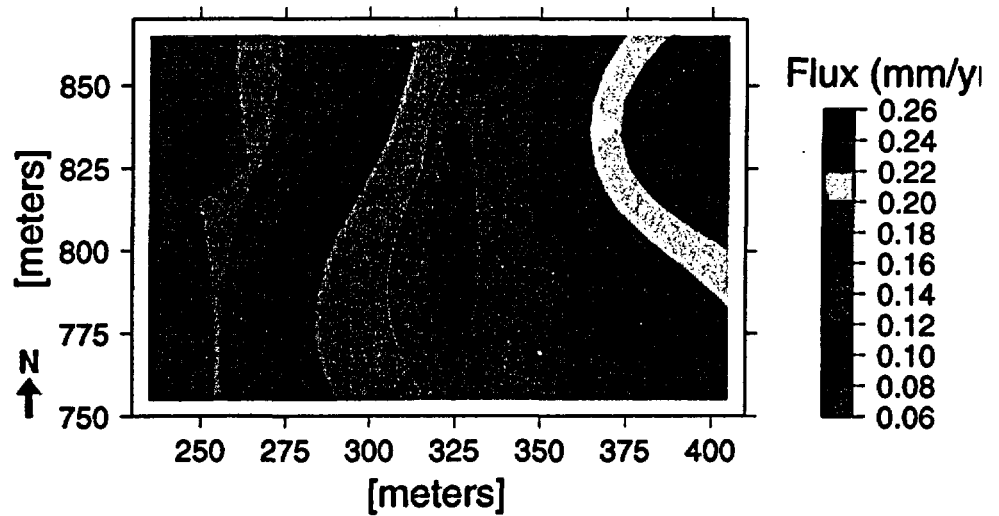


Figure 11.9.11
Contour map of fluid flux magnitudes at the TSw33-TSw-34 layer (1094m), for an infiltration rate of 0.1 mm/yr. A locally higher flux region is apparent in the center of the domain, which is absent in the unmodified submodel (Fig. 11.9.4).

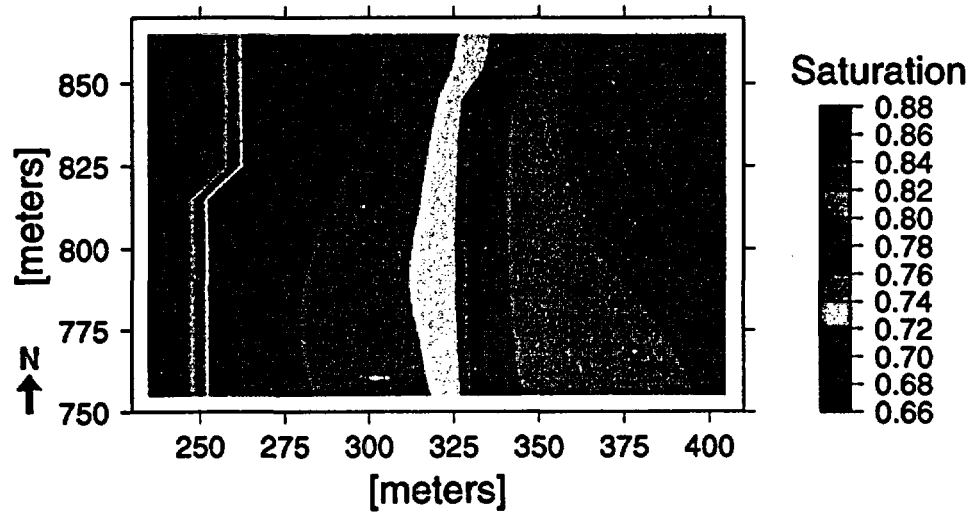


Figure 11.9.12.
Contour map of liquid saturations at the TSw33-TSw-34 layer (1094m), for an infiltration rate of 0.1 mm/yr. The values and patterns differ little from the unmodified saturations at this level (Fig. 11.9.4).

Submodel of Percolation Flux at the Repository

At an infiltration rate of 5.0 mm/yr, the local perturbations of fluid vectors are enhanced relative to the 0.1 mm/yr simulation. It is most evident in the PTn (Fig. 11.9.13) and in the CHn. In the PTn a near vertical fast flow path about 100 meter high developed in the west side of the domain that passes directly into the top of the TSw. It is about 30 meters in diameter and most of the flux is transmitted through two elements. Contours of the fluxes in the TSw, projected onto the base of the figure, show strong variations in fluxes, but clearly attenuated compared to the fluxes in the PTn. Even so, the fluxes are locally up to 20 mm/yr, a factor of four higher than the infiltration rate. Other less well-defined paths are also evident in the east side of the domain. Another aspect of the increased channeling of fluxes through heterogeneities in the PTn is that there is less fluid reaching the eastern boundary and diverted downward. Extrapolated to the conditions near a fault, the fluxes reaching the fault would be correspondingly less.

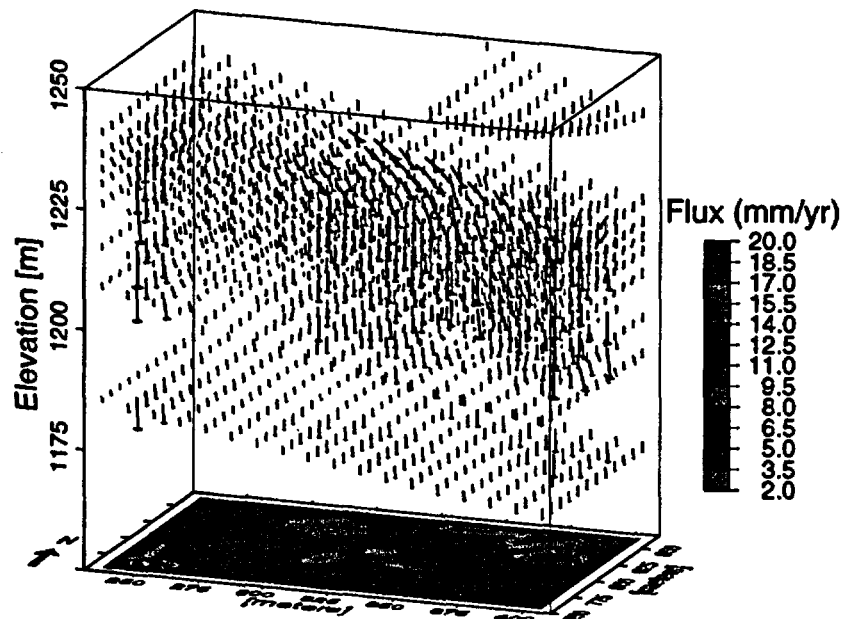


Fig. 11.9.13

Flux vectors for the base of the TCw, the PTn and uppermost two layers of the TSw, at an infiltration rate of 5.0 mm/yr. Locally strong fluxes in the PTn are channeled into permeability highs and into the TSw. The flux contours are for the lowermost layer shown (TSw32) and projected onto the base of the diagram.

Again, near the top repository horizon (about 1094 m) patterns of flux variations are quite evident (Fig. 11.9.14), but their magnitudes have diminished relative to those seen in the TSw just below the PTn. The values of the liquid saturations are affected little (Fig. 11.9.15), yet in the region of increased percolation fluxes they are correspondingly higher.

Submodel of Percolation Flux at the Repository

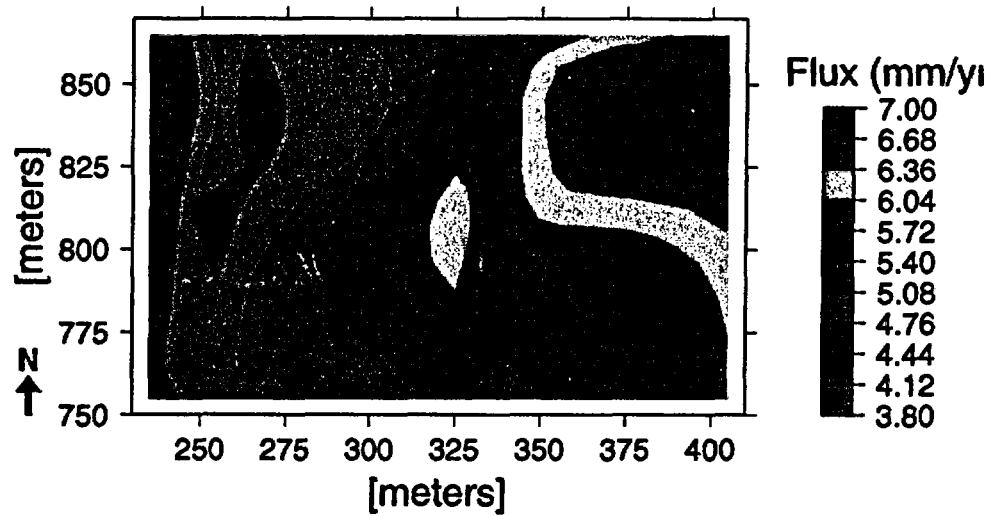


Figure 11.9.14
Contour map of fluid flux magnitudes at the TSW33-TSW-34 layer (1094m), for an infiltration rate of 5.0 mm/yr.

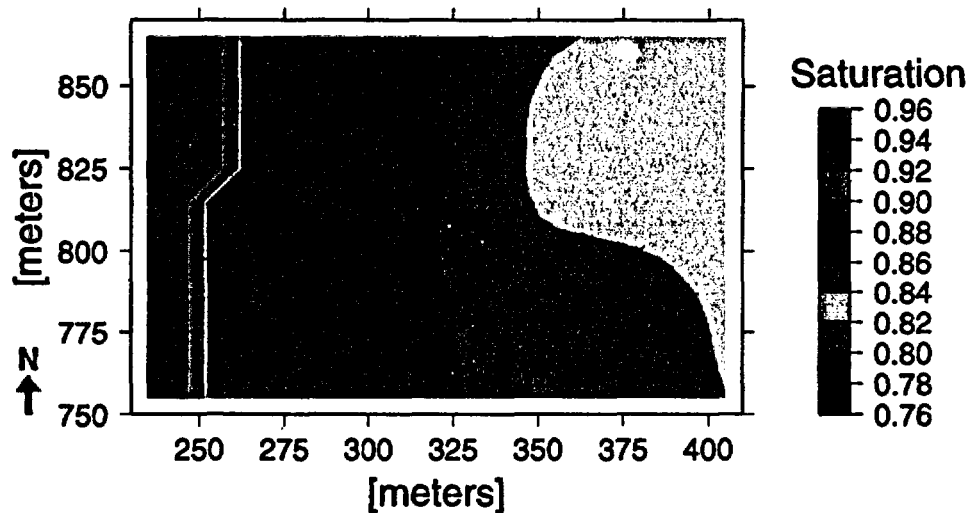


Figure 11.9.15
Contour map of liquid saturations at the TSW33-TSW-34 layer (1094m), for an infiltration rate of 5.0 mm/yr.

Although we do observe some local channel structures, there does not seem to have developed the dendritic or plume-like saturation fronts observed in the simulations by Pruess and Antunez (1995). In contrast to the latter study, the stochastic heterogeneities we applied to the permeability field are of a much

smaller magnitude than the original differences between hydrogeological units. Another difference is in the ratio of the correlation length scales of our heterogeneities to the length-scale of the simulation domain which is close to one, compared to about 0.01 for the Pruess and Antunez (1995) simulations. This would suggest that if such permeabilities were present over a large area of the UZ model, and if it had a spatial resolution on the order of 10m, we may also observe larger-scale features having local perturbations of the kind observed in our simulations.

As would be expected, permeability variations of a couple of orders of magnitude imposed on the UZ model led to variations in the local fluxes and flow patterns. However, because of the predisposition of the PTn to channel larger fluxes down-dip in the submodel, the presence of local heterogeneities acted as near-vertical "drains" for this already magnified flux.

As these are steady-state results, the variations may be substantially amplified during transient events and as locally high saturations would further modify the percolation fluxes. At the level of the repository, some attenuation of the flux variations has weakened the strong differences seen in the PTn and the top of the TSw, yet significant variations still persist. Liquid saturations are little affected, yet this may be expected because the porosities were left unmodified.

Such local variations in permeabilities may either tend to have an accumulative effect on the larger-scale flow patterns or be "averaged out". Yet the proximity of such structures to faults and areas of higher infiltration rates may create strong local disturbances in the flow patterns and fluxes into the repository.

11.10 Summary

A submodel in which to investigate mass fluxes at the repository horizon was chosen near the location of the North Ghost Dance Fault Alcove, between the ESF and the Ghost Dance Fault. The three-dimensional submodel spans 160m E-W by 100m N-S and has 10m square grid elements (in plan view) with variable thicknesses derived from the UZ model. Analysis of flux vectors from a three-dimensional UZ model simulation (chapter 9: Wu et al., 1996) showed that around the submodel site fluxes are predominantly vertical at the level of the proposed repository, although significant horizontal flow exists in the underlying CH1vc and PP3vp units, and less so in the TCw and PTn.

Steady-state simulations were performed using TOUGH2, at infiltration rates of 0.1 mm/yr and 5.0 mm/yr to give bounds to the likely percolation fluxes at the repository horizon. It was found that the eastward dip of the highly permeable PTn unit allowed strong lateral flow which was subsequently diverted downward at the impermeable eastern boundary of the submodel. As this is also the approximate position of the trace of the Ghost Dance Fault and

because the offset of the PTn may be nearly complete in this area, the flow observed may be analogous to the effect of the fault. At the level of the repository, fluxes are in general near-vertical and liquid saturations are directly correlated with variations in rock properties and to a lesser degree, the flux magnitudes. While the saturations and fluxes were higher for the 5.0 mm/yr infiltration rate the overall flow patterns were similar. Comparison of 0.1 mm/yr infiltration rate results from the submodel (average over a layer at the repository horizon) and from a large element in the UZ model showed a difference of only 12% in the flux with liquid saturations and fluxes higher in the UZ model. Because the submodel can account for smaller spatial scale differences in rock properties and flow phenomena, these differences highlight the importance submodel-scale simulations.

A three-dimensional stochastic permeability field was generated using simulating annealing (SIMAND3D code) and used to modify the UZ model permeabilities (fracture and matrix). The porosity and other rock parameters were left unchanged. Simulations were performed using TOUGH2 (also at infiltration rates of 0.1 and 5.0 mm/yr) to investigate the spatial characteristics of fluxes and saturations at the repository horizon. Permeability heterogeneities increased the variations in fluxes at the repository horizon, but saturations were little changed because they are a stronger function of the porosity and capillary pressure differences. In the Paintbrush and Calico Hills units several vertical "fast paths" developed that were several tens of meters in diameter and about 100 meters long. The strong lateral (down dip) flow in the PTn was subsequently channeled into these local permeability highs, resulting in fluxes a factor of four higher in the upper layers of the TSw.

We consider the results and conclusions expressed in this chapter to be scientifically valid, although they are non-Q.

11.11 References

- Antunez E. and K. Pruess, The use of the turning bands method (TBM) to generate stochastic aperture distributions in heterogeneous fractures, Lawrence Berkeley Laboratory Report LBL-35581, Lawrence Berkeley Laboratory, Berkeley, CA, 1994.
- Birkholzer, J.T., C.F. Tsang, Y. Tsang, and J.S.Y. Wang, Drift scale modeling, Yucca Mountain Milestone T6540, Scaling and modeling testing for use in TSPA, Sandia National Laboratory, Albuquerque, NM, 1996 (preliminary.)
- Fabryka-Martin J.T., P.R. Dixon, S. Levy, B. Liu, H.J. Turin, and A.V. Wolfsburg, Summary report of chlorine-36 studies: systematic sampling for chlorine-36 in the Exploratory Studies Facility, Los Alamos National Laboratory Milestone Report 3783AD (Level 4), Los Alamos National Laboratory, Los Alamos, NM, 1996.

Submodel of Percolation Flux at the Repository

- Flint A.L., J.A. Hevesi, and L.E. Flint, Conceptual and numerical model of infiltration for the Yucca Mountain area, Nevada, U. S. Geological Survey Water Resources Investigation Report, U. S. Geological Survey, Denver, CO, 1996.
- Forsyth P.A., Y.S. Wu, and K Pruess, Robust numerical methods for saturated-unsaturated flow with dry initial conditions in heterogeneous media, *Advances in Water Resources* 18, pp. 25-38, 1995.
- Hudson D.B. and A.L. Flint, Estimation of shallow infiltration and presence of potential fast pathways for shallow infiltration in the Yucca Mountain area, Nevada, U.S. Geological Survey Water-Resources Investigations Report, U. S. Geological Survey, Denver, CO, 1996 (in review).
DTN GS960508312212.006 Non-Q
- Long, J.C.S., K. Karasaki, A. Davey, J. Peterson, M. Landsfeld, J. Kemeny, and S. Martel, An inverse approach to the construction of fracture hydrology models conditioned by geophysical data, *Int. J. Rock Mech. Min. Sci. Geomech. Abstr.*, 28, pp. 121-142, 1991.
- Pruess K., TOUGH2-A general-purpose numerical simulator for multiphase fluid and heat flow, Lawrence Berkeley Laboratory Report LBL-29400, Lawrence Berkeley Laboratory, Berkeley, CA, 1991.
ACC# NNA.19940202.0088
- Pruess K. and E. Antunez, Application of TOUGH2 to infiltration of liquids in media with strong heterogeneity, *Proceedings of the TOUGH Workshop '95*, Lawrence Berkeley Laboratory Report LBL-36872, Lawrence Berkeley Laboratory, Berkeley, CA, pp. 69-76, 1995.
- Rousseau J.P., E.M. Kwicklis, and D.C. Gillies, Hydrogeology of the unsaturated zone, North Ramp area of the Exploratory Studies Facility, Yucca Mountain, Nevada, U.S. Geological Survey Water-Resources Investigations Report, U. S. Geological Survey, Denver, CO, 1996 (draft).
- Sahimi M., Flow phenomena in rocks: from continuum models to fractals, percolation, cellular automata, and simulated annealing, *Reviews of Modern Physics*, v. 65 (4), pp. 1393-1534, 1993.
- Wessel P. and W.H.F. Smith, New version of the generic mapping tools released, *EOS Trans. Amer. Geophys. U.*, v. 76, pp. 329, 1995.
- Wilson, M.L., Sensitivity analyses for total system performance assessment, In: *Proceedings of the Fourth Annual International Conference on High-Level Radioactive Waste Management*, American Nuclear Society and American Society of Civil Engineers, Eds., Las Vegas, NV, v. 1, pp. 14-21, 1993.
ACCN: NNA.19930702.0013

Submodel of Percolation Flux at the Repository

Xiang Y., S. Mishra, and B. Dunlap, Parametric analysis of a TOUGH2 model for the unsaturated zone at Yucca Mountain, Proceedings of the TOUGH Workshop '95, Lawrence Berkeley Laboratory Report LBL-37200, UC-1240, Lawrence Berkeley Laboratory, Berkeley, CA, pp. 58-68, 1995.

**SIMULATION OF COUPLED PROCESSES
IN A TWO-DIMENSIONAL
WEST-EAST CROSS-SECTION
OF YUCCA MOUNTAIN, NEVADA**

*S. Finsterle, T.M. Bandurraga, C. Doughty,
and G.S. Bodvarsson*

August 1996

12.1 Introduction

12.1.1 Importance of Coupled Processes at Yucca Mountain

Predicting flow and transport at Yucca Mountain requires a good understanding of the pertinent physical processes, their relative importance, and their interaction. In addition, knowledge about a large number of model parameters is required. In this study, we focus on the coupling of different processes, and illustrate how the combination of hydrologic and thermal effects determine liquid, gas and heat flow as well as transport characteristics. Moreover, we examine whether the conceptual model and parameter values used in the unsaturated zone (UZ) model are able to provide a consistent picture of the overall system behavior, i.e. whether the model is able to reproduce the observations made at Yucca Mountain, and whether it correctly mimics its salient features. This work provides the basis for extending coupled process modeling over the entire 3-D model domain of the UZ model.

Simulation of coupled processes requires accurate modeling of a variety of physical processes which occur on different spatial scales, are either highly transient or required to reach near steady-state conditions, involve both fracture and matrix flow and their interaction, and are sensitive to different parameters, most of which are not well known. Furthermore, parameter values optimized to explain a certain effect may contradict data which are governed by another process. For example, differences between the gas isotope ages in the Tiva and Topopah units as well as the pneumatic pressure signal require relatively low gas permeabilities for the Paintbrush unit. On the other hand, the ^{36}Cl data may necessitate fast moisture-flow path through some fractures in the Paintbrush. The attempt to explain both effects in a single model is thus a challenge. At the same time, modeling coupled processes provides an opportunity to discriminate between alternative scenarios. While a certain effect may be accounted for by more than one conceptual model, a comparison of modeling results with all available data may render certain aspects of the model unlikely. New features and parameters become relevant, such as the properties of the major faults and their offsets, boundary conditions such as variable and locally increased infiltration rates, certain geologic features such as the apparent discontinuity in the Calico Hills zeolites, etc. (see Chapter 1, Bodvarsson et al. 1996).

The simulations presented in this chapter will involve no calibration, i.e. it is assumed that the previous calibration efforts described in Chapter 3 and Chapters 7 through 10 as well as Ahlers et al. (1996) have produced a reasonable UZ site scale model. By taking a representative cross-section through the repository hori-

Simulation of Coupled Processes in a Two-Dimensional West-East Cross-Section of Yucca Mountain, Nevada

zon of the UZ model and subjecting it to comparisons with observed data of gas pressure, moisture tension, saturation, and temperature will give it a rigorous test that should reflect the robustness and conversely the limitations of the UZ model.

12.1.2 Purpose of Study

The modeling study described in this report is an attempt to reproduce and partly explain a variety of data and observations using a two-dimensional west-east cross-section of Yucca Mountain. A dual-porosity, dual-permeability representation of the fracture-matrix system will be developed for transient simulations where the resolution of the driving pressure and temperature gradients at the fracture-matrix interface is important. Multiphase flow processes under non-isothermal conditions are taken into account. A single parameter set which combines estimates from individual calibration studies is used (see Ahlers et al., 1996, as well as Chapter 3 and Chapters 7 through 10).

The objective of this effort is to demonstrate that the salient features of flow and transport at Yucca Mountain are reproduced by the unsaturated zone model. Matching observations of different types validates the conceptual model and checks the consistency of the parameter set, thus increasing the reliability of the subsequent model predictions.

Following a general description of the modeling approach in Section 12.2, we discuss a few selected process simulations and relate the results to the observed data. The observations are only briefly described; the reader is referred to the parallel reports and the literature. The processes and data considered in this study are summarized in Table 12.1.2.1.

Process	Observation	Section
steady-state flow	saturation	12.3.1
	water potential	12.3.2
	temperature	12.3.3
gas flow	gas circulation and isotope ages	12.4.2
	pneumatic pressure response	12.4.3
liquid flow and transport	liquid flow	12.5.1
	^{36}Cl pulse	12.5.2

12.1.3 QA Status of Data and Software Used in this Chapter

The simulation discussed in this chapter are based on a parameter set for rock properties derived from borehole data and inverse modeling. The QA status is described in Bandurraga et al. (1996), Chapter 3. Furthermore, we make qualitative comparisons between the modeling results and data available for

Simulation of Coupled Processes In a Two-Dimensional West-East Cross-Section of Yucca Mountain, Nevada

the cross-section under investigation. The QA status of these data is summarized in Table 12.1.3.1.

Data Type	Bore-hole	Author	DTN	QA-Status
saturation	SD-7	Flint	GS951108312231.009	Q
saturation	UZ#16	Flint	GS940508312231.006	Q
saturation	UZ-6s	Loskot	GS921208312211.013	non-Q
water potential	SD-7	Flint	GS951108312231.009	to be Q
temperature	H-3	Sass	GS930208318523.001	non-Q
temperature	UZ-7a	Rousseau	GS960308312232.001	to be Q
infiltration map	-	Flint	-	to be Q
³⁶ Cl	ESF	Fabryka-Martin	-	to be Q
pneumatic data	SD-7	Patterson	-	to be Q
gas isotopes	UZ-6s	Thorstenson	-	non-Q

The data listed in Table 12.1.3.1 as "to be Q" are in the process of being qualified by the U.S. Geological Survey. The "non-Q" data do not effect the conclusions of this report.

All the simulations were performed using computer programs that underwent software qualification. The main simulation program is TOUGH2 (Pruess et al., 1996). The ECM module software qualification is described in Wu et al. (1996).

This work and its conclusions will be Q once the geological model and the data listed in Table 12.1.3.1 achieve Q status. At present, they provide strong corroborating evidence for the conclusions reached in this modeling study.

12.2 Model Development

In this chapter we briefly describe the modeling approach, discuss initial and boundary conditions and model assumptions that are common in all the following simulations.

12.2.1 Two-Dimensional Cross-Section

We have selected a vertical west-east cross-section, which starts about 1 km west of the Solitario Canyon fault, passes boreholes USW UZ-6, USW UZ-6s, and USW SD-7, intersects the Ghost Dance and Dune Wash faults, contains borehole UE-25 UZ#16, and extends about 1.5 km beyond the Bow Ridge fault to the east. The corresponding Nevada North coordinate is 231,800 m.

Simulation of Coupled Processes in a Two-Dimensional West-East Cross-Section of Yucca Mountain, Nevada

This cross-section was selected because it contains boreholes that showed various processes. borehole SD-7 has a perched water zone and rather descriptive moisture tension and saturation profiles. Borehole UZ#16 also has good quality saturation data in addition to measured ^3H concentrations in the Calico Hills units that reflect less than 40 years travel time from the ground surface. The conceptual model of the area (see Chapter 2, Bandurraga et al. 1996) identifies a vitric "hole" in the zeolitic zone of the Calico Hills formation that has potentially great implications for radionuclide transport at the site. Borehole UZ-6 and UZ-6s have very active shallow gas flows that outflow during winter and inflow during the summer. In addition, the latest infiltration map indicates large variability in average infiltration with highest infiltration at the crest of Yucca Mountain, and then declining to the east and west of this cross-section. Thus, the data associated with this cross-section provides a near-unique opportunity to investigate coupled processes involving gas, moisture, heat, and chemical transport at Yucca Mountain.

The model boundaries and layering are taken from the unsaturated zone site-scale model (Wittwer et al., 1995; Chapter 2, Bandurraga et al., 1996; Chapter 5, Haukwa et al., 1996). However, the discretization was modified, with a 50 m grid spacing in the horizontal direction and refined gridding around the faults. The mesh is shown in Figure 12.1.1 (borehole UZ-6s is not shown since is nearly coincident with UZ-6). Note the vertical exaggeration of about 6:1 in this and all the following figures.

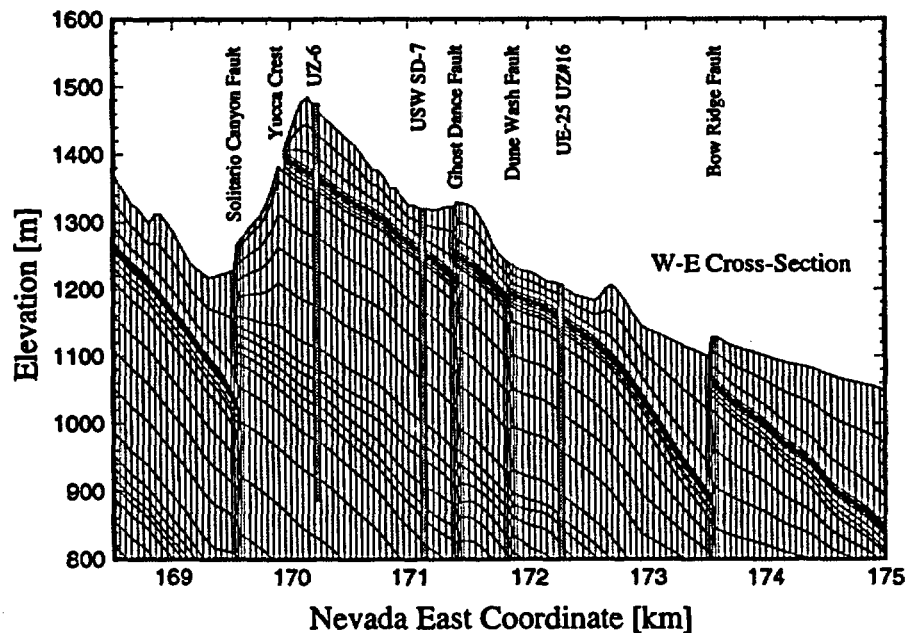


Figure 12.2.1.1
Grid of the west-east cross-section along Nevada Coordinates N 231800.

Simulation of Coupled Processes in a Two-Dimensional West-East Cross-Section of Yucca Mountain, Nevada

12.2.2 Hydrostratigraphy

The hydrostratigraphy employed in the model is visualized in Figures 12.2.1 and 12.2.2.2 where permeabilities in the matrix and fracture continuum are shown, respectively. Figures 12.2.2.3 and 12.2.2.4 show the matrix and fracture α -parameters of the van Genuchten model. The matrix porosity field is depicted in Figure 12.2.2.5. The model consists of 23 hydrostratigraphic units and contains four faults. The hydrogeologic properties have been determined from laboratory measurements and inverse modeling, and are described in Chapter 3, Bandurraga et al. (1996). Most units are densely fractured. As shown in Chapter 6 (Doughty et al., 1996), the fracture-matrix system can be accurately represented by an Effective Continuum Model (ECM) whenever steady-state conditions prevail. The ECM model is described in Pruess and Tsang (1994) and Chapter 4 (Wu et al., 1996). For highly transient simulations, however, where changes of fluid pressures, temperatures, and phase compositions propagate rapidly through the fractures, while invading the tight matrix blocks much more slowly, fluid and heat flow from the fractures into the matrix and vice versa has to be modeled explicitly. We employ the method of Multiple Interacting Continua (MINC; Pruess and Narasimhan, 1982, 1985; Pruess, 1991). The MINC method is a generalization of the classic dual-porosity concept where fracture-matrix flow is modeled by means of one-dimensional strings of nested grid blocks. The MINC approach is more general as it allows for global flow in both fracture and matrix continua. In this study, only two continua are specified, and global fracture-fracture as well as matrix-matrix flow is considered, i.e. we use a dual-porosity, dual-permeability approach to model the fractured-porous units at Yucca Mountain.

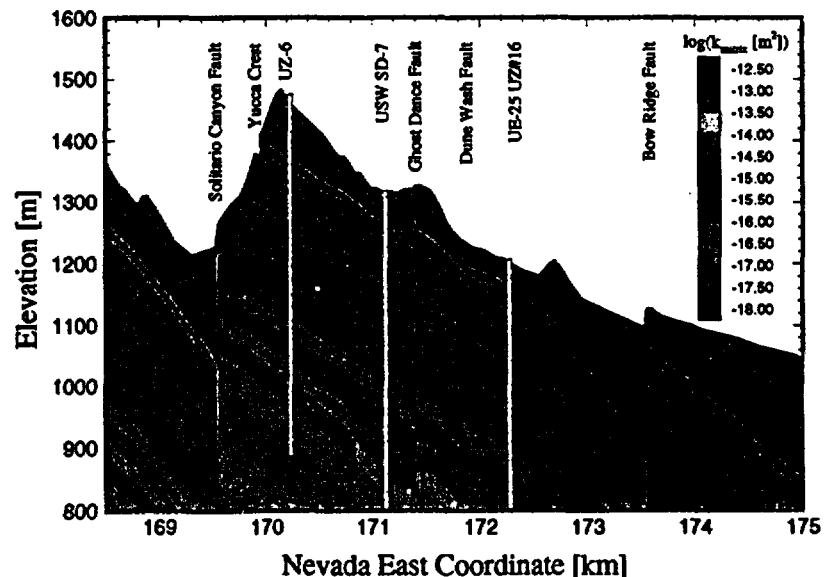


Figure 12.2.2.1
Matrix permeabilities.

Simulation of Coupled Processes in a Two-Dimensional West-East Cross-Section of Yucca Mountain, Nevada

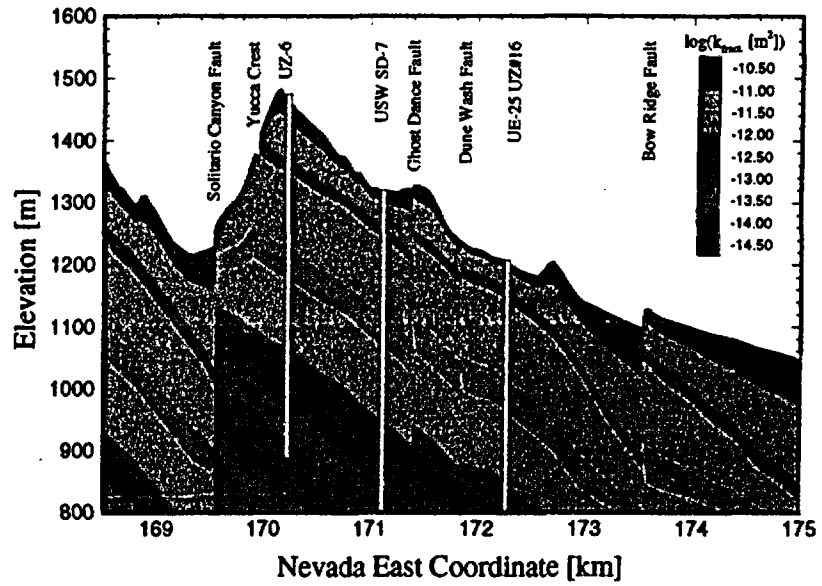


Figure 12.2.2.2
Fracture permeabilities.

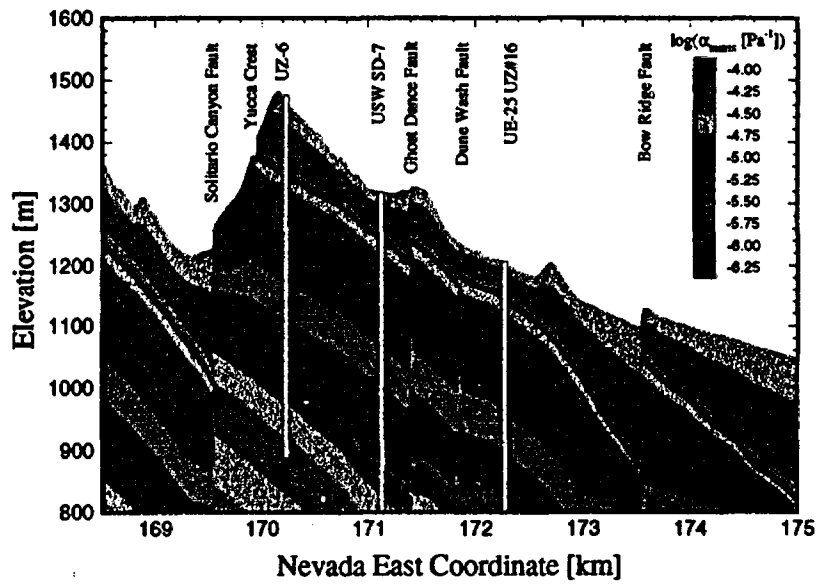


Figure 12.2.2.3
Matrix α -parameters of the van Genuchten model.

Simulation of Coupled Processes in a Two-Dimensional West-East Cross-Section of Yucca Mountain, Nevada

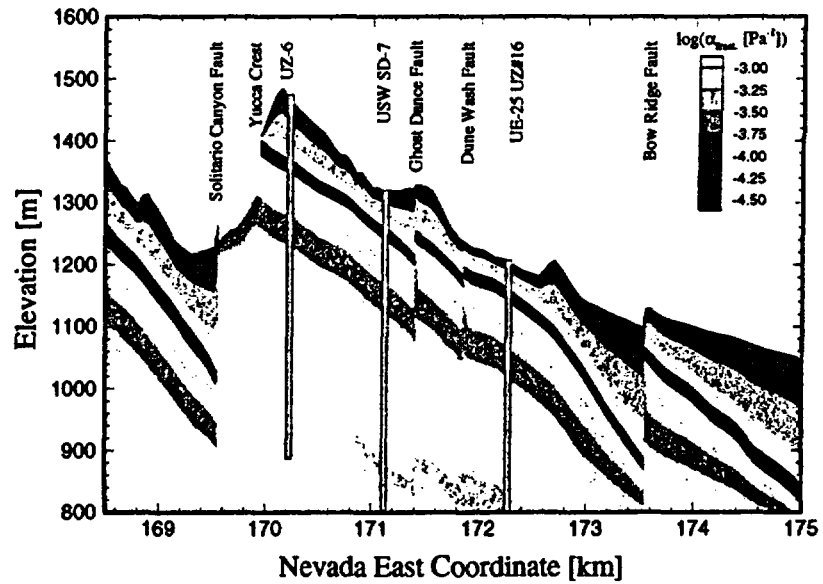


Figure 12.2.2.4.
Fracture α -parameters of the van Genuchten model

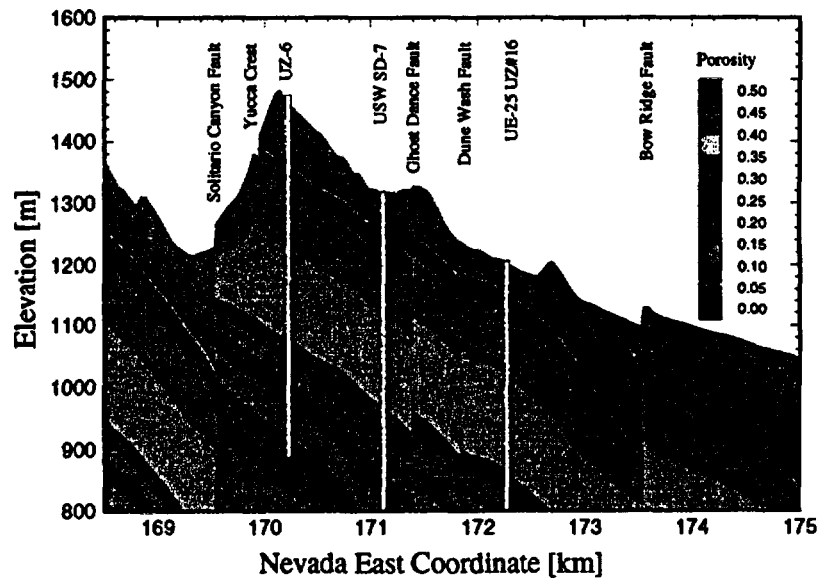


Figure 12.2.2.5.
Matrix porosities.

12.2.3
Initial and Boundary
Conditions

Boundary conditions for all steady-state runs have been selected as follows. We first deal with the land surface where atmospheric conditions are prescribed. In order to arrive at elevation-dependent atmospheric conditions, a numerical, one-dimensional, gas-filled column was set up. Based on data at Yucca Crest (Thorstenson et al. 1989), an average temperature of 15.9 °C at elevation 1484 m was prescribed, and a temperature of 19.9 °C was fixed at an elevation of 1084 m, corresponding to a lapse rate of 0.01 °K/m. Gas pressure at Yucca Crest was set to 85 kPa, and relative humidity was assumed to be 20%. A high-resolution simulation to steady state was performed with a no flow boundary at the bottom, yielding a static gas pressure profile under non-isothermal conditions. The resulting pressures, temperatures, and air mass fractions were then assigned to the 2-D model according to the elevation of each boundary grid block of the cross-section.

Next, a single-phase gas simulation with the 2-D model assuming 100% relative humidity was performed, yielding gas pressures at the water table where temperature was fixed at 32 °C. The resulting pressures, which are on the order of 93 kPa, were then fixed at the bottom boundary, and saturation was set to one at the water table and 0.3 elsewhere. A variable recharge rate which is based on an infiltration map provided by A. Flint, USGS, was specified at the surface (Figure 12.2.3.1). The average flow rate over the model domain is about 3 mm/year, with regions of high infiltration up to 20 mm/year, and very small infiltration, for example, east of the Bow Ridge fault. The enthalpy of the infiltration water was assumed to be 75.6 kJ/kg, which corresponds to a temperature of 18 °C. The system was run to steady state using the ECM formulation, yielding the pressure, temperature, and saturation distribution in both the fractures and the matrix under capillary-gravity equilibrium for the assumed infiltration rate and elevation-dependent atmospheric conditions. These results are described in Section 12.3. The system state from the ECM simulation are then transferred to the corresponding MINC model. This result will be used as the initial condition for the subsequent transient runs described in Sections 12.4 and 12.5.

Simulation of Coupled Processes In a Two-Dimensional West-East Cross-Section of Yucca Mountain, Nevada

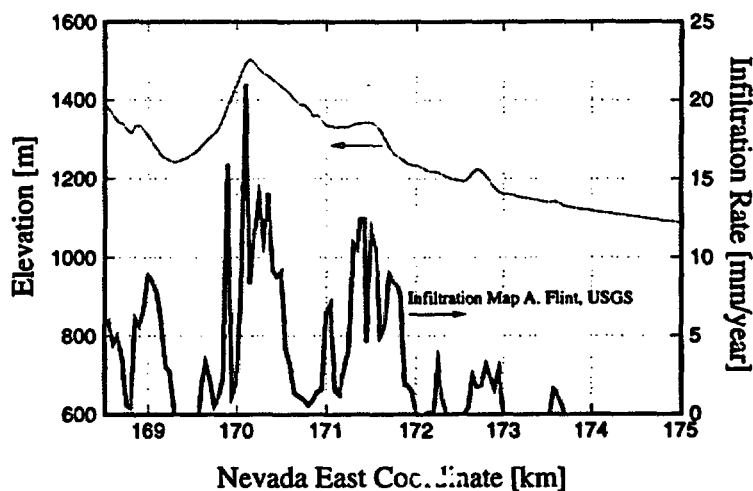


Figure 12.2.3.1

Infiltration rates applied at the surface of the model, interpolated from infiltration map provided by A. Flint, USGS.

12.3 Steady-State Conditions

In this chapter we describe the results of the steady-state simulation. Steady-state conditions are considered important since they reflect the long term behavior of the system. Most of the field data are considered to represent steady-state or near steady-state conditions. We compare the simulation results with saturation, water potential, and temperature data.

12.3.1 Saturation

The saturation and water potential data were obtained from cores and drill cuttings. The drilling and coring methods as well as the collection of drill cuttings are reported to only minimally disturb the water content of the rock (see for example Loskot (1993) and references therein). Saturation was derived by first measuring a composite gravimetric water content using oven-drying methods. Bulk- and grain-density measurements were performed to calculate porosity and eventually saturation. We compare our modeling results with saturation data from boreholes SD-7, UZ#16 and UZ-6s. More details about the data can be found in Chapter 3, Bandurraga et al. (1996).

Figures 12.3.1.1 and 12.3.1.2 show the simulated saturation distribution in the matrix and fracture continuum, respectively. In the non-welded PTn unit, where no fracture continuum exists, saturations in the two figures are identical.

Simulation of Coupled Processes in a Two-Dimensional West-East Cross-Section of Yucca Mountain, Nevada

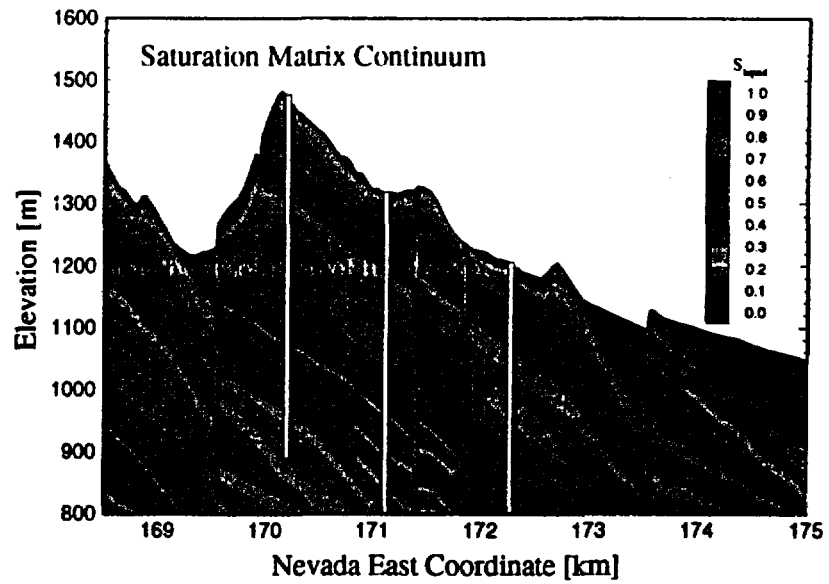


Figure 12.3.1.1
Simulated saturation distribution of matrix continuum.

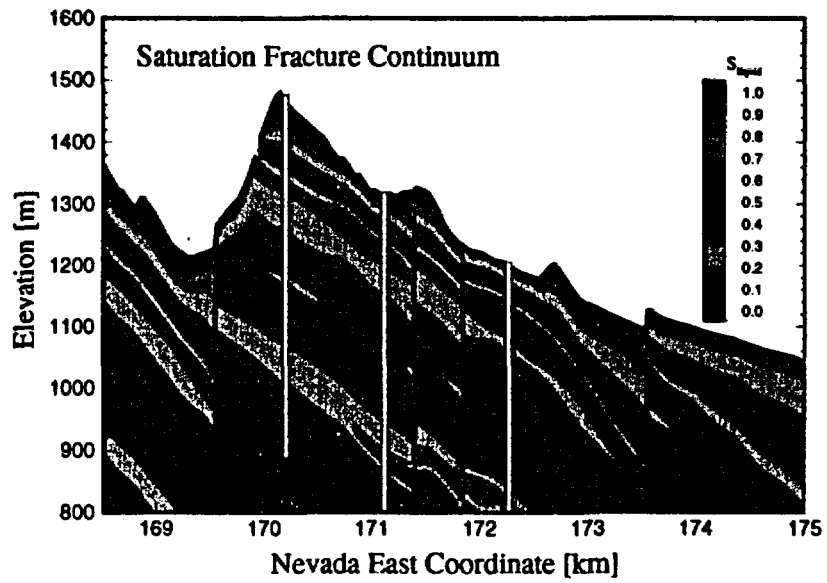


Figure 12.3.1.2
Simulated saturation distribution of fracture continuum.

Simulation of Coupled Processes in a Two-Dimensional West-East Cross-Section of Yucca Mountain, Nevada

The saturation pattern mainly reflects the ratio in capillary strength between the fractures and the matrix, and between adjacent units. Deviations from this general observation are a result of variable infiltration rates, lateral flow diversion, and the impact of the faults. For example, elevated saturations are seen between coordinate 169.8 and 170.6 km, and again between 171.0 and 171.8 km, where higher infiltration rates are applied (see Figure 12.2.3.1). On the other hand, dryer conditions are encountered east of the Bow Ridge Fault where low infiltration rates are assigned. Furthermore, due to the west-east tilting of the layers, water tends to accumulate west of the faults until the saturation is high enough to enter the fault zone (Wittwer et al., 1995). Saturations tend to be high in the Tiva Canyon above the non-welded Paintbrush unit, in the vitrophyre layers of the Topopah Spring, and above perching layers such as the zeolites of the Calico Hills formation.

Comparisons between the calculated and measured saturation profiles in boreholes SD-7, UZ#16, and UZ-6s are shown in Figures 12.3.1.3, 12.3.1.4, and 12.3.1.5, respectively. The match is comparable to the one obtained by calibrating the one-dimensional columns (Chapter 3, Bandurraga et al., 1996).

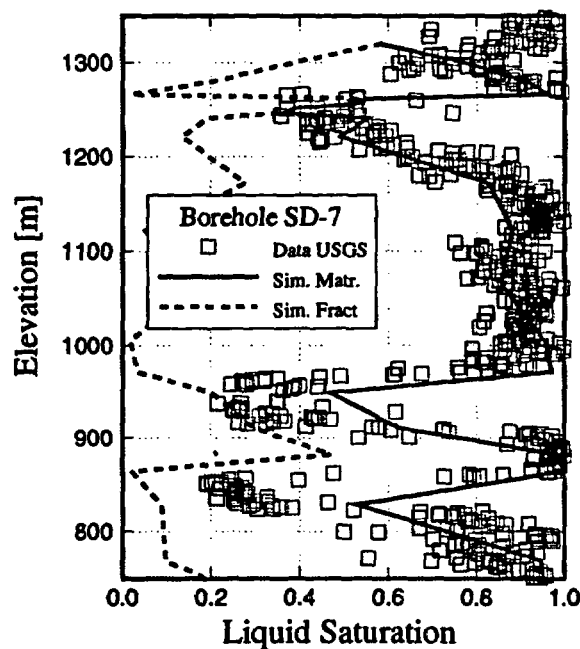


Figure 12.3.1.3
Comparison between calculated and measured saturation profile in borehole SD-7. Data from L. Flint, USGS.

Simulation of Coupled Processes in a Two-Dimensional West-East Cross-Section of Yucca Mountain, Nevada

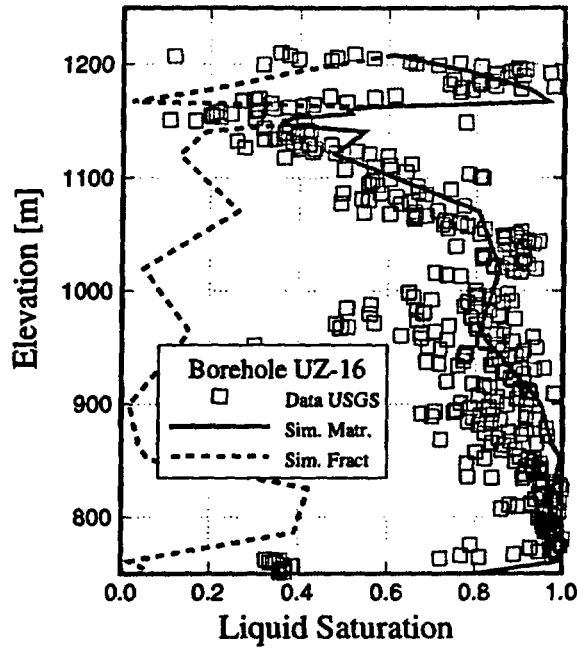


Figure 12.3.14
Comparison between calculated and measured saturation profile in borehole UZ#16. Data from L. Flint, USGS.

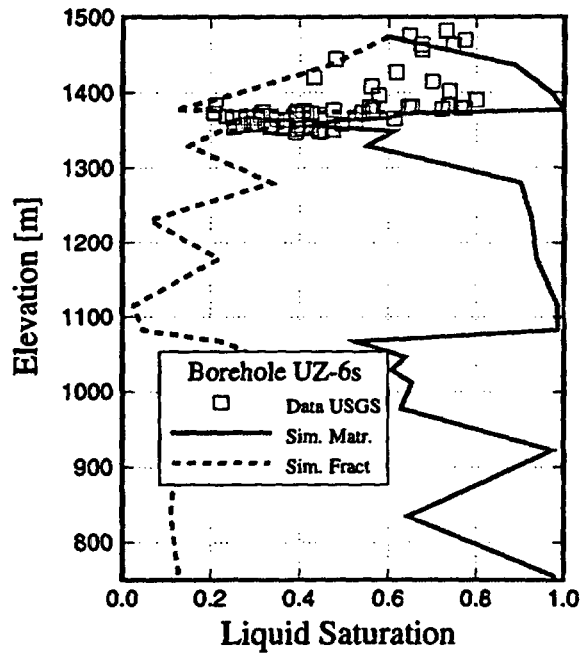


Figure 12.3.15
Comparison between calculated and measured saturation profile in borehole UZ-6s. Data from C. Loskot, USGS.

Simulation of Coupled Processes in a Two-Dimensional West-East Cross-Section of Yucca Mountain, Nevada

12.3.2 Water Potentials

Figure 12.3.2.1 shows the modeled capillary pressure distribution. The water potential in the fracture and matrix continuum are identical at steady-state due to the equilibrium assumption of the effective continuum concept. Figure 12.3.2.2 shows a comparison between the calculated and observed water potentials at borehole SD-7. The comparison is rather poor mainly due to difficulties with capillary pressure measurements at suctions near zero, and in obtaining measurements that represent in-situ conditions on the scale of a grid block.

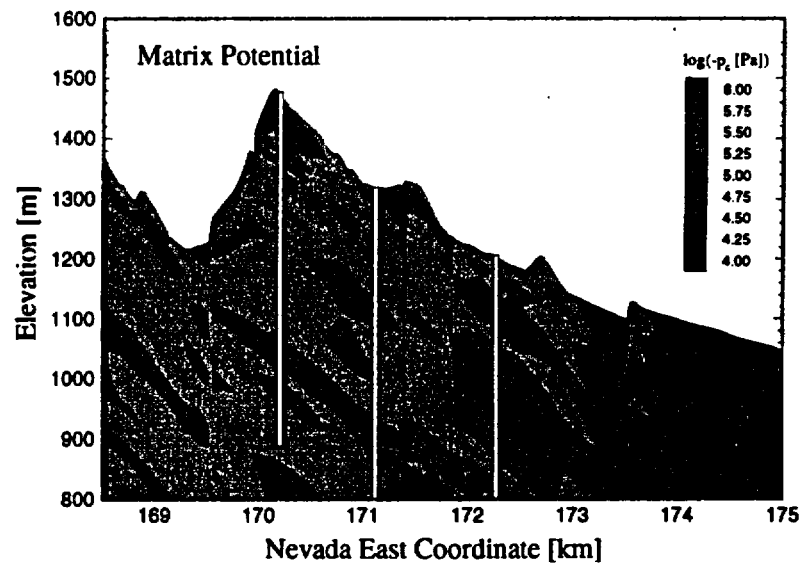


Figure 12.3.2.1
Modeled water potential distribution.

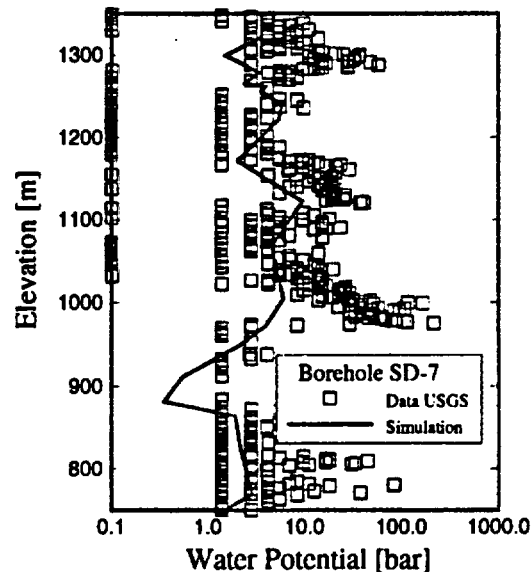


Figure 12.3.2.2 Comparison between calculated and observed water potentials in borehole SD-7. Data from L. Flint, USGS.

12.3.3
Temperature

Following up on the discussion of results described in Chapter 9 (Bodvarsson et al., 1996), we examine the temperature gradients within our cross-sectional model and compare them to the prescribed infiltration rate. The hypothesis is that changes in temperature gradients within the unsaturated zone are primarily due to heat consumption caused by infiltration water. Geothermal heat flows upwards mainly by conduction and - to a lesser extent - convection of latent heat in the vapor phase. Part of this energy is consumed in order to bring the temperature of the downwardly percolating water into thermal equilibrium with the surrounding rock. Provided that thermal conductivity and the total heat flux is known, measuring temperature gradients is considered a means to estimate percolation flux. Furthermore, assuming that lateral flow of liquid and heat is relatively small, the estimated percolation flux can be related to the infiltration rate. This hypothesis is numerically tested using the calculated temperature distribution shown in Figure 12.3.3.1 as a synthetic data base. Recall that the model uses a variable infiltration rate, and that temperatures are kept constant at the water table and the surface. Conductive and convective heat flow is considered where the heat conductivity is a function of saturation. Consumption, transport, and release of latent heat due to evaporation, vapor flow in the gas phase, and condensation, is also taken into account. The resulting heat flow pattern is shown in Figure 12.3.3.2. We notice lower heat flow rates underneath high infiltration regions (see also Figure 12.2.3.1). Furthermore, strong perturbations can be observed within and in the immediate vicinity of the faults. Upward flow of humid air in the faults generally increases heat flow. On the other hand, condensation and generally higher saturations especially west of the faults lead to increased percolation fluxes and thus lower vertical heat flow immediately next to the faults. A more quantitative examination of temperature, heat flux and their correlation to percolation flow rates are discussed in the remainder of this section.

Simulation of Coupled Processes in a Two-Dimensional West-East Cross-Section of Yucca Mountain, Nevada

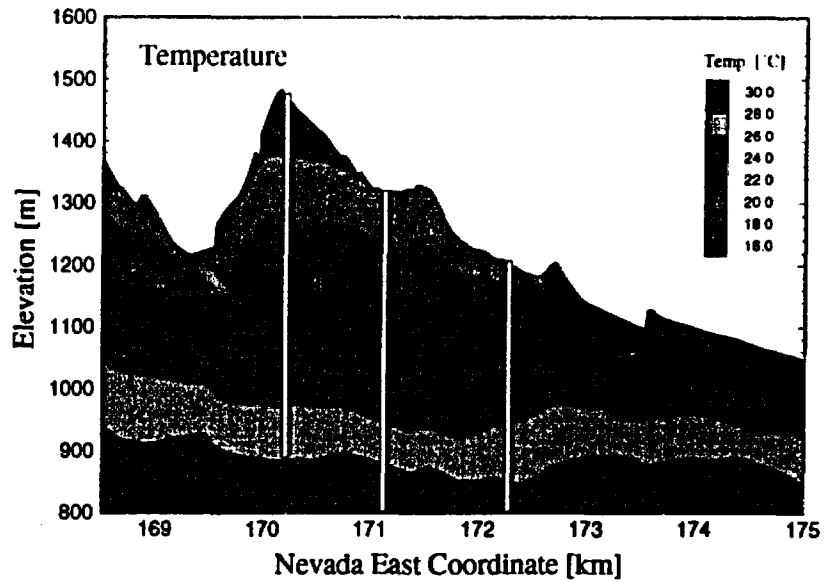


Figure 12.3.3.1
Simulated temperature distribution.

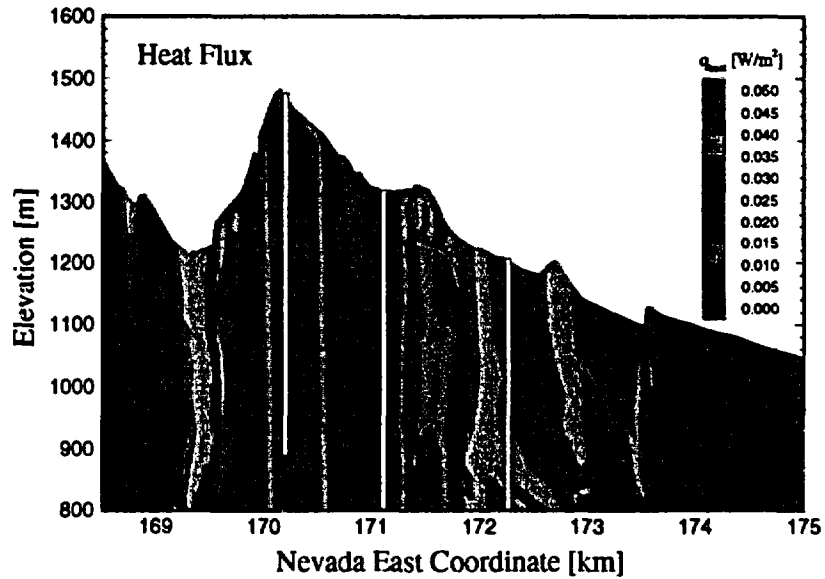


Figure 12.3.3.2
Vertical heat flux.

From the temperature distribution shown in Figure 12.3.3.1, we extract the temperature T and elevation z of the top and bottom elements of the Topopah Spring unit, and calculate the gradient $\Delta T/\Delta z$ (see Figure 12.3.3.3). No data from the faults themselves are analyzed, since they are expected to be inconsistent with the flow processes in the undisturbed tuffs. The gradients are continuous. Next, the liquid flow rate in the center of the Topopah Spring layer is used to represent percolation flux. A total of 135 simulated gradients and flow rates were evaluated along the profile. The percolation flux is then plotted against the temperature gradient (Figure 12.3.3.4). Low percolation fluxes seem to be related to higher temperature gradients, and high rates tend to be associated with low gradients, as suggested by the heat balance consideration. A regression line was fitted through the synthetic data despite considerable scattering. The regression line is very close to the theoretical one derived from a simple one-dimensional energy balance equation where the geothermal heat flux $E = 45 \cdot 10^{-3} \text{ W/m}^2$ is equated to the sum of conductive upward heat flow and the downward energy flux in the percolation water:

$$E = \lambda \cdot \nabla T - q_l \cdot \rho_l \cdot c_l \cdot \Delta T \quad (12.3.3.1)$$

Here, $\lambda = 1.73 \text{ W/m}^\circ\text{C}$ is heat conductivity, q_l is the volumetric liquid flow rate, $\rho_l = 1000 \text{ kg/m}^3$ is water density, $c_l = 4187 \text{ J/kg}^\circ\text{C}$ is the specific heat of liquid water, $\Delta T = 14 \text{ }^\circ\text{C}$ is the temperature change the downwardly percolating water undergoes as it moves from the surface to the water table. For zero and 10 mm/year percolation flux, the temperature gradient amounts to approximately 2.6 and 1.5 $^\circ\text{C}/100 \text{ m}$, respectively, which is consistent with the slope of the fitted line shown in Figure 12.3.3.4.

The scattering seen in Figure 12.3.3.4, i.e. the deviation of the actual percolation flux from the one predicted by the regression model, is an indication of lateral heat flux. The heat anomalies are a result of flow diversions within Topopah Spring, variable thickness of the unsaturated zone, changes in saturation leading to changes in the heat conductivity, and the impact of vertical features such as faults. Moreover, lateral heat flow is also affected by the variability in the percolation flux itself. The combined effect of the above factors leads to local temperature gradients which are not consistent with the general correlation represented by the straight line in Figure 12.3.3.4.

Figure 12.3.3.5 is an attempt to localize regions with a strong anomaly regarding the relation between temperature gradient and percolation flux. In Figure 12.3.3.5, the data points from the previous figure are connected according to the East coordinate of the sample location, so that the origin of individual data points and their position with respect to faults can be identified. We first note that the above mentioned relationship between temperature gradient and percolation flux is locally violated in many places. For example, starting at the western model boundary, the temperature gradients increase despite increasing

percolation fluxes. A similar behavior can be observed when approaching the Dune Wash Fault from the west. Crossing the Solitario Canyon Fault leads to a reduced temperature gradient despite an almost constant percolation flux. On the other hand, a constant temperature gradient is seen west and East of the Ghost Dance Fault despite a doubling of the water flow rate. Almost no effect of the Bow Ridge Fault can be seen which happens to be in an area of generally low and almost constant infiltration. This is remarkable because the Bow Ridge Fault exhibits a rather large offset. The differences in behavior reflect the variability of the factors that cause the anomaly. A detailed energy balance calculation including horizontal and vertical heat flow by conduction, convection, and diffusion would be extremely useful to explain the entire thermal regime at Yucca Mountain.

The regression line relating temperature gradient and percolation flux cannot be directly measured in the field. Simple one-dimensional energy balance calculations or modeling studies such as the one presented here have to be performed. Furthermore, independent estimates of heat conductivity are required. The potential error made by using a regression line for infiltration rate estimation is qualitatively depicted in Figure 12.3.3.4. We finally estimate the infiltration rate using the regression line shown in Figure 12.3.3.4 and the "observed" temperature gradients shown in Figure 12.3.3.3. We further make the assumption that liquid flow is predominantly vertical. The estimated infiltration rate using this method is shown in Figure 12.3.3.6, and is compared to the actually prescribed infiltration rate. The general pattern of relatively high and low infiltration rates is reasonably well reproduced. The average flux over the entire cross-section is about the same, a result of the straight-line fit shown in Figure 12.3.3.4. Small-scale fluctuations are not identified due to the diffusive nature of heat and fluid flow in the unsaturated zone.

We conclude that temperature gradient measurements provide a means for estimating percolation fluxes or even infiltration rates. This conclusion is based on the assumption that the linear regression model derived here is correct. It further assumes that independent estimates of heat conductivity are available, and that accurate temperature measurements in a layer of relatively uniform saturation and predominantly vertical heat and fluid flow can be made. Temperature gradients should be measured in regions that are not affected by the fault zones. A large number of temperature gradient measurements are required to obtain an integral measure of infiltration rate and its uncertainty.

The local, two- and three-dimensional effects discussed above, as well as complicated coupled heat and fluid flow processes have a relatively large impact on the temperature distribution. The actual percolation flux may be locally quite different from the one estimated with a simple regression model, as shown in Figure 12.3.3.4. Uncertainty in the input parameters should be related to the potential errors made by neglecting lateral heat flow phenomena.

Simulation of Coupled Processes in a Two-Dimensional West-East Cross-Section of Yucca Mountain, Nevada

These conclusions should be confirmed in laboratory and large-scale percolation experiments, along with three-dimensional modeling studies. A detailed sensitivity analysis is required to further assess the uncertainty of the estimated infiltration rates.

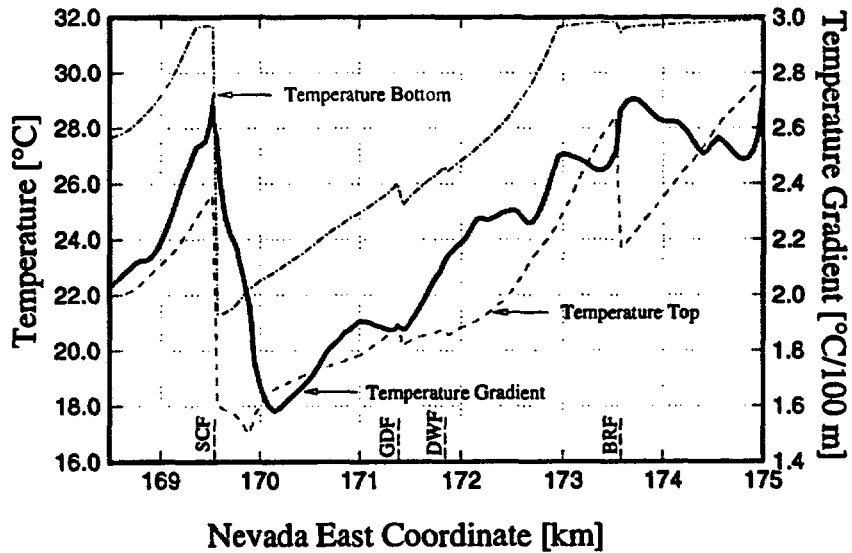


Figure 12.3.3.3
Calculated temperature and temperature gradient in Topopah Spring along the profile.

Simulation of Coupled Processes In a Two-Dimensional West-East Cross-Section of Yucca Mountain, Nevada

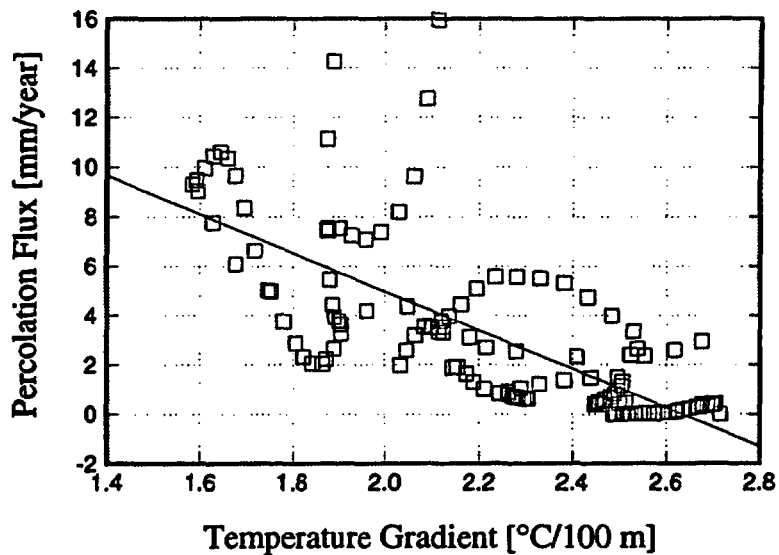


Figure 12.3.3.4
Calculated percolation flux as a function of temperature gradient.

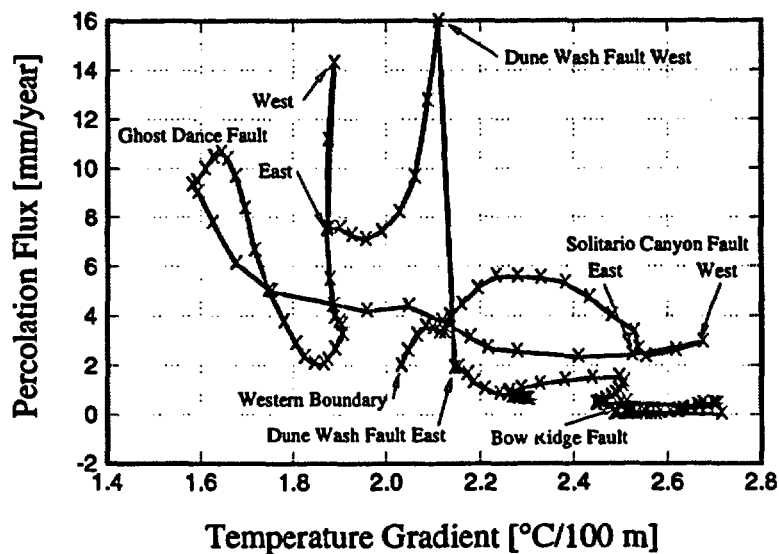


Figure 12.3.3.5
Impact of faults on temperature gradient and percolation flux.

Simulation of Coupled Processes in a Two-Dimensional West-East Cross-Section of Yucca Mountain, Nevada

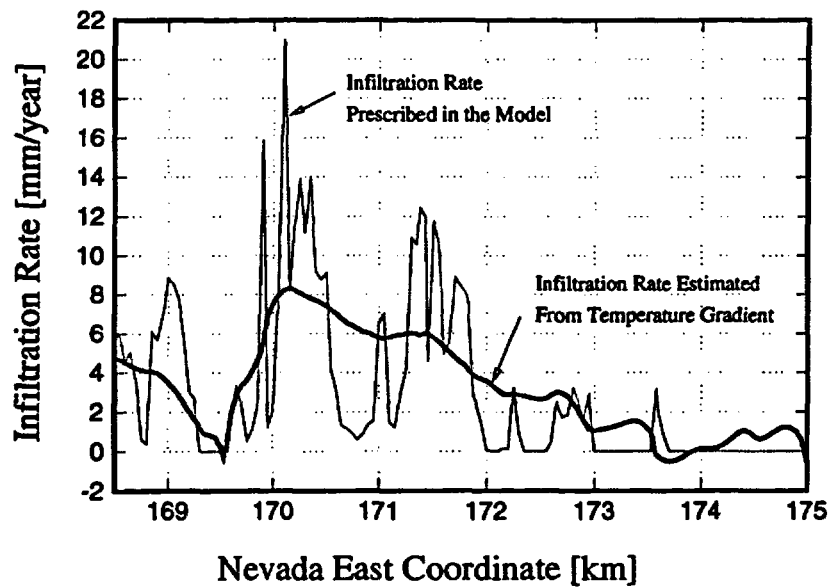


Figure 12.3.3.6
Infiltration rate estimated from simulated temperature gradient data, compared to actually prescribed infiltration rate.

In Figures 12.3.3.7 and 12.3.3.8, the calculated temperatures are compared to two profiles of nearby boreholes, USW H-3, and USW UZ-7a, respectively. The offset between the calculated and observed temperature profiles are mainly due to differences in the boundary conditions. Observed temperature data near the surface are affected by seasonal variations, whereas the calculated temperature near the water table is affected by the constant temperature boundary condition. Nevertheless, The temperature gradient is reasonably well reproduced.

Simulation of Coupled Processes in a Two-Dimensional West-East Cross-Section of Yucca Mountain, Nevada

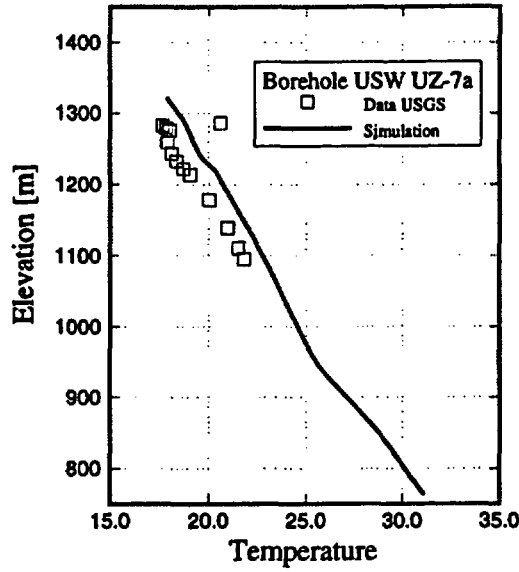


Figure 12.3.3.7
Comparison between calculated and measured temperature profiles in borehole UZ-7a. Data from Rousseau, USGS.

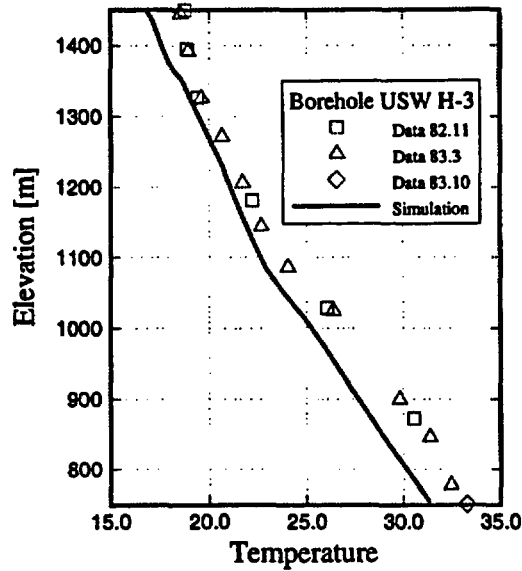


Figure 12.3.3.8
Comparison between calculated and measured temperature profiles in borehole H-3. Data from Sass, USGS.

12.4 Gas Flow

12.4.1 Introduction

Gas flow and pneumatic pressure propagation at Yucca Mountain has been studied in detail by Ahlers et al. (1996). The gas flow pattern may provide indications regarding permeability and connectivity of faults and fractures. The gas phase has the potential to transport significant amounts of heat energy and water in form of vapor, affecting temperature and saturation distribution under both ambient conditions and after emplacement of heat-generating waste packages. Furthermore, gas and vapor flow may be an important transport mechanism for certain radionuclides such as ^{14}C and tritium.

Data reflecting gas flow at Yucca Mountain include (1) measurements of gas flow in two unlined boreholes (UZ-6 and UZ-6s) near Yucca Crest (Weeks, 1987, 1991; Thorstenson et al., 1990), (2) isotopic gas age measurements (Yang et al., 1985; Thorstenson et al., 1990), and (3) pneumatic pressure data (Rousseau et al., 1995; Patterson, 1996).

We study the gas circulation pattern assuming steady-state flow conditions and estimate gas ages (see Section 12.4.2). Response of gas pressures to atmospheric pressure changes are studied in Section 12.4.3.

12.4.2 Gas Circulation Pattern

Gas flow measurements at boreholes UZ-6s and UZ-6 have been correlated to changes in temperature, relative humidity, barometric pressure, and wind conditions near Yucca Crest (Weeks, 1987, 1991; Thorstenson et al., 1990). The boreholes continuously outflow gas during wintertime. Lower rates or even flow reversal can be observed during summertime. About 80% of the total gas flux observed at the borehole head enters the borehole in the top 30 meters (Thorstenson et al., 1990).

Several mechanisms have been identified as the driving force for gas flow near Yucca Crest (Weeks, 1987, 1991; Thorstenson et al., 1989), namely (1) topographic-induced flow due to temperature and density gradients between the air column in the atmosphere and the gas in the pore space, (2) barometric pressure changes, and (3) wind effects. We focus here on the long-term gas flow pattern as a result of thermal and topographic effects. The high influx of gas near the top of the borehole is not considered here because of insufficient resolution of that zone in the model.

Figure 12.4.2.1 shows the liquid saturation in the fracture continuum and the gas flow pattern, visualized by particle tracking. Gas flow pattern and travel times are highly sensitive to small changes in the parameters, boundary

Simulation of Coupled Processes in a Two-Dimensional West-East Cross-Section of Yucca Mountain, Nevada

conditions, and the flow dimensionality. Nevertheless, the following general observations can be made.

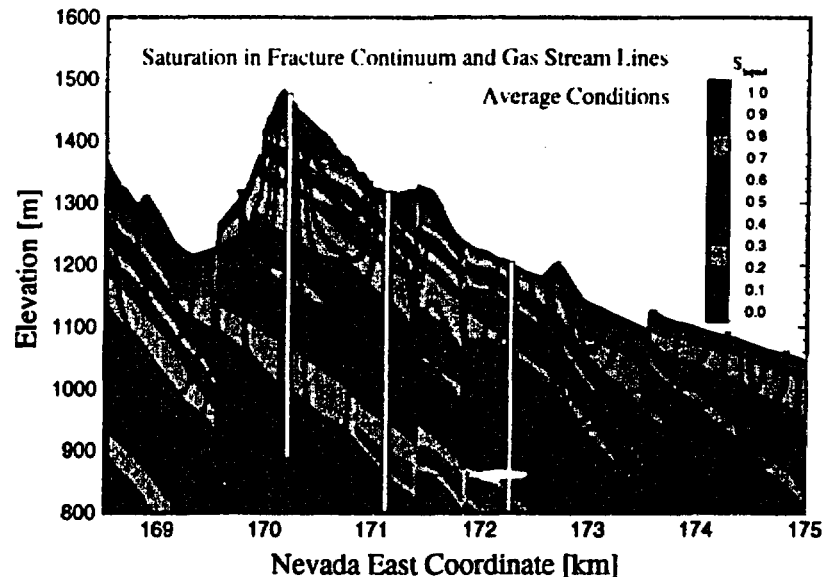


Figure 12.4.2.1

Calculated liquid saturation in fracture continuum and gas particle tracks. Travel time between each mark is 100 years.

Gas flow cells develop almost independently between major faults. Gas flux in the faults tends to be high and of changing flow direction, depending on its location with respect to topographic features such as depressions, slopes, or ridges. For example, the Solitario Canyon fault, which is located in a topographic low, exhibits gas intake, with a clockwise gas flow cell developing to the west and an anti-clockwise circulation cell developing to the east. This is a relatively stable flow pattern. The situation east of Yucca Crest is less stable. The topographic effect tends to induce clockwise circulation cells, with gas intake at lower elevations and outflow towards the higher elevations. However, these circulation cells are interrupted by the faults and local variations in surface elevation. The Ghost Dance fault encounters upward gas flow from the cell to its east, and tentatively downward flow to its west. Since it is located on a small topographic high, the net gas flow direction is upward. These flow patterns are likely to be changed by small daily and seasonal variations in boundary conditions.

Even under averaged annual conditions, travel times within the Tiva Canyon are relatively short, especially towards Yucca Crest, leading to gas ages less than 100 years near the surface. Wind as an additional driving force may further enhance gas circulation at shallow depths (Weeks, 1991). Note, however, that local variations may occur with relatively old gases in regions where gas flow is predominantly upward. In general, gas travel times beneath the Paintbrush unit are predicted to be much longer, on the order of 10^4 years, which is

Simulation of Coupled Processes in a Two-Dimensional West-East Cross-Section of Yucca Mountain, Nevada

consistent with the observed gas ages from isotope data (Yang et al., 1985; Thorstenson et al., 1990).

12.4.3 Barometric Pressure Response

The response to barometric pressure fluctuations at the surface was observed in specially instrumented boreholes such as USW NRG-6, USW NRG-7a (Rousseau et al., 1995), and SD-7 (Patterson, 1996). The reduction of amplitude and increase of time lag with depth was used to estimate effective gas diffusivity (Ahlers et al., 1996). It was further shown, that the construction of the Exploratory Studies Facility (ESF) has a significant effect on the observed pneumatic data, with an increase of amplitude and the appearance of a low frequency signal (Rousseau et al., 1996; Ahlers et al., 1996).

Recent data from borehole SD-7 (Patterson, 1996) cover a period before and after the construction of the ESF. In the numerical model, we prescribe the barometric pressure at the surface as a function of time, and - after the ESF is in place - also in the grid block representing the tunnel. Simulated pneumatic pressures are recorded at the depths of the sensors, and compared to the data. There is excellent agreement between the observed data (symbols) and the simulation results (solid lines) as shown in Figure 12.4.3.1.

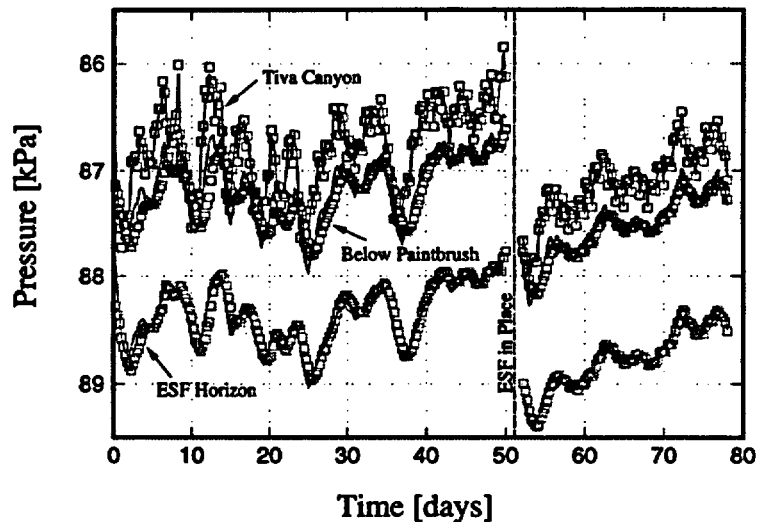


Figure 12.4.3.1
Simulated and observed pneumatic response to barometric pressure fluctuations in SD-7.
Preliminary data from USGS (Patterson, 1996).

12.5 *Liquid Flow and Transport*

12.5.1
Liquid Flow Rates

No direct observation of liquid flow rates are available, so only simulation results are discussed in this section. In Figure 12.5.1.1, total saturation, which is close to the matrix saturation, is contoured, overlaid by a vector plot of the total liquid flow rate. Recall the vertical exaggeration of 6:1. The vertical flow component is visualized in Figure 12.5.1.2, along with vectors showing the horizontal flux component. Liquid flow is predominantly downward, and mirrors the infiltration pattern (see Figure 12.2.3.1). However, there are significant lateral flow diversions at sloping interfaces, especially on top of the non-welded Paintbrush unit, and between Topopah Spring and Calico Hills. Liquid tends to be diverted along the sloping interfaces until high saturations are built up or a fault zone is encountered. Saturation and vertical flow components are increased immediately west of a fault. It is important to realize that the flow vectors shown in Figure 12.5.1.2 represent average Darcy fluxes over the thickness of the corresponding grid blocks. Actual pore water velocities in the relatively thin water layer above perching units may be much higher. The indicated fluxes must therefore be interpreted with care, taking into account the thickness of the respective grid block, and, where horizontal flow becomes vertical, the aspect ratio of the element.

Simulation of Coupled Processes in a Two-Dimensional West-East Cross-Section of Yucca Mountain, Nevada

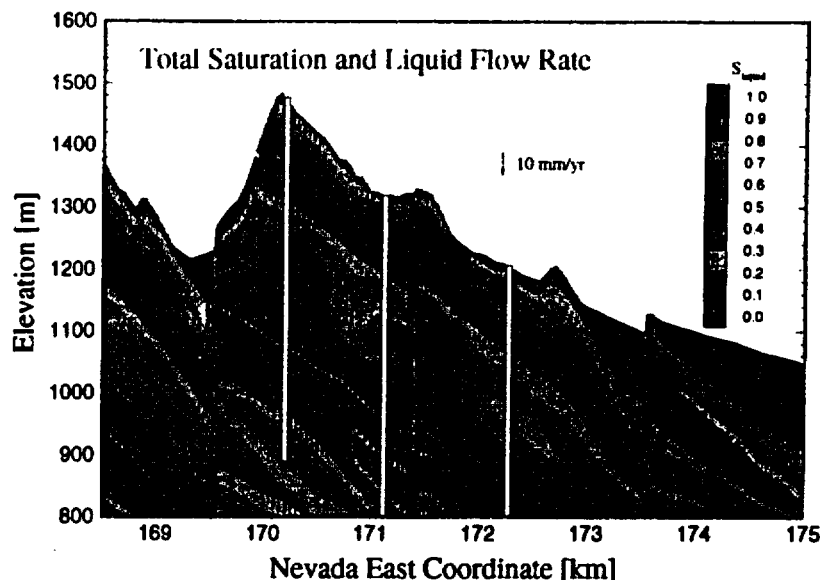


Figure 12.5.1.1
Total liquid saturation and liquid flow vectors.

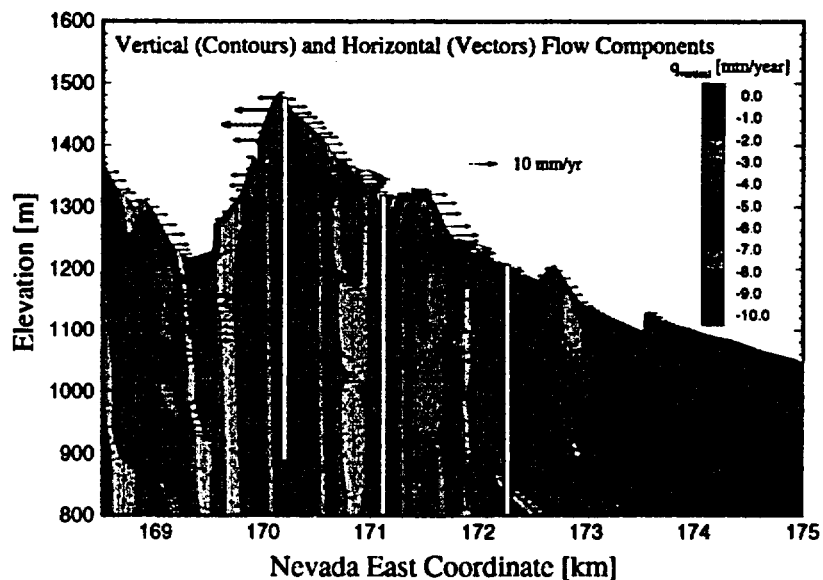


Figure 12.5.1.2
Vertical (contours) and horizontal (vectors) flow components.

12.5.2
Fast Path

A transient dual-porosity, dual-permeability simulation of a liquid pulse has been performed to identify potential fast paths for infiltration water. The presence of a bomb-pulse ^{36}Cl signal in the ESF (Fabryka-Martin et al., 1996) implies very short travel times from the surface to the repository horizon. Fol-

Simulation of Coupled Processes In a Two-Dimensional West-East Cross-Section of Yucca Mountain, Nevada

lowing an assumed infiltration event that leads to almost fully saturated conditions in the top layers of the Tiva Canyon unit, water and environmental tracers percolate predominantly through the fault zones, but also in the fracture network, which slightly affects the saturation in the adjacent matrix blocks. Figure 12.5.2.1 shows the simulated change of liquid saturation in the fracture continuum 50 years after release of the infiltration pulse. The deepest penetration of the pulse can be observed near the fault zones and underneath regions with generally high infiltration. Water flows through the fractures to the repository horizon and reaches the elevation of the ESF. Saturation in the fracture continuum is plotted as a function of time for five locations along the profile of borehole SD-7 (Figure 12.5.2.2). The liquid pulse reaches the bottom of the Tiva Canyon unit almost instantly, and about 2 years are required to pass the Paintbrush unit. In this simulation, the repository horizon is reached after 30 years, and the top of the Calico Hills after about 80 years. No significant increase in saturation can be observed near the water table at the end of the simulated period of 1000 years. Note, however, that travel times through the faults are extremely short (on the order of a few weeks to reach the water table). In summary, the presence of bomb-pulse ^{36}Cl in the ESF can be explained with the current site-scale model properties, provided that fracture flow is initiated by a high infiltration event. More discussion of chemical transport at Yucca Mountain can be found in this report (Chapter 6, Doughty et al., 1996; Chapter 8, Wu et al., 1996; Chapter 10, Fairley et al., 1996; and Chapter 11, Sonnenthal et al., 1996).

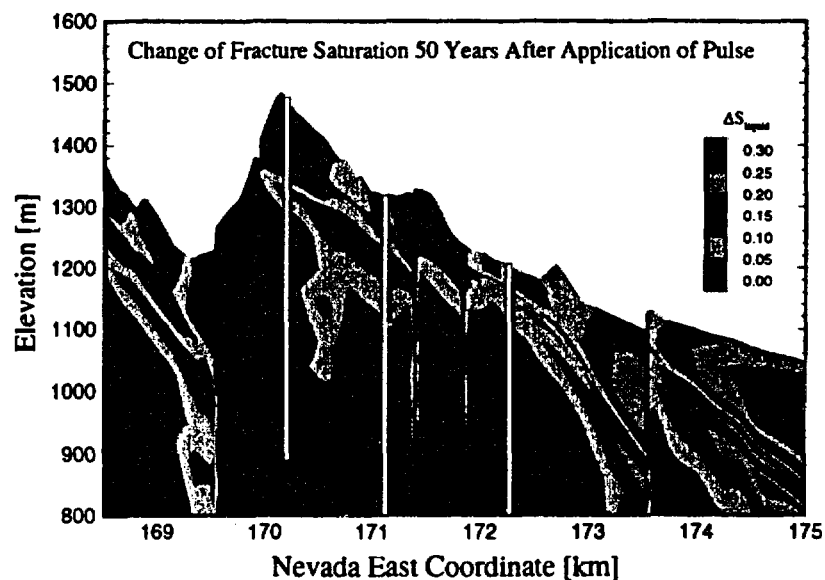


Figure 12.5.2.1
Simulated change of liquid saturation 50 years after release of infiltration pulse.

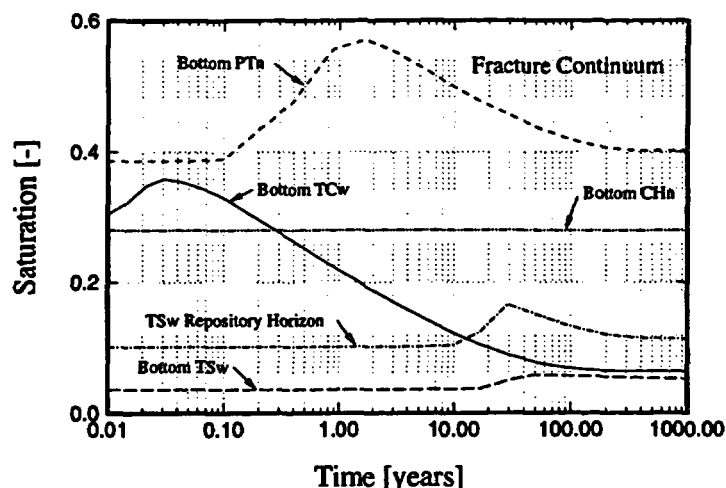


Figure 12.5.2.2
Simulated liquid saturation as function of time in fracture continuum, near borehole SD-7

12.6 Summary and Concluding Remarks

A number of numerical simulation studies in a dual-porosity, dual-permeability model of a two-dimensional west-east cross-section have been performed. The model includes the main features currently implemented in the LBNL/USGS 3D UZ site-scale model of Yucca Mountain. A variety of coupled processes on different spatial and temporal scales have been simulated, using a single conceptual model and a single parameter set which was determined independently from data inversion studies (Ahlers et al., 1996; Bandurraga et al., 1996, Chapter 3). The modeling results were compared to observed data whenever available, or discussed in a more qualitative sense to see whether they are able to reproduce the overall system behavior according to our current understanding.

The conclusions reached in this study are based on the parameter set derived under QA standards (see Chapter 3; Bandurraga et al., 1996, and references therein). The geologic model shown in Figures 12.2.2.1 through 12.2.2.5 is not yet Q. The simulation results are compared to a number of data, the QA status of which is summarized in Section 12.1.3. This work and its conclusions will be Q once the geological model and the data listed in Table 12.1.3.1 achieve Q status. At present this data may be considered as corroborating evidence for these conclusions. We believe that the qualitative conclusions derived in this study are scientifically valid.

Simulation of Coupled Processes in a Two-Dimensional West-East Cross-Section of Yucca Mountain, Nevada

As a general conclusion, the current conceptual model of the unsaturated zone at Yucca Mountain yields predictions that are consistent with a large variety of observations. The parameters used in the model seem reasonable in the view of the existing data. Modifications have to be made if (1) local conditions deviate from the average situation, (2) the process under consideration depends on parameters that could not be accurately determined due to a lack of sensitive data, and (3) the scale of the process differs from the one for which effective parameters have been identified.

More specifically, the observed saturation distribution was reasonably well reproduced assuming steady-state conditions. The modeling results show that variations are mainly due to variations in the infiltration pattern which are not well known. A detailed model has to be set up to address the issue of perched water. Water potentials are difficult to match mainly because of large uncertainties in the data and conceptual difficulties. The model reveals the sensitivity of temperature and heat flow to the percolation flux and infiltration rate. Measuring temperature gradients across a layer of more or less constant saturation may provide a means to estimate percolation flux.

Gas flow at Yucca Mountain exhibits a complicated circulation pattern, driven by topographic and thermal gradients, and other effects such as wind forces and the impact of faults. The observed gas ages are reasonably well reproduced by the model, considering the high sensitivity of the results to the applied boundary conditions and the large local variability of flow rates and flow direction. The pneumatic data responding to barometric pressure changes have been simulated, taking into account the effect of the ESF. The simulations results agree very well with the data observed in borehole SD-7.

The liquid flow pattern is again determined by the variable infiltration rates. The modeled flow field is predominantly vertical, with lateral diversions at contacts and due to variations in saturation and water potential. Note, however, that three-dimensional effects may be significant. Furthermore, prediction of transport in the liquid phase requires much higher resolution, especially near sloping layers of low vertical permeability, where water is accumulated and horizontally diverted in a thin layer of relatively high velocity.

Finally, a transient simulation of a high infiltration event demonstrates that small amounts of liquid and potential tracers may travel very fast through the mountain along faults and fractures, explaining the potential of detecting bomb-pulse ^{36}Cl concentration in the Topopah Spring unit.

The simulations discussed here were based on existing parameter sets, i.e. no new data was derived as a result of this modeling study.

12.7 References

- Ahlers, C. F., C. Shan, C. Haukwa, A. J. B. Cohen, G. S. Bodvarsson, Calibration and prediction of pneumatic response at Yucca Mountain, Nevada, using the LBNL/USGS three-dimensional, site-scale model of the unsaturated zone, Yucca Mountain Project Milestone OB12M, Lawrence Berkeley National Laboratory, Berkeley, CA, 1996.
- Fabryka-Martin, J. T., P. R. Dixon, S. Levy, B. Liu, H. J. Turin, and A. V. Wolfsberg, Summary report of Chlorine-36 studies: Systematic sampling for Chlorine-36 in the Exploratory Studies facility, Level 4 Milestone Report 3783AD, Los Alamos National Laboratory, Los Alamos, NM, 1996.
- Loskot, C.L., Geohydrologic Data From Test Hole USW UZ-6s, Yucca Mountain, Nye County, Nevada, Open-File Report 93-60, U.S. Geological Survey, Denver, Colorado, 1993.
ACCN:NNA.19930518.0073
DTN:GS921208312211.013 Non-Q
- Phillips, O. M., Infiltration of a liquid finger down a fracture into superheated rock, *Water Resour. Res.*, 32, 1665-1670, 1996.
- Patterson, G. L., Data transmittal of pneumatic pressure records from April 4, to June 27, 1996, for borehole USW SD-7, Yucca Mountain, Nevada, U.S. Geological Survey, Denver, Colorado, 1996.
- Pruess, K., TOUGH2 - A general-purpose numerical Simulator for Multiphase fluid and heat flow, Report LBL-29400 UC-251, Lawrence Berkeley National Laboratory, Berkeley, CA, 1991.
ACCN:NNA.19940202.0088
- Pruess, K, and T. N. Narasimhan, On fluid reserves and the production of superheated steam from fractured vapor-dominated geothermal reservoirs, *J. Geophys. Res.*, 87, (B11), 9329-9339, 1982.
ACCN: NNA.19900702.0038
- Pruess, K, and T. N. Narasimhan, A practical method for modeling fluid and heat flow in fractured porous media, *Soc. Pet. Eng. J.*, 25(1), 14-26, 1985.
ACCN: NNA.19890522.0235
- Pruess, K., and Y. W. Tsang, Thermal modeling for a potential high-level nuclear waste repository at Yucca Mountain, Nevada, Lawrence Berkeley National Laboratory Report LBL-35381 UC-600, Lawrence Berkeley National Laboratory, Berkeley, CA, 1994.
ACCN: HQO.19940506.0005
- Pruess, K., A. Simmons, Y. S. Wu, and G. Moridis, TOUGH2 software qualification, Lawrence Berkeley National Laboratory Report LBL-38383 UC-814, Lawrence Berkeley National Laboratory, Berkeley, CA, 1996.

Simulation of Coupled Processes in a Two-Dimensional West-East Cross-Section of Yucca Mountain, Nevada

- Rousseau, J. P., C. L. Loskot, J. Kume, M. Kurzmarck, N. D. Brian, K. Thomas, and A. J. Greengard, In-situ borehole instrumentation and monitoring data for USW NRG-7a and USW NRG-6, Yucca Mountain, Nye County, Nevada, 1995.
DTN:GS950208312232.003 Q
- Rousseau, J. P., E. M. Kwicklis, and C. Gillies, Eds., Hydrogeology of the unsaturated zone, north ramp area of the Exploratory Studies Facility, Yucca Mountain, Nevada, USGS WRI-96xxxx, U.S. Geological Survey, Denver, Colorado 1996 (draft.)
- Thorstenson, D. C., H. Haas, E. P. Weeks, and J. C. Woodward, Physical and chemical characteristics of topographically affected airflow in an open borehole at Yucca Mountain, Nevada, Proceedings of the Topical Meeting on Nuclear Waste Isolation in the Unsaturated Zone FOCUS '89, Las Vegas, NV, 256-270, September 17-21, 1989, American Nuclear Society, 1990.
ACCN:NNA.19900723.0196
DTN: GS930508312261.004 Non-Q
- Weeks, E. P., Effect of topography on gas flow in unsaturated fractured rock: concepts and observations, Geophysical Monograph 42, AGU, 165-170, 1987.
ACCN: HQS.19880517.3214
- Weeks, E. P., Does the wind blow through Yucca Mountain?, Proceedings of Workshop V: Flow and Transport through Unsaturated Fractured Rock - Related to High-Level Radioactive Waste Disposal, NRC, 43-53, 1991.
ACCN:MOL.19941006.0033
DTN: GS940608312261.003 Non-Q
- Wittwer, C., G. Chen, G. S. Bodvarsson, M. Chornack, A. Flint, L. Flint, E. Kwicklis, and R. Spengler, Preliminary development of the LBL/USGS three-dimensional site-scale model of Yucca Mountain, Nevada, Report LBL-37356, UC-814, Lawrence Berkeley National Laboratory, Berkeley, CA, 1995.
- Wu, Y. S., G. Chen, and G. Bodvarsson, Preliminary analysis of effects of thermal loading on gas and heat flow within the framework of the LBNL/USGS site-scale model, Report LBL-37729 UC-814, Lawrence Berkeley National Laboratory, Berkeley, CA, December 1995.
- Wu, Y. S., S. Finsterle, P. Frazer, and A. Simmons, Software qualification for ITOUGH2 and various equation-of-state (EOS) modules and auxiliary modules for TOUGH2 and ITOUGH2, Report Lawrence Berkeley National Laboratory, Berkeley, CA, August 1996 (draft).

Simulation of Coupled Processes in a Two-Dimensional West-East Cross-Section of Yucca Mountain, Nevada

Yang, I. C., H. H. Haas, E. P. Weeks, and D. C. Thorstenson, Analysis of gaseous-phase stable and radioactive isotopes in the unsaturated zone, Yucca Mountain, Nevada, Proceedings of the NWWA Conference on Characterization and Monitoring of the Vadose (Unsaturated) Zone, 488-506, 1985.

ACCN:NNA.19900403.0266

DTN: GS930508312271.021 Non-Q

**THERMAL LOADING STUDIES USING
THE UNSATURATED ZONE MODEL**

C. Haukwa, Y.S. Wu, and G.S. Bodvarsson

August 1996

13.1 Introduction

13.1.1 Importance of the Thermal Loading Studies

In addition to effects of natural geothermal heat flow, the heat generated as a result of nuclear waste emplacement within the repository will significantly affect fluid flow and heat transfer in the unsaturated zone and the saturated zone immediately below it. Quantitative evaluation of the thermohydrologic effects of thermal loading on the performance of the potential nuclear waste repository at Yucca Mountain is essential for characterization of the behavior of the unsaturated zone and site performance studies, as well as for adequate design of the engineering barrier at the repository.

Extensive studies of the effects of unsaturated zone thermal loading have been carried out (Busheck 1991, 1992, 1993; Duffner, 1993; Nitao, 1988; Pruess, 1990; and Ryder, 1990). All these studies predict extensive boiling due to thermal loading at the repository horizon dependent of the thermal load. The studies, however, do not explicitly include the geology nor do they use simplified horizontal layering along a cross-section.

In this chapter we examine the effects of thermal loading at the repository horizon using a 2-D vertical North-South cross-section (of the 3-D site-scale model), which crosses the entire repository block through its center, and extends about 500 meters below the water table. The model explicitly includes the (UZ-SZ) geological layering along the cross-section. Using this model, we investigate fluid and heat transfer in the unsaturated zone (UZ) and the long term response of the UZ and saturated zone (SZ) to thermal loading at the repository. The numerical simulations reported were carried out using the Q code TOUGH2 (Pruess, 1991).

13.1.2 Thermal Loading and the UZ Model

The effects of thermal loading on the ambient moisture and heat flow were studied using a North - South 2-D vertical cross-section model through the repository block area. Figure 13.1.1 shows the location of the 2-D cross-section A-A' used in this study. This cross-section through the repository block was chosen primarily because it crosses the longest extent of the repository. This section also allows us to investigate the influence of the N-S hydrogeologic layering and the vitric-zeolitic interface in the Calico Hills on fluid flow both at ambient condition and during thermal loading at the repository.

13.1.3
Thermal Goals

Thermal goals (temperature limits) for the rock units within and below the potential repository at Yucca mountain have been documented. (TRW, 1996). One of the temperature limits sets a maximum of 115°C for the interface of the Topopah Springs (TSw) tuff and the underlying Calico Hills (CHn) Non-welded units. This temperature limit was intended to address the concerns that mineralogical changes would occur due to dehydration or re-crystallization induced by repository heating. These changes could have physical and chemical consequences that could be detrimental to waste isolation (TRW, 1996). More recent studies indicate a thermal limit of 90-100°C is more appropriate for the zeolitic Calico Hills units, which are estimated to be about 100 m below the potential repository horizon (TRW, 1996). Another limit sets a maximum of 200°C at one meter distance from the repository drift wall, because silica phase inversion and temperature gradients can adversely affect the thermal mechanical stability of the repository walls. The thermal cladding limit of 350°C was set to address the potential for canister deterioration under thermal loading due to a combination of stress, corrosion and fatigue. Both the repository drift and the waste canisters are on a much smaller spatial scale than that addressed by the 3-D site-scale unsaturated zone model which is intended to provide mountain scale response to thermal loading. Therefore the site scale model will only be used to investigate the potential for violation of only the first thermal limit, i.e. 90-100°C, within the top Calico Hills zeolitic layers.

13.1.4
Purpose of this Study

The purpose of this study is to investigate the effect of repository thermal loading on the temperature distribution and fluid flow paths within the saturated and unsaturated zone. The adequacy of the unsaturated zone model and the ECM scheme in prediction of the evolution of temperature within the unsaturated zone will be explored. We further investigate the need for using a combined saturated-unsaturated zone model in simulating the UZ thermal response.

13.1.5
Modelling Approach

In this study the repository is represented by a 6.0 m thick zone which is over 4 km along the cross section with an average elevation of 1,070 masl. The repository horizon is modeled with a slope of a gradient of about 1% in order to maintain the repository at a minimum 50 m above the Calico Hills unit. This results in a nearly 40 m difference in elevation over the 4 km repository length. This is consistent with the 3-D model and it is designed to accommodate the dipping in the geological layering in the north, south and west boundaries of the repository domain (Chapter 5, this report). For thermal loading studies we assume that thermal loading at the repository horizon over the emplacement period can be represented by an equivalent uniform thermal load at an Area Power Density (APD) of 83 kW/acre. At this thermal load, equivalent generic total heat versus time decay curves (M&O, 1995) were used to provide a time dependent heat generation table. This provides a transient heat source at the repository. Under this thermal loading scenario, we performed numerical simulations for the following cases: 1) Net infiltration rate of 0.1 mm/year

using the ECM method; 2) Infiltration rate of 4.4 mm/year, using the ECM model; 3) Infiltration rate of 4.4 mm/year using a dual-permeability (dual-k) model. The simulations were carried out for a maximum time of 100,000 years to investigate both the heating and cool down cycles after waste emplacement.

**13.1.5.1
Numerical Grid, Material
Properties and Boundary
Conditions for UZ Thermal
Loading Studies**

Figure 13.1.1 shows a plan view of the 3-D-model and the location of the N-S 2-D vertical cross-section (A-A') used in the thermal hydrological studies. The 2-D vertical cross-section used in this study is refined from the 3D site scale model and has a total of 3774 elements and 6438 connections. For thermal studies this 2-D vertical cross-sections extends 500 below the water table into the saturated zone, down to the Tram Tuff hydrogeological model unit. This extension allows for explicit coupling of the saturated and the unsaturated zone in order to examine the effects of thermal loading on the water table and the saturated zone.

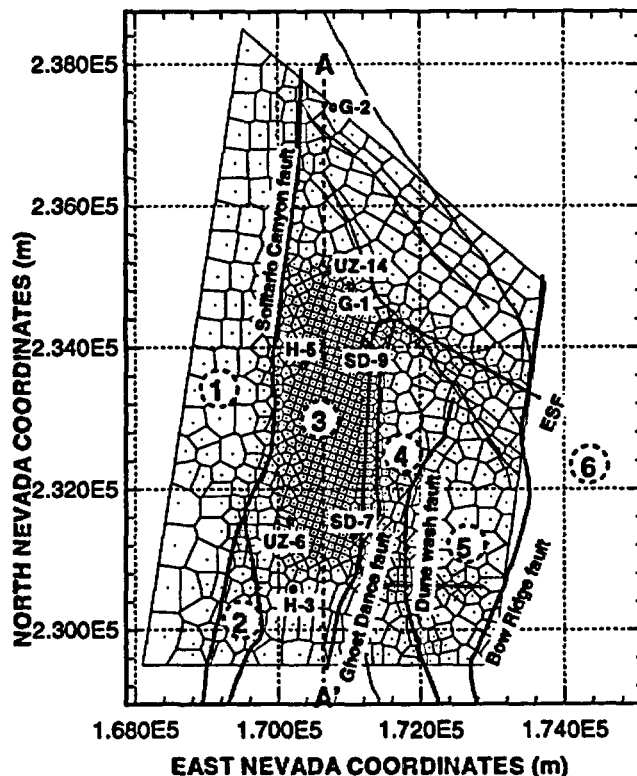


Figure 13.1.1
Areal grid of the 3-D UZ model showing location of N-S cross-section, boreholes.

The repository horizon is explicitly represented by a 6 m thick repository layer, bounded by 10 m thick layers. This repository horizon is mainly within the Topopah Springs model stratigraphic sub-layer five. The final model con-

sists of 27 non-uniform grid layers in the four welded and non-welded hydrogeological units (Chapter 2, this report).

The material properties of rocks are explicitly allocated based on the elevation of element node, model layer and the hydrogeological unit thickness. The pinchout of the Paintbrush, (PTn-2 and PTn-4) sub-layers as well as the zeolitic-vitric interface in the top of the Calico Hills (CHn) unit is explicitly modeled. Rock properties required for numerical simulations in the Tiva Canyon (TCw), Paintbrush (PTn), Topopah Springs (TSw), and Calico Hills (CHn) units were obtained from inverse modeling studies using moisture tension and liquid saturation data (Bandurraga et al., 1996, Chapter 3, this report). Different material properties were obtained depending on the infiltration rate assumed in the inversions in Chapter 3. For the thermal loading studies we use properties obtained for a uniform infiltration rate of 0.1 and spatially variable rates averaging 4.4 mm/year. The properties for the vitric and zeolitic Bullfrog (Bf) units as well as the Tram (TM) vitric and zeolitic units below the water table were assumed to be the same as for the Prow Pass model layers, since there are not sufficient data available do an inversion for the saturated zone in the 3D site scale model.

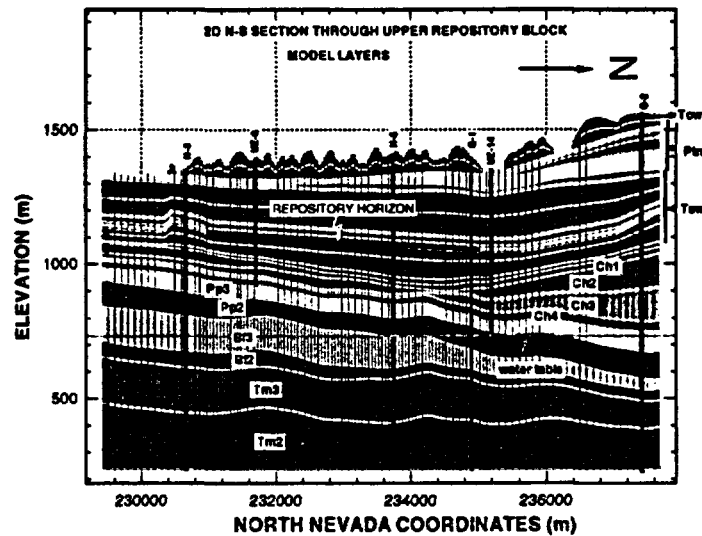


Figure 13.1.2
2-D UZ North-South Cross section A-A', showing model grid layers and hydrogeological units used.

The model parameters for the 2-D cross-sections were the same as those for the 3-D model unsaturated flow studies (Chapter 8, this report). For the thermal studies the following additional thermal properties and model boundary conditions were used.

Constant temperature and constant pressure conditions are specified on both top and bottom boundaries. The bottom boundary temperature was based on the observed temperature distribution from bore holes and the geothermal heat-flow maps (Bodvarsson et al., 1996, Chapter 9, this report). The top boundary temperature was calculated based on surface elevation and observed mean annual temperature. The spatially variable bottom boundary temperature, at 500 m below the water table, is based on extrapolation of temperature profiles and using estimated saturated thermal conductivity of these formations. This extrapolation results in an increase of about 5°C from the measured values at the water table. The thermal conductivities used in the model are based on estimated saturated and unsaturated thermal conductivity of the hydrogeologic units (Sass et al., 1988). Steady state saturated zone conditions were computed assuming a water table at 730 masl, and a hydrostatic gradient below the water table. Other properties used in the model have already been discussed Chapters 3 and 4.

Boreholes UZ-14, G-1, G-2, H-3, H-5 and UZ-6 are within 300 m of this cross-section were used to control geological layering (Figure 13.1.2). Borehole UZ-14 was in addition used to validate the rock properties using the observed saturation data (Figure 13.1.3). Our computed ambient liquid saturations matches well with the measured saturation data in UZ-14, as shown in Figure 13.1.3.

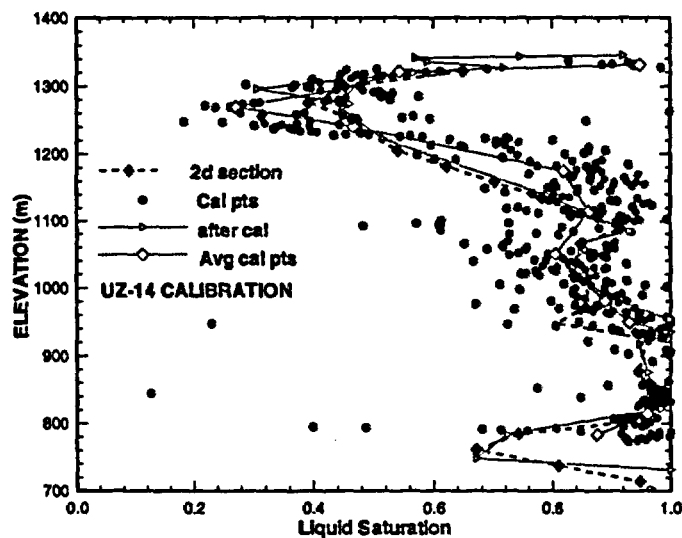


Figure 13.1.3
Comparisons between the observed and simulated saturation for borehole UZ-14, using the 2-D section, the USGS measured values, and infiltration rate of 0.1 mm/year. Data from L. Flint, USGS.

**13.1.5.2
ECM and Dual-k Approaches**

The saturated zone and the unsaturated zone at Yucca Mountain consist of different hydrogeologic units that exhibit varying degrees of fracturing. The Tiva Canyon (Tcw), and the Topopah Springs (TSw) hydrogeologic units contain extensive vertical conductive fractures. The Paintbrush (PTn), and vitric CHn though very permeable, shows little evidence of fracturing. The zeolitic Calico Hills hydrogeologic units have a low permeability matrix with few fractures (Chapter 3, this report).

Numerical models of geological systems generally consist of large computational blocks. For example, the 3-D Site Scale model consists of grid blocks with an average dimension of 10-100 m. These large blocks contain tens to hundreds of fractures that are combined with the matrix to provide an effective continuum with hydraulic properties that mimic the behavior of both the matrix and the fractures. This method of modeling fractured porous media is called the ECM (Effective Continuum method, Chapter 4, this report).

In order to effectively capture the physics of the response of a fractured porous medium and to evaluate the effectiveness of the ECM approach, we also developed a dual-permeability model for the new 3-D model (Wu et al., Chapter 8, 1996) and the 2-D cross-section model of the Yucca mountain.

For the dual-k model a fracture porosity of 1% was used with fracture aperture and density the same as those used in the 3-D model (Chapter 8, this report). The PTn and the saturated zone were simulated using the ECM. The dual-k model was used to simulate thermal loading using an infiltration of 4.4 mm/year (Flint, 1996), which is the average of the spatially variable rates.

**13.2 ECM simulation Results with 0.1 mm/year
Infiltration**

**13.2.1
Temperatures**

Figure 13.2.1 shows the ambient temperature in the 2-D cross-section using a uniform infiltration of 0.1 mm/year and the ECM model. The temperature is mainly controlled by the geothermal gradient and the saturated thermal conductivity (Data from Sass et al., 1988). This ambient temperature distribution is consistent with inferred heat flow maps and the temperature distribution at the water table (Chapter 9, this report). Estimated ambient temperatures at the repository horizon is 23-26°C and about 29-32°C at the water table.

Starting with these ambient conditions, as shown in Figure 13.2.1, a time dependent heat source was applied uniformly at the repository horizon for a total of 100,000 years. The heat source was based on tabulated heat decay data at an equivalent APD of 83 kW/acre (M&O, 1995). Figures (13.2.1- 13.2.6) show the evolution in temperature for this case. Boiling begins 10 years after thermal loading is imposed. For a period of 10-2000 years following emplace-

Thermal Loading Studies Using the Unsaturated Zone Model

ment, a complete dry-out zone develops at the repository. The peak temperature rises to 104° C at the central part of the repository. In the regions immediately above and below the repository, boiling also occurs. Within the central part of the potential repository, this boiling zone extends about 100 meters above and below the dry-out region, as shown in Figures. 13.2.2 and 13.2.4. In this zone convective heat transfer dominates with the temperature at about 97°C.

In 1,000 years the temperature above the central heated area of the 2-D cross-section rises substantially. The temperature increases to about 10°C at the ground surface, the temperature rises to 55°C at 50 m below the water table (Figure 13.2.3). At this time the repository temperature is 104°C, the temperature at the base of the PTn is 67°C and the temperature at the top of the Calico Hills is 92°C. The computed maximum temperature at the water table is 59°C in about 5,000 years, long after repository temperatures have decreased (Figure 13.2.3, 13.2.4).

At the repository horizon temperatures rise to boiling conditions within 10-100 years and remain constant (Figure 13.2.5). After 2,000 years the computed unsaturated zone and repository temperatures begin to decline, although local boiling still occurs at the repository horizon. In 10,000 years the repository temperature drops to 70°C and is 30°C after 100,000 years. The computed near-surface temperature (Figure 13.2.6) shows local variation along the cross-section, dependent mainly on the elevation of the surface. Peak temperature is 29°C, which is about 12°C above the ambient value, and occurs after 500-1,000 years of thermal loading.

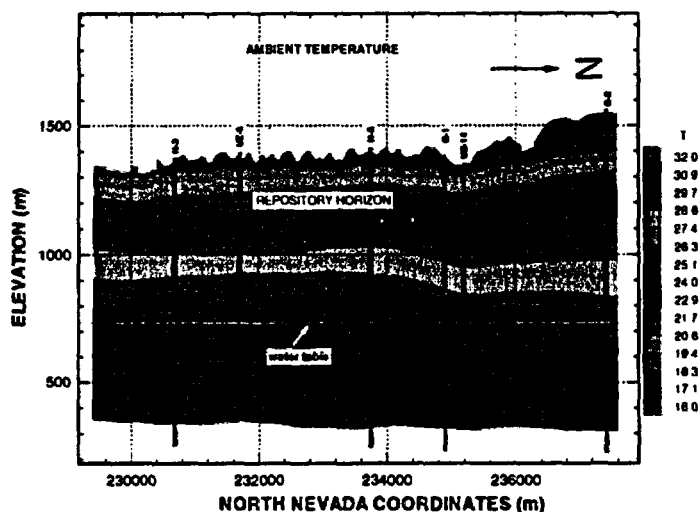


Figure 13.2.1 2-D UZ cross-section model. Ambient temperature at infiltration rate 0.1 mm/year.

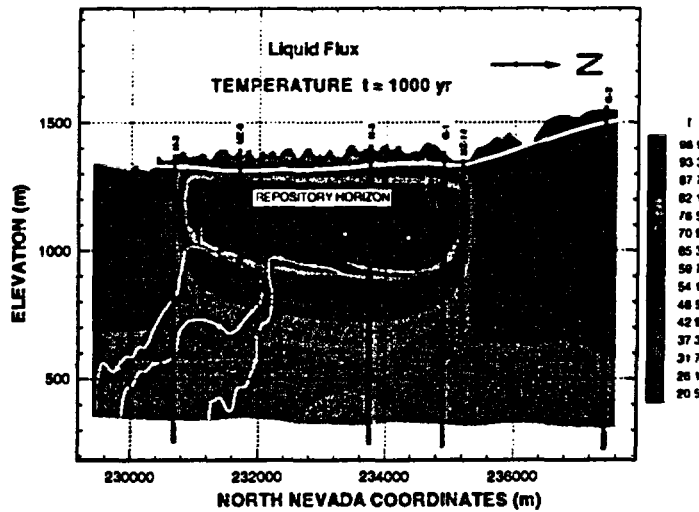


Figure 13.2.2
Temperature distribution after 1000 years thermal loading. APD = 83 kW/acre, infiltration = 0.1 mm/year.

r.

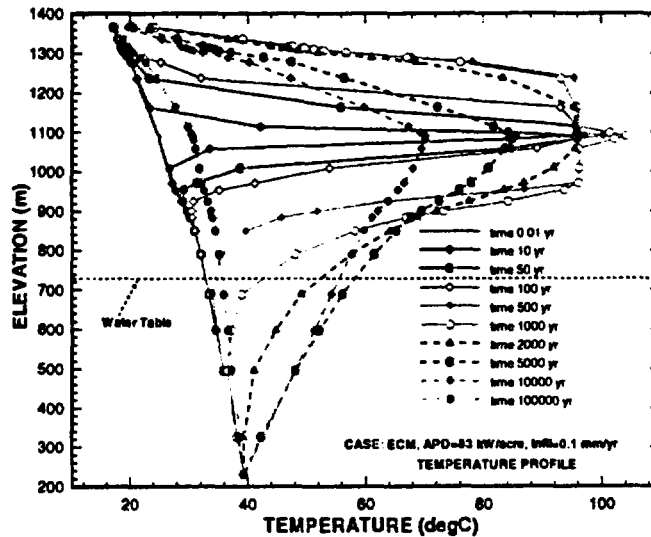


Figure 13.2.3
Vertical temperature profiles through the center of the repository block during 1,000 years of thermal loading. APD = 83 kW/acre, infiltration = 0.1 mm/year.

Thermal Loading Studies Using the Unsaturated Zone Model

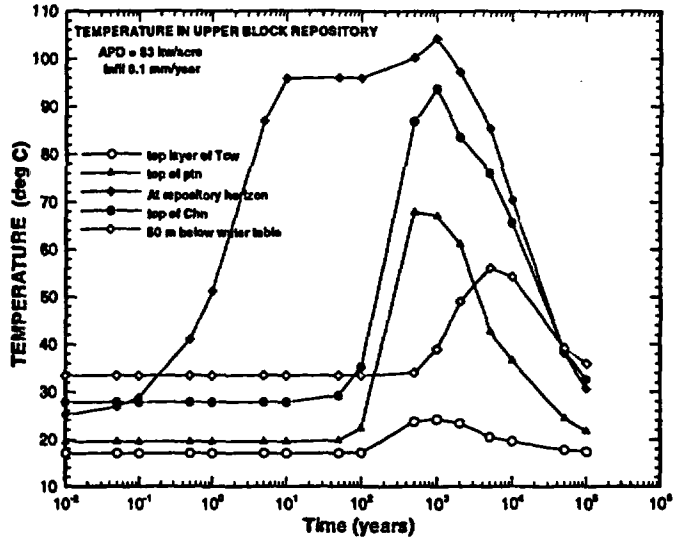


Figure 13.2.4 Temperature at various depths at the center of the repository during 100,000 years of thermal loading. APD = 83 kW/acre, infiltration = 0.1 mm/year.

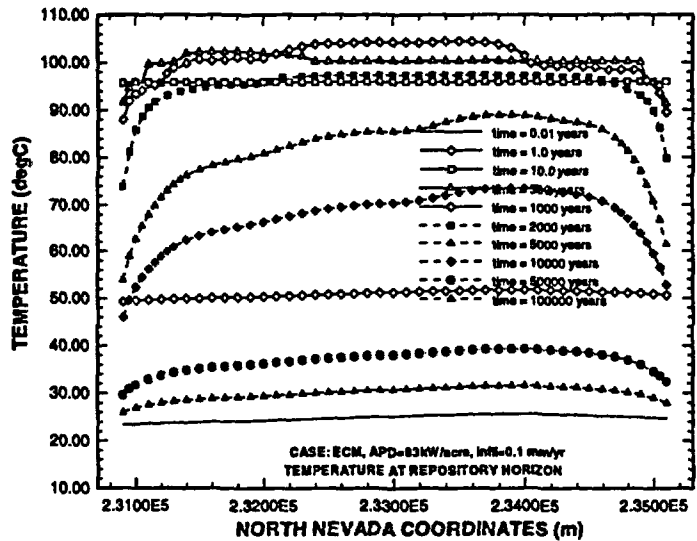


Figure 13.2.5 Temperature in the repository horizon during thermal loading, APD 83 kW/acre, infiltration = 0.1 mm/year.

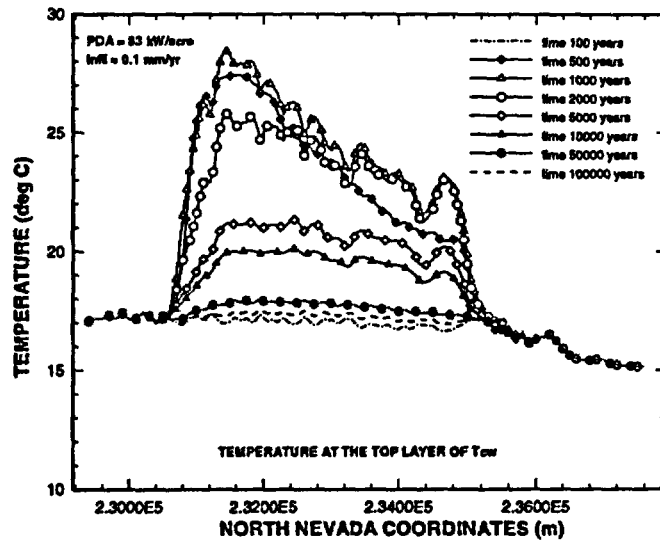


Figure 13.2.6
Temperature at the land surface during thermal loading, APD 83 kW/acre, infiltration = 0.1 mm/year.

13.2.2
Saturation

Figure 13.2.7 to 13.2.11 show the variation of saturation in the matrix and fracture continua in the 2-D cross-section at a uniform infiltration of 0.1 mm/year. Under ambient conditions, (Figure 13.2.7), most of liquid phase in the unsaturated zone remains in the matrix continuum with a high liquid saturation in the zeolitic Calico units. As discussed before, the simulated ambient saturation matches the measured data for UZ-14 (Figure 13.1.3). The fracture continuum shows low liquid saturation, particularly in the bottom layers of the TSw and vitric Calico Hills, Prow Pass and Bullfrog layers. Thermal loading causes substantial changes in the saturation distribution, especially near the repository region. For this case we examine the evolution of saturation in the matrix and fracture continua to understand the behavior of the unsaturated zone moisture flow under thermal loading. Boiling conditions exist at the repository and the regions immediately above and below the repository. Throughout the thermal loading cycle the boiling zone is confined to the upper layers of the TSw, and it does not extend into the PTn (Figure 13.2.8-13.2.9). During the boiling period, the saturations inside and outside the boiling zone show both spatial and temporal variations, which are produced by a complex evolution of boiling and condensation processes over time.

In about 500 years the liquid saturation at the repository horizon drops to zero and matrix liquid saturation at the top of the Calico Hills rises slightly due to vapor condensation, as shown in Figure 13.2.9. Figure 13.2.10 shows the evolution of saturation in a vertical column of the center of the repository. Repository thermal loading leads to a localized decrease in matrix saturation in the regions above and below the repository. Two condensation caps are formed

Thermal Loading Studies Using the Unsaturated Zone Model

near the southern and northern ends of the repository, where rapid cooling by convection cells maintains low local temperatures (Figure 13.2.12).

Until 2,000 years the repository region remains relatively dry as repository as the rate of vaporization exceeds the net infiltration. The gas flux vectors show strong convection patterns near the repository. Circulation cells develop near both ends of the repository, and gas flows away from the repository in the central region above and below the repository horizon. Below the repository the condensate flows laterally along the zeolitic-vitric interface into the vitric zones, because of the low permeability in the zeolitic formations. The lowest saturation at the repository occurs in the period when the largest boiling zone developed (Figure 13.2.11).

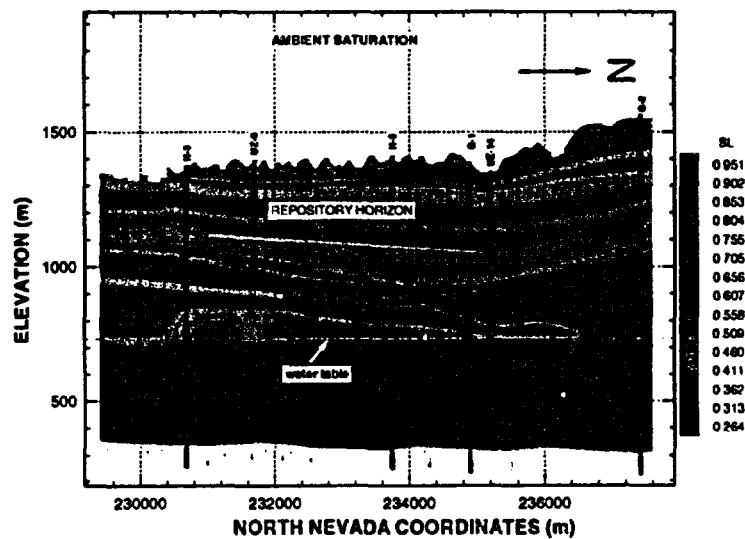


Figure 13.2.7
Ambient liquid saturation in the matrix and liquid flux, infiltration = 0.1 mm/year.

Thermal Loading Studies Using the Unsaturated Zone Model

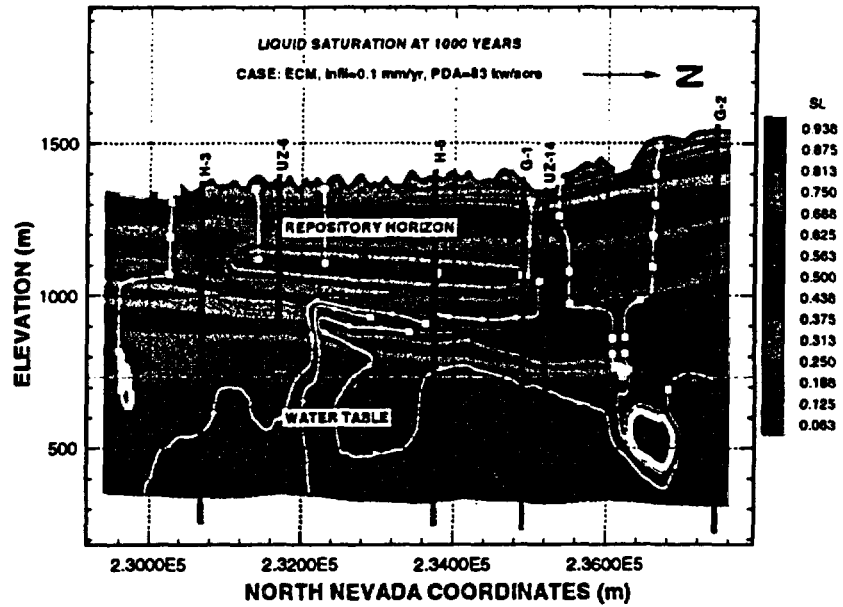


Figure 13.2.8
Liquid Saturation after 1000 years thermal loading APD = 83 kW/acre, infiltration = 0.1 mm/year.

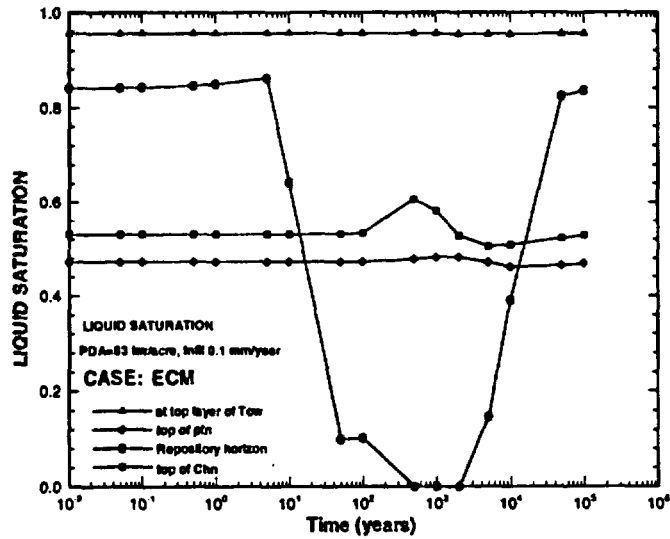


Figure 13.2.9
Liquid saturation at various depths in the center of the repository block during 100,000 years of thermal loading. APD = 83 kW/acre, infiltration = 0.1 mm/year.

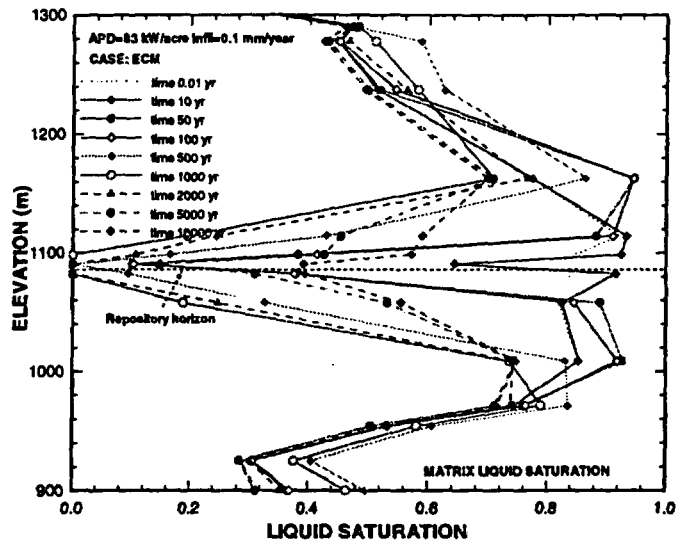


Figure 13.2.10
Vertical saturation profiles through the center of the repository block during 100,000 years of thermal loading. APD = 83 kW/acre, infiltration = 0.1 mm/year.

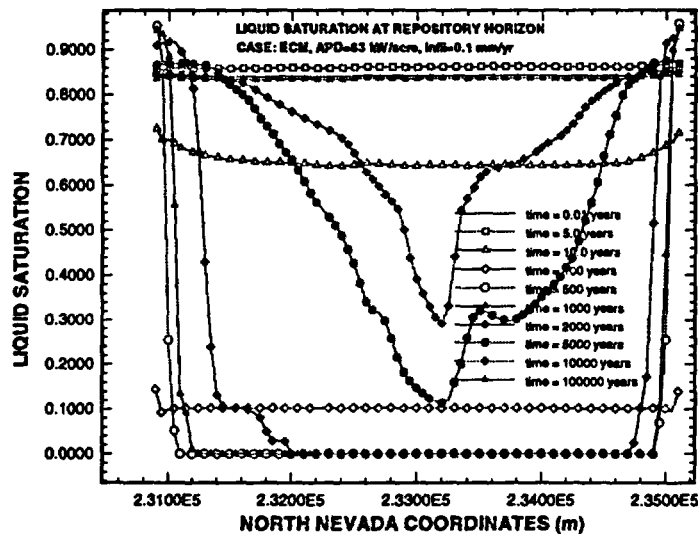


Figure 13.2.11
Liquid saturation in the repository horizon during thermal loading, APD 83 kW/acre, infiltration = 0.1 mm/year.

13.2.3
Percolation Flux

Under ambient conditions, the percolation flux at the repository is almost the same as the infiltration rate used in the simulation and the flow is mainly vertical at about 0.1 mm/year (Figure 13.2.7). With thermal loading effects, heat generated by the emplaced waste results in large increases in both gas and

liquid percolation flux around the repository, due to vaporization, pressurization, desaturation, and strong capillary suction.

For most of the simulated thermal loading period the repository acts as a barrier to downward water movement. Some lateral flow develops at a zone of 100 - 150 m above the repository, mainly within the TSw due to strong gas convection and vapor condensation (Figure 13.2.12). Above the boiling zone, temperature drops rapidly, and vapor mixes with downward flowing infiltrated water, which results in vapor condensation. Below the repository, liquid is displaced by expanding gases down to the zeolitic Calico Hills layers which causes southward lateral flow. At the zeolitic/vitric interface, a zone with high liquid vertical flux develops and extends down to the water table (Figure 13.2.12). The source of this the liquid is vapor condensation.

Figures 13.2.13 and 13.2.14 show respectively the vertical liquid fluxes on the top and bottom boundaries of the 6 m repository. On the figures, "positive" flux values denote downward flow, and "negative" denote upward flow. As shown in the two figures, the liquid flux has increased by 3-4 orders of magnitude compared to the ambient flux during 10-500 years after waste emplacement (prior to total dry-out). There is also enhanced liquid flow towards the repository horizon from above and below. At bottom of the repository, strong capillary suction overcomes gravity. Throughout the thermal loading cycle liquid flow at repository horizon is always towards the repository.

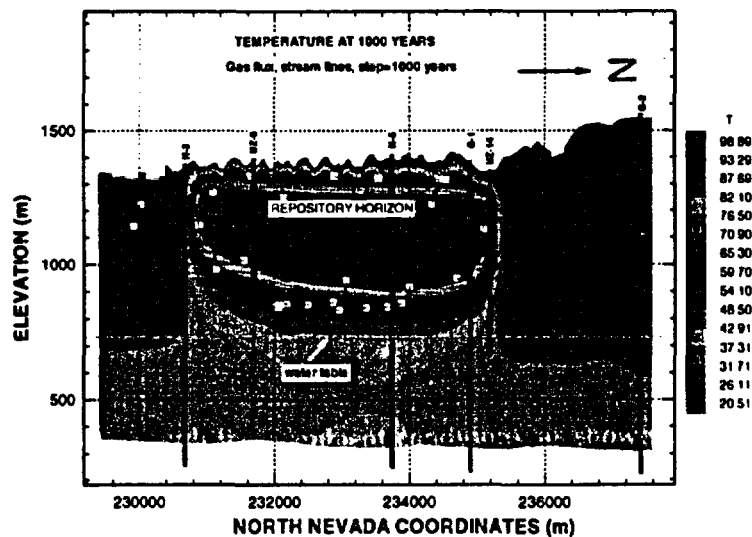


Figure 13.2.12
Gas flux profiles in the repository horizon after 1000 years emplacement, APD= 83 kW/acre, infiltration = 0.1 mm/year.

Thermal Loading Studies Using the Unsaturated Zone Model

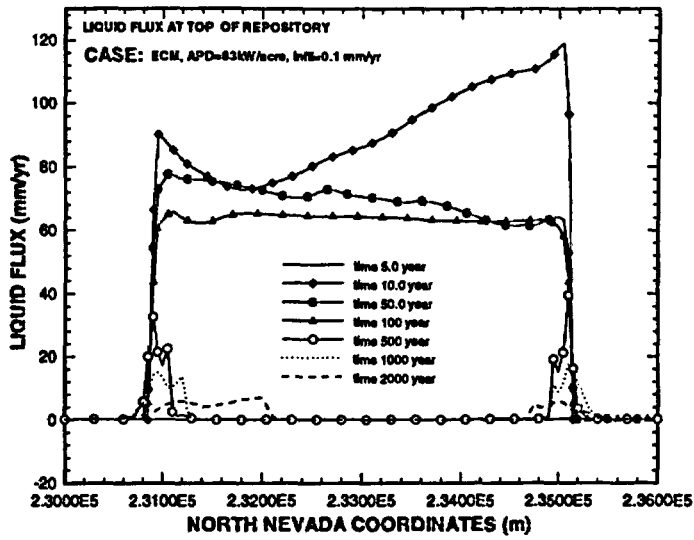


Figure 13.2.13
Liquid Flux crossing the top boundary of the repository, APD = 83 kW/acre, Infiltration 0.1 mm/year.

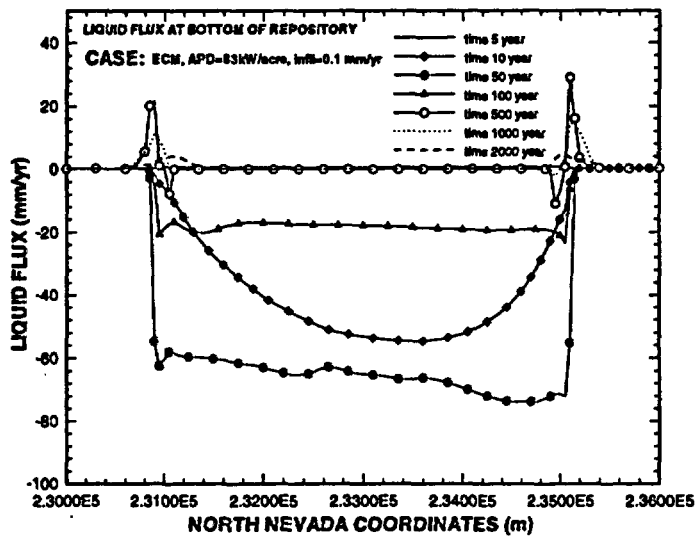


Figure 13.2.14
Liquid Flux crossing the bottom boundary of the repository, APD = 83 kW/acre, Infiltration 0.1 mm/year.

13.3 *ECM Simulation Results with 4.4 mm/year Infiltration*

13.3.1 Temperature

The ambient temperature distribution simulated using the ECM model with a uniform infiltration rate of 4.4 mm mm/year is almost the same as the one obtained using a 0.1 mm/year infiltration rate (Figure 13.2.1). This indicates that the temperature is mainly controlled the by fixed geothermal gradient and the thermal conductivity, and is not significantly affected by the infiltration rates used. Starting with these ambient conditions, a time dependent heat source was applied uniformly at the repository horizon for a total of 10,000 years, as in the previous case.

Figures 13.3.1- 13.3.6 show the evolution of temperature for this case. As for the 0.1 mm/year infiltration case, boiling conditions develop in 10 years. After 100 years (Figure 13.3.1-13.3.3), a boiling zone, extends about 50 m above and below the repository. This boiling condition continues for 2000 years of thermal loading. Unlike the case for 0.1 mm/year infiltration, complete dry-out conditions do not develop at the repository throughout the thermal loading cycle, because net liquid influx exceeds the rate of vaporization at the repository horizon. Within the central part of the potential repository, the boiling zone extends further, reaching a maximum of 50 m below and 150 m above the repository horizon during 500 to 1,000 years the (Figures. 13.3.1-13.3.3). In the boiling zone convective heat transfer dominates, and the temperature remains constant at about 95°C. In 1,000 years, the temperature at the land surface above the central heated area of the 2-D cross-section rises to 28°C, and to 93°C at the base of the PTn. The temperature is 95°C at the repository, 75°C at the top of Calico Hills and 55°C 50 m below the water table (Figure 13.3.4). The computed maximum temperature at the water table is 58°C and occurs in 5,000 years, long after repository temperatures have decreased (13.3.3, 13.3.4).

At the repository horizon temperatures rise to boiling conditions from 10 to 100 years and remain constant for several thousands of years thereafter (Figure 13.3.5). After 2,000 years the computed unsaturated zone and repository temperatures begin to decline even though local boiling still persists at the repository horizon. In 10,000 years, maximum temperature is only 72°C at the repository. The computed surface temperature (Figure 13.3.6) shows local variations dependent mainly on the elevation of the ground surface. Maximum temperature at the land surface is 31°C, or 14°C above the ambient condition, after 500-1000 years of thermal loading

Although computed maximum temperature at the repository horizon is less than that for the 0.1mm case, the temperatures above the repository horizon are higher since, in this case, the boiling zone is mainly above the repository horizon.

Thermal Loading Studies Using the Unsaturated Zone Model

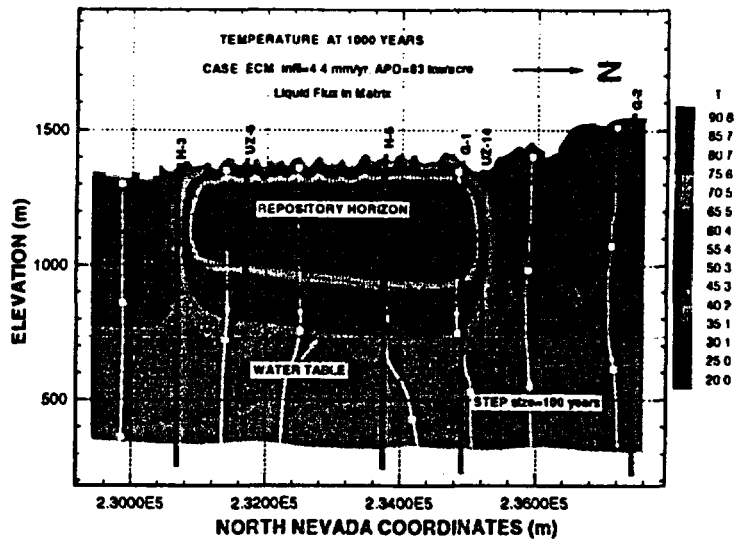


Figure 13.3.1
Temperature distribution after 1000 years thermal loading. ECM, APD = 83 kW/acre, infiltration = 4.4 mm/year. Vectors and flow paths show liquid Flux in matrix continuum.

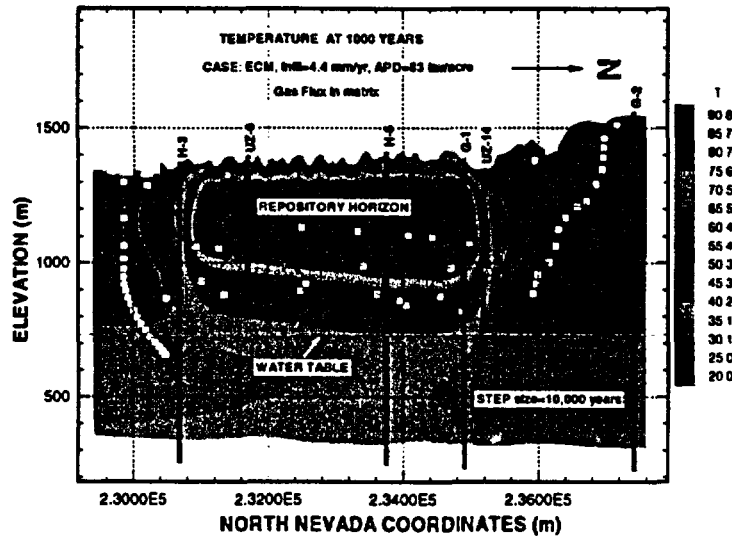


Figure 13.3.2
Temperature distribution after 1000 years thermal loading. ECM; APD = 83 kW/acre, infiltration = 4.4 mm/year. Vectors and flow paths show Gas flux matrix continuum.

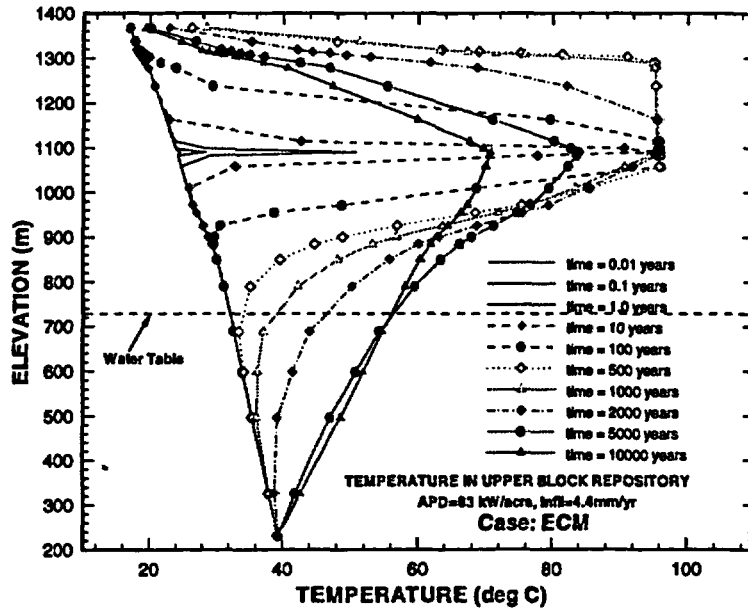


Figure 13.3.3
Vertical temperature profiles through the center of the repository block during 10,000 years of thermal loading; ECM, APD = 83 kW/acre, infiltration = 4.4 mm/year.

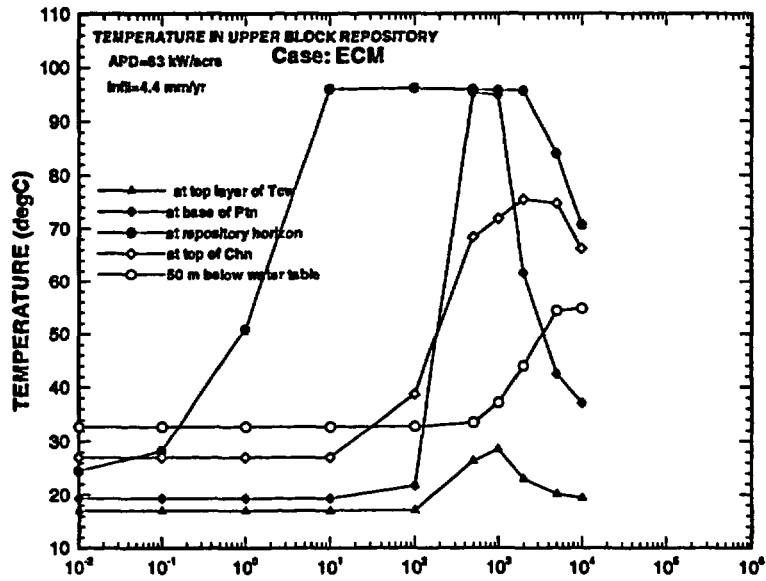


Figure 13.3.4
Temperature at various depths at the center of the repository during 10,000 years of thermal loading; ECM, APD = 83 kW/acre, infiltration = 4.4 mm/year.

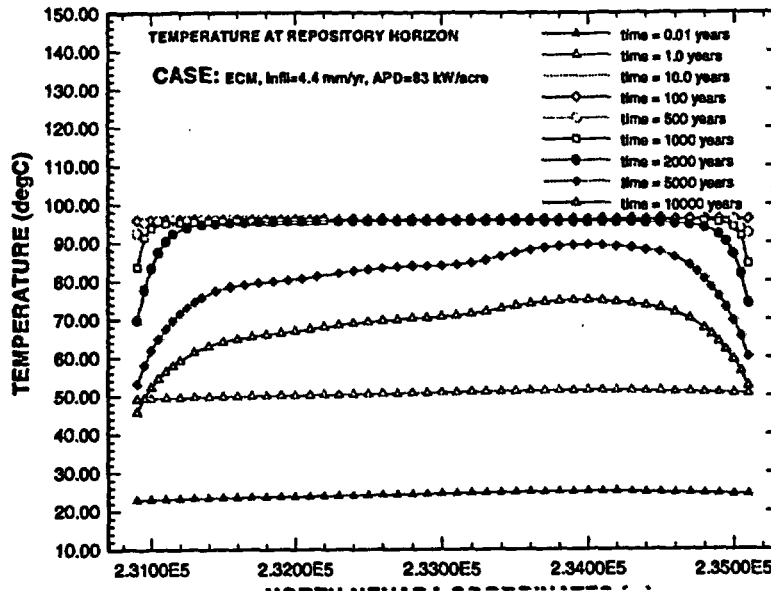


Figure 13.3.5
Temperature in the repository horizon during thermal loading; ECM, APD 83 kW/acre, infiltration = 4.4 mm/year.

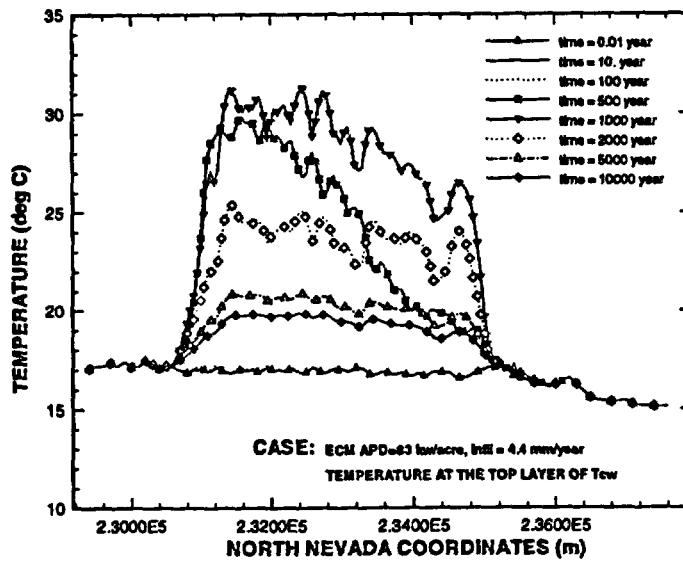


Figure 13.3.6
Temperature at the land surface during thermal loading; ECM, APD 83 kW/acre, infiltration = 4.4 mm/year.

**13.3.2
Saturation**

Figures 13.3.7 and 13.3.8 show the ambient saturation in the matrix and fracture continua in the 2-D cross-section. Most of the liquid phase in the unsaturated zone is in the matrix continuum (Figure 13.3.8). The fracture continuum has low saturation, particularly in the bottom layers of the TSw and vitric Calico Hills, Prow Pass and Bullfrog layers. Thermal loading significantly changes the saturation distribution, particularly, near the repository region. For this case we examine the evolution of saturation in the matrix and fracture continua to understand the behavior and effects of thermal loading on moisture flow and distribution in the unsaturated zone. In particular we are interested in short and long term responses, to be compared with dual-k modeling results.

As discussed before, the extent of the boiling zone, as indicated by the temperature profiles, is up to 150 m above and 50 m below the repository horizon. This boiling zone extends to the base of the PTn units in 100-1000 years. During the thermal loading cycle, the saturation distributions are significantly changed, spatially and temporally, near the repository boiling zone in the unsaturated zone. Figure 13.3.9 and 13.3.10 show the saturation in the matrix and fracture continuum at 1,000 years. Repository thermal loading leads to a decrease in saturation of the matrix close to the repository and an increase in saturation in the condensation zone, at 50 m above the repository (Figure 13.3.9). During this period the net influx into the repository exceeds the rate of vaporization caused by heating. Under the high infiltration rate, there is a net downward flow, even through the low permeability zeolitic Calico Hills Formations, throughout the thermal loading cycle. The gas flux vectors also show strong convection patterns near the repository.

To better understand the evolution of saturation and evaluate the rewetting phase in the thermal loading cycle we examined a 1-D vertical column at the center of the repository. For this column the evolution of saturation in the matrix continuum over the loading cycle was investigated (Figures 13.3.11, 13.3.12). The saturation in the matrix is found to change significantly only in the boiling zone, within 100 m from the repository. The minimum saturation is 0.38 for the matrix continuum, in about 100 years, when boiling conditions are established. Between 100 and 1000 years, boiling continues and expands, but the liquid saturation within the boiling zone rises. In this zone convective heat transfer dominates with a constant temperature at about 95°C. After 100 years, the rate of heat generation from the repository is not high enough to vaporize the liquid influx into the boiling region, causing the liquid saturation to increase.

Matrix liquid saturation at the top of the CHn increases and reaches its maximum in 100 years (Figure 13.3.11). The increase in saturation at the top of the CHn is mainly due to condensation of repository heat driven vapor flux. Figure 13.3.12 shows that maximum saturation changes in saturation are within about 100 m of the repository horizon. The matrix saturation at the southern and northern ends of the repository remains essentially unchanged

throughout the thermal loading cycle (Figure 13.3.13) and that rewetting of the repository horizon occurs uniformly. At about 1,000 years, though the boiling zone is still extensive, the average matrix liquid saturation at the repository recovers to a value of 0.85 from about 0.38 at 100 years. Rewetting of the de-saturated zone leads to an end of the boiling period and the decline in saturated zone temperature.

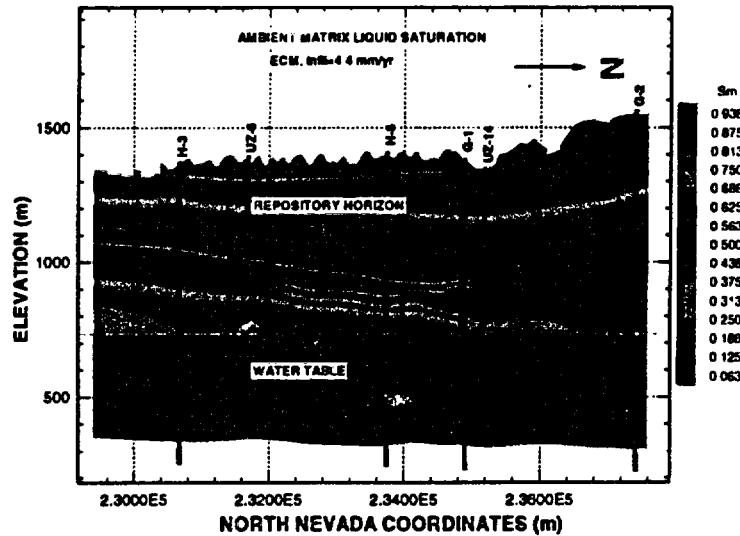


Figure 13.3.7
Matrix continuum ambient liquid saturation; ECM, APD 83 kW/acre, infiltration = 4.4 mm/year. Vectors show liquid flux in matrix.

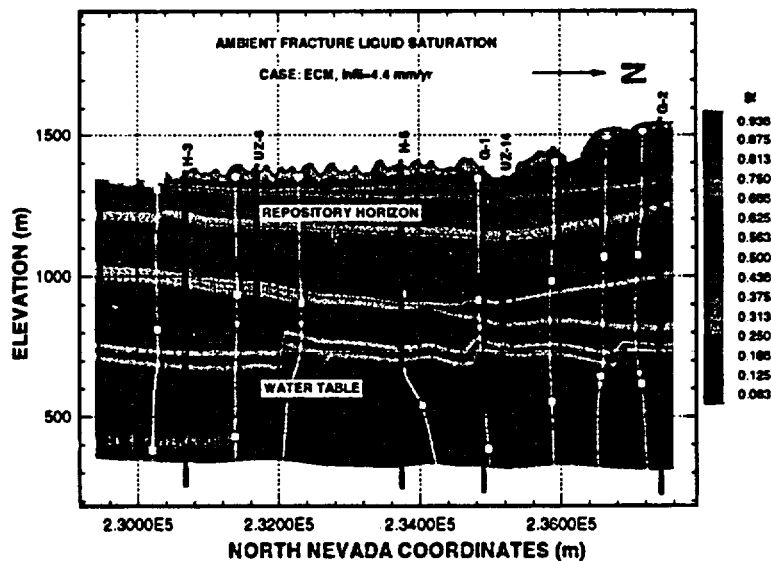


Figure 13.3.8
Fracture continuum ambient liquid saturation; vectors show liquid flux; ECM, APD 83 kW/acre, infiltration = 4.4 mm/year. Vectors show liquid flux in fractures.

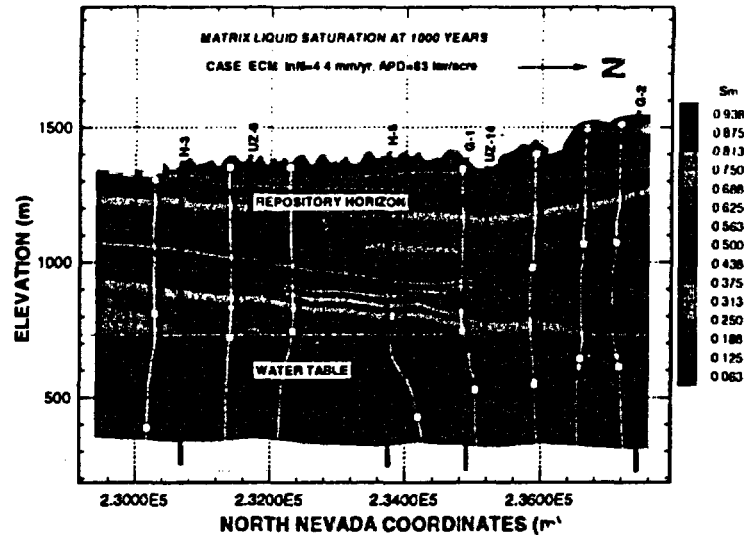


Figure 13.3.9 Matrix continuum liquid saturation after 1000 years thermal loading, APD = 83 kW/acre, infiltration = 4.4 mm/year; ECM.

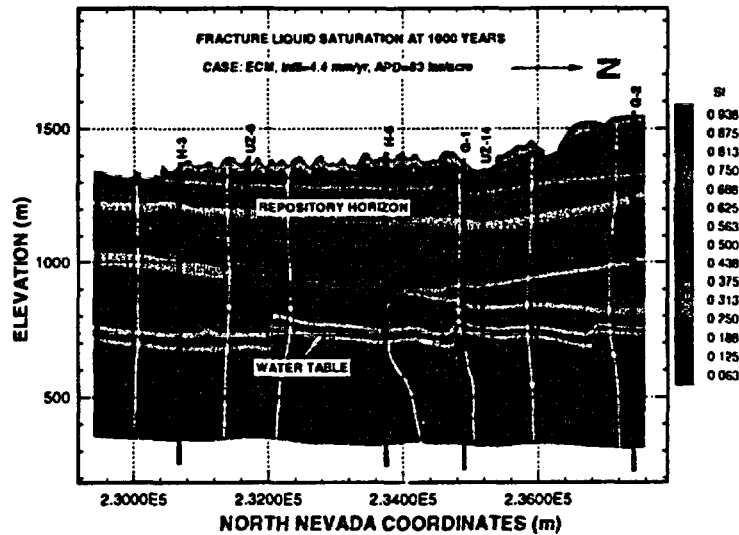


Figure 13.3.10 Fracture continuum liquid saturation after 1000 years thermal loading ECM, APD = 83 kW/acre, infiltration = 4.4 mm/year; vectors show liquid flux.

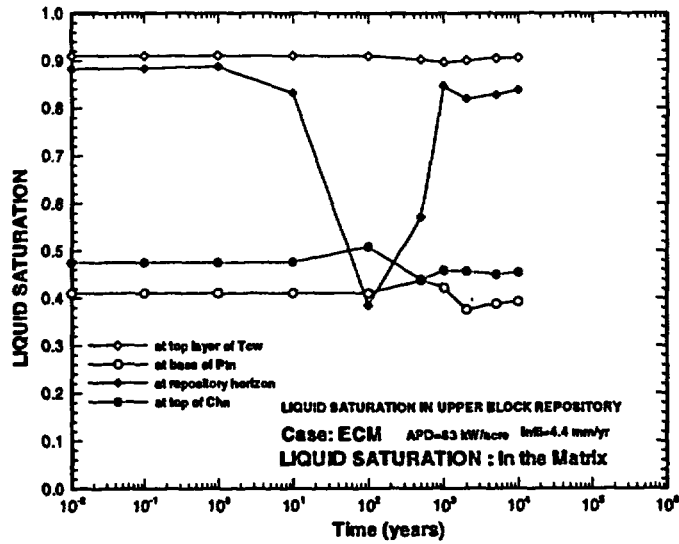


Figure 13.3.11
 Liquid saturation at various depths in the center of the repository block during 10,000 years of thermal loading; ECM, APD = 83 kW/acre, infiltration = 4.4 mm/year.

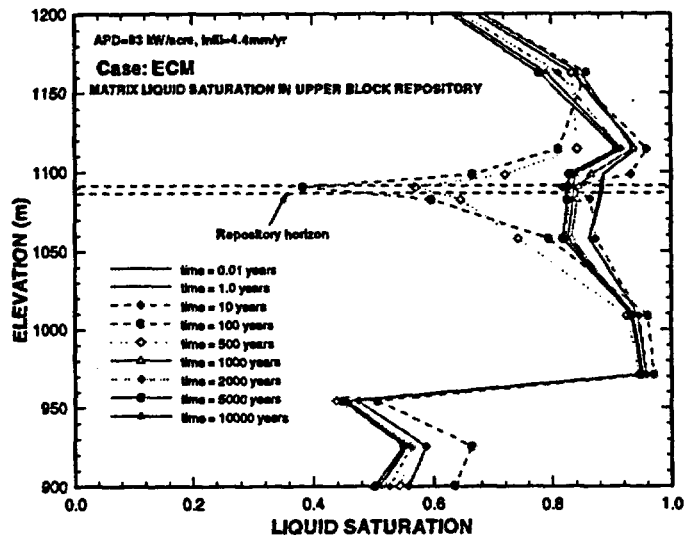


Figure 13.3.12
 Vertical saturation profiles through the center of the repository block during 10,000 years of thermal loading; ECM, APD = 83 kW/acre, infiltration = 4.4 mm/year.

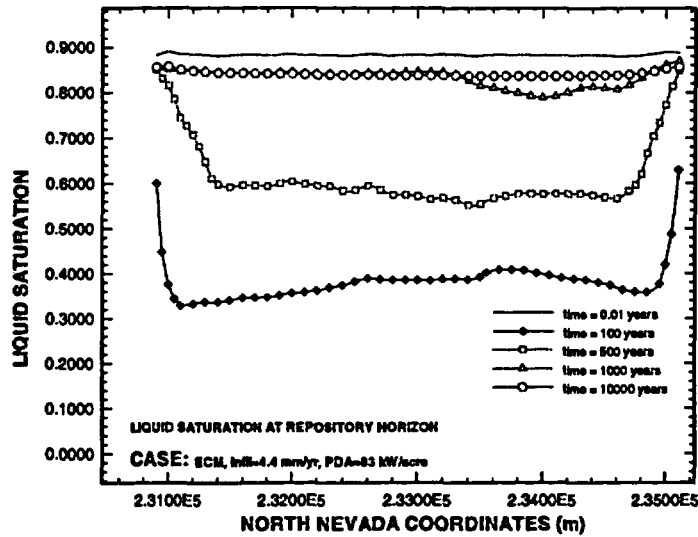


Figure 13.3.13
Liquid saturation in the repository horizon during thermal loading; ECM, APD 83 kW/acre, infiltration = 4.4 mm/year.

**13.3.3
Percolation Flux**

The changes in percolation flux at the repository horizon are associated closely with changes in saturation conditions, which are related to the intensity of boiling, dry-out and rewetting processes. Figure 13.3.14-13.3.15 show the detailed evolution of the vertical liquid fluxes versus thermal loading time on the top and bottom boundaries of the repository. Similar to the case of the lower infiltration of 0.1 mm/year, Figure 13.3.14 and 13.3.15 show a huge increase in the liquid flux into the repository during the thermal loading, and no liquid flow out.

For the first 10 years after waste emplacement, repository liquid saturation decreases and the liquid influx into the repository increases by a factor of 10 to 30 due to strong capillary suction, as compared with the ground surface infiltration (Figure 13.3.14). This indicates that most of the influx liquid is released from the nearby matrix or condensation, not from the surface infiltration. After 100 years the influx into the repository decreases to an average of about 10 mm/year at the bottom boundary and about 60 mm/year at the top boundary of the repository.

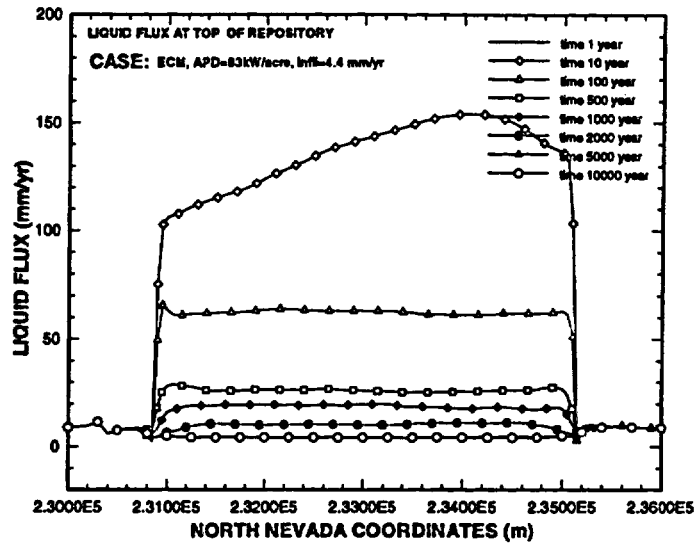


Figure 13.3.14
Liquid Flux crossing the top boundary of the repository; ECM, APD = 83 kW/acre, Infiltration 4.4 mm/year.

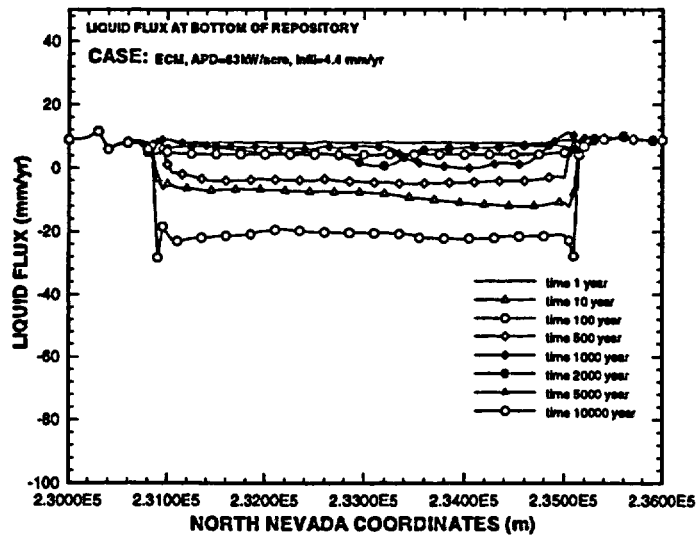


Figure 13.3.15
Liquid Flux crossing the bottom boundary of the repository; ECM, APD = 83 kW/acre, Infiltration 4.4 mm/year

13.4 Dual-k Simulation Results with 4.4 mm/year Infiltration

13.4.1 Temperature

The ambient temperature in the 2-D cross-section, simulated using the dual-k model with an infiltration rate of 4.4 mm/year, is similar to that of the ECM case. As in the ECM study, the dual-k simulation uses the thermal loading scenario of an equivalent APD of 83 kW/acre. Figure 13.4.1 to 13.4.8 show the spatial and temporal changes in temperature for this case. Boiling conditions develop after about 100 years of thermal loading. At 500 years (Figure 13.4.1, 13.4.2), the temperatures within the zone 100 m above and below the repository reach 95°C, and strong convective heat transfer occurs at or near boiling conditions. This boiling condition lasts for an additional 500 years (Figure 13.4.3 and 13.4.4). Unlike in the case of the ECM study with 4.4 mm/year infiltration, complete dry-out conditions do not develop at the repository throughout the thermal loading cycle.

The simulated boiling zone extends to a maximum of 100 m vertically above and below the repository horizon for 500-1000 years, as shown in Figure 13.4.5. In this period, convective heat transfer dominates and the temperature remains constant at about 95°C in the boiling zone. In 1,000 years, temperature near the land surface rises to about 25°C, and 65°C at the base of the PTn. At the same time, the repository temperature reaches 94°C, and the temperatures at the top of Calico Hills and at 50 m below the water table are at 76°C and 57°C (Figure 13.4.6), respectively. The computed maximum temperature at the water table is 59°C, which occurs at about 5,000 years.

At the repository horizon temperatures rise to boiling conditions in 20-100 years and remain constant (Figure 13.4.5, 13.4.6 and 13.4.7) until 2,000 years when the computed repository temperatures begin to gradually decline. After 10,000 years temperature at the repository, decreases to 60°C, and further drops to 42°C after 25,000 years. The computed surface temperature (Figure 13.4.8) shows that the highest temperature near the ground surface is 28°C in 1,000 years.

Predicted temperature at the surface and at the base of the PTn are less than those obtained from the ECM case at the same infiltration rate, since, in this case, boiling extends further below the repository. However, both the Dual-K and ECM predict similar temperature rise at the top of the Calico Hills (75-76°C) which are well below the breakdown temperature for zeolites.

Thermal Loading Studies Using the Unsaturated Zone Model

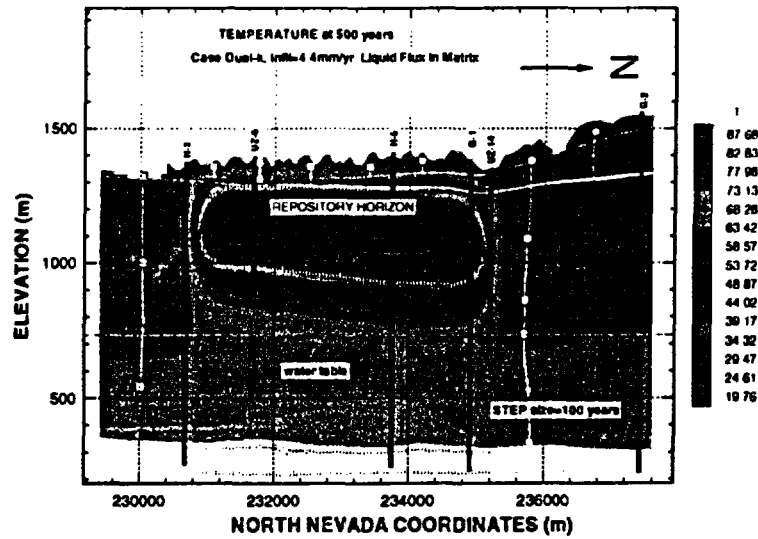


Figure 13.4.1
 Temperature distribution after 500 years thermal loading; Dual-k, APD = 83 kW/acre, infiltration = 4.4 mm/year. Vectors and flow paths show liquid Flux in matrix continuum.

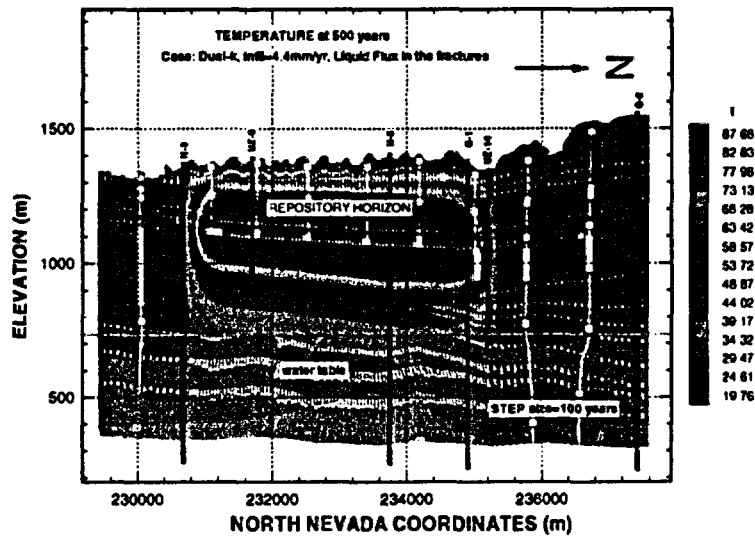


Figure 13.4.2
 Temperature distribution after 500 years thermal loading; Dual-k, APD = 83 kW/acre, infiltration = 4.4 mm/year. Vectors and flow paths show liquid flux in fracture continuum.

Thermal Loading Studies Using the Unsaturated Zone Model

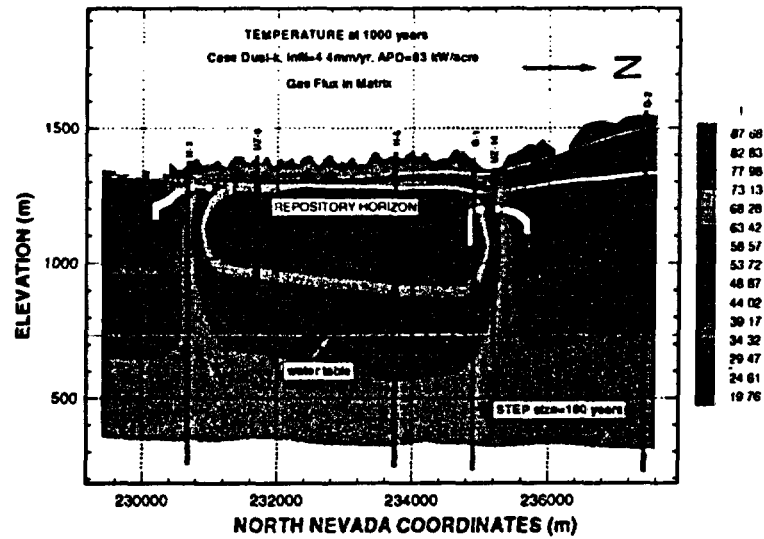


Fig 13.4.3
Temperature distribution after 1000 years thermal loading; Dual-k, APD = 83 kW/acre, infiltration = 4.4 mm/year. Vectors and flow paths show gas flux in matrix continuum.

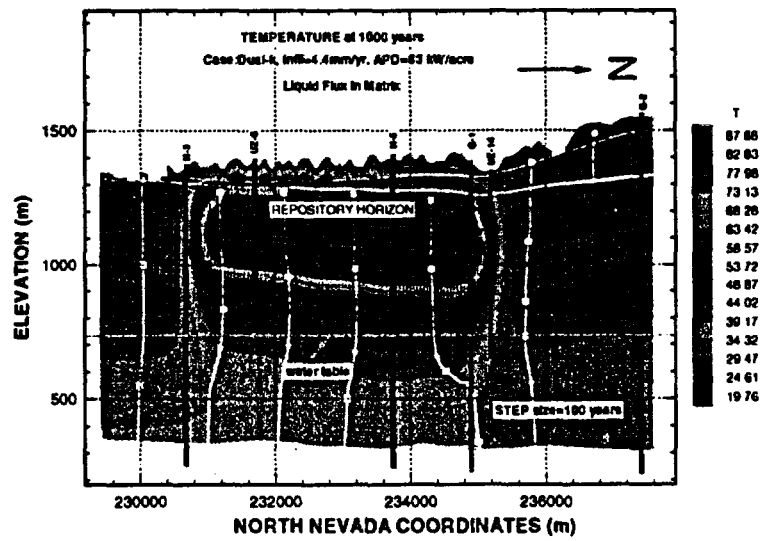


Figure 13.4.4
Temperature distribution after 1000 years thermal loading; Dual-k, APD = 83 kW/acre, infiltration = 4.4 mm/year. Vectors and flow paths show liquid flux in matrix continuum.

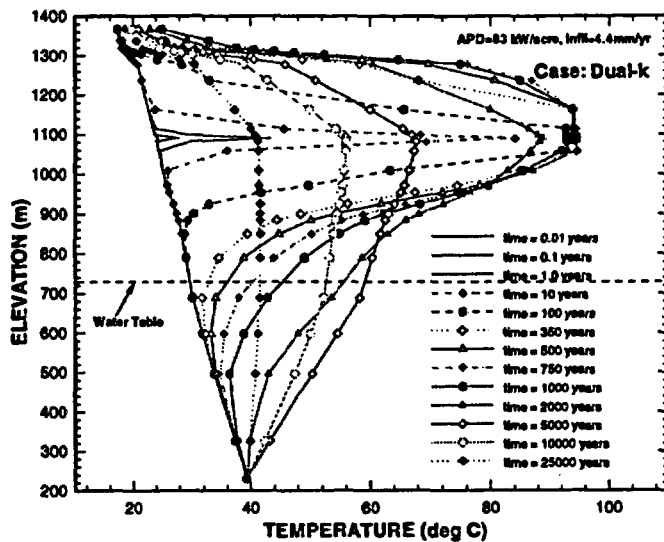


Figure 13.4.5
Vertical temperature profiles through the center of the repository block during 25,000 years of thermal loading; Dual-k, APD = 83 kW/acre, infiltration = 4.4 mm/year.

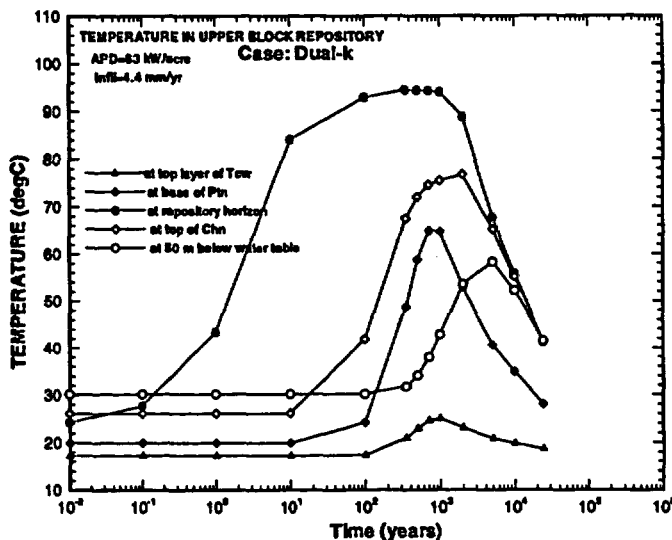


Figure 13.4.6
Temperature at various depths at the center of the repository during 25,000 years of thermal loading; Dual-k, APD = 83 kW/acre, infiltration = 4.4 mm/year.

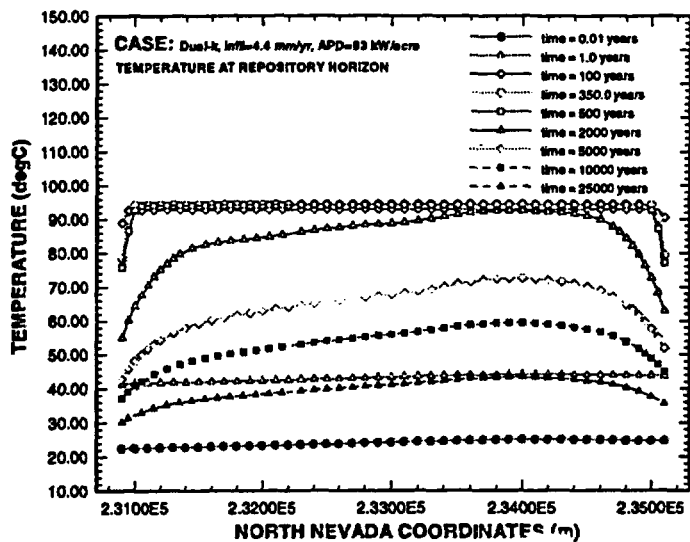


Figure 13.4.7
 Temperature in the repository horizon during thermal loading; Dual-k, APD 83 kW/acre, infiltration = 4.4 mm/year.

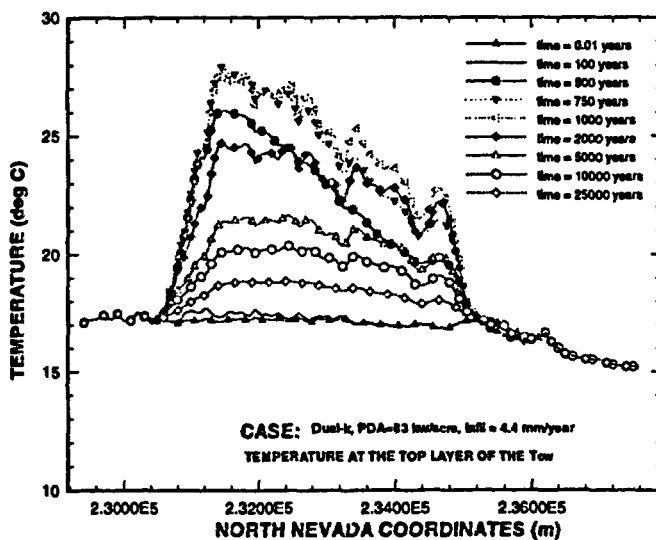


Figure 13.4.8
 Temperature at the land surface during thermal loading; Dual-k, APD 83 kW/acre, infiltration = 4.4 mm/year.

**13.4.2
Saturation**

Figures 13.4.9 and 13.4.10 show the simulated ambient saturations, for the matrix and fractures, respectively. As can be seen from the figures, the liquid saturations in the matrix are much higher than those in the fractures. These ambient saturation distribution in the fracture and matrix continua is very similar to the ambient saturation for the ECM case with 4.4 mm/year infiltration.

Figure 13.4.11 and 13.4.12 show the matrix saturation distributions after 500 and 1000 years of thermal loading, respectively. The matrix saturation at the repository is the lowest in 500 years. After 500 years the matrix saturation at the repository horizon increases, while temperature remains nearly constant during this period (Figure 13.4.5). As in the ECM case, not enough heat is generated to vaporize the liquid influx towards the repository.

The gas flux shows strong convection patterns near the repository throughout the boiling period (Figure 13.4.13 and 13.4.14). Circulation cells develop at both the southern and northern ends of the repository. Vapor condensation zones are formed directly above the repository, below the TCw. This condensed liquid drains back to the repository, resulting in a local increase in influx at the top boundary of the repository. Below the repository heat driven gas flow moves up-dip of the repository, along the top of Calico Hills to form circulation cells at the southern end of the repository (Figures 13.4.14).

To better understand the saturation changes and the rewetting processes in the thermal loading cycle, we again use a 1-D vertical column from the 2-D grid to look at saturation variations (Figures 13.3.15a, 13.3.15b) in the matrix and the fracture continua. The matrix saturation changes along the column are shown in Figure 13.4.15a, and the fracture saturations are presented in Figure 13.4.15b. The minimum matrix liquid saturation is about 40%, and the fracture saturation is as low as 5%, at about 100 years, as soon as boiling conditions are established. Like the ECM case with 4.4 mm/year infiltration, no complete dry-out occurs in either the fracture or matrix with the dual-k simulations.

Liquid saturation at the top of the Calico Hills rises slightly in about 100 years, both in the matrix and the fracture continuum (Figures 13.4.16, 13.4.17). This saturation increase is mainly due to condensation of repository driven vapor flux. Figure 13.4.18 shows that matrix saturation near the south and north ends of the repository horizon remains unchanged throughout the thermal loading cycle and that rewetting processes are very uniform. In 1,000 years of thermal loading, though the boiling zone is still extensive, average liquid saturation at the repository recovers to 75% in the matrix (Figure 13.4.18), and to 15% in the fractures (Figure 13.4.19). A comparison of Figure 13.4.18 and 13.4.19 shows that rewetting of the fracture continuum lags significantly behind that for matrix continuum.

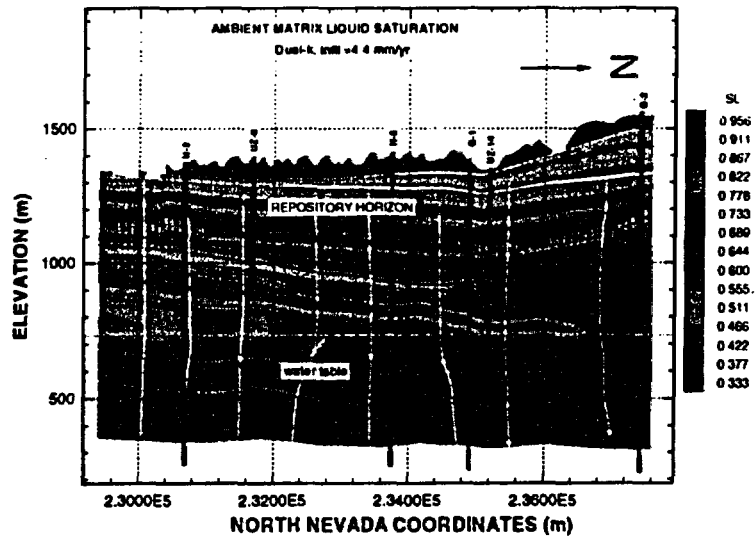


Figure 13.4.9
Matrix continuum ambient liquid saturation; Dual-k, APD 83 kW/acre, infiltration = 4.4 mm/year. Vectors show liquid flux in matrix.

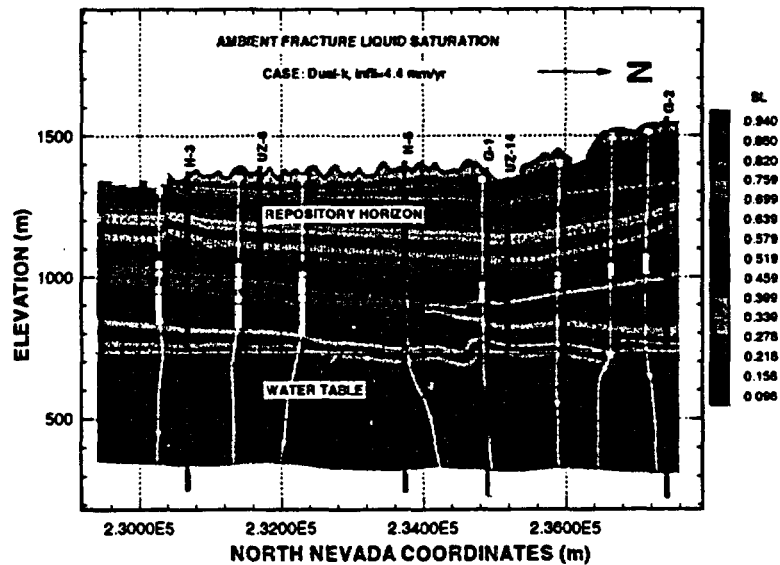


Figure 13.4.10
Fracture continuum ambient liquid saturation; vectors show liquid flux; Dual-k, APD 83 kW/acre, infiltration = 4.4 mm/year. Vectors show liquid flux in fractures.

Thermal Loading Studies Using the Unsaturated Zone Model

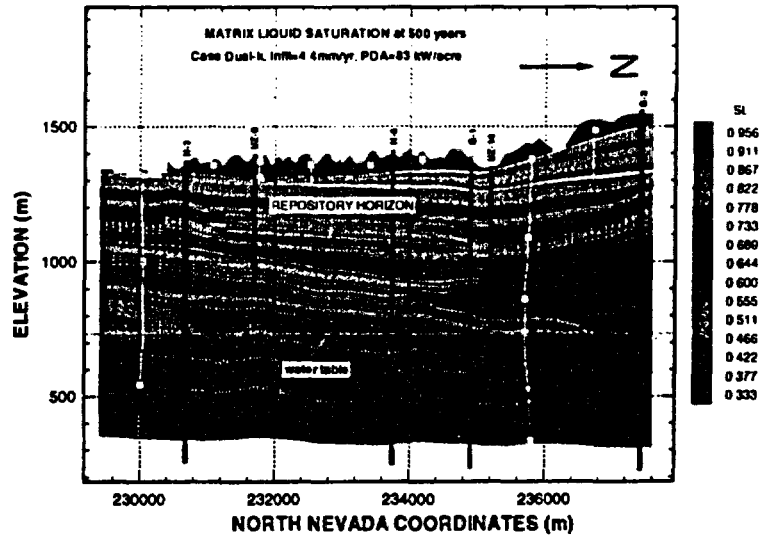


Figure 13.4.11 Matrix continuum liquid saturation after 500 years thermal loading Dual-k, APD = 83 kW/acre, infiltration = 4.4 mm/year.

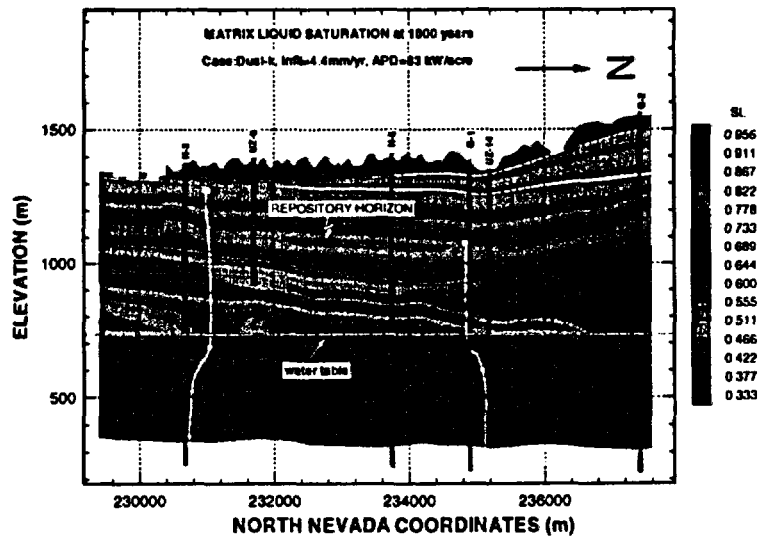


Figure 13.4.12 Matrix continuum liquid saturation after 1000 years thermal loading Dual-k, APD = 83 kW/acre, infiltration = 4.4 mm/year.

Thermal Loading Studies Using the Unsaturated Zone Model

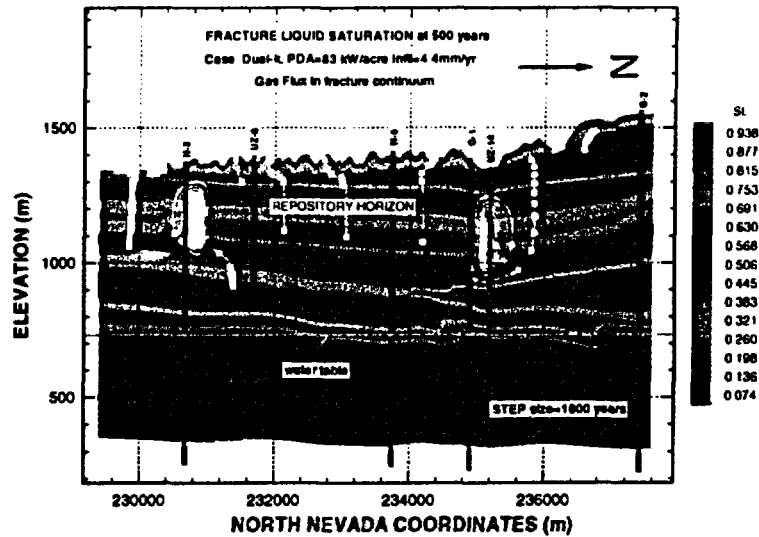


Figure 13.4.13
 Fracture continuum liquid saturation after 500 years thermal loading Dual-k, APD = 83 kW/acre, infiltration = 4.4 mm/year; vectors show liquid flux.

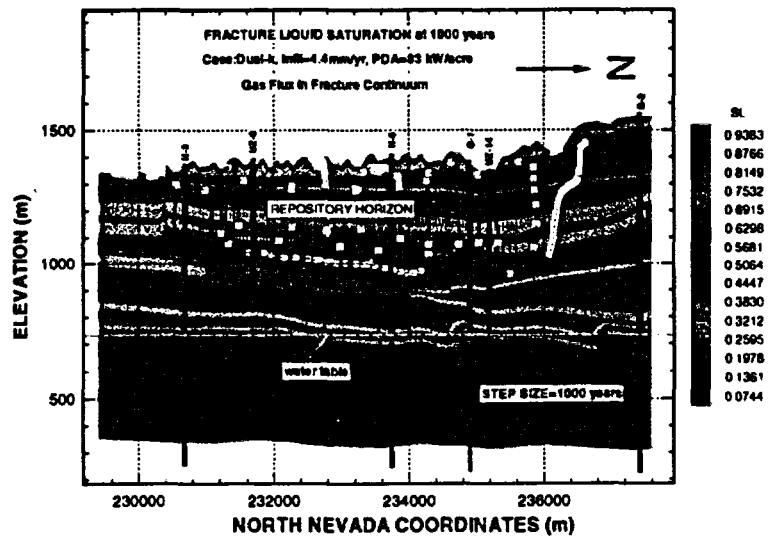


Figure 13.4.14
 Fracture continuum liquid saturation after 1000 years thermal loading Dual-k, APD = 83 kW/acre, infiltration = 4.4 mm/year; vectors show liquid flux.

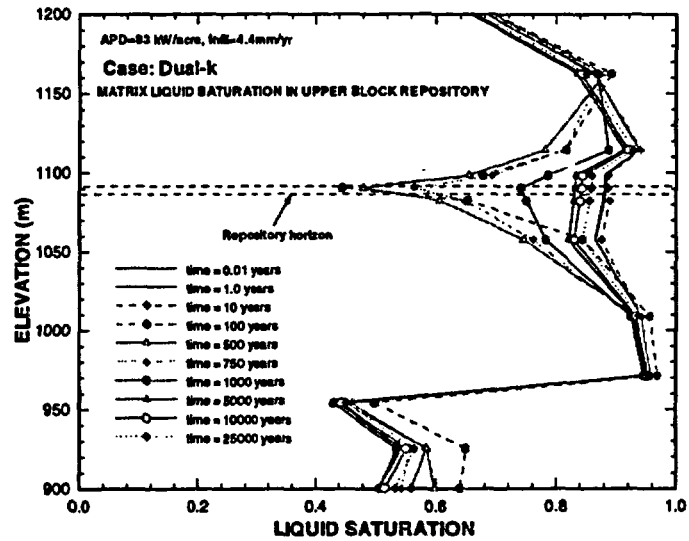


Figure 13.4.15a
Matrix vertical saturation profiles through the center of the repository block during 25,000 years of thermal loading; Dual-k, APD = 83 kW/acre, infiltration = 0.1 mm/year.

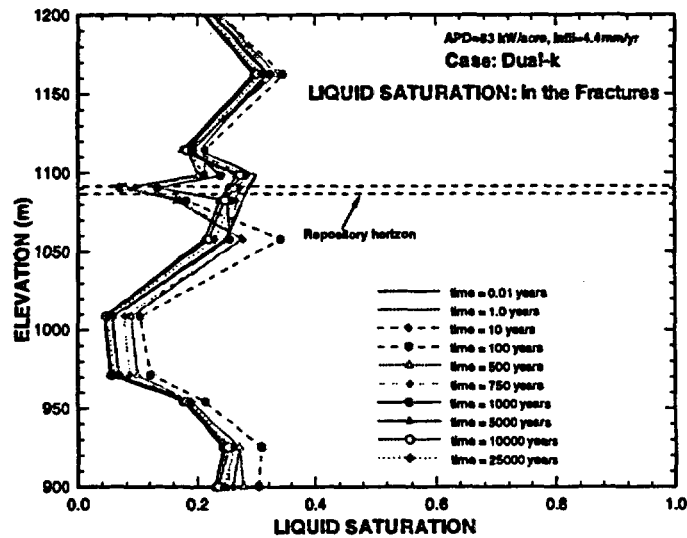


Figure 13.4.15b
Fracture vertical saturation profiles through the center of the repository block during 25,000 years of thermal loading; Dual-k, APD = 83 kW/acre, infiltration = 0.1 mm/year

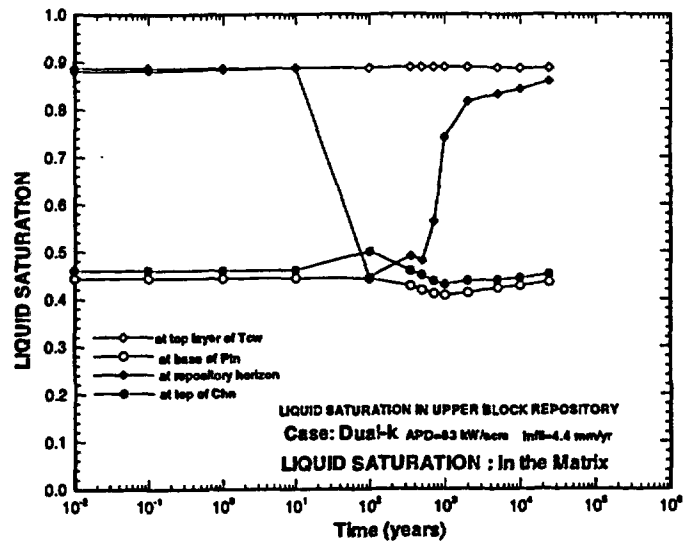


Figure 13.4.16 Matrix Liquid saturation at various depths in the center of the repository block during 10,000 years of thermal loading; Dual-k, APD = 83 kW/acre, infiltration = 4.4 mm/year.

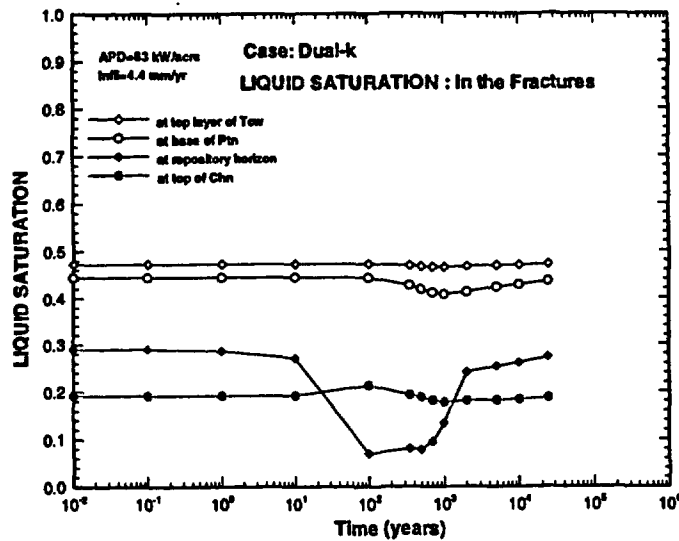


Figure 13.4.17 Fracture Liquid saturation at various depths in the center of the repository block during 10,000 years of thermal loading; Dual-k, APD = 83 kW/acre, infiltration = 4.4 mm/year.

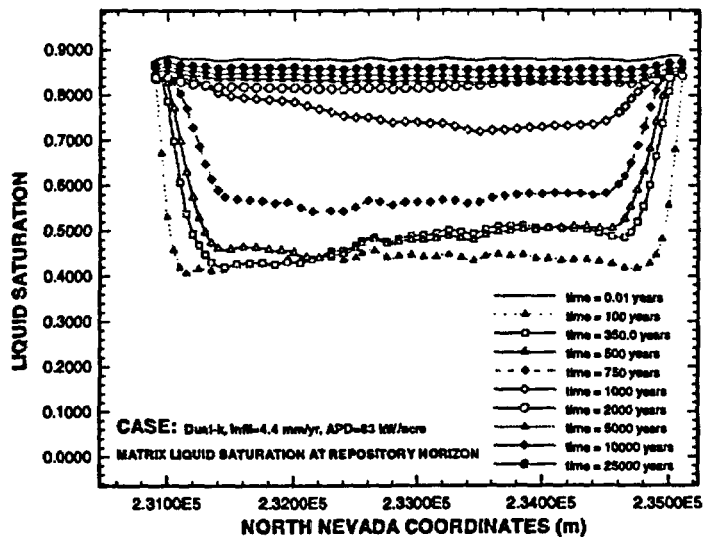


Figure 13.4.18
 Matrix Liquid saturation in the repository horizon during thermal loading; Dual-k, APD 83 kW/acre, infiltration = 4.4 mm/year.

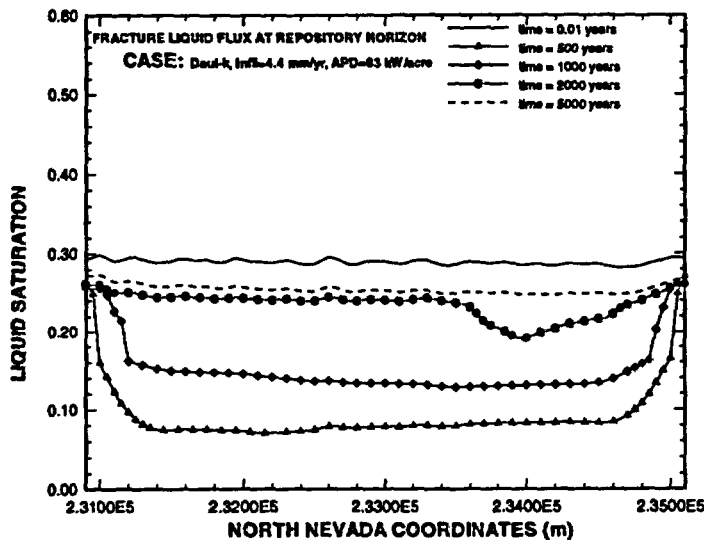


Figure 13.4.19
 Fracture Liquid saturation in the repository horizon during thermal loading; Dual-k, APD 83 kW/acre, infiltration = 4.4 mm/year.

**13.4.3
 Percolation Flux**

The repository percolation fluxes simulated by the dual-k model are shown in Figures 13.4.20-13.4.23. Figures 13.4.20 and 13.4.21 gives the liquid influx into the repository from matrix flow Figures 13.4.22 and 13.4.23 show the influx

from the fracture. As can be seen from the four figures, both matrix flow and fracture flow into the repository increase by as much as 10 times, during the thermal loading period compared to the ambient infiltration rate of 4.4 mm/year. It is interesting to note that the contribution of the fracture flow into the repository is no more than 10 to 20% of the total liquid influx. This suggests that the matrix flow is more important to the rewetting processes of the repository during the thermal loading cycle.

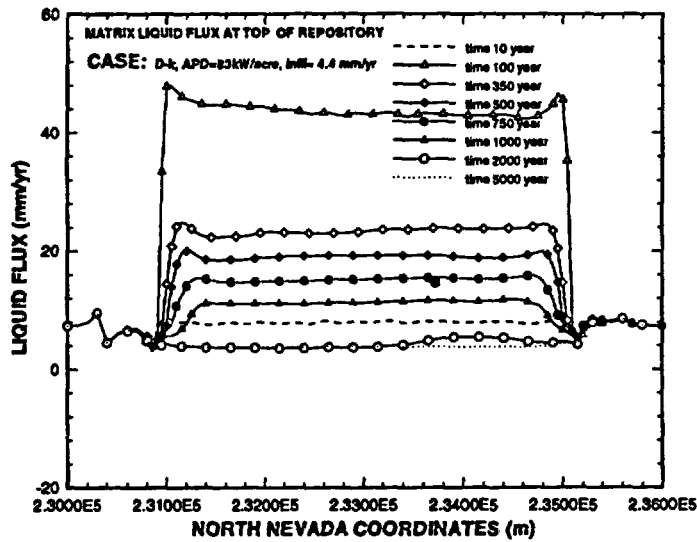


Figure 13.4.20
Matrix liquid flux crossing the top boundary of the repository; Dual-k, APD = 83 kW/acre, Infiltration 4.4 mm/year.

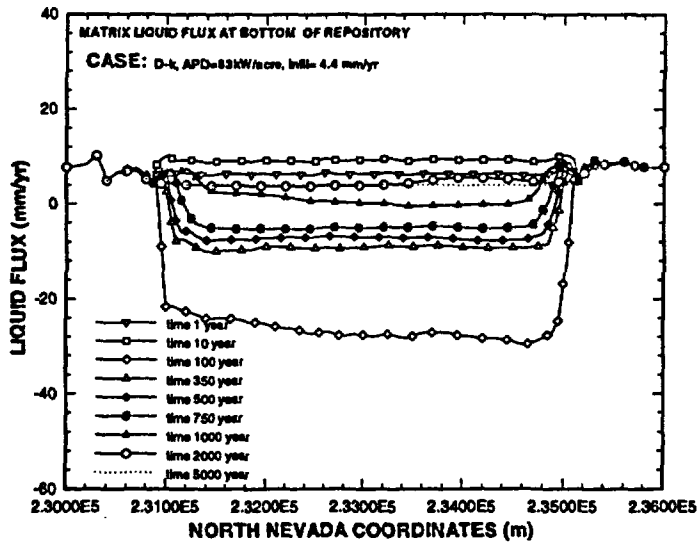


Figure 13.4.21
Matrix liquid flux crossing the bottom boundary of the repository; Dual-k, APD = 83 kW/acre, Infiltration 4.4 mm/year.

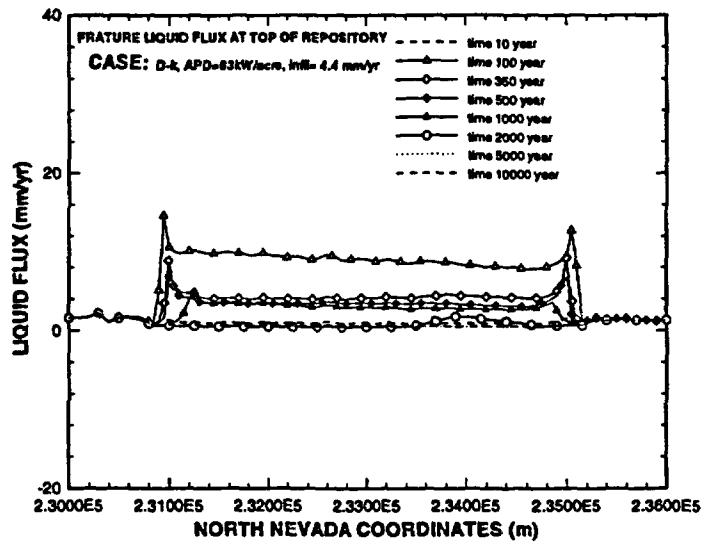


Figure 13.4.22
Fracture liquid flux crossing the top boundary of the repository; Dual-k, APD = 83 kW/acre, Infiltration 4.4 mm/year.

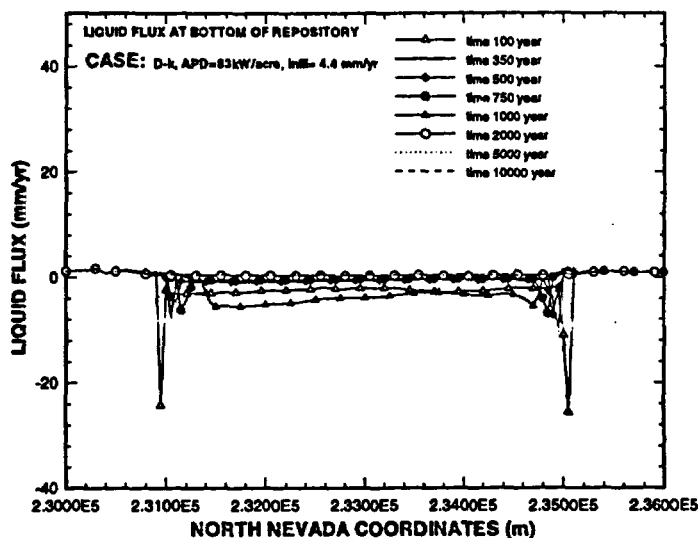


Figure 13.4.23
Fracture liquid flux crossing the bottom boundary of the repository; Dual-k, APD = 83 kW/acre, Infiltration 4.4 mm/year.

13.5 Comparisons of Percolation Fluxes Using the Two Modeling Approaches.

13.5.1 Liquid Fluxes

The simulated liquid percolation fluxes using the ECM and the dual-k approaches are compared in Figures 13.5.1 and 13.5.2. Figure 13.5.1 shows spatial distributions of the liquid fluxes along the repository at different times. The figure indicates a similar pattern of the flux variations over the thermal loading period. However, Figure 13.5.1 and 13.5.2 show that at an early time, 10 years, the ECM model predicts a much higher downward matrix flow into the repository. At the same time the dual-k model gives much smaller vertical flow, about at the ambient condition. The reason is a much "drier" condition obtained from the ECM model at this time. At later times, after 100 years, the two models give similar flux calculations. The flow crossing the bottom boundary of the repository, is very similar for the two models during the entire thermal loading period.

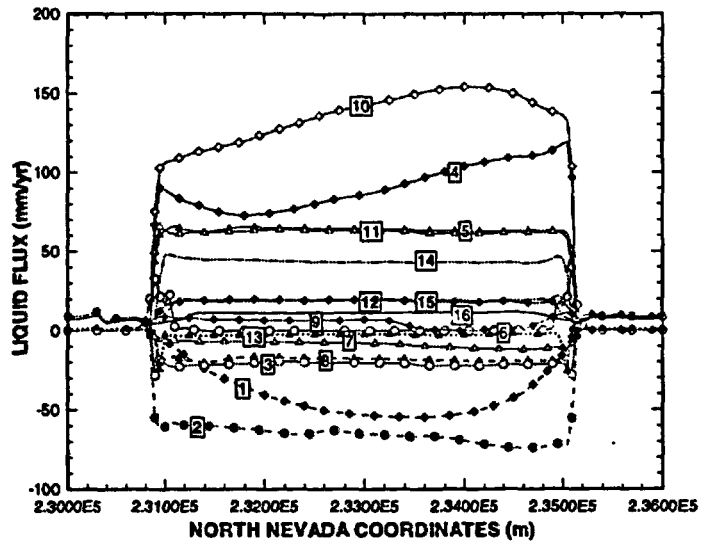


Fig 13.5.1
 Matrix liquid flux crossing the top and bottom boundary of the repository; for different infiltration rates; ECM and Dual-k, APD = 83 kW/acre; the numbers on curves correspond to the following; a) 1-3 is for (10, 50, 100 years), 0.1 mm/yr., bottom boundary; b) 4-6 is for (10, 100, 1000 years), 0.1 mm/yr., top boundary; c) 7-9 is for (10, 100, 1000 years), 4.4 mm/yr., ECM bottom boundary; d) 10-12 is for (10, 100, 1000 years), 4.4 mm/yr., ECM, top boundary; e) 13 is for 100 years 4.4 mm/yr., Dual-k, top boundary, fracture, f) 14-16 is for (100, 500, 1000 years) 4.4 mm/yr., Dual-k, top boundary, matrix.

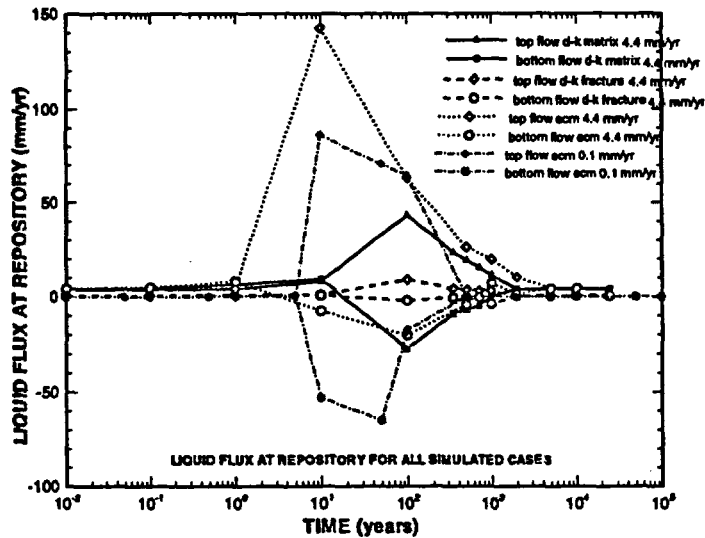


Figure 13.5.2
 Matrix liquid flux crossing the top and bottom boundary at the center of the repository; for different infiltration rates; ECM and Dual-k, APD = 83 kW/acre.

13.5.2
Gas Fluxes

Similar to the comparisons with liquid fluxes, discussed above, Figures 13.5.3 and 13.5.4 shows the simulated gas mass fluxes using the ECM and the dual-k approaches at the repository. As shown in the two figures, similar gas fluxes are predicted by the models. The only notable difference is at early times. During the early times the ECM model predicts much higher gas fluxes than those from the dual-k model. The gas flow is affected significantly by thermal loading near the repository, and increases by many orders of magnitude from 10 to 1,000 years. After 1,000 years, gas flow gradually decreases to ambient conditions.

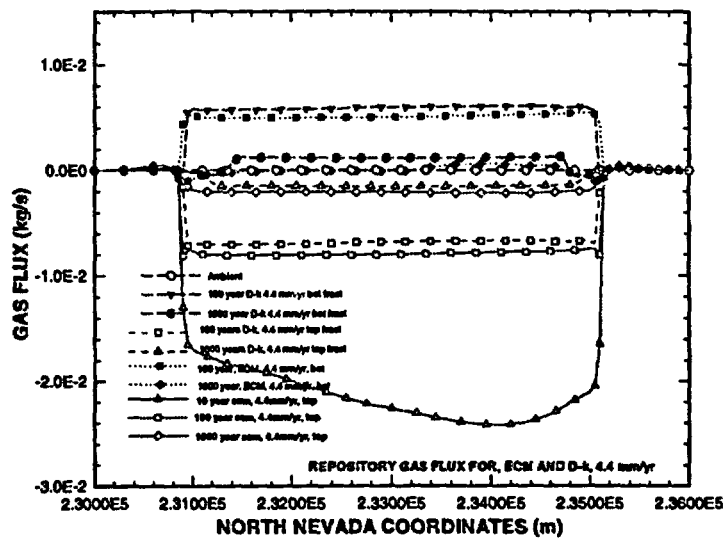


Figure 13.5.3
Matrix and Fracture gas flux crossing the top and bottom boundary of the repository; for different infiltration rates; ECM and Dual-k, APD = 83 kW/acre

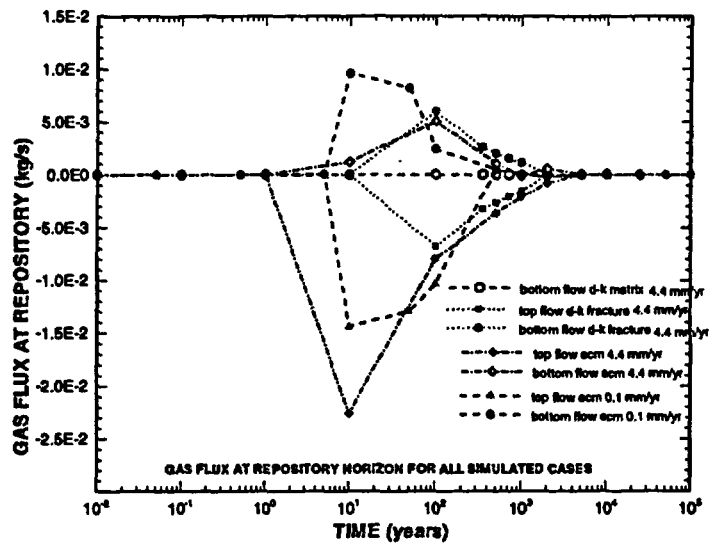


Figure 13.5.4
Matrix and Fracture gas flux crossing the top and bottom boundary at the center of the repository; for different infiltration rates; ECM and Dual-k, APD = 83 kW/acre.

13.6 Concluding Remarks

A systematic study of effect of thermal loading on the moisture, gas and heat flow in the unsaturated zone of Yucca Mountain has been carried out. The study is based on a 2-D north-south vertical cross-section, using both the ECM and the dual-k modeling approaches. The 2-D model covers both unsaturated and saturated zones to investigate the effects of the water table thermal conditions. Numerical simulations were carried out using the Q code TOUGH2, and the Q equation of state model EOS3, but are based on the non-Q geological model and parameters discussed in Chapters 2 and 3. Based on this data model and parameters, we obtain the following conclusions which are overall non-Q but are scientifically valid.

Examination of the temperature profiles during thermal loading indicates that the location of the model bottom boundary at the water table or at 500 meters below the water table does not affect repository thermo-hydrological behavior during the boiling period under thermal loading. However the coupled UZ-SZ model predicts about a 30°C temperature increase at the water table. This indicates that if a fixed temperature boundary is applied at the water table, the model may overestimate the rate of cooling of the repository.

Thermal loading at the repository results in significant changes in the a moisture and temperature distributions in the Mountain. Strong liquid and

gas flow fields several orders of magnitude above ambient develop near the repository. With the thermal loading scenario and the coarse grid used, the maximum temperature at the repository is 104°C for 0.1 mm/year infiltration case and about 95°C for the 4.4 mm/year infiltration. The average temperature of the boiling zone is about 95°C . This boiling zone is confined to the TSw hydrogeological unit.

The simulations show that there is substantial increase in near surface temperatures, about $10\text{-}20^{\circ}\text{C}$ in the area directly above the repository. The predicted maximum surface temperature occurs $750\text{-}1000$ years after thermal loading begins. The predicted maximum temperature for top of the Calico Hills is about 92°C for the 0.1 mm/yr infiltration case, but about $75\text{-}76^{\circ}\text{C}$ for the 4.4 mm/yr infiltration case. Therefore, at low infiltration rates, temperatures on top of the Calico Hills could lead to mineral changes in the Zeolitic units.

The intensity of the boiling and rewetting processes at the repository are controlled by the available heat and liquid at the repository horizon. For the low infiltration rate case, the repository "dries out" after 100 to 500 years. For the rock properties used in the TSw hydrogeological unit, heat pipe conditions develop above and below the repository in $10\text{-}100$ years. This enhances heat transfer from the repository to the water table and to the land surface. For the 0.1 mm/year infiltration case the boiling zone is very extensive. Dry-out conditions develop and last about 2000 years in this case. At a higher infiltration rate, 4.4 mm/year , no complete dry-out zone is predicted and the liquid always flows into the repository throughout the thermal loading cycle.

This study also shows that for a 4.4 mm/year infiltration rate, the ECM and Dual-k model approaches provide similar simulation results, in terms of temperature and moisture flow and distributions. The only difference is that at the early times, the ECM model predicts more extensive boiling conditions than that from the dual-k model. This is because the ECM model simulates a "drier" repository condition.

Even though various aspect of the thermo-hydrological behavior of the mountain under thermal loading are examined in this and previous studies (Wu et al, 1995), there is still a need for more detailed investigations using a 3-D UZ model to investigate the three-dimensional effects of thermal loading. Further comparison between the ECM and the dual-k approaches may be needed in modeling studies of thermal loading effects. Based on the 2D section studies, more effort should be focused on (a) incorporating updated geological models, and fracture/matrix rock and fault properties into the 3D model; (b) coupling UZ and SZ domains; (c) a sensitivity analysis using the ECM and the dual-k models; (d) effects on ambient moisture, gas and heat flow under different infiltration scenarios; and (e) coupling site-scale with drift-scale models.

13.7 References

- Buscheck T.A., and J.J. Nitao, Repository heat driven hydrothermal flow at Yucca Mountain, Part 1: modeling and analysis, Nuclear Technology Vol. 104, Dec., 1993.
- Buscheck, T.A., and J.J. Nitao, The impact of thermal loading on repository performance at Yucca Mountain, Proc. 3Rd Int. High-Level Radioactive Waste Management Conf., Las Vegas, NV, April 12-16, 1992, American Nuclear Society (1992); see also UCRL-JC-109232, Lawrence Livermore National Laboratory (1992).
ACCN: NNA.19930125.0078
- Buscheck, T.A., and J.J. Nitao, Modeling hydrothermal flow in variably saturated, fractured, welded Tuff during the prototype engineered barrier system field test of the Yucca Mountain Project, Proc. 5Th Workshop Flow and Transport Through Unsaturated Fractured Rock, Tuscon, AZ, Jan 7-10, 1991, University of Arizona; see also UCRL-ID-106521, Lawrence Livermore National Laboratory (1991).
ACCN: NNA.19911212.0238
- Flint, A.L., E.L. Flint, and J.A. Helvesi, Conceptual and numerical model of infiltration for the Yucca Mountain area, Nevada, U.S. Geological Survey, Water Resources Investigation Report-96, Denver, CO, 1996.
- Nitao, J.J., Numerical modeling of the thermal and hydrological environment around a nuclear waste package using the equivalent continuum approximation: Horizontal emplacement, UCID-21444, Lawrence Livermore National Laboratory (1988).
ACCN: NNA.19890317.0021
- Pruess K., TOUGH2 - A general purpose numerical simulator for multi-phase fluid and heat flow, Lawrence Berkeley Laboratory Report LBL-29400, Lawrence Berkeley Laboratory, Berkeley, CA; 1991.
ACCN: NNA.19940202.0088
- Pruess, K., J.S.Y. Wang, and Y.W. Tsang, On thermohydrologic conditions near high-level waste emplaced in partially saturated fractured Tuff. 1. Simulation studies with explicit consideration of fractures effects. Waste Resources Research Vol. 26 No.6, pp 1235-1248, June 1990.
ACCN: NNA.19910328.0073
- Ruffner, D., G.L. Johnson, E.A. Platt, J.A. Blink. And T. Doering, Drift emplaced waste package thermal response, Proc. 4Th High-Level Radioactive Waste Management Conf., Las Vegas, NV, April 26-30, 1993, American Nuclear Society (1993).
ACCN: NNA.19930303.0198

Thermal Loading Studies Using the Unsaturated Zone Model

Ryder, E.E., Comparisons of predicted far-field temperatures for discrete and smeared heat sources, Proc 4th Int. High-Level Radioactive Waste Management Conf., Las Vegas, NV, April 26-30, 1993, American Nuclear Society (1993).

Sass J. H., A.H. Lachenbruch, W.W. Dudley, Jr., S.S. Priest, and R.J. Munroe, Temperature, thermal conductivity and heat flow near Yucca mountain, Nevada some tectonic and hydrologic implications, U.S. Geological Survey report USGS-OFR-87-649; DE89 002697, U.S. Geological Survey, 1988.
ACCN: NNA.19890123.0010
DTN: GS950408318523.001 Non-Q

TRW, Thermal loading study for FY 1995, Report B000000000-01717-5705-00016, January 31, 1996.

Witherspoon, P.A., A. Freeze, F. A. Kulacki, N. Moore, F.W. Shwartz, Y.C. Yordos, K.A. Mrotek, and R.A. Levich, Report of the thermohydrologic modeling and testing program peer review record memorandum, Yucca Mountain Project Report, 1996.

**FRACTURE COATINGS AND
FRACTURE CHARACTERISTICS WITH
IMPLICATIONS FOR FLOW
ALONG FAST PATHWAYS**

A. Simmons

August 1996

14.1 Introduction

The main parameter needed for total system performance assessment and for testing key hypotheses of the DOE Waste Isolation Strategy is percolation flux at the repository horizon. Percolation flux will be the key factor in estimating seepage into drifts, waste dissolution, and in evaluating transport along fast pathways through the unsaturated zone. A series of borehole tests in the underground Exploratory Studies Facility (ESF) is planned to attempt to derive an *in situ* estimate of percolation flux from measurement of saturation and moisture tension in cores and by direct observation. Other lines of evidence should be used to support *in situ* investigations, however, and one of these may be through the depositional record of fracture coatings. The purpose of this chapter is to summarize knowledge of fracture characteristics and fracture coatings at Yucca Mountain and to propose a means of using this information to bound uncertainties in models of percolation flux through the repository horizon.

Mineral-lined fractures provide a good record of water movement and its relation to climate variations. The U.S. Geological Survey has undertaken a program of U-series and ^{14}C dating of calcite and opal to establish a history of deposition of fracture and cavity fillings and to bound past percolation flux through the repository horizon. Los Alamos National Laboratory has examined extensive sections of borehole core to characterize the mineralogy of fracture linings, to relate mineralogy to differences in water chemistry, hydrothermal conditions, and source regions, and to assess the role of fracture coatings in retardation of radionuclides. Glassley (1995) simulated the step-wise evaporation of water under equilibrium conditions (described later in this chapter) as a preliminary estimate of how solids might precipitate along fracture walls during a thermal pulse, with consequent alteration of flow properties. The combined information from these studies has allowed us to develop an approach to modeling predicted flux through the repository horizon based on precipitation and dissolution rates of solids with interaction between rock matrix and percolating water under steady and transient conditions.

The characteristics of fractures and their coatings may provide useful parameters for calibration of the site-scale unsaturated zone flow model, whose purpose is to characterize flow pathways and processes in the unsaturated zone at Yucca Mountain [see chapter 1 of this report (Bodvarsson et al.) for a thorough description of calibration of this model]. Fracture parameters such as aperture, orientation, and density are needed in calibration of the gas flow model component (Ahlers et al., 1995, 1996). Fracture coatings are important in

investigating fracture-matrix interactions and are key considerations for permeability and for determination of flow pathways and percolation flux [see chapter 10 (Fairley et al.) and chapter 11 (Sonnenthal et al.) of this report]. As such, use of fracture characteristics as a calibration parameter may allow us in the future to discriminate among conceptual flow models and to select a preferred model. At this time, however, we intend to apply many conceptual models and will see how fracture characteristics play a role in each of them. In this chapter we summarize fracture properties, mineralization, and age dating that provide insights into percolation flux in the past. We present previous modeling results and outline a planned approach for predicting flux at the repository horizon based on current knowledge, collaboration with others studying fracture coatings, and confirmation by *in situ* tests that will be augmented by model predictions.

**14.1.1
Quality Assurance Status of
Data and Software Used in
This Chapter**

Data in this chapter are taken from several key sources and are both qualified (Q) and unqualified (non-Q). Accession numbers and data tracking numbers, when available, are provided in the reference list. Data taken from full-periphery ESF maps are preliminary (non-Q) and have not been reported to the ATDT (Beason, 1996). Fracture characteristics data of Anna (1996) are qualified. Data taken from Rousseau and others (1996) in Table 14.1 are considered qualified because they rely on qualified core from boreholes. The acquired data as reported in the ATDT were not consulted, however. Information on mineral coatings presents a gray area because much of the core originally examined (G-1, G-2, GU-3, G-4, UE-25a#1) was not qualified, but all of the x-ray diffraction and petrographic analyses conducted by Los Alamos was done under a full QA program. Other cores examined by Los Alamos (UZ-14 and UZ-16) were qualified (Carlos, 1993; 1994). Modeling results of Glassley (1995) were reported as non-Q. Groundwater composition data (Beason et al., 1993) is non-Q. Information taken from regional stress studies (Stock and Healy, 1988; Swolfs and others, 1988) is non-Q. U-series and ¹⁴C ages from Paces (1996) are Q, but isotope ages taken from Szabo and Kyser (1990) are non-Q.

14.2 Fracture Distribution and Characterization

As previously stated, determination of percolation flux and knowledge of fracture-matrix interactions are important components of conceptual models of flow in the unsaturated zone at Yucca Mountain. Various aspects of the unsaturated zone flow model rely on knowledge of fracture distribution within the mountain and fracture characteristics, such as moisture tension [chapter 8 of this volume (Wu et al.)], temperature and heat flow calibration [chapter 9 (Wu et al.)], environmental isotope calibration [chapter 10 (Fairley et al.)], and thermal loading predictions [chapter 13 (Haukwa et al.)]. Characterization of fractures at Yucca Mountain has been undertaken by outcrop mapping, measurement in boreholes, and detailed mapping in the ESF. Throckmorton

and Verbeek (1995) conducted a regional study of fracture orientation on numerous outcrops, particularly the Tiva Canyon Member, at Yucca Mountain. They differentiated joints and fractures formed during initial cooling and contraction of the ignimbrite sheets from those that resulted from fracturing of the rock as a result of tectonic processes. They determined that the cooling joints either strike dominantly to the northwest (about N45°W) or to the northeast (N50°E) and dip near vertically. Along with a set of cooling joints that runs sub-parallel to the foliation direction of the tuff, the cooling joints form an orthogonal, three-dimensional network. Throckmorton and Verbeek (1995) also identified four sets of tectonic fractures within the North Ramp area, all of which are extensional. The first set strikes north-south and dips nearly vertically. The second set strikes northwest and generally dips steeply to the southwest. The third set strikes northeast and dips nearly vertically. The fourth set strikes east-west and is nearly vertical. Anna's (1996) characterization of fractures in the Tiva Canyon Member beyond the ESF starter tunnel showed fairly close agreement with three sets identified by Throckmorton and Verbeek (1995) as being tectonic fractures, although he did not differentiate as to whether the fracture sets were due to cooling or tectonics. One dominant orientation noted by Anna (1996) is N5°W, 76°SW; another is N54°W, 83°SW; and the third is N38°E and is vertical.

Rousseau and others (1996) indicated that the number of fracture sets and sequence of fracture formation in the Paintbrush nonwelded hydrogeologic unit (PTn) are similar to those documented for the welded units of the Paintbrush Group (Throckmorton and Verbeek, 1995). A network of cooling joints is developed where pyroclastic flows in the PTn are welded. The network consists of two orthogonal sets that are steeply dipping, and less frequently, a third subhorizontal set. A younger network of tectonic fractures consists of at least three sets of steeply dipping fractures, the oldest of which is oriented north-south, followed by northwest-trending, and then by northeast-trending sets.

Overall fracture intensity of the PTn is low and fractures are poorly connected within and between PTn lithostratigraphic units. Each of the PTn units appears to have its own fracture network with characteristic fracture spacing, intensity, and termination style; however, most of the fractures in the PTn are stratabound and terminate at welding breaks or lithologic breaks. In the ESF, PTn exposures have much lower fracture densities than observed in surface exposures (Rousseau et al., 1996). Nearly all PTn discontinuities in the ESF are minor faults with dips less than 75 degrees and slickensides that indicate predominantly dip-slip movement, most likely of tectonic origin. These planar zones are generally <4 cm wide and nearly all have thin (<0.5 cm) silica or calcite fillings (Rousseau et al., 1996). See chapter 10 of this volume (Fairley et al.) for details of effects of fracture coatings in reducing permeability through the PTn.

Fracture Coatings and Fracture Characteristics with Implications for Flow Along Fast Pathways

From detailed maps of the ESF, dominant fracture orientations were determined from equal area net plots (Beason, 1996). Within the middle non-lithophysal zone of the Topopah Spring welded unit (TSw) between stations 28+00 and 56+31, four orientations were indicated: a small set at N105°W, 20°SW; two dominant sets, one at N55°W, 83°SW, and another at N35°E, 80°NW; and a weaker set at N22°E, 80°NW. These agree quite well with the four sets of tectonic fractures identified by Throckmorton and Verbeek (1995) if the N22°E set is viewed as north-south. No dominant subhorizontal orientations were identified.

Fracture densities were averaged from histograms of boreholes USW UZ-14, USW UZ-9, USW NRG-7a, USW NRG-6, USW NRG-5, and USW NRG-4 (all in Rousseau et al., 1996). We compared this information to fracture density data determined from ESF mapping (Beason, 1996). Results are tabulated for comparison in Table 14.1. The borehole data show a somewhat higher fracture density in the TCw, PTn, and in the upper part of the TSw than that indicated by ESF observations, but otherwise compare quite closely. One possible way to account for this discrepancy is by different counting methods; every borehole fracture may have been counted, regardless of length, whereas some minimum cutoff length was set for fractures mapped in the ESF. Undoubtedly some fracturing of core also occurred during drilling.

Stratigraphic Unit	Borehole Designators						
	ESF	UZ-14	SD-9	NRG-7A	NRG-6	NRG-5	NRG-4
Tiva: xtal-rich		-	-	-	-	-	-
Tiva: xtal poor	1.4	-	-	-	4.3	-	-
Tiva: vitric		-	9.2	0.7	6.6	-	-
Yucca Mountain		3.3	3.4	1.4	-	-	-
Bedded Tuff	0.5	1.3	-	3.3	3.4	-	0.7
Pah Canyon		0.7	0.3	1.3	1.7	-	0.7
xtal-rich vitric-TSw	3	9.2	15.8	6.6	2.6	-	3.3
u. non-lithophysal-TSw	1.8	1.3	1	5.6	9.2	-	3.3
u. lithophysal-TSw	1.4	1.7	0.7	1.7	2.6	0.7	0.7
mid non-lithophysal-TSw	4.4	4.3	3.3	4.6	5	9.9	-
lower lithophysal-TSw	-	1.4	1.7	2.3	2.6	4.6	-
lower non-lithophysal-TSw	-	4.3	6.6	4.3	-	-	-
xtal-poor vitric-TSw	-	2.8	0.4	3.3	-	-	-

Fracture Coatings and Fracture Characteristics with Implications for Flow Along Fast Pathways

Table 14.1
Fracture densities (in fractures per meter) as determined from ESF and borehole data.

Stratigraphic Unit	Borehole Designators						
	ESF	UZ-14	SD-9	NRG-7A	NRG-6	NRG-5	NRG-4
Calico Hills Unit	-	0.7	1.7	-	-	-	-
Prow Pass	-	0.7	1.7	-	-	-	-
Bullfrog	-	0.7	-	-	-	-	-

1) Borehole data from Rousseau et al., 1996.
 2) ESF data from full-periphery ESF maps (Beason et al., 1996).
 3) Fractures were identified macroscopically by visual inspection.

Data from these boreholes indicate a similar trend that includes: 1) high fracture density near the contacts between vitric zones (both crystal-rich and crystal-poor) and non-lithophysal units in the TSw; 2) relatively higher fracture density within the non-lithophysal units as compared to the lithophysal units; 3) relatively lower fracture density within the PTn; and 4) very low fracture density within the Calico Hills Formation and the Prow Pass and Bullfrog Tuff Members of the Crater Flat Tuff.

Little information on fracture aperture distributions is available. Anna (1996) arrived at a range of apertures of 100-300 microns in the TCw using the cubic law and 500 microns by seismic velocity calculations. (The cubic law relates the aperture of a parallel plate fracture to its effective permeability). Aperture values used in this report (chapter 11; Sonnenthal et al.) were derived from air permeability data, using 2 darcies for horizontal permeability and 10 darcies for vertical permeability. Under the infinite parallel plate model, apertures were calculated to be 200 microns, which compares well to 180 microns used in TSPA (Wilson et al., 1993). The fracture spacing then used in the percolation flux model (chapter 11) is 3-15 fractures/meter, which is close to the moving average cited by Day and Beason (1996) for ESF fractures in the TSw. Furthermore, mineralogic data from borehole cores and the ESF substantiate the presence of wide fracture apertures in some places. In the upper lithophysal interval of the TSw, radiating stellerite crystals indicate significant open apertures (>3 mm) in some fractures (Carlos, 1994).

We can say something about the relationship between aperture and liquid permeability based on knowledge of the stress field, on pneumatic data, and on fracture density. Studies by Stock and Healy (1988) and Swolfs and others (1988) showed that the horizontal stress field in the North Ramp study area is 25-50% less than the vertical stress field. Because of this, loading across high-angle fractures will be less than across low-angle fractures and the apertures of high-angle fractures will tend in general to be larger than the apertures of frac-

tures with low-angle orientations, resulting in higher vertical permeabilities (Rousseau et al., 1996).

In situ pressure data (Rousseau et al., 1996) showed that lithostratigraphic units could be divided into four distinct pneumatic systems: 1) the TCw; 2) the Paintbrush nonwelded (PTn) hydrogeologic unit that includes the crystal-poor vitric base of the Tiva Canyon Tuff, the Yucca Mountain and Pah Canyon Tuffs with associated bedded tuffs and the crystal-rich top of the Topopah Spring Tuff; 3) the TSw; and 4) the pre-Topopah Spring bedded tuff, nonwelded tuffs of the Calico Hills Formation, and pre-Calico Hills Formation bedded tuff (CHn). Very little phase attenuation and amplitude lagging of the pressure signal occurred in the TCw, indicating little difference between pneumatic pressure of the unit and atmospheric pressure. Pneumatic characteristics of subunits within the PTn were quite different from one location to another. Locally the pneumatic characteristics of the crystal-rich vitric zone (PTn) appear to be dominated by fracturing. Pressure data from the TSw showed negligible attenuation and lagging of the pneumatic pressure signals transmitted across the vitric PTn. Pneumatic diffusivity of the TSw unit is very high; fractures within the TSw are apparently very permeable and highly interconnected within both the lithophysal and non-lithophysal units (Rousseau et al., 1996; Ahlers et al., 1995, 1996). ESF data indicate that fracturing in the TSw repository host sequence is likely strata bound (Day and Beason, 1996). Free-draining fractures were not observed. Air permeability measurements of ≥ 10 darcies were measured in the TCw and indicate a horizontal to vertical anisotropy of 10:1 in the TCw (Day and Beason, 1996), probably due to sub-horizontal unloading fractures. In contrast, a vertical to horizontal anisotropy of 3-10:1 exists in the TSw (Day and Beason, 1996), which is partially explained by the absence of sub-horizontal orientations in this horizon.

Regression analysis by Rousseau and others (1996) indicated a small correlation between increasing fracture density and increased air permeability. Although the exact cause of the relationship is unclear, it may be a function of fracture aperture. If fracture density and permeability are correlated in this way, a few fractures with large apertures will result in a high permeability value, whereas fracture zones with many small apertures will have lower permeability. Conversely, if there is little correlation, then a few fractures with large apertures will have equivalent permeabilities to many fractures with small apertures. Individual fracture permeabilities are often controlled by aperture, which in turn is influenced by the degree of mineral coatings on fracture walls. The next section summarizes our knowledge of fracture mineralization.

14.3 Distribution and Characterization of Fracture Coatings

In this section, fracture-lining minerals are described according to their stratigraphic location at Yucca Mountain, followed by generalizations about the sequence of their formation and compositional differences above and below the water table. Special attention is then paid to calcites because of their importance in age dating and in percolation flux determination, which is the key flow parameter in the unsaturated zone flow model. The location of boreholes from which fracture coatings were characterized from core sections is shown in Figure 14.3.1.

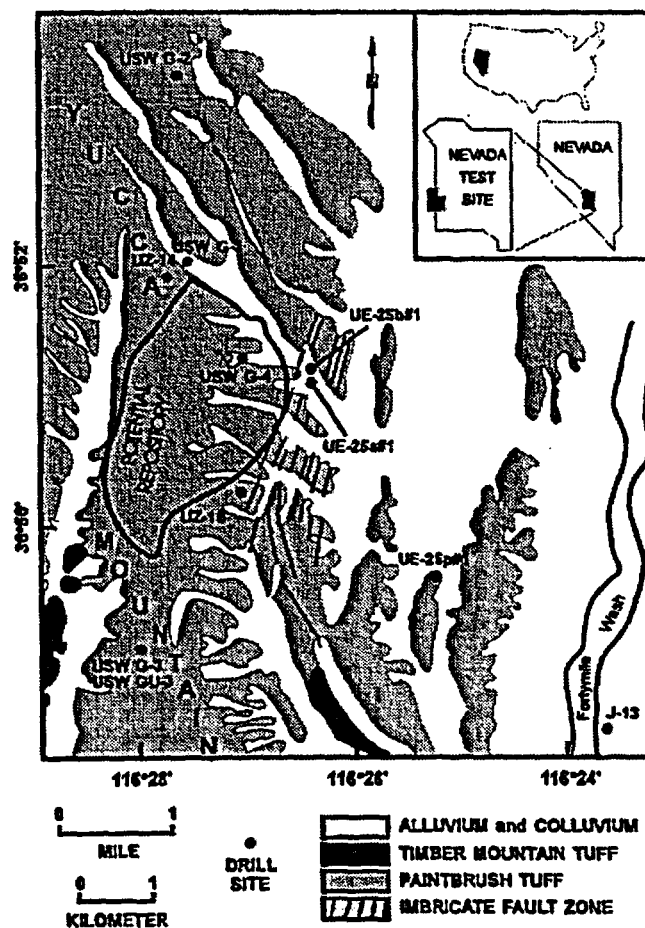


Figure 14.3.1
Location map showing Yucca Mountain, generalized lithologic units, and drillholes mentioned in this report from which core was analyzed by Los Alamos National Laboratory (modified from Carlos et al., 1995a).

**14.3.1
Stratigraphic Control**

In the upper part of the TCw in UE25 UZ-16, coatings are tridymite, calcite, opal, and clay. Below this, calcite is predominant and seals some fractures. Lower still in the Tiva, opal becomes more frequent along with ubiquitous calcite, and prismatic zeolites or tridymite may coat some fractures (Carlos, 1993). In drill core from USW UZ-14, there were no coated fractures in the Pah Canyon Member (Carlos, 1994).

According to studies by Carlos and others (1995a), in the Topopah Spring Member calcite and/or opal are the most abundant fracture coatings in the first 300 feet with increasingly abundant tridymite and quartz overlain by calcite at greater depths to the base of the upper lithophysal zone. Within the lithophysal zone, prismatic heulandite or stellerite coat some fractures and in some are overlain by calcite. Below the upper lithophysal zone the dominant coatings are manganese oxides frequently overlain by zeolites (mordenite, heulandite, or stellerite). Tridymite and hematite, along with fluorite, calcite, and opal coat some lithophysal cavities. The clays smectite, palygorskite, and sepiolite are common in fractures of the Paintbrush Group in drill core USW GU-3; smectite occurs in all drill cores and ubiquitously throughout the section at Yucca Mountain but its abundance varies. It usually is a late-formed mineral. Calcite commonly appears to be the last mineral deposited wherever it occurs, and its distribution across the mountain is variable (Carlos et al., 1991). This sequence is maintained to the vitrophyre. Few coated fractures exist below the vitrophyre in the Topopah Spring Member.

**14.3.2
Sequence of Coatings in
TSw**

The sequence of fracture coatings reveals something of water chemistry at the time of deposition and also provides insights into paleoclimate, which allows predictions to be made of future climate changes that can be used in the unsaturated zone flow model (see chapter 8 of this volume; Wu et al.). From the five drill cores USW G-1, USW G-2, USW GU-3, USW G-4, and UE-25a#1, Carlos and others (1991) derived a general sequence of mineral deposition in fractures in the devitrified tuff above the TSw vitrophyre. The first-formed fractures are connected to lithophysal cavities and originally contained tridymite, which may or may not now be transformed to cristobalite or quartz and may contain other vapor-phase minerals, e.g., hematite and/or fluorite. They appear to have been formed during degassing and devitrification of the tuff. The second fractures to form were smooth, nearly planar features which may be cooling fractures. The first coatings on these fractures are often manganese oxides that are sometimes coated with fine-grained mordenite crusts (Carlos et al., 1991). Since these fractures are often slickensided and since most of the tectonic movement at Yucca Mountain occurred prior to 10.5 Ma, it is postulated that these fractures formed prior to this time. After formation of fractures related to lithophysal cavities and planar fractures, the third type of fracture to form has rough walls without slickensides, and therefore formed after most of the tectonic activity had ended at Yucca Mountain. Coarse-grained stellerite,

heulandite, and mordenite appear to have formed after fine-grained mordenite that occurs in planar fractures.

Fracture-lining minerals in the Paintbrush Group vary both with depth and laterally across Yucca Mountain, whereas fracture coatings in tuffs below the Paintbrush Group are related to the mineralogy of the tuffs and follow a consistent pattern of distribution, with predominantly quartz, calcite, and manganese oxides in the devitrified intervals and mordenite and clinoptilolite in the zeolitic intervals minerals (Carlos et al., 1990, 1991; Carlos, 1993). Variation in zeolite fracture mineralogy can be attributed to small local differences in silica activity and chemical conditions (Chipera et al., 1993). At lower silica activities, (e.g., equilibrated with cristobalite or tridymite), stellerite and/or heulandite are most likely to form. The dominant control on heulandite vs. stellerite deposition is the concentration of dissolved cation species in the ground water (Carlos et al., 1995b), especially relative concentrations of Ca, Sr, and Mg. Furthermore, fractures in the Paintbrush Group contain a generally calcic suite of minerals, including calcite, Ca-zeolites (stellerite, heulandite, and mordenite), Ca-smectite, and Mn-oxide minerals, along with silica polymorphs. Pore water extracts from the Paintbrush Group where it is above the water table (Yang, 1992) have a different chemistry from that of groundwater from the Paintbrush Group below the water table (Benson et al., 1983), with markedly increased Ca, Mg, K, and Sr above the water table. Above the water table the Mn-oxides in fractures are principally lithiophorite, rancieite, and todorokite with exchangeable cations Na, K, Ca, Ba, and Ce (in order of abundance). Below the water table cryptomelane-group Mn-oxide minerals (cryptomelane, hollandite, coronadite) and lesser amounts of todorokite and pyrolusite occur. Exchangeable cations in this group include K, Ba, Pb, Sr, Na, and Ca. The Mn oxides are key past recorders of water-rock interaction (Vaniman et al., 1992). The contents of pore waters, compared with the composition of ground water below the water table, appear to be reflected in the fracture-lining mineral assemblages in the Paintbrush Group (Carlos et al., 1995a).

14.3.3 Calcite

Calcite occurs in many forms and in several generations throughout most strata at Yucca Mountain. For this reason, and because of the dependence on Ca concentration in groundwater with respect to formation of particular mineral species over others, calcite is the most important fracture coating to consider in calibration of the unsaturated zone flow model, with opal and silica polymorphs being second. The earliest-formed calcite is the most abundant calcite in the tuffs; it occurs in fractures, in faults, in the matrix, and as pseudomorphs of feldspar phenocrysts in deep intervals where hydrothermal alteration of 10.7 Ma is preserved (Bish, 1989). Calcite is generally found at shallower depths at Yucca Mountain only within fractures and as a late precipitate within lithophysal cavities. Calcites deposited in fractures above the water table have a broad range of ages; U-series ages of 26 to >400Ka have been obtained, and ^{14}C ages cluster between 33-45 Ky (Szabo and Kyser, 1990). Both

the U-series ages and the observed fracture-coating mineral sequences (Carlos et al., 1991) indicate that calcite is usually the latest formed authigenic mineral above the water table.

Szabo and Kyser, (1990) also analyzed opals and found that all gave U-series ages of >400Ka; however, fracture mineralogy studies (Carlos et al., 1991) show that some opal deposits formed on top of some calcites. The parageneses of fracture deposition suggest that calcite and opal may have been deposited under a variety of conditions beginning soon after tuff emplacement, but that deposition of calcite and perhaps opal continued during Pleistocene episodes of greater flow through the unsaturated zone and may be, at least with respect to calcite, continuing under present conditions (Vaniman et al., 1992).

Vaniman and Whelan (1994) noted a strong genetic connection between calcretes formed at the surface and calcites deposited in underlying fractures in the unsaturated zone. Szabo and Kyser (1990) suggested from stable isotope data that the coarser-grained calcites deposited in unsaturated fractures over the last 400 Ka formed from meteoric waters. Unsaturated zone calcite $\delta^{13}\text{C}$ values indicate input of pedogenic carbon, and $^{87}\text{Sr}/^{86}\text{Sr}$ increases from shallow ground water ratios near the water table to pedogenic values near the surface (Marshall et al., 1992). Whether all calcites and opal in unsaturated fractures were precipitated from solutions transported from the surface is unknown, but it is possible that downward transport was involved in the formation of the chain-structure clays, sepiolite, found in fractures as deep as 146 m, and palygorskite, found in fractures as deep as 253 m (Carlos et al., 1991; Vaniman et al., 1992).

14.4 Flux

As stated previously, stable isotope data indicate that the low-temperature calcite and opal deposits filling fractures and cavities at Yucca Mountain were deposited by meteoric waters percolating through the unsaturated zone. The coatings contain information about the times of deposition (U-series and ^{14}C) and the isotopic character of the waters from which they precipitated ($\delta^{13}\text{C}$, $\delta^{18}\text{O}$, $\delta^{87}\text{Sr}$, $^{234}\text{U}/^{238}\text{U}$). The mass of calcite and opal per unit volume of host rock may be related to the past water flux which transported the ions to sites where they precipitated from solution, possibly under evaporative conditions. Because it is known that the water table elevation varied by as much as sixty meters under wetter paleoclimatic conditions at Yucca Mountain (Levy, 1991), precipitation of minerals under unsaturated conditions must be demonstrated in order for assumptions of evaporative deposition to be valid. This demonstration has yet to be made rigorously, but mineral textures suggest that crystals grew in open spaces rather than under saturated conditions.

Fracture Coatings and Fracture Characteristics with Implications for Flow Along Fast Pathways

Paces (1996) sampled two types of secondary coatings in the ESF: 1) coatings lining steep-to shallow-dipping fractures and fracture zones (typically present on the footwall), and 2) mineral-coated floors of open lithophysal cavities that are typically intersected by narrow aperture fractures. Traces of major faults in the ESF (Bow Ridge, Drillhole Wash, and Sundance) are not mineralized. The lithophysal cavities typically contain a thin rim of high-temperature, vapor-phase minerals (tridymite +/- hematite) formed during cooling immediately following emplacement of the tuffs that are often overlain by coatings of calcite and silica representing deposition from low-temperature aqueous solutions. The form of silica near the base of the coatings is commonly non-layered to massive, where present, and is composed of undifferentiated quartz and chalcedony, with minor opal on or near the outermost, free-face calcite surfaces. Opal forms the latest depositional event on some samples and on others shows evidence of calcite overgrowths (Paces, 1996). Calcite constitutes the bulk of the volume of most occurrences, generally as even coatings of equigranular blocky prisms to thin, upright and sometimes large (≥ 2 cm) "blades" (Paces, 1991).

Steeply dipping fracture occurrences generally contain calcite, locally overlying earlier massive silica deposits. In fractures containing open space, which occur commonly and sometimes have centimeter-scale apertures (Paces, 1996), mineral deposition is preferentially located on the footwall with a complete absence of calcite on the hanging wall. Tall calcite blades and bubbly or laminated opal common to lithophysal cavities are unusual in steeply dipping fractures. Layering of the calcite and opal coatings indicate that mineral growth occurred progressively outward from the tuff matrix substrate into open space, which provides evidence of unsaturated conditions during mineral growth. Paces (1996) found no obvious differences in age between lithophysal cavity and fracture-filling occurrences. Therefore, the lithophysal cavities would be just as likely to experience percolation of water as the fracture pathways. Furthermore, the data suggest a crude correlation between decreasing isotopic age of fracture coatings and increasing depth in the ESF (Paces, 1996), which suggests the deposition of material from younger waters at greater depth, and may provide corroborating evidence for rapid percolation flux along fast pathways.

Preliminary data indicate that calcite and opal are not common in discrete zones which contain bomb-pulse ^{36}Cl (Peterman and Paces, 1996), but are consistent with slow percolation through the rock mass. They determined U-series ages of opal and calcite ranging from 37 to >500 Ky. ^{14}C ages of calcite range from 16 to >40 Ky. Peterman and Paces (1996) reasoned that calcite and opal were deposited under unsaturated conditions in which fractures and cavities were not filled with water, because deposition requires open space for evaporative concentration, but evaporative concentration has not been demonstrated conclusively. Typically the calcite and opal occur in fractures and cavities with openings greater than several millimeters. In single fractures with variable openings, narrow intervals contain little or no mineralization whereas wider zones are mineralized. Deposits are thicker and more complex on low-angle

features. Mineral textures suggest low-volume water films migrating down fracture surfaces into cavities. Isotopic exchange with the tuff matrix, as shown in $\delta^{13}\text{C}$ and $\delta^{18}\text{O}$ ratios, indicates modification of infiltrating water during percolation by rock-water interaction. Rock-water interaction may be unlikely under evaporative conditions, but rock-matrix interaction is a plausible mechanism for concentrating solutions to supersaturation and precipitation. According to Peterman and Paces' (1996) mass balance calculations, depositional rates were slow, on the order of micrometers per thousands of years, indicating low flux.

Crystal growth may be continuous over long time periods or may terminate, only to begin at a later time when conditions change. The growth rate is an important factor to consider in estimating percolation flux, but sampling methods often require material with different ages and isotopic apparent ages may not accurately reflect a single date. Whether or not an isotopic analysis represents an individual layer depends on the layer thickness and ability of the sampler to discriminate between layers. To address the issue raised by sampling, and the fact that measured isotopic ratios are dependent on sample thickness and growth rate, Peterman and Paces (1996) arrived at two end-member conceptual models to explain percolation flux based on mineral coating data, one in which continuous deposition occurs and one in which deposition is episodic (see Figure 14.4.1). Their continuous deposition model (Figure 14.4.16) assumes that growth of secondary minerals has occurred at a constant, but extremely low rate resulting in a continuum of infinitely thin layers. In the continuous deposition model, the isotopic ratio represents multiple layers so that the calculated age reflects a mixed age intermediate between the age of the outermost and innermost layers. When secondary mineral growth is very slow, younger ages will be obtained for smaller samples from the same surface and isotopes with shorter half-lives will yield younger calculated ages for the same material.

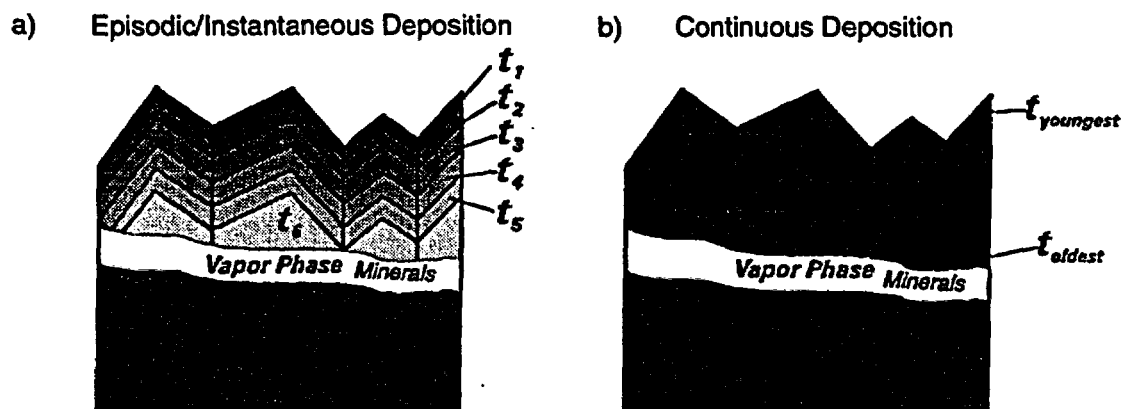


Figure 14.4.1
Schematic of two conceptual models of percolation flux developed by U.S. Geological Survey and based on mineral coating apparent ages (from Peterman and Paces, 1996). t = relative time of deposition of layers. a) episodic/instantaneous model; b) continuous deposition model.

If mineral deposition is episodic or instantaneous (Figure 14.4.1a), discrete mineral layers form over time intervals that are brief relative to the half-lives of the isotopic dating methods being used, and deposition is rapid relative to the interval between events. In this situation, measured isotopic ratios are uniform because the isotopic analysis represents a single layer, so that the calculated age represents the age of the discrete depositional event, and different isotopic clocks will record concordant ages for the same materials analyzed.

Natural systems of mineral deposition may experience periods of both rapid, episodic mineral growth as well as more continuous growth periods. However, data collected from ESF secondary mineral deposits are grossly consistent with the concept of continuous deposition, including both U-series and ^{14}C ages of outermost materials. Therefore, calculated ages are likely to reflect a mixture of ages of older and younger materials. As sampling methodology is refined and analyzed layers become smaller, apparent ages will more closely approximate actual intervals of deposition.

An understanding of depositional modes is critical for defining the style of percolation and secondary mineral deposition, as well as for addressing the connection between fracture-filling histories and time-dependent climate-based infiltration. These are important parameters for determining percolation flux. The implied flux would be substantially lowered under conditions of continuous deposition because the depositional record is extended over a much greater time interval.

14.5 Simulations of Formation of Fracture Coatings

Mineral coatings may form on fracture walls by different mechanisms depending on whether conditions are saturated or unsaturated. The relative importance of different mechanisms causing precipitation needs to be evaluated. Evaporation of water is one important consideration for establishing the nature of secondary precipitates. The solids that may develop will reflect the initial composition of water evaporated. Interaction of water with the rock matrix will tend to alter the initial composition with increasing time along the flow path. Little modeling has been done in this area in the Yucca Mountain Project to date, but as an initial attempt to investigate the effects of evaporation on the composition of precipitates that could form, Glassley (1995) considered scenarios in which water evaporation began with J-13 well water, a water that is close to equilibrium with New Zealand high-silica rhyolite similar in composition to that at Yucca Mountain (Bruton et al., 1993). J-13 was chosen as an initial bounding composition without consideration of rock-water interaction; more realistically, water flowing along fractures will experience some degree of interaction with surrounding rock that will modify its composition. However, these preliminary simulations applied to an extreme case in which evaporation occurs at high rates relative to dissolution or precipitation of rock components.

The evaporation of water was simulated using the EQ3/6 code (Wolery, 1992 a, b; Wolery and Daveiler, 1992) by removing water at a specified rate during reaction progress in an EQ6 simulation. J-13 water was evaporated at constant temperatures of 31°C and 90°C as well as at increasing temperatures between 31°C and 90°C using arbitrary relationships between amount of water evaporated and temperature change. Phases that precipitated included calcite, dolomite, silica polymorphs, saponite, and stilbite, as well as minor quantities of low-solubility fluorapatite, nontronite, and pyrolusite. Glassley's (1995) simulation results showed that the most significant variable controlling evolution of the water chemistry and the solids that precipitate is the composition of the coexisting gas phase (CO₂ and O₂) and whether gas and water are in equilibrium. This can be seen in the divergence of pH and Eh as evaporation proceeds in both cases. When the gas composition is fixed, pH and Eh vary inversely, whereas when CO₂ and O₂ are not fixed and the system is open, pH decreases and Eh increases due to changes in oxygen partial pressure. These effects influence total concentration of elements that occur in silicates and carbonates that have solubilities sensitive to moderate changes in solution pH. Further modeling under evaporative conditions should consider the consequences of reacting Topopah Spring Tuff with evaporating waters and should consider waters of various compositions, such as unsaturated zone pore water, perched water and saturated zone water. Additional modeling should consider precipitation mechanisms other than evaporation.

14.6 Uncertainties

The estimation of percolation flux from apparent ages of fracture coating minerals and from deposition models is a useful approach, but as with any approach, it carries associated uncertainties that must be remembered and accounted for. First, the possibility of dissolution of mineral coatings under wetter conditions must be accounted for, both in reaction-path models and in apparent age models. Paces (1996) looked for (but found little) evidence of dissolution in mineral textures and in U-series disequilibrium systematics with formation of thorium. In addition, as calculated ages approach the upper limits of an isotopic clock, the less capable they are of resolving age information for the material sampled.

One of the most important uncertainties to account for is the channelized nature of flow. The channelized nature of flow makes predictions of percolation flux integrated over the site a more difficult challenge than flux along a single fracture. *In situ* tests designed to address this problem are planned for the period of performance confirmation testing after the 1998 Viability Assessment. These tests will draw on numerous additional lines of evidence to determine flow. They will also test the travel time and pathway of water flowing through fractures. Thoma and others (1992) have shown that the existence of fracture coatings could significantly decrease the travel time and increase the travel depth of water flowing through fractures. If a fracture face is not coated, water can be imbibed across it into the adjacent porous matrix by capillary suction forces, once fracture flow has begun. However, if flow across the fracture face is inhibited by coatings or some other means, then flow down the fracture face could continue. The amount of water retained by the fracture will depend on the properties of the fracture, the matrix, and the fracture/matrix interface, in addition to the matrix saturation and the magnitude and duration of the infiltration event. Tokunaga and Wan (in press) measured the hydraulic conductivity of an unconfined block of Bishop Tuff over a range of near-zero matric pressure potentials. They demonstrated the capacity of natural, rough surfaces to conduct water at high velocities and under tension and showed that surface film flow, in addition to aperture contributions, may help explain observations of short travel times for solutes transported to deep, unsaturated fractured rock. Simulation of formation of fracture coatings as discussed in the next section should also help to estimate percolation flux by bounding scenarios for formation of coatings and may help to reduce uncertainties in the unsaturated zone flow model).

14.7 Summary and Recommendations

Fracture characteristics such as orientation, density, size, connectivity, aperture, and mineral linings are important parameters for calibration of the unsat-

urated zone site-scale flow model because they relate to fracture permeability and may be able to tell something about percolation flux. In addition, fracture characteristics are important to understanding fracture-matrix interactions, which play a role in selection of conceptual flow models (e.g., equivalent continuum, dual-porosity-dual permeability), and provide important constraints on travel-times along pathways (i.e. film flow along coated fractures may be much more rapid than along uncoated fractures).

ESF mapping has begun to improve our information base on fracture characteristics, particularly in three dimensions, but more data on fracture apertures, length, tortuosity, and connectivity are needed. The project has a good information base on fracture coatings and sequence of formation (from both Q and non-Q core), with some insights as to differences in paleoclimate conditions, hydrothermal alteration, groundwater chemistry, and silica activity that were likely responsible for producing variations in mineral coating composition. Calcite is the latest mineral to form, although it may also have formed during early episodes of deposition and is the mineral most likely to form fracture coatings under present conditions (This statement is based on non-Q data but is believed to be scientifically valid). Opal is also widely distributed along fractures and lithophysae and the potential for its deposition under present conditions needs to be investigated and modeled more thoroughly. U-series and ^{14}C apparent age dating by the U.S. Geological Survey (Peterman and Paces and associates) has led to the construction of two conceptual models of episodic and continuous deposition of calcite and opal (non-Q) that provide simple bounding conditions for evaporative precipitation which may help to constrain percolation flux through Yucca Mountain. Their models appear to be more consistent with a low flux concept over long time periods, whereas other models [i.e. film flow, insights from environmental isotopes and perched water occurrence and composition discussed in chapter 10 of this volume (Fairley et al.) and percolation flux modeled in chapter 11 of this volume (Sonnenthal et al.)] are more consistent with rapid flux along preferential fast pathways. It is likely that more than one flow regime, and perhaps at least three, exists at Yucca Mountain, and the relative contribution of each should be evaluated in terms of performance assessment (this statement is non-Q).

Bearing in mind the uncertainties (discussed previously) that are inherent in estimating flux from fracture coating apparent ages, the Yucca Mountain Project should continue to explore various models of precipitation, including those due to evaporation and supersaturated conditions, as well as examine models that account for dissolution and re-precipitation of mineral coatings. Reaction-path modeling using realistic water and mineral compositions along with rock-water interaction, and accounting for relative humidity/evaporative conditions in fractures, should help to constrain the physical and chemical conditions necessary for deposition of materials along fracture walls. This information can then be used in predictions of future conditions (e.g. plugging or opening of fractures under a thermal regime with attendant changes in perme-

ability) and predictions of percolation flux that can be used in calibration of the unsaturated zone flow model in conjunction with travel-time of environmental isotopes, moisture balance, and future climate.

14.8 References

- Ahlers, C.F., T.M. Bandurraga, G.S. Bodvarsson, G. Chen, S. Finsterle, and Y.S. Wu, Summary of model calibration and sensitivity studies using the LBNL/USGS three-dimensional unsaturated zone site-scale model, Yucca Mountain Project Milestone 3GLM107M, Lawrence Berkeley Laboratory, Berkeley, CA, 1995.
ACCN: MOL.19960208.0091-0097
DTN: LB092995312293.001 Non-Q
- Ahlers, C.F., C. Shan, C. Haukwa, A.J. B. Cohen, and G.S. Bodvarsson, Calibration and prediction of pneumatic response at Yucca Mountain, Nevada using the LBNL/USGS three-dimensional site-scale model of the unsaturated zone, Yucca Mountain Project Milestone OB12M, Lawrence Berkeley Laboratory, Berkeley, CA, 1996.
- Anna, L., Preliminary three-dimensional discrete fracture model, Tiva Canyon tuff, Yucca Mountain area, Nye County, Nevada, U. S. Geological Survey Water-Resources Investigation Report, Denver, CO, (draft).
DTN: GS960408312281.001 Q
- Beason, S., ESF, North Ramp and Main Drift, full-periphery geotechnical maps for stations 00+60 to 30+00, U.S. Bureau of Reclamation/U.S. Geological Survey (preliminary), Denver, CO, 1996.
- Benson, L.V., J.H. Robison, R.K. Blankennagel, and A.E. Ogard, Chemical composition of ground water and the locations of permeable zones in the Yucca Mountain area, Nevada, U.S. Geological Survey Open-File Report 83-854, Denver, CO 1983.
DTN: GS930308312323.001 Non-Q
- Bish, D.L., Evaluation of past and future alterations in tuff at Yucca Mountain, Nevada, based on the clay mineralogy of drill cores USW G-1, G-2, and G-3, Los Alamos National Laboratory Report, LA-10667-MS, Los Alamos National Laboratory, Los Alamos, NM, 1989.
ACCN: NNA19890126.0207
- Carlos, B.A., Preliminary description of fracture-lining minerals in drill core UE25 UZ-16, Yucca Mountain Project Milestone 4013, Los Alamos National Laboratory, Los Alamos, NM, 1993.
- Carlos, B.A., Preliminary description of fracture-lining minerals in drill core USW UZ-14, Yucca Mountain Project Milestone 4005, Los Alamos National Laboratory, Los Alamos, NM, 1994.

Fracture Coatings and Fracture Characteristics with Implications for Flow Along Fast Pathways

Carlos, B.A., D.L. Bish, and S.J. Chipera, Manganese oxide minerals in fractures of the Crater Flat Tuff in drill core USW-G-4, Los Alamos National Laboratory Report LA-11787-MS, Los Alamos National Laboratory, Los Alamos, NM, 1990.

ACCN: NNA.19900206.0163

DTN: LA00000000039.001 Non-Q

Carlos, B.A., D.L. Bish, S.J. Chipera, and S. Craven, Fracture-lining manganese oxide minerals in a silicic tuff, *Chemical Geology* 107, pp. 47-69, 1993.

ACCN: NNA.19931028.0002

Carlos, B.A., D.L. Bish, and S.J. Chipera, Fracture-lining minerals in the lower Topopah Spring Tuff at Yucca Mountain, Proceedings of the Second International High Level Radioactive Waste Management Conference, Las Vegas, Nevada, April 28-May 3, 1991, American Nuclear Society, La Grange Park, IL, pp. 486-493, 1991.

ACCN: NNA.19910206.0039

Carlos, B.A., S.J. Chipera, and D.L. Bish, Distribution and chemistry of fracture-lining minerals at Yucca Mountain, Nevada, Los Alamos National Laboratory Report LA-12977-MS, UC-814, Los Alamos National Laboratory, Los Alamos, NM, 1995a.

Carlos, B.A., S.J. Chipera, and Snow, Multiple episodes of zeolite deposition in fractured silicic tuff, Los Alamos National Laboratory Report MS4079, Los Alamos National Laboratory, Los Alamos, NM, 1995b.

Chipera, S.J., D.L. Bish, and B.A. Carlos, Equilibrium modeling of the formation of zeolites in fractures at Yucca Mountain, Nevada, paper presented at Zeolite 1993 Conference, Boise, ID, June 20-28, 1993.

ACCN: HQO.19940518.0009

Day, W. and S. Beason, Geological structure at Yucca Mountain, presentation given to U.S. Nuclear Waste Technical Review Board, Denver, CO, July 9-10, 1996.

Glassley, W.E., Report on near-field geochemistry: water composition changes due to evaporation, Yucca Mountain Milestone MOL26, Lawrence Livermore National Laboratory, Livermore, CA, 1995.

Marshall, B.D., J.F. Whelan, Z.E. Peterman, K. Futa, S.A. Mahon, and J.S. Stuckless, Isotopic studies of fracture coatings at Yucca Mountain, Nevada, USA, in *Rock-Water Interaction*, Proceedings of the Seventh International Symposium on Water-Rock Interaction, WRI-7, Park City, Utah, July 13-18, 1992, A.A. Balkema, Rotterdam and Brookfield, Capetown, South Africa, pp. 737-740, 1992.

ACCN: NNA.19921029.0034

Fracture Coatings and Fracture Characteristics with Implications for Flow Along Fast Pathways

Paces, J. B., Memorandum to R.W. Craig dated February 23, 1996 concerning "Submission of Milestone 3GQH455", 1996.
DTN GS960208315215.001 Q

Peterman, Z.E. and J.B. Paces, Paleohydrology - age control from U-series and ¹⁴C dating of calcite and opal in the ESF, presentation given to U.S. Nuclear Waste Technical Review Board, Denver, CO, July 9-10, 1996.

Rousseau, J. P., E.M. Kwicklis, and D.C. Gillies, Hydrogeology of the unsaturated zone, North Ramp area of the Exploratory Studies Facility, Yucca Mountain, Nevada, U. S. Geological Survey Water Resources Investigations Report, Denver, CO, 1996 (draft).

Stock, J.M., and J.H. Healy, Stress field at Yucca Mountain, Nevada, in Carr, M.D., and Yount, J.C., eds., Geologic and hydrologic investigations of a potential nuclear waste disposal site at Yucca Mountain, southern Nevada, U. S. Geological Survey Bulletin 1790, Denver, CO, pp. 87-93, 1988.
ACCN: NNA.19940318.0075
DTN: GS930283117481.001 Non-Q

Swolfs, H.S., W.Z. Savage, and W.L. Ellis, An evaluation of the topographic modification of stresses at Yucca Mountain, Nevada, in Carr, M.D., and Yount, J.C., eds., Geologic and hydrologic investigations of a potential nuclear waste disposal site at Yucca Mountain, southern Nevada, U. S. Geological Survey Bulletin 1790, Denver, CO, pp. 95-101, 1988.
ACCN: NNA.19920407.0019
DTN: GS930483117481.002 Non-Q

Szabo, B.J., and T.K. Kyser, Ages and stable-isotope compositions of secondary calcite and opal in drill cores from Tertiary volcanic rocks of the Yucca Mountain area, Nevada, Geological Society of America Bulletin 102, pp. 1714-1719, 1990.
ACCN: NNA.19910225.0068
DTN: GS930108315215.010 Non-Q

Throckmorton, C.K., and E.R. Verbeek, Joint networks in the Tiva Canyon and Topopah Spring tuffs of the Paintbrush Group, southwestern Nevada, U.S. Geological Survey Open-File Report 95-2, Denver, CO, 1995.

Tokunaga, T.K., and J. Wan, Water film flow along surfaces of porous rock, Lawrence Berkeley Laboratory Report, Berkeley, CA, 1997 (draft).

Thoma, S.G., D.P. Gallegos, and D.M. Smith, Impact of fracture coatings on fracture/matrix flow interactions in unsaturated porous media, Water Resources Research 28, pp. 1357-1367, 1992.

Fracture Coatings and Fracture Characteristics with Implications for Flow Along Fast Pathways

Vaniman, D.T., and J.F. Whelan, Inferences of paleoenvironment from petrographic, chemical, and stable-isotope studies of calcretes and fracture calcites, Proceedings of the Fifth International High Level Radioactive Waste Management Conference, Las Vegas, Nevada, May 22-26, 1994, American Nuclear Society, La Grange Park, IL, pp. 2730-2737, 1994.

ACCN: NNA.19940607.0171

DTN: LA000000000000075.001 Q

Vaniman, D.T., D.L. Bish, M.H. Ebinger, and S.J. Chipera, Precipitation of calcite, dolomite, sepiolite, and silica from evaporated carbonate and tuffaceous waters of southern Nevada, in Water-Rock Interaction, Proceedings of the Seventh International Symposium on Water-Rock Interaction, WRI-7, Park City, Utah, July 13-18, 1992, A.A. Balkema, Rotterdam and Brookfield, Capetown, South Africa, pp. 687-692, 1992.

ACCN: NNA.19930105.0015

Wilson, M.L., J.H. Gauthier, R.W. Barnard, G.E. Barr, H.A. Dockery, E. Dunn, R.R. Eaton, D.C. Guerin, N. Lu, M.J. Martinez, R. Nilson, C.A. Rautman, T.H. Robey, B. Ross, E.E. Ryder, A. F. Schenker, S.A. Shannon, L.H. Skinner, W.G. Halsey, J. Gansemer, L.C. Lewis, A.D. Lamont, I.R. Triay, A. Meijer, and D.E. Morris, Total system performance assessment for Yucca Mountain - SNL Second Iteration (TSPA-1993), Sandia National Laboratories Report SAND93-2675, Sandia National Laboratories, Albuquerque, NM, 1994.

ACCN: NNA.19940112.0123

Wolery, T.J., EQ3/6, A software package for geochemical modeling of aqueous systems: package overview and installation guide, UCRL-MA-110662, Pt. 1, Lawrence Livermore National Laboratory Report, Livermore, CA, 1992a.

ACCN: NNA.19921023.0028

Wolery, T.J., EQ3NR, A computer program for geochemical aqueous speciation-solubility calculations: theoretical manual, user's guide, and related documentation, UCRL-MA-110662, Pt. III, Lawrence Livermore National Laboratory Report, Livermore, CA, 1992b.

ACCN: NNA.19921218.0010

Wolery, T.J., and S.A. Daveler, EQ6, a computer program for reaction path modeling of aqueous geochemical systems: theoretical manual, user's guide, and related documentation (version 7.0) UCRL-MA-110662, Pt. 1V, Lawrence Livermore National Laboratory Report, Livermore, CA, 1992.

ACCN: NNA.19930127.0030

Yang, I.C., Flow and transport through unsaturated rock -- data from two test holes, Yucca Mountain, Nevada, Proceedings of the Third International High Level Radioactive Waste Management Conference, Las Vegas, Nevada, April 12-16, 1992, American Nuclear Society, La Grange Park, Illinois, pp. 732-737, 1992.

ACCN: NNA.19930112.0137

DTN: GS920908312272.011 Non-Q

LLYMP9610093
October 28, 1996

QA: N/A

YUCCA MOUNTAIN PROJECT

ERRATA MEMORANDUM

TO: Recipients of Lawrence Livermore Lab Informal Reports

FROM: LLNL-YMP Publications Office

SUBJECT: Page missing from reference list - UCRL-ID-125343, "*Thermodynamic Data Base Needs for Modeling Studies of the Yucca Mountain Project*" by C. Palmer, R. Silva and J. Bucher, 1996.

The attached page from the above subject report was inadvertently left out of the final print copy. Please add page 33 to your report reference section.

We apologize for the error.

References continued

- [62] Kittrick, J.A., 1971. "Stability of Montmorillonites: II. Aberdeen Montmorillonites," *Soil Sci. Soc. Amer. Proc.*, vol. 35, 820-823.
- [63] U.S. Department of Energy, 1988. "Site Characterization Plan, Alteration to the Environment Caused by Nonwaste Package Components, Yucca Mountain Site, Nevada Research and Development Area, Nevada," DOE/RW-0199, vol. VII, Part B, Chap. 8, Section 8.3.4.2H, p. 8.3.4.2-31. Nuclear Waste Policy Act (Section 113), Office of Civilian Radioactive Waste Management, Washington, D.C.
- [64] Brown, P.W., E. Franz, G. Frohnsdorff, and H.F.W. Taylor, 1984. "Analyses of the Aqueous Phase during Early C₃S Hydration," *Cement Concrete Res.*, vol. 14, 257-262.
- [65] Brown, P.W., J. Pommersheim, and G. Frohnsdorff, 1985. "A Kinetic Model for the Hydration of Tricalcium Silicate," *Cement Concrete Res.*, vol. 15, 35-41.
- [66] Glasser, F.P., D.E. Macphee, and E.E. Lachowki, 1987. "Solubility Modelling of Cements: Implications for Radioactive Waste Immobilization," *Mat. Res. Soc. Proc.*, vol. 84, 331-341.
- [67] Macphee, D.E., K. Luke, F.P. Glasser, and E.E. Lachowski, 1989. "Solubility and Aging of Calcium Silicate Hydrates in Alkaline Solutions at 25°C," *J. Am. Ceram. Soc.*, vol. 72, 646-654.
- [68] Wu, Z-Q. and J.F. Young, 1984. "Formation of Calcium Hydroxide from Aqueous Suspensions of Tricalcium Silicate," *J. Am. Ceram. Soc.*, vol. 67, 48-51.
- [69] Babushkin, V.I., G.M. Matveyev, and O.P. Mchedlov-Petrossyan, 1985. *Thermodynamics of Silicates*, Springer-Verlag, 459 pp.